A RECONFIGURABLE TACTILE DISPLAY BASED ON POLYMER MEMS TECHNOLOGY

A Thesis
Presented to
The Academic Faculty

by

Xiaosong Wu

In Partial Fulfillment
of the Requirements for the Degree
Docter of Phylosiphy in the
School of Polymer, Textile and Fiber Engineering

Georgia Institute of Technology
April 2008

A RECONFIGURABLE TACTILE DISPLAY BASED ON POLYMER MEMS TECHNOLOGY

Approved by:

Dr. Mark G. Allen, Advisor
School of Electrical and ComputerEngineering
Georgia Institute of Technology

Dr. Donggang Yao
School of Polymer,Textile and Fiber Engineering
Georgia Institute of Technology

Dr. Anselm C. Griffin
School of Polymer,Textile and Fiber Engineering
Georgia Institute of Technology

Dr. David G. Bucknall
School of Polymer,Textile and Fiber Engineering
Georgia Institute of Technology

Dr. Wayne J. Book
School of Mechanical Engineering
Georgia Institute of Technology

Date Approved: March 12, 2008

ACKNOWLEDGEMENTS

I would like to first thank my advisor Prof. Allen for his guidance, advice, mentoring, and research support throughout these years. He is one of the most brilliant professors I have ever met. Many thanks for giving an opportunity to work closely with him and getting a chance to explore the filed of MEMS. I have learned and grow tremendously under his guidance.

I would like to thank my doctoral committee members, Prof. Griffin, Prof. Book, Prof. Yao, and Prof. Bucknall for their evaluations of my research work. I appreciate their advice and support, which was invaluable to my degree completion.

Many thanks also go to both previous and current members of the Microsensor and Microactuator group who provided me initial guidance to start the right direction, helped with equipment trainings, and answer questions I had. In particular, I would like to thank Dr. Guang Yuan, Dr. Yoon-Kyu Yoon, Dr. Seong-O Choi, Dr. Seong-Hyok Kim, Dr. Chang-Hyeon Ji, Yanzhu Zhao, and Preston Galle for their support and help.

A note of thanks also goes to Dr. Haihong Zhu for helpful discussion on the mechanical design and system integration.

Life in the lab would be difficult and day-to-day would not have gone smoothly without the help from our supporting staff members. I would also like to express my gratitude to Mr. Richard Shafer and Ms. Purnima Sharma, for their help with the technical and administrative works.

Finally, I would like to thank my parents whose love for their children is unlimited and whose motivation for higher education is never wavered. I would never be here without them. I thank them for their unconditional love and support. I would like to thank my sister for believing in me. She is my best friend, my pioneer and strong supporter.

TABLE OF CONTENTS

LIST OF TABLES

LIST OF FIGURES

SUMMARY

A tactile display provides information such as shape, texture, temperature, and hardness to a user. Ultimately, a tactile display could be used to recreate a virtual object that may be stored in a computer. However, such advanced displays are not yet widely available, primarily due to the lack of low cost, large area, compact actuator arrays that can stimulate the large numbers of receptors of the user and that can also meet the high requirements for user safety and comfort. This research focuses on the development of polymer microfabrication technologies for the realization of two major components of a pneumatic tactile display: a microactuator array and a complementary microvalve (control) array.

In this work, the concept, fabrication, and characterization of a kinematically-stabilized polymeric microbubble actuator ("endoskeletal microbubble actuator") is presented. A systematic design and modeling procedure was carried out to generate an optimized geometry of the corrugated diaphragm to satisfy membrane deflection, force, and stability requirements set forth by the tactile display goals. A mass-manufacturable actuator has been fabricated using the approaches of lithography and micromolding. A prototype of a single endoskeletal bubble actuator with a diameter of 2.6mm has been fabricated and characterized.

In addition, in order to further reduce the size and cost of the tactile display, a microvalve array can be integrated into the tactile display system to control the pneumatic fluid that actuates the microbubble actuator. A piezoelectrically-driven and hydraulically-amplified polymer microvalve has been designed, fabricated, and tested. An incompressible elastomer was used as a solid hydraulic medium to convert the small axial displacement of a piezoelectric actuator into a large valve head stroke while maintaining a large blocking force. The function of the microvalve as an on-off switch for a pneumatic microbubble tactile actuator has been demonstrated.

Compared to present technologies, the microvalve developed can achieve large flow rate control due to its amplification mechanism, can avoid complex sealing problem because solid rather than liquid medium is used, and can form a dense valve array due to the small lateral dimension of the actuator used.

To further reduce the cost of the microvalve, a laterally-laminated multilayer PZT actuator has been fabricated using diced PZT multilayer, high aspect ratio SU-8 photolithography, and molding of electrically conductive polymer composite electrodes. This fabrication process is simple and straightforward compared to previous lateral lamination approaches. An 8-layer device has shown a displacement of 0.63 micron at 100V driving voltage, which agrees well with simulation results. The lateral lamination fabrication process provides a valuable alternative for making compact, low-voltage, multilayer piezoelectric micro-actuators as microvalve driving element.

A refreshable Braille cell as a tactile display prototype has been developed based on a 2x3 endoskeletal microbubble array and an array of commercial valves. The prototype can provide both a static display (which meets the displacement and force requirement of a Braille display) and vibratory tactile sensations. Along with the above capabilities, the device was designed to meet the criteria of lightness and compactness to permit portable operation. The design is scalable with respect to the number of tactile actuators while still being simple to fabricate.

CHAPTER 1

INTRODUCTION

1.1 Haptic Interface

Among the five senses humans utilize to interact with the environment, hearing and sight are the only two that have been actively explored in the development of current computer-human interaction systems. Although these systems show remarkable capabilities in generating the visual and sound components of virtual environments with good fidelity, they are mainly observational rather than interactive. There is no way to manipulate the environment. The additional usage of touch, termed haptic sensation, has the potential to become revolutionary means of communication for many areas of engineering, art, science, and medical diagnosis.

The human haptic sense is composed of two submodalities: the kinesthetic sense (muscles and joints), which responds to motions and forces exerted by the interaction of the body with the external environment; and the tactile sense (skin, or cutaneous), which is mediated by a variety of sensing receptors that respond to pressure, vibration, displacement, and temperature [1]. Ideally, a haptic interface should stimulate the nerves mapped to both components. In reality, the two submodalities are often addressed separately. Also, most work on haptic displays concentrate on the kinesthetic sense. Tactile displays are much less developed, especially considering the advancement in current tactile sensor technology. This is primarily due to the lack of low cost, large area, compact actuator arrays that can stimulate the large number of receptors of the user while simultaneously meeting high requirements for user safety and comfort.

1.2 Tactile Display –Applications and Specifications

Tactile displays can be divided roughly into three categories, based on the type of stimulation: electro-cutaneous, thermal, and mechanical. Electro-cutaneous displays

create touch sensations by passing a small electric current through the skin. Thermal-cutaneous displays provide stimulation of temperature variations [2]. Mechanical tactile displays can be further categorized by the stimulation modes, into vibration, lateral displacement (skin stretch), and skin indentation [3]. The majority of research effort is focused on the skin indentation tactile displays that distribute stimulations by inducing pressure on the skin via a number of actuators. They have received the most attention for various applications, as they offer the most significant potential to represent the fingertip deformations that occur in touch interactions with everyday objects.

Examples of applications for tactile displays can be found in [4]:

Braille systems

3-D surface generation

Teleoperation and telepresence

Sensation substitution

Laboratory prototypes for studying different tactile parameters

Entertainment

Online shopping

Mediated social touch

1.2.1. Refreshable Braille Display (RBD)

Braille, a worldwide standard system for displaying text information for the visually-impaired, is by far the most successful tactile tool. Braille is a tactile language consisting of raised dots of various arrangements that represent characters. One Braille cell, representing a single character, comprises an array of 2 x 3 dots. The international Braille building standard is shown in Figure 1.1 as an example [5]. Each dot is 1.5 mm in diameter with pitch of 1mm between adjacent dots.

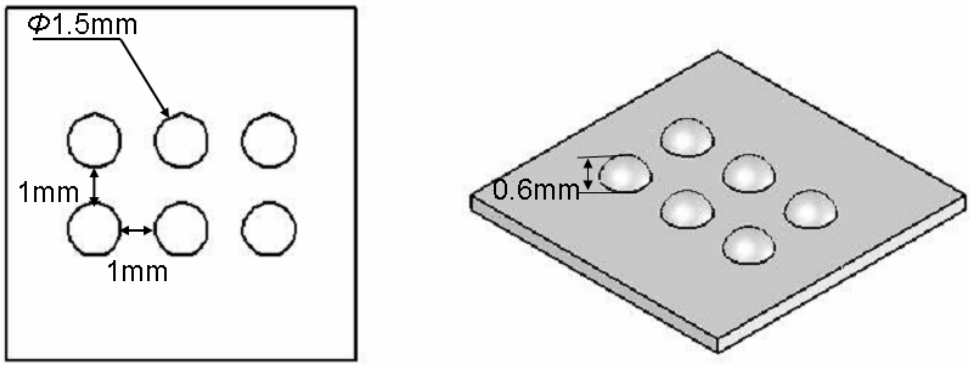

Figure 1.1 International building standard for Braille cell.

A refreshable Braille display (RBD) is a tactile display that converts text information from a computer to Braille dots for the blind to read. Most contemporary RBDs contain only one single line of 25 to 80 Braille cells due to the high manufacturing cost and large volume of piezoelectric bimorph actuators they utilize. Figure 1.2a shows an example of a commercial RBD that contains 80 cells [6]. Typical RBD devices start at 3,800 USD and might cost up to 20,000 USD with the most popular displays costing between 7,500 and 15,000 USD.

(a) (b)

Figure 1.2 (a) Powerbraille 80 from Blazie Engineering (b) Rotating Wheel from NIST.

The "Rotating Wheel" RBD has been developed by the National Institute of Standards and Technology mainly to reduce the cost of conventional Braille systems

(Figure 1.2b). The working principle of this device is to rotate the cells of Braille under the fingertip and the different characters are refreshed in this way. It is enough in this case to have three actuators for the whole device [7]. The drawback of this device is that the reader can not easily skip forward or retrieve backward in the middle of a paragraph and change reading speed easily and arbitrarily. The vibration caused by the rotating wheel also interferes with the reading.

Cost is not the only drawback when further applications of Braille displays are considered: 1) Displaying 2D graphical information is practically impossible due to the burdensome piezo-actuator module that drives the pin. 2) Portability in the current RBDs is quite limited.

1.2.2. 3-D Surface Generation System -Digital Clay

A team at the Georgia Institute of Technology is working on the development of a novel type of 3-D human-computer interaction device named “Digital Clay”. Digital Clay can be used both as an input and as an output device, either by a physically manipulation of the surface of the clay by the user or by computer controlled actuation of fluidic actuators embedded within the structure [8]. Figure 1.3 shows a schematic illustration of Digital Clay being used for shape editing.

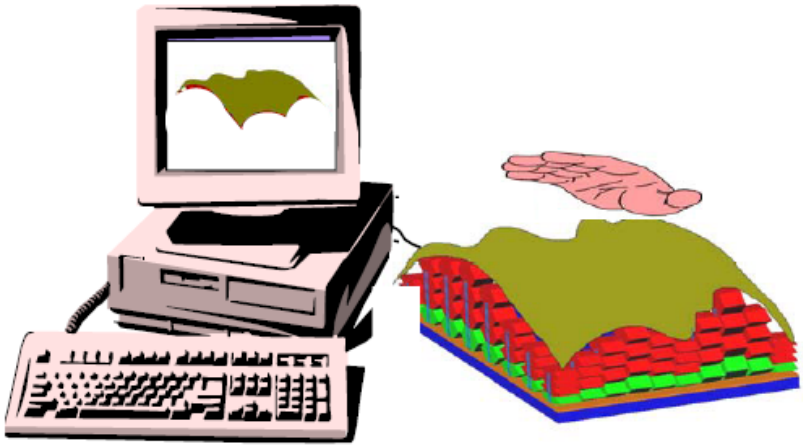

Figure 1.3 Schematic of Digital Clay in use

As a 3-D shape generation device, Digital Clay will not only allow improve the ease with which the visually impaired use computers, but can also be used to provide computer aided engineering design, training, rehabilitation, scientific research aid to medical diagnoses, 3-D dynamic mapping, game, and entertainment.

Since tactile actuators in tactile display act as pixels in visual display, one single actuator is often referred to as one "taxel" in tactile displays, or sometimes, "haptcel" in haptic display devices. Currently, a 5 x 5 cell array prototype has been designed and demonstrated with the following features (Figure 1.4): Resolution: 5x5 with 5mm center to center distance in 2-D linear pattern, Haptcel's linear speed: 0~50mm/second， Bandwidth: 40 Hz， Haptcel's stroke: > 48 mm [9].

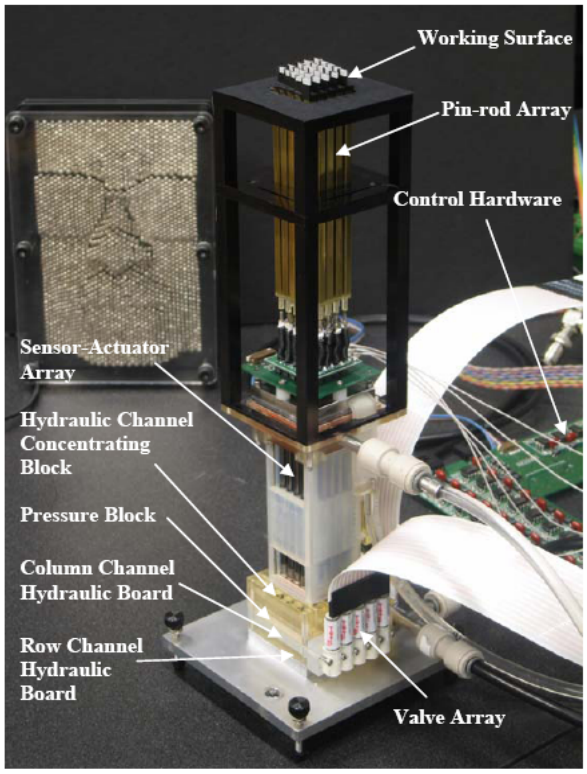

Figure 1.4 a 5 x 5 cell array prototype of "Digital Clay".

1.2.3. Teleoperation and Telepresence

Teleoperation is concerned with human control of a remote slave device (typically a robot manipulator arm) using a local master device. It allows the user to perform complex manipulation tasks in hazardous environments at no personal risk. Improved control of the slave manipulator can potentially be achieved by incorporating tactile feedback. Figure 1.5 shows three examples of the tactile display for this application, the ARRL haptic interface [10], the Toshiba DataGlove [11], and the CyberTouch [12].

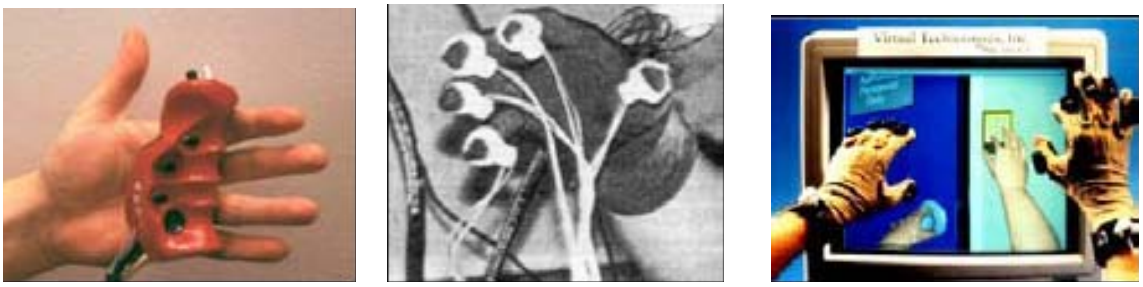

(a) (b) (c)

Figure 1.5 Tactile displays for teleoperation (a) ARRL Interface (b) Toshiba DataGlove (c) CyberTouch from Virtual Technologies

1.2.4. Laboratory Prototypes to Study the Different Tactile Parameters

Various laboratory prototypes have been built for research purposes such as studying the roles of mechanoreceptors and the development of texture renders. Konyo and Tadokoro [13] developed an interface using an electroactive polymer (EAP) known as IPMC or ICPF to reproduce the feeling of touching a surface (Figure 1.6a). Wagner et al. [14] proposed a tactile interface driven by RC servo-motors (Figure 1.6b). Ino at the University of Hokkaido developed another interface that gives thermal feedback [15] (Figure 1.6c).

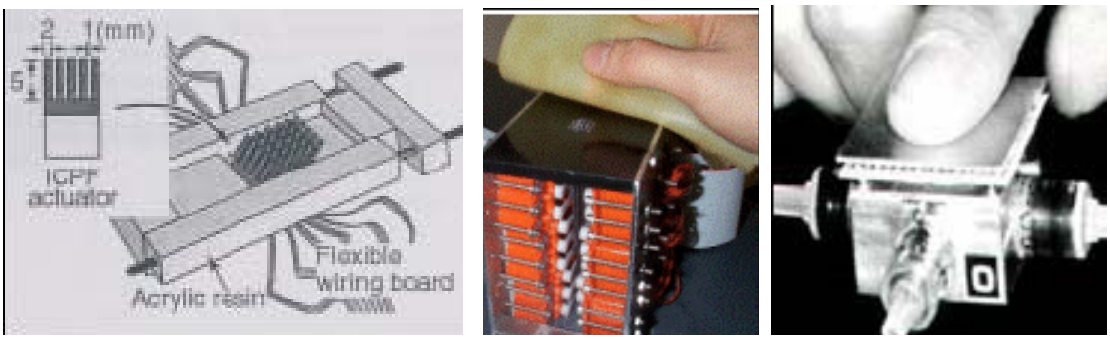

(a) (b) (c)

Figure 1.6 Tactile displays for tactile sensation research (a) Tactile interface based on EAP (b) Harvard tactile interface (c) Thermal tactile display.

1.2.5. Sensation Substitution

Optacon is a tactile-vision substitution system (TVSS) [16] that converts printed letters to a spatially distributed vibrotactile representation on the fingertip, using a miniature handheld camera (Figure 1.7a). The VITAL (stands for VIbro-TActiLe) display (Figure 1.7b) translates and shows a black and white picture on a 8x8 display [17].

(a) (b)

Figure 1.7 Tactile displays for sensation substitution (a) Optacon II (b) VITAL interface

1.2.6. Entertainment

According to a survey to 1,075 game players in North America [18], vibration feedback is a popular feature for the majority of gamers. Almost 3 in 4 respondents (72

percent) agree that rumble/vibration feedback enhances their gaming experience. The addition of other tactile sensations such as texture and temperature change will greatly enhance the experience of game playing.

1.2.7. Online Shopping

Nowadays one of the main drawbacks of online shopping is the lack of ability to touch the merchandise. Customers would be more willing to purchase online if they can gain a sense of what products would actually feel like, especially in the case of apparel such as clothing and shoes.

1.2.8. Mediated Social Touch

Mediated/remote social touch allows people to touch each other over a distance [19]. This application has interesting potential, such as the communication of simple ideas, establishing a feeling of connectedness between distant lovers, or the recovery from stress.

1.3. Requirements for Tactile Display and Research Motivation

A practical display should fulfill a large set of requirements and be capable of generating more than one sensation. The size of the display can be as compact as being mountable on a computer mouse and being able to stimulate only one fingertip; or it can be as large enough to allow large area 2-D or 3-D graphic information to be presented. The cost of making such devices should be low, and the display should be safe. Also, the displays should be able to resist prolonged exposure to skin abrasion, and be impervious to various contaminants including dirt and skin secretions. Finally, the displays should allow the freedom of active exploration, because active touch, which involves voluntary movement, provides more information than passive touch does.

Tactile displays should also meet specifications derived from physiological and psychophysical experimental data. However, taking into account the different sensing frequency ranges and indentation thresholds of different receptors under skin, it is not easy to provide a clear list of performance parameters for an ideal tactile display. In addition, some requirements, such as reconfiguration rate, are different for large screens and for compact displays. At present, physiological and psychophysical parameters in human haptic sensation have not been translated into parameters for tactile displays, as work is still ongoing in the field of tactile processing, and there are no standard experimental procedures to define the parameters [3]. The following table is an attempt to describe the basic requirements for "ideal" displays according to the physiology of touch.

Table 1.1 Tactile displays requirements

	Resolution	**Stroke**	**Force**	**Bandwidth**
Static (indentation)	1.5mm	0.5mm	50-100mN	1-3Hz
Dynamic (vibration)	1mm	10-100μm	10mN	10-300Hz

A prerequisite to meet all the requirements for a tactile display, which is based on a tactile array, is to make the appropriate choice of actuator technology. As can be seen in Table 1.1, the actuator needs to be miniaturized to meet the 1mm resolution requirement, and at the same time be able to provide large stroke and force within a frequency range of 1-300Hz. Also, to meet the low-cost requirement, mass manufacturability is another desirable feature of the actuator technology. Ultimately, it is desirable to have the actuator driving the tactile element to have the same order of the size of the element itself, in order to produce dense and multi-dimensional arrays of tactile display elements.

An actuator meeting all the requirements, which previously seemed unachievable, now becomes quite conceivable with the emergence of MicroElectroMechanical Systems (MEMS) technology. MEMS technology enables batch-fabrication and integration of miniaturized system containing both electrical and mechanical components with characteristic size ranging from nanometers to millimeters. The design parameters of an ideal tactile display fall within the capability of this technology, and the cost issue can be resolved through the batch fabrication offered by this technology.

MEMS technology can be implemented using a number of different materials. Polymers are excellent candidate materials for MEMS tactile actuators due to their great variety of material characteristics, low cost, mature processing technology in the macroscale, and safety. Elastomers are especially favorable by virtue of their compliant and durable nature that ensures comfort and endurance. A large number of polymer microfabrication technologies have been established over the past years.

These technologies can be divided into two groups: direct techniques that include photolithography [20-22], laser patterning [23], and stereolithography [24] and replication techniques that include miromolding and hot embossing [25-28].

1.4. Objectives

The goal of this research is to develop MEMS fabrication technologies for the realization of crucial elements, including a polymer pneumatic microactuator array and a complementary microvalve array, of a mass producible, low cost tactile display.

The objectives of this study are:

1. Design and fabricate polymer pneumatic microactuators (microbubbles) based on MEMS technology that are scalable and cost effective;
2. Demonstrate the microbubble actuators in a 2-D tactile display prototype, including an integrated, fully functional, refreshable Braille display and a vibrating 2-D tactile display;

3. Design and fabricate a microvalve to control each microbubble actuator;

4. Develop a MEMS piezoelectric stack microactuator as the driving element for the microvalve.

1.5. Thesis Outline

The body of this work is divided into seven chapters. In Chapter 1, the background and application of the tactile display are introduced. The specification of an ideal tactile display has been discussed which led to the objective of this thesis research work.

Chapter 2 reviews the literature on tactile display and MEMS tactile displays. Various actuation technologies for the tactile actuator and microvalve technologies are discussed in this chapter. A conclusion is drawn at the end of this chapter with regard to what type of components and actuation technologies will be developed for this thesis work.

Chapter 3 describes the design, fabrication and characterization of the pneumatic tactile actuator. The concept of a kinematically-stabilized endoskeletal microbubble actuator is introduced. Several polymer MEMS fabrication technologies are presented. These include the SU-8 lithography, micromolding, and stereolithography. The test results of these microbubble actuators are interpreted and analyzed in this chapter. Those results show the microbubble actuator developed met the criteria for being used in a tactile display and they were ready to be implemented.

Chapter 4 extends the work in Chapter 3 to a refreshable Braille cell based on a 2x3 array of the microbubble actuators described in Chapter 3. The modified design, the fabrication and assembly process as well as the characterization of the Braille cell are detailed in this chapter. Chapter 4 also demonstrates that the Braille cell, as a prototype of tactile display, can provide both static skin indentation (which meets the displacement and force requirements of a Braille display) and vibratory tactile sensations. However, as

the bulky size of the valves used hinders the realization of a light and compact Braille cell, there is a call for microvalves that can be densely packed.

Chapter 5 covers the design, fabrication and characterization of a solid-hydraulically amplified microvalve for controlling the microbubble actuator. This chapter introduces the concept of axial solid hydraulic amplification. It also reports the analytical and experimental analysis on the amplification mechanism. Both static and dynamic flow characteristics of the microvalve are reported. The successful controlling of a microbubble actuator by a microvalve is also demonstrated. Other potential applications of this microvalve are reviewed at the end of this chapter. To further reduce the cost of the microvalve, PZT stack actuator fabricated by MEMS technology needs to be developed as a replacement for the commercial ones used in the current microvalve.

Chapter 6 is devoted to present a simple lateral lamination scheme for the fabrication of multilayer piezoelectric actuators. A finite element analysis on the proposed actuator is described first. The characterization of an electrically conductive polymer composite as moldable electrode material is reported. The test result of an 8-layer piezoelectric actuator is shown and compared with the analytical result.

Chapter 7 provides a concluding summary of the whole work. The contributions of this thesis work are presented. Some recommendations on potential future research are discussed in the end.

CHAPTER 2

LITERATURE REVIEW

2.1. Actuation Technology for the Tactile Displays

2.1.1. Conventional Technology

A list of previously reported tactile displays categorized by actuation technology is as follows:

Electromechanical Tactile Displays:

1. Electromagnetic
2. Shape Memory Alloys (SMA)
3. Piezoelectric

Pneumatic Tactile Displays

Thermopneumatic Tactile Displays

Electrostatic and Electroactive Tactile Displays

Rheological Tactile Displays

Magnetorheological Tactile Displays

Surface acoustic wave (SAW) Tactile Displays

One of the earliest-reported technologies for tactile display is electromagnetic actuation [29-33]. Electromagnetic actuators offer high stroke and force, but the intricacy of assembly increases the cost of the display and interpixel magnetic interference limits the resolution. In the case of electric motors, the interfaces are rather bulky and cannot be portable. Piezoelectric actuators possess very fast response (>100 Hz bandwidth), and therefore have been used to build vibrotactile devices [34, 35]. SMA wire technology is widely used in tactile displays [36-40]. However, the drawbacks of SMA actuators are

their low bandwidth and high hysteresis. Pneumatic tactile displays use a pump as the main source of power and controll valves to modulate the fluid pressure against a flexible wall or rod at the end of the pipe [1, 41, 42]. They can generate high forces and strokes (2 N and 5 mm, respectively, in [1]) at a moderate bandwidth (5 Hz in [1]). Electrorheological (ER) fluids change their apparent viscosity when subjected to an electric field, and pressure difference can be obtained. The response is very fast (millisecond range) but the actuator size is rather large and high voltages are required [43]. Magnetorheological (MR) fluids behave in the same way as ER fluids, but using a magnetic field used to change viscosity. The response is also in the millisecond range, although the only results reported are from a low resolution prototype (diameter of a circular taxel is 4.5 cm) [44]. Thermopneumatic actuation utilizes the transition from liquid to gas to provide volume change [45] as an actuation principle for tactile displays. Electroactive polymer (EAP) arouses the interest of research yet they are not yet widely used [46, 47] due in part to the high driving voltages required. Surface acoustic wave (SAW) devices generate acoustic waves to stimulate the skin and generate a frequency-modulated sensation of roughness [48]. Each of the approaches discussed above has its own advantages and disadvantages. Due to the tradeoffs between bandwidth, integration capacity and cost, none of the approaches has been found optimal for tactile displays.

2.1.2. MEMS Technology

2.1.2.1 Non-pneumatic MEMS Microactuator

Several research groups turned to MEMS technology and several different types of tactile display have been fabricated. Among them, an electrothermal RBD requires 50s to raise and retrieve a dot, but no force data is reported (Figure 2.1a) [5]. A 6 x 4 array of sheet-type RBD based on an ionic polymer metal composite actuator has a maximum displacement of 0.4mm and 1.5gf (~14.7mN) generated force; however, it still

requires 0.9s to reach 0.2mm displacement (Figure 2.1b) [49]. A thermopneumatic tactile display is reported recently. The actuator array consists of a flexible diaphragm and a bottom plate, which are bonded to create a cavity between them. A micro needle and a micro heater are formed on the diaphragm, and the sealed cavity is filled with a liquid. These components are manually assembled to form a 3x3 arrayed actuator device with a dimension of 15x15x1 mm. The device has a needle displacement of 61μm with 457mJ input energy [50].

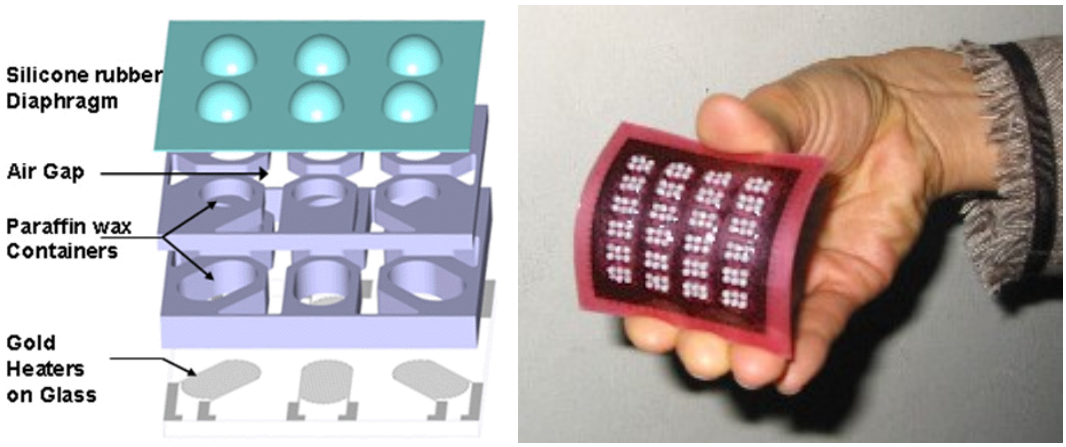

(a) (b)

Figure 2.1 MEMS tactile displays (a) An electrothermal RBD cell (b) A 6 x 4 array of sheet-type RBD

2.1.2.2 Pneumatic MEMS Microactuator

As can be noticed from their performance discussed above, tactile displays utilizing MEMS actuators face several challenges in design and fabrication. First, MEMS actuators are so miniaturized that may not survive the mechanical load of a touch. Second, the stroke length and force of the actuation may not be consistently large to cause a touch sensation. Such concerns can be addressed by the concept of pneumatic tactile display using an array of microvalves and an elastic surface layer proposed elsewhere [51]. The pneumatic display concept is illustrated in Figure 2.2.

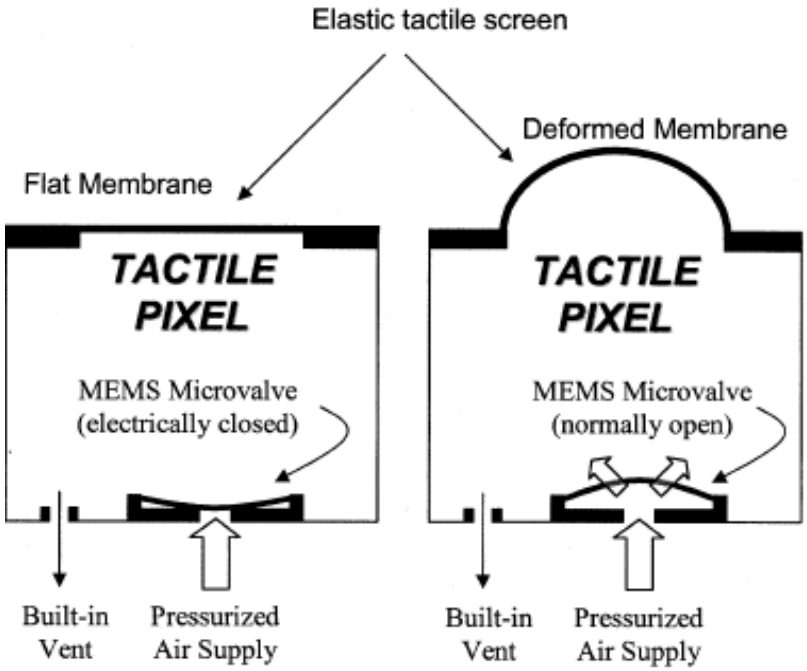

Figure 2.2 Schematic conceptualization of a single pixel of a pneumatic tactile display utilizing a MEMS microvalve [51]

In the pneumatic tactile display, the deforming elastomer membrane acts like a "tactile screen" to protect the microvalves against the excessive force of touch while amplifying their actuation and thereby increasing the tactile acuity of the display.

Previously, several micro balloon types of pneumatic microactuators made of elastomer such as silicone rubber or polyurethane (PU) elastomer have been fabricated using MEMS technology. These actuators have been used in end-effectors [52], acoustic impedance control [53], aerodynamic control [54], and a microfinger [55]. However, balloons formed from planar isotropic membrane typically deflect omni-directionally into a spherical shape, which makes them undesirable for indentation type of tactile display applications requiring more directional or linear movements as shown in Figure 2.3a. Furthermore, the relationship between pressure and radius is non-monotonic for balloon actuators, raising instability issues for balloon actuators under widely-varying external loads [56]. The external load varies from several tens of millinewton (when a finger is

actively touching the tactor) to zero (when the finger is lifted). This may cause a balloon actuator to accidentally hyper-inflate at the high driving pressure to inflate against a designed finger load when the load is not present.

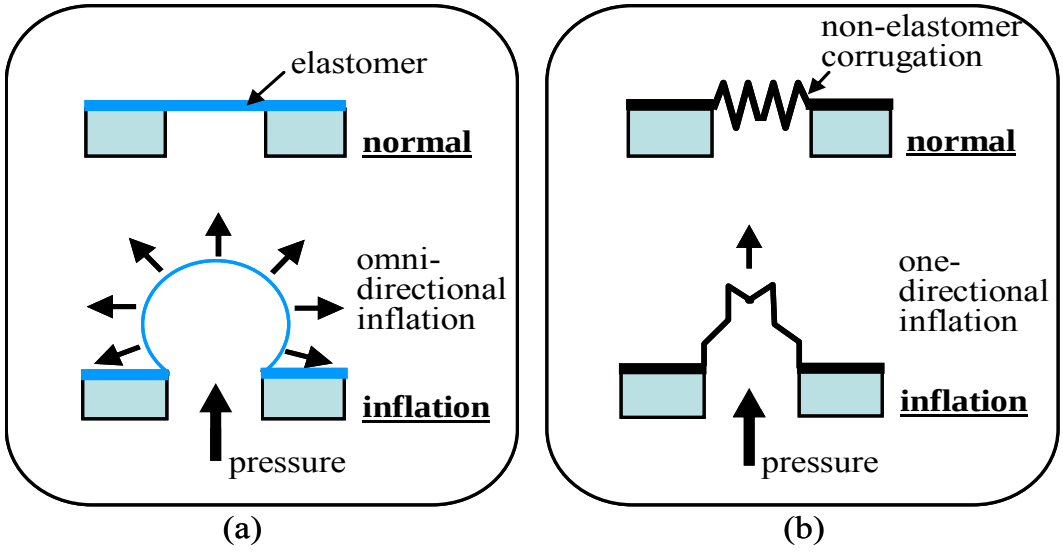

Figure 2.3 Polymer pneumatic actuators: (a) elastomer diaphragm actuator (b) non-elastomer based microcorrugated diaphragm actuator

Bellows actuators with corrugated side walls characteristically have large linear deflection in their axial direction. Their implementation in the vertical dimension using micromachining techniques has been demonstrated [57, 58]. For these vertical devices, however, the complexity of fabrication and process time increase as the number of corrugations of the bellows increases.

Alternatively, a corrugated diaphragm made of non-elastomeric material with relatively high modulus can be used to achieve axial deflection preferentially, as shown in Figure 2.3b. Corrugated diaphragms are widely used in altimeters, pressure gauges, speakers, and other applications that require large linear deflections. MEMS-based corrugated parylene diaphragms have been reported in the applications of pressure transducer and electromagnetic actuator [59, 60]. However, applications of tactile display require even larger deflection of corrugated diaphragms, which could not be

achieved through parylene corrugated diaphragms because they often have poor self-restoration properties under large deflection. When large deformation occurs, parylene corrugated diaphragms can reach a local stability point, not being able to return to the original position even after the removal of the external pressure.

2.2. MEMS Microvalve Technology for a Pneumatic Tactile Display

2.2.1. MEMS Microvalve Review

Solenoid valves represent the state of the art of miniaturized valves. However, these valves suffer from fundamental limitations such as relatively large mass and volume, and high power consumption. The mass limitation comes from the need for several turns of copper wire wound around a high-permeability core material for generating the requisite actuation force [61]. Although significant progress has been made in the miniaturization of solenoid valves, these miniaturized valves perform marginally with regard to valve actuation time or seating force.

Fine control of flow rate, relatively fast response compared to conventional valves, low production cost, small size, and low power consumption are examples of favorable microvalve characteristics. Over the last several decades, significant work has been done on the development of various types of MEMS microvalves. Thermopneumatically actuated valves were first designed and built by Angell and Zdeblick at Stanford University in the late 1970's [62, 63]. The principle of operation is illustrated in Figure 2.4.

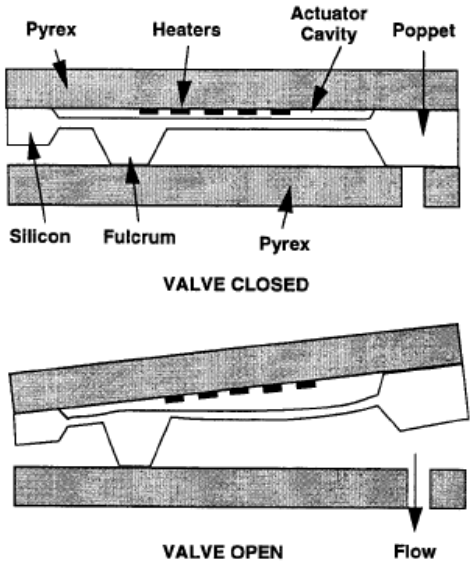

Figure 2.4 Thermpneumatic valve concept by Angell and Zdeblick et al.

Valve operation at pressure up to 3000psi has been reported for a normally-open type valve. Valve strokes of up to 150μm can be reached and power levels to open the valve range between 0.5 to 2W. Issues with this valve technology are its limited operating temperature range. Another limitation of this valve is the use of silicon-to-silicon valve seats. Any contaminant that may locate itself on the seat may cause the valve to stay open and cause leakage.

Shape-memory alloy can be deformed plastically at low temperatures. Upon heating above its so called transition temperature, the alloy "remembers" its original, or parent, state and returns to this state. Shape memory alloy valves have been operated at up to 100 - 400 psi inlet pressure [64], have achieved maximum flow rates of 6000 sccm and have response times of about lms to open and 20 ms to close [65]. Overall valve cycle times are larger again, due to the time required for cooling the valve, causing it to close.

Several normally-open electrostatic valve designs have been proposed. One such design was developed by Ohnstein et a1. at Honeywell and is shown in Figure 2.5 [66].

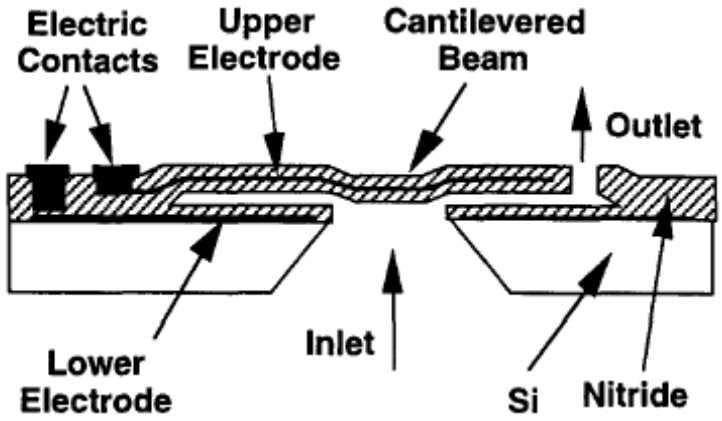

Figure 2.5 Electrostatic mcirovalve concept by Honeywell.

Here, a cantilevered beam is deflected by applying an electrostatic force between an electrode formed by a conductive layer embedded in the beam and another electrode embedded in the silicon material surrounding the seat. These metal electrodes are formed between silicon nitride passivation layers. Since the beam is formed through the removal of a sacrificial layer located between it and the valve seat, the valve is normally open and requires a constant force to bend the beam downward to close the valve. The valve could be closed with 30 V applied against pressures of about 2 psi and held closed against pressures of about 14 psi. At a voltage of 30 V, valve leakage was 6 x 10^{-2}sccm.

Several different types of electromagnetically actuated microvalves were found in the literature. However , due to current limitations of MEMS-machining techniques in providing a sufficient number of coil turns, these valve types typically use external coils or a permanent magnet, resulting in MEMS-hybrid valve versions [67, 68]. One such type is shown in Figure 2.6 [68]. This valve features a valve cap (poppet), integrated with a spiral-shaped spring, and fabricated using sputter-deposited thin film magnetic NiFe material. As can be seen when inspecting Figure 2.6, this valve requires a rather specific packaging arrangement, limiting its use in tightly integrated devices.

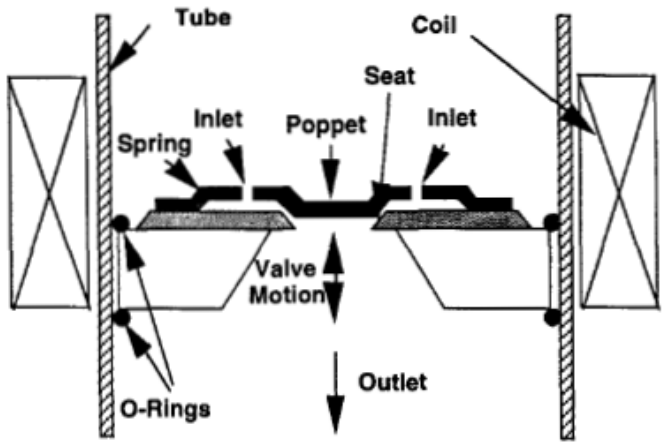

Figure 2.6 Electromagnetic microvalve concept by Yanagisawa et.al.

2.2.2. Microvalves for a Pneumatic Tactile Display

Until recently, the majority of the research effort has focused on developing microvalves for microfluidic systems that operate under low pressure and require low flow capability at low operating frequency [69-71]. Because of the limitations of micromachining processes and relatively small actuation force and stroke of the valve head, microvalves had limited use in applications that require regulation of flows with high flow rate at high differential pressure, for example a pneumatic tactile display. In a pneumatic tactile display system, each pneumatic actuator is an inflatable cell that is connected to two common pressurized reservoirs through a dedicated valve. The actively controlled microvalves should be able to regulate high gas flow under high pressure and at high frequency, have small volume and consume minimum power. Due to the inherent characteristics of the tactile display system and microbubble actuator inflated by a pressurized air source, a densely packed array of valves with switching frequency of up to 200Hz and capable of handling large differential pressure of 90kPa is required.

A MEMS electrostatic microvalve for an elastic membrane type pneumatic RBD was demonstrated in [51]. In that work, an elastomeric membrane was actuated under a pressure load of 27.6 kPa. As compared to previous bulk-micromachined microvalves

[72, 73], the new microvalve can perform against a larger pressure differential with similar actuation voltages. It can be noted, however, that even though the valves are fast (an advantage for tactile display applications), electrostatic microvalves are unable to operate at very high pressure levels due to the limited forces that can be provided by electrostatic means and thus appear not very useful for tactile display applications. For example, 27.6 kPa working pressure per Braille dot is far below the force requirement for finger exploration.

2.2.3. Piezoelectric Microvalves

Piezoelectric actuators are used in a number of applications such as precision positioners for metrology and interferometry, ultrasonic transducers, and scanning microscopes [74-76].

With its large bandwidth, large force, and low power consumption, piezoelectric actuators have become promising candidates for driving microvalves at high pressure and high frequency. However, their drawback is small stroke (up to 0.1% strain) even at a large applied voltage, which restricts orifice gap and in turn limits maximum achievable flow rate.

Prior approaches to overcome this drawback include adoption of a stack-type piezoelectric actuator, piezoelectric bimorph structures, and hydraulic amplification mechanisms [77-85].

The most adopted solution to this challenge is to use a stack-type piezoelectric actuator to drive the valve membrane. A piezoelectric-stack driven device in which the stack is attached directly to the moveable valve membrane is presented in the literature [77-80]. As an example, a piezoelectric microvalve designed by Esashi et al. is shown in Figure 2.7. The valve consists of a Pyrex wafer featuring the valve outlet and the valve seat, a silicon wafer, a so called movable “valve mesa” and integrated knife-edge sealing ring, and the piezoelectric actuator mechanism. The piezoelectric stack actuators are

connected to the valve body via a 9 mm long glass tube, bonded to the movable "valve mesa" using epoxy. The valve is normally closed and upon applying voltage to the actuator it contracts, thus pulling the movable valve mesa off the valve seat, opening the valve.

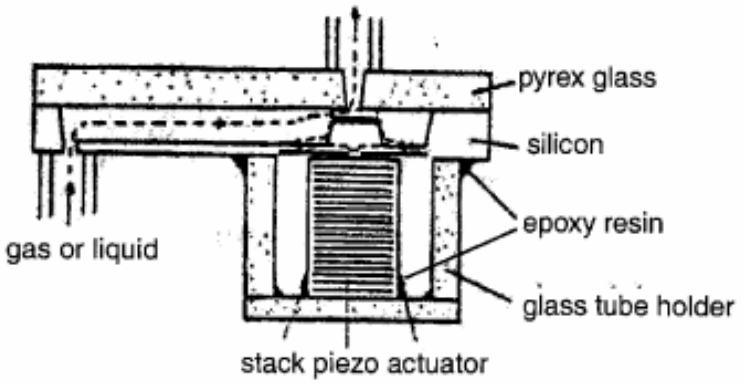

Figure 2.7 Piezoelectric valve based on PZT stack actuator concept by Esashi et al.

The valve requires between 50-100 V to open the valve, depending on pressure and flow rate. Flow rates through the valve were varied between 0.1-90 sccm by varying the voltage between 0-100 V at a pressure of 0.75 atm. The common disadvantage of all the piezoelectric microvalves using a stack actuator is: in order to attain reasonable valve deflection, the piezoelectric stack material is required to be excessively long, and therefore the overall device mass and size are too large.

A large valve stroke of 80μm was achieved for a piezoelectric bimorph microvalve, but was limited to very low differential pressure [81].

A unique solution to this problem is to design a microvalve with a means to hydraulically amplify the stroke of a piezoelectric bulk-type material into a significantly larger (l0x-40x) valve membrane stroke, yet still maintain high frequency, high force capability [82-85].

Roberts et al. presented a hydraulically amplified PZT cylinder-driven microvalve with large stroke (20-30μm) and a 40x hydraulic amplification with high bulk modulus

silicone oil were obtained in [82, 83]. However a complex fabrication process including 22 photolithography steps was required for the microvalve shown in Figure 2.8.

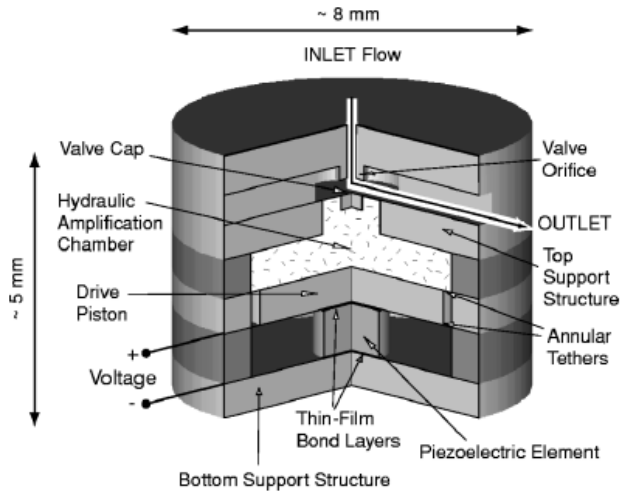

Figure 2.8 A schematic of the piezoelectrically driven hydraulic amplification microvalve by Roberts et al.

Rogge et al. demonstrated a normally-closed polymer microvalve with PZT bending disk and solid hydraulic amplification as shown in Figure 2.9. Silicone gel serves as a transition medium to increases the displacement of the piezo disk up to the 25-fold. It also simplifies the manufacturing process and allows a flexible adaptation to different pressure requirements up to a differential pressure of 150 kPa switched with 300V.

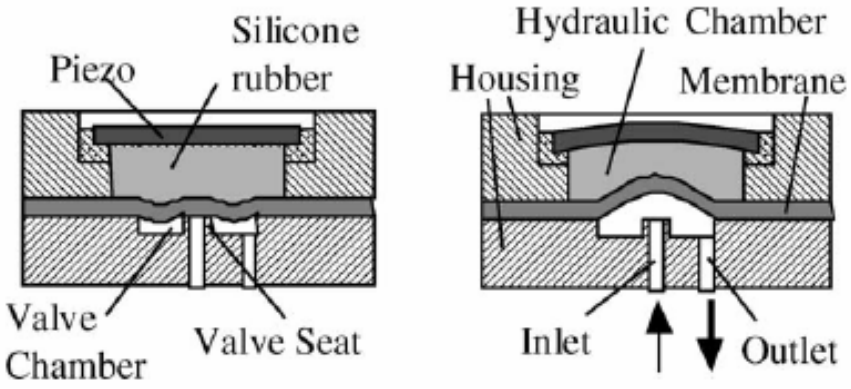

Figure 2.9 Schematic design of the solid-hydraulically amplified microvalve by Rogge et al. in the open state (left) and the open state (right).

The overall dimensions of the valve are 13mm × 13mm × 3mm, and the inner diameter of the valve seat is 200μm. However, the large lateral dimension (13mm × 13mm) of the PZT disk used prevented the formation of a dense valve array [84].

2.3. Conclusion

Based upon the literature review on tactile display and current technology, the realization of a reconfigurable tactile display device relies on the development of the following two components and corresponding technologies.

In chapter one, it is mentioned that the tactile display devices should meet a series of requirement including stroke, force in order to provide both a static display (which meets the displacement and force requirement of a Braille display) and vibratory tactile sensations. Along with the above capabilities the device should be light and compact permitting portable operation. The design should be scalable with respect to the number of taxels while still being simple and cost-effective to fabricate. After reviewing all the available actuation technology, it is concluded that pneumatic actuation would be the best candidate. What needs to be developed is a pneumatically-driven, directional-inflatable microbubble actuator.

Next, because pneumatic operation requires fluidic control components, microvalve needs to be developed. Based on the literature survey on the MEMS microvalve technology, piezoelectric actuated microvalve is superior for the application of a pneumatic tactile display. However, some kind of amplification mechanism needs to be adopted and implemented with the piezoelectric actuator because the increase of the piezoelectric stroke is a big challenge.

The final step is to develop integration technology including assembly the display, packaging process and testing.

The next chapter describes the design, modeling, fabrication and characterization a polymer pneumatic actuator array as the actuation scheme for the tactile display system.

CHAPTER 3

ENDOSKELETAL MICROBUBBLE ACTUATOR

3.1 Concept of Endoskeletal Microbubble Actuator

The concept of a mass-manufacturable endoskeletal microbubble actuator capable of reversible vertical deflection is shown in Figure 3.1. The microbubble actuator has a kinematic stabilization design by combining two polymeric layers with complementary functions as shown in Figure 3.1: a microcorrugated parylene diaphragm layer as a "skeleton" to provide a directional deflection in a desired axial direction while suppressing undesired lateral deflections and an overcoated elastomer diaphragm layer as a "skin" to help the extended membrane recoil to its original shape, ensuring diaphragm stability.

In this study, the skeletal corrugated sections of the microbubble array are obtained using a single lithographic mask through continuously-rotating inclined exposure [21, 22] followed by sacrificial material molding and polymer coating. This approach not only makes endoskeletal bubble actuators mass-manufacturable, but can also be scaled down to even smaller dimension, if required.

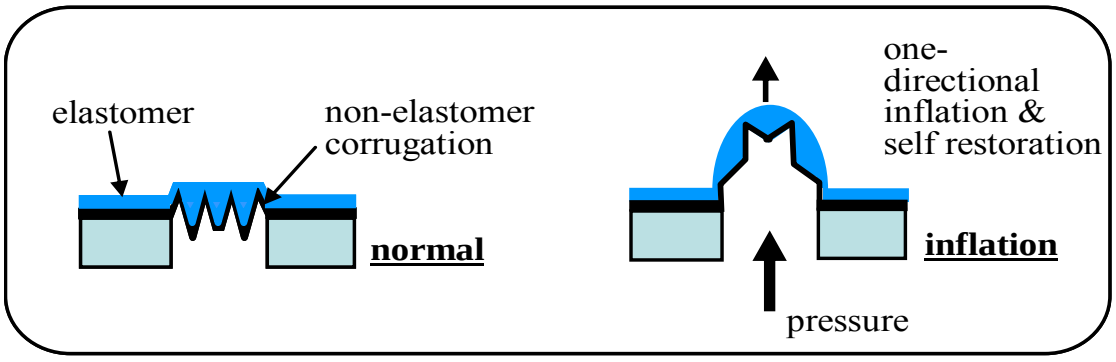

Figure 3.1 Endoskeletal microbubble actuator concept.

3.2 Materials for Endoskeletal Microbubble Actuator

The material for the skeleton and the skin are considered as the first and essential step in developing the endoskeletal microbubble actuator. The skeletal material, from which the corrugated diaphragm will be made, should be flexible in order to provide large deflection. On the other hand, the skin material should have high elasticity and an even lower Young's modulus than the skeletal material so that the overall stiffness will be dominated by the skeletal material.

3.2.1. Skeletal Material

Parylene C (poly-monochloro-para-xylylene) has been selected as the skeletal material due to its low Young's modulus and conformal coating capability over microstructures [86]. Moreover, its low permeability to gas and moisture and high chemical resistance make it suitable for the application of pneumatic and hydraulic actuators.

Parylene is the generic name for members of a series of thermoplastic polymer: poly-para-xylylene. Parylene's unique properties include precise conformity to substrate topography, pin-hole free coverage in very thin layers, and the ability to penetrate and coat complex surfaces. Parylene synthesis and deposition is best described by a vapor deposition polymerization process (VDP) as shown in Figure 3.2 [87].

Materials to be coated are placed in the chamber on the right (**Error! Reference source not found.**). High-purity parylene dimer, a white, crystalline powder, is placed in the vaporizer zone to the left. The system is closed and evacuated until the proper vacuum is reached. The temperature of the vaporization zone is gradually raised to around 160°C. The parylene dimer then begins to sublime forming a gas. As the pressure increases in this zone, the gas moves downstream into the cracking or pyrolysis furnace maintained at 690°C. As the parylene dimer passes through this heated zone the molecule is split to form two identical reactive monomers.

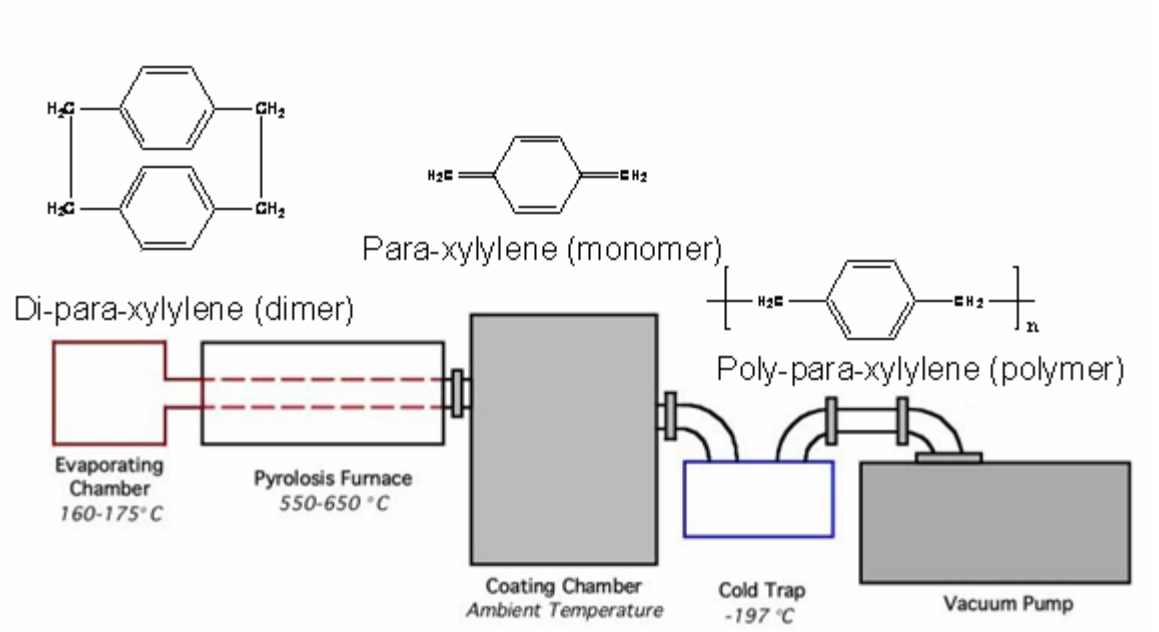

Figure 3.2 Parylene deposition map

These reactive molecules stream out of the furnace zone into the deposition at room temperature. By this time the parylene molecules have very high energies, and thus would bounce around the chamber many times before finally polymerizing on the surface to be coated. This is the reason for the great penetrating power of parylene. No liquid phase has ever been isolated, and the substrate temperature never rises more than a few degrees above ambient. Additional components of this system are the mechanical vacuum pump and associated protective cold traps.

Although a variety of substituted dimers are commercially available, such as Parylene N, Parylene C, and Parylene D, the most commonly used parylene is Parylene C. Figure 3.3 shows the molecular structures of a series of parylenes [88].

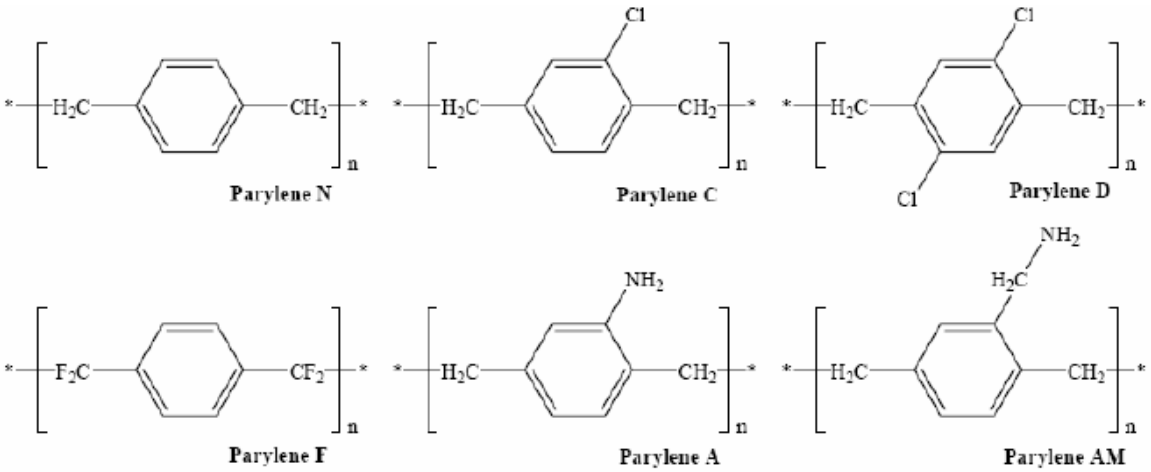

Figure 3.3 Parylene series.

Traditionally, parylene has been used as a coating material for electronics and medical instruments. Recently, parylene, especially parylene C, has been explored in microelectronics and MEMS field. The main reason for utilizing and studying parylene material for MEMS application lies in its conformal room temperature vapor deposition characteristics and its excellent mechanical and electrical properties. In MEMS field, parylene C has been used in many applications including structural material [60, 89, 90], bonding material [91], dry lift-off resist [92] , and electroplating mask [93]. Table 3.1 lists some engineering properties of three types of parylenes [94].

Table 3.1 Physical properties of parylene

Property		Parylene N	Parylene C	Parylene D
General				
Density [g/cm^3]		1.110	1.289	1.418
Refractive index		1.661	1.639	1.669
Mechanical				
Tensile modulus [GPa]		2.4	3.2	2.8
Tensile strength [MPa]		45	70	75
Yield strength [MPa]		42	55	60
Elongation to break [%]		30	200	10
Coefficient of friction, static/dynamic		0.25/0.25	0.29/0.29	0.35/0.31
Thermal				
Melting point [℃]		420	290	380
Glass transition point [℃]		< 90	< 90	< 90
Coefficient of expansion at 25℃ [K^{-1}]		6.9×10^{-5}	3.5×10^{-5}	
Heat capacity at 25℃ [J/(g·K)]		1.3	1.0	
Thermal conductivity at 25℃ [W/(m·K)]		0.12	0.082	
Electrical				
Dielectric constant	at 60 Hz	2.65	3.15	2.84
	at 1 kHz	2.65	3.10	2.82
	at 1 MHz	2.65	2.95	2.80
Dissipation factor	at 60 Hz	0.0002	0.020	0.004
	at 1 kHz	0.0002	0.019	0.003
	at 1 MHz	0.0006	0.013	0.002
Dielectric strength at 25 μm [MV/m]		235-275	185-220	215
Volume resistivity at 23℃, 50% RH [Ω·cm]		1.4×10^{17}	8.8×10^{16}	2×10^{16}
Surface resistivity at 23℃, 50% RH [Ω·cm]		1×10^{13}	1×10^{14}	5×10^{6}
Barrier				
Water absorption [%]		< 0.1	< 0.1	< 0.1
Water vapor transmission at 37℃ [ng/(Pa·s·m)]		0.0012	0.0002	0.0002

3.2.2. Skin Material

Ideally, the material of the skin should be highly compliant and elastic. However, all natural and synthetic elastomers are viscoelastic. While they show a much larger elastic region than other inorganic materials or thermoplastics, the deformation curve within the elastic region is not linear; in addition, a large hysteresis loop is observed

during cyclic testing. The mechanical properties of two types of common castable elastomers, polydimethylsiloxane (PDMS, Sylgard 184, Dow Corning) and polyurethane (PU, Poly 74-20, Polytek), especially their elastic and hysteresis properties, are characterized by static tensile tests according to ASTM D882. The mechanical properties of parylene C thin film have also been characterized. Table 3.2 lists the mechanical properties of parylene C and elastomers PDMS and PU.

Table 3.2 Mechanical properties of candidate polymer materials

	Young's Modulus (MPa)	Tensile strength (MPa)	Elongation at break (%)	Yield Strength (MPa)	Yield elongation (%)
Parylene	2000	68	200	68	3.7
PU	0.26	0.86	600	/	/
PDMS	2.00	6.27	250	/	/

3.3 Fabrication Process Development

The endoskeletal microbubble concept was proposed and the materials for the skeleton and skin were selected. Before the design of the geometry and setting dimension of the microbubble actuator, one of the interesting and essential tasks was to study the fabrication processes using two chosen polymer materials. To do this, mold masters with a much larger dimension with various types of geometries are fabricated. Pneumatic actuators based on these mold masters were made through a series of coating and molding processes. The purpose of this investigation was to test the feasibility of the proposed fabrication approach after a mold master is made on a macro scale, without having to go through time-consuming trial to make the micromachined mold masters. The proposed approach included parylene deposition process on different geometries, development of molding process, and elaotomer coating process. After confirming the

feasibility of the approach, the best condition for each step was to be investigated. Another purpose of the investigation is to find out the limits of each the process regarding the material chosen, based on which the fabrication process could be modified and optimized.

Macro-scale corrugated linear and angular actuators were first investigated. Linear bellows actuators of 6mmx10mm have been designed, analyzed, fabricated and characterized. These bubble actuators were made by parylene coating and have deflections of approximately 25mm – about 5mm in height when fully shrunk and up to 30mm when inflated. Figure 3.4 shows the photos of the linear bellows-shaped bubbles and 3 types of angular bubble actuators. Among all four types of bubble actuators, 1), 3) and 4) can be scaled down to smaller than mm scale and batch-fabricated by MEMS technology.

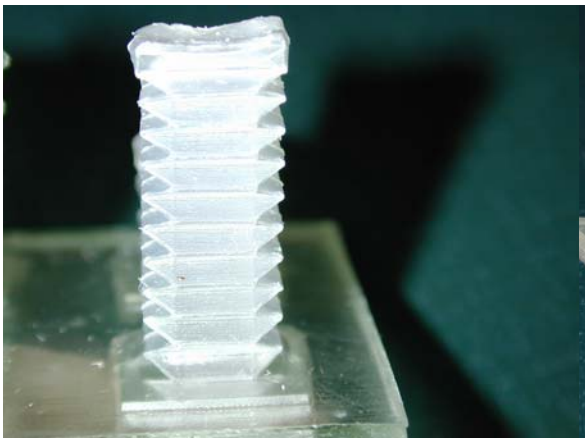

1) Linear bellows-shaped bubble

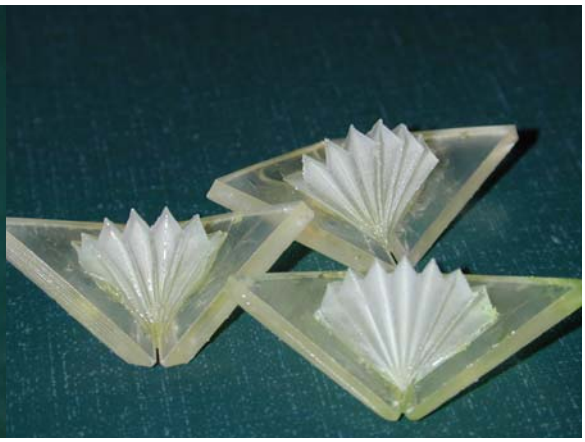

2) Lantern-shaped angular bubbles

3)“Half-bellows” angular bubble

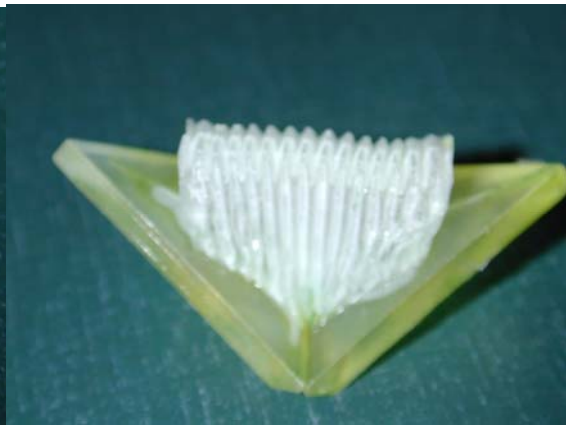

4) Inclined “Half-bellows” angular bubble

Figure 3.4 Prototypes of 4 types of bubble actuators

Figure 3.5 shows the schematic and pictures of the fabrication process for the lantern-shaped angular bubble actuators. Fabrication processes for the three other types of bubbles follow the same route. The sequential process is 1) building corrugated molds by rapid prototyping tool; 2) mold transferring by PDMS; 3) casting sacrificial materials, and 4) Parylene coating and removing sacrificial materials.

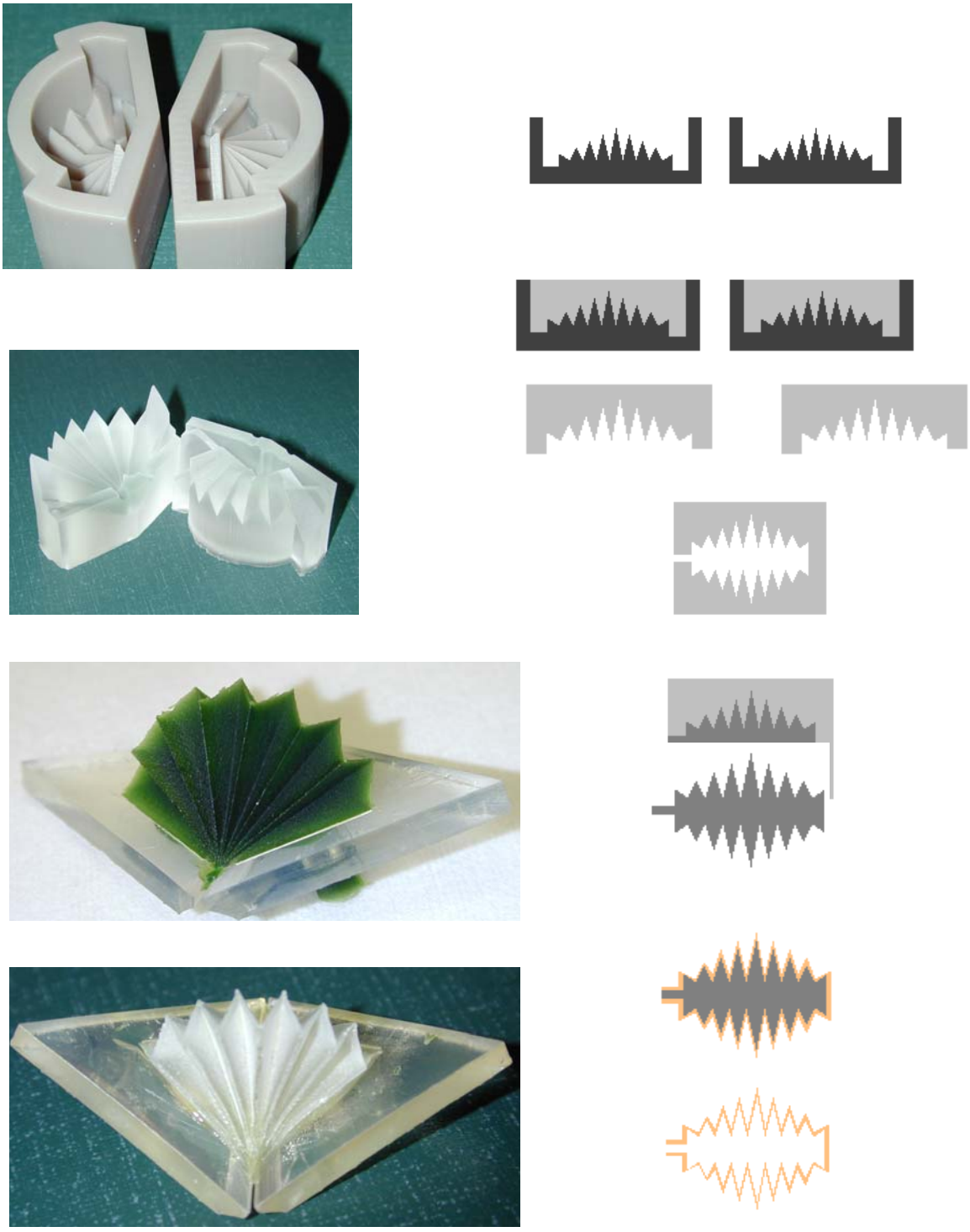

Figure 3.5 Fabrication process of bubble actuators: 1) Corrugated mold made with wax; 2) Transferred PDMS mold; 3) Cast sacrificial materials; 4) Remove sacrificial material after parylene coating.

Pictures of the pneumatically-driven bellows in shrunk state and in expanded state are shown in Figure 3.6.

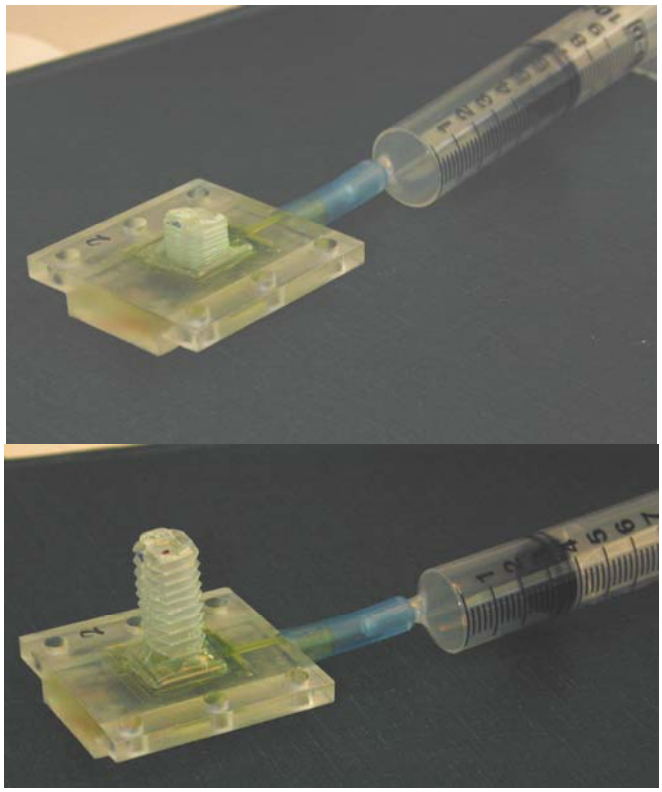

Figure 3.6 Pneumatically-driven bellows actuator. Top: Bellows in deflated shape; Bottom: Bellows in inflated shape.

In order to enhance reversible deflection, an elastomer layer needs to be incorporated onto the parylene skeleton. First, a literature survey of different approaches for elastomer depositions was conducted. The applicability of dry process such as plasma polymerization and vapor deposition polymerization, and wet process such as dip coating and spray coating, has been investigated. Micro dip coating process was selected as an initial method because dip coating can provide a thin shell structure as well as preserve the elastic property of elastomers, while other processes cannot guarantee elasticity (dry process) after processing or are too difficult to control the thickness and uniformity (spray coating).

Experiments using PDMS have been carried out in dip coating on straight, tapered and corrugated molds in different dimension scales. Free standing PDMS corrugated structures with a thickness of about 100μm were obtained. Dip coating on corrugated molds with thin, pre-deposited parylene layer was also carried out. Comparison of two bellows bubble structures made by parylene coating with or without PDMS over-coating is shown in Figure 3.7. It can be seen that larger restoring force is observed from a parylene-PDMS composite film after hyper-expanding the two bellows.

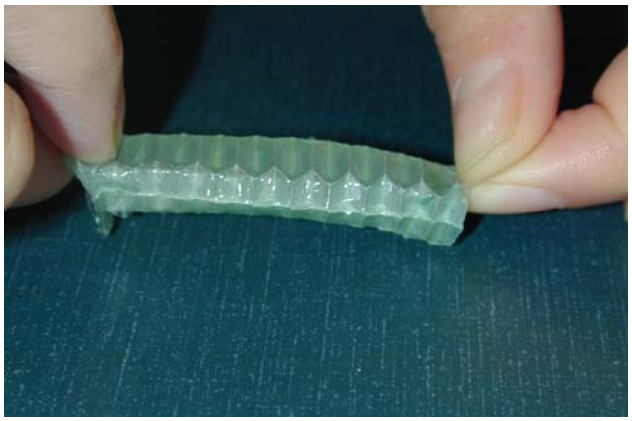

(a)

(b)

Figure 3.7 Comparison of parylene bellows with or without PDMS (a) Hyper expansion of bellows; (b) parylene bellows with (top) and without PDMS layer

On a large planar surface, spin coating can be used instead of dip coating. With these results, it was possible to design the microbubble actuator based a corrugated diaphragm micromold that can be batch fabricated by MEMS technology.

3.4 Design of Endoskeletal Microbubble Actuator

3.4.1. Design of the Corrugation Profile

Commonly-used corrugation profiles include “sinusoidal”, “trapezoidal”, “triangular”, “rectangular”, and “toroidal” [95] profiles. Sinusoidal and toroidal profiles are difficult to obtain by conventional MEMS technology because of the round surfaces. The rectangular profile can be obtained by a single lithography process. However, the rectangular profile has the largest flexural stiffness in the tangential direction compared with other profiles. Also, such a profile adds difficulties to mold release. Therefore, triangular and trapezoidal profiles were considered for microcorrugation.

3.4.2. Design of the Number and Angle of the Corrugation

One of the major concerns about a corrugated diaphragm in many applications is the mechanical sensitivity. In this study, the maximum achievable deflection is also of great interest. The maximum achievable deflection increases with both the number of corrugations and the corrugation depth. The number of corrugations can be changed by simply modifying the photomask design. Note that with a given outer diameter of the diaphragm, an increase in the number of corrugations results in the reduction of the corrugation width. A diameter of 2.6mm has been selected first for the bubble actuator.

Because the fabrication of the corrugated diaphragm is accomplished through rotational inclined exposure, the corrugation depth is determined by the width of the dark circular pattern on the photomask and the inclined angle. In order to increase the corrugation depth, the inclined angle has to be decreased (i.e. steeper side wall), which results in an acute angle of each corrugation tooth. This leads to difficulties in

subsequent demolding processes, such as increased susceptibility to mechanical instability and mechanical insensitivity due to relatively vertical sidewall with limited lateral working space. After various structures with various angles between 15° and 30° had been tested, an inclined angle of 17° was chosen as the second parameter for the diaphragm design, which would provide both relatively large deflection and fabrication stability.

Next, the sensitivities of various devices as functions of corrugation number and diaphragm thickness at a pressure load of 100Pa have been investigated using a finite element analysis (FEA) tool (ANSYS v.8.0, Ansoft, Inc.). The results are shown in Figure 3.8. A 2-D axisymmetric model was utilized for the corrugated diaphragm.

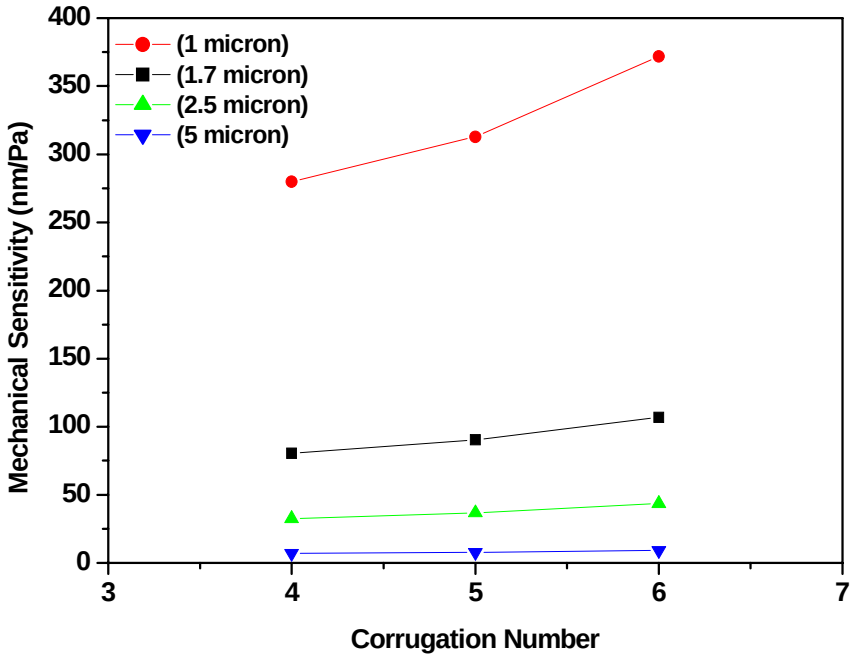

Figure 3.8 Mechanical sensitivity as a function of corrugation number and thickness of parylene corrugated diaphragm as modeled by ANSYS

In general, the diaphragm sensitivity increases as the corrugation number increases for all the four diaphragms with different thicknesses. However, as the

thickness goes beyond 2.5 μm, the variation in the corrugation number only has a negligible effect on the resulting mechanical sensitivity (defined by displacement per unit applied pressure) of corrugated diaphragms. The sensitivity is approximately inversely proportional to the square of the diaphragm thickness, as also observed in silicon nitride corrugated diaphragm [96]. Because of its large sensitivity and large deflection, a profile with 6 corrugations was selected. The preferred thickness of the diaphragm is less than 2.5μm.

A design of diaphragm with 6 corrugations, an inclined angle of 17°, and a diameter of 2.6 mm has been adopted for the fabrication of endoskeletal microbubble actuators. Deeper corrugations in the center of the diaphragm enhance the vertically-oriented center deflection. The schematic view of the corrugated diaphragm is shown in Figure 3.9, and the dimensions are listed in Table 3.3 with three thickness, t =1μm, 2μm and 5μm, considered.

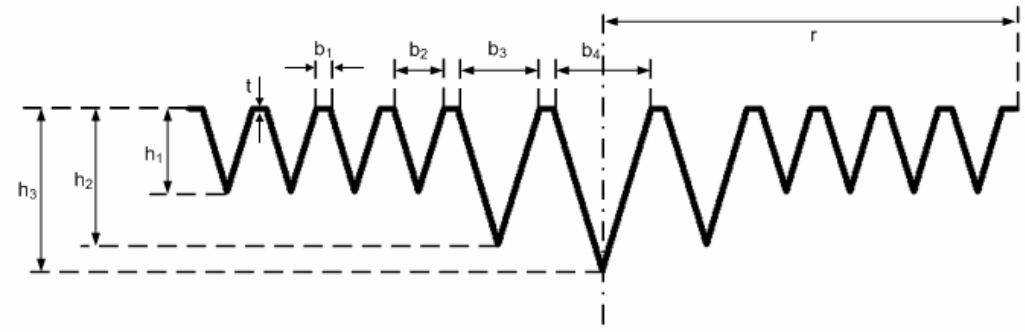

Figure 3.9 Schematic cross-sectional view of a corrugated diaphragm with 6 corrugations

Table 3.3 Characteristic dimensions of the corrugated diaphragm with 6 corrugations

Symbol	r	b_1	b_2	b_3	b_4	h_1	h_2	h_3
Dimension (mm)	1.3	0.05	0.15	0.25	0.3	0.245	0.409	0.491

3.4.3. Stiffness

The FEA results of the center displacement of three endoskeletal microbubble actuators as functions of applied pressure are determined from the ANSYS finite element program and are plotted in Figure 3.10. Two ANSYS element types are used in the simulation. One is plane 82 for parylene and the other is hyper 84 for PU elastomer. Plane 82 is a 2-D 8 node structural solid element with large strain capability and hyper 84 is a hyperelastic solid element based on the Mooney-Rivlin non-linear elastic model [97].

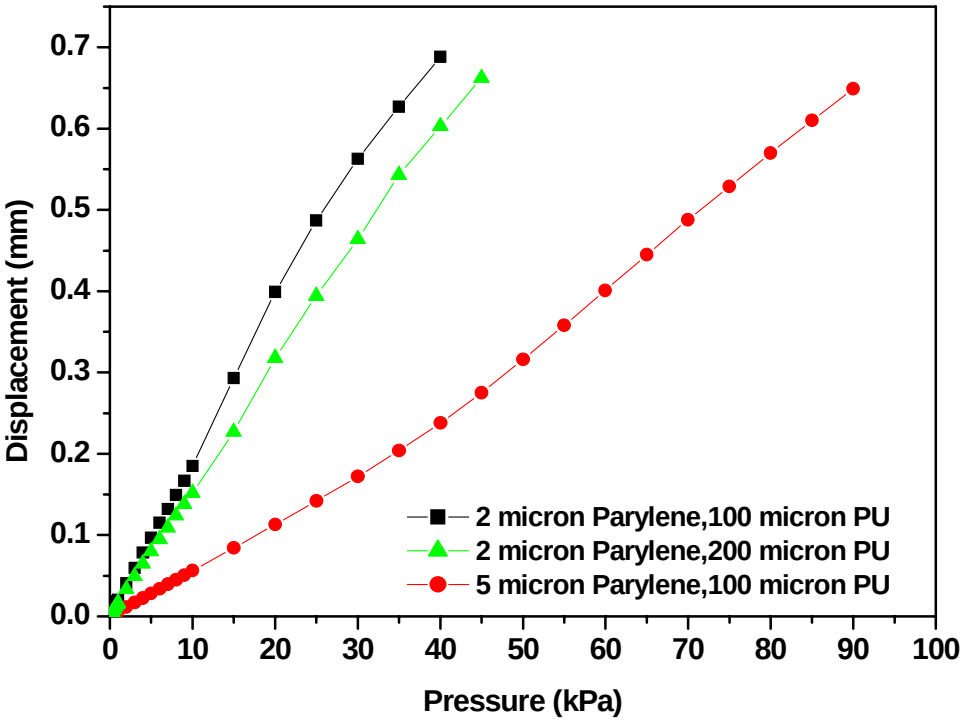

Figure 3.10 Computed results of center displacement of endoskeletal bubble actuators with composite diaphragms of 2-μm-thick parylene and 100-μm-thick PU, 2-μm-thick parylene and 200-μm-thick PU, and 5-μm-thick parylene and 100-μm-thick PU

The Mooney-Rivlin constants used in ANSYS simulation are derived from the stress-strain curve obtained by a uniaxial tensile test. These three endoskeletal bubble actuators are: with 2-μm-thick parylene and 100-μm-thick PU, with 2-μm-thick parylene

and 200-μm-thick PU, and with 5-μm-thick parylene and 100-μm-thick PU. The deflection curves for the two actuators having the same parylene thickness but different PU thickness are adjacent close to each other. However, the slopes of the curves of the two actuators with different parylene thickness but identical PU thickness are much different. It is concluded that the mechanical stiffness of the endoskeletal bubble actuator is dominated by the thickness of parylene as desired

3.5 Fabrication

3.5.1. SU-8 Micromold for Corrugated Diaphragms

3.5.1.1 SU-8 Photolithgraphy

SU-8 is a negative, epoxy-type, near-UV photoresist based on EPON SU-8 epoxy resin (from Shell Chemical) that has been originally developed, and patented by IBM [98, 99]. This photoresist can be as thick as 2 mm, and aspect ratio of developed patterns greater than 20 have been demonstrated with standard contact lithography equipment. These astounding results are due to the low optical absorption in the UV range which only limits the thickness to 2 mm for the 365nm-wavelength where the photo-resist is the most sensitive (i.e., for this thickness very little UV light reaches the bottom of the structure).

3.5.1.2 Fabrication Process

In this research, a combination of triangular and trapezoidal profiles is obtained using a continuously-rotating inclined UV exposure technique as shown in Figure 3.11. The mask layout for corrugation fabrication contains six concentric dark circles. A photo-patternable negative tone epoxy (SU-8, Microchem, Inc.) is spin-coated on a glass

substrate, and soft-baked. The substrate is mounted on a rotational stage with an inclined angle. An appropriate optical dose of UV-exposure in rotational mode (Figure 3.11a) is carried out after the mask with concentric circular pattern is placed on the substrate. After post-exposure baking and development of the substrate, a combination of triangular (lower portion of the tooth) and trapezoidal (upper portion of the tooth) profiles is obtained, which is illustrated in Figure 3.11b (the cross-sectional view of A-A' in Figure 3.11a). The dimensions of the corrugations are determined by the width and intervals between two concentric circles as well as the inclined angle.

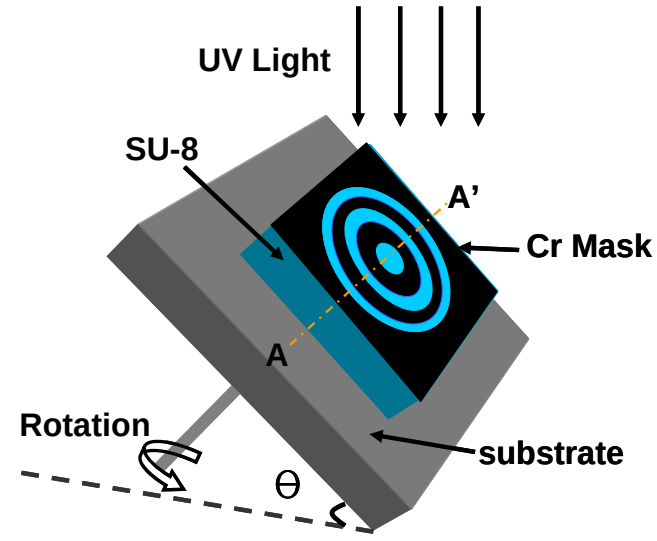

(a)

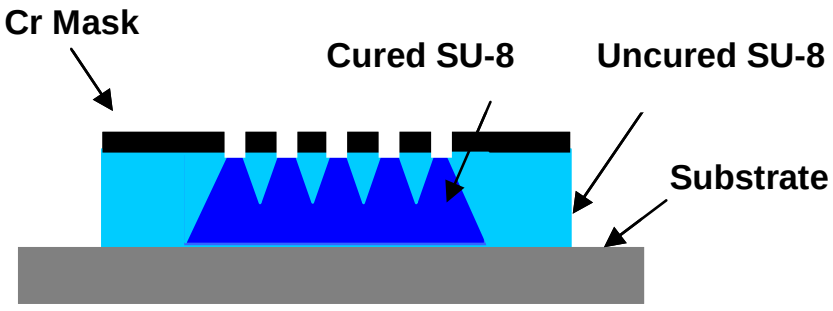

(b)

Figure 3.11 Continuously-rotating inclined exposure for concentrically corrugated diaphragm with slanted side walls: (a) exposure scheme and (b) cross-sectional view of A-A'

Figure 3.12 details the overall fabrication process of the endoskeletal microbubble actuators. All the subsequent fabrication processes after obtaining a SU-8 micromold are described in the following sections.

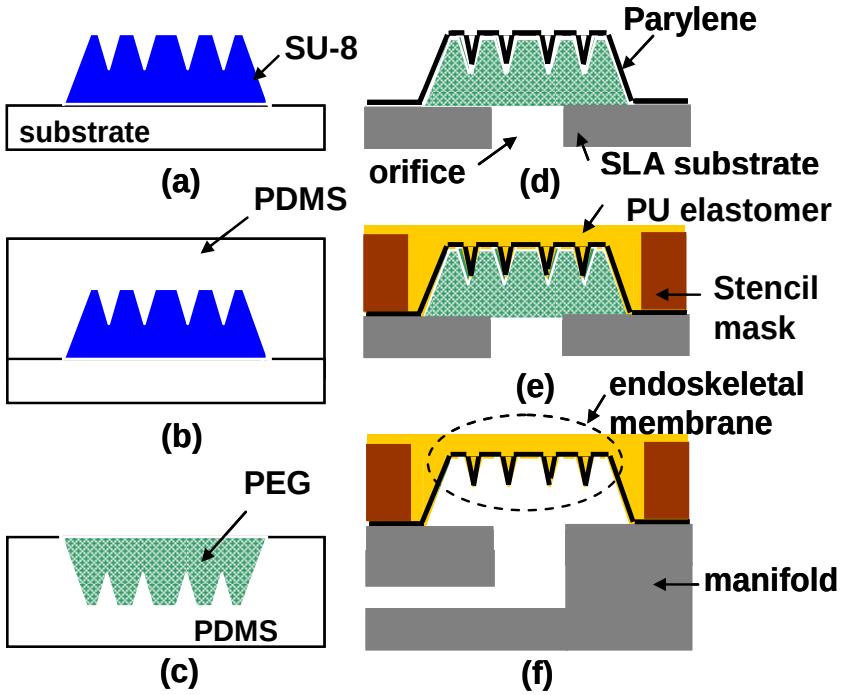

Figure 3.12 Overall fabrication process

3.5.2. Micro Transfer Molding of PEG .Sacrificial Micromold

3.5.2.1 Replication Technology

Replication is the most beneficial technology in polymer microfabrication and the secret of the success of commercial microfluidic devices. Currently, hot embossing, microinjection molding and soft-lithographic micromolding are three common replication methods for polymer microfabrication. Among them, the application of soft-lithographic micromolding e.g. microtransfer molding (μTM), micromolding (μM) and micromolding in capillaries (MIMIC) has proven to be a suitable, technically simple and low-cost route to obtain replications with high fidelity [27]. The soft-lithographic micromolding does

not require a rigid metal master or metal mold or the high temperature and pressure used in hot embossing and injection molding. The PDMS negative can be used multiple times and allow submicron features to be replicated with good fidelity. The master, which is normally a micromachined silicon, metal or polymer structure can be preserved. The casting material can be a large variety of thermoplastics and thermosets by reaction molding.

3.5.2.2 Stereolithography (SLA)

Stereolithography is the most widely used rapid prototyping technology. Stereolithography builds plastic parts or objects a layer at a time by tracing a laser beam on the surface of a vat of liquid photopolymer [100]. The laser source used in this work is a solid state Nd: YVO_4 and the wavelength used for epoxy resin exposure was 354.7nm. There is a large selection of materials commercially available, which have different material properties mimicing those of several engineering thermoplastics. The photopolymer used in this work is epoxy acrylate. A schematic of the stereolithography apparatus and its operation is shown in Figure 3.13 [101].

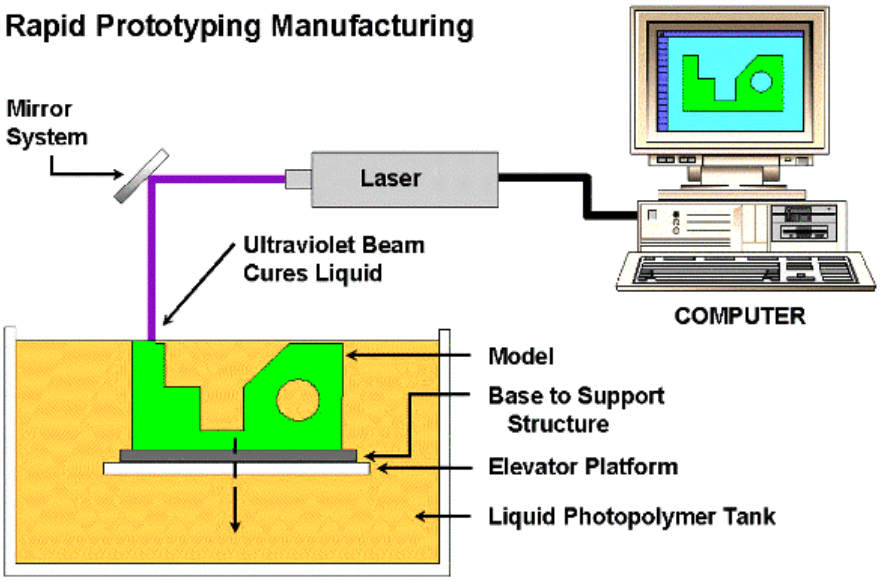

Figure 3.13 Schematic of stereolithography apparatus

The procedure to produce an SLA part is as follows:

1. A 3-D CAD model of the object is created by using CAD program;

2. A computer program will "slice" the CAD model into cross-sectional contours, one on top of the other;

3. The stereolithography machine will create the support structures for levitating the part above the platform that the part will be resting upon;

4. The slices are created by tracing the 2D contours from the CAD models in a vat of photopolymer resin with a laser;

5. Each slice is created when the platform that the parts rested on is lowered into the vat, exposing only a thin layer of resin to the laser at any one time;

6. The final step is cleaning, post-curing under UV exposure, and detail finishing the part.

3.5.2.3 Fabrication Process

Referring to Figure 3.12, an initial polymer mold is formed using the inclined rotational lithography technique (Figure 3.12a). A 10:1 mixture of PDMS elastomer base and curing agent is well mixed and degassed, and then cast onto the SU-8 master pattern to obtain a negative replica (Figure 3.12b). After curing at room temperature for 24 hrs, the PDMS negative is separated from the substrate. Polyethylene glycol (PEG, Kindt Collins) as a sacrificial material is cast into the PDMS mold (Figure 3.12c) in its molten state at 60 ºC. Excess PEG is scraped off the surface of the mold. An epoxy substrate having a matching orifice array pattern with the corrugation array is fabricated by stereolithography (SLA). The PEG corrugation array is aligned and bonded onto the epoxy substrate. During the transfer step, the PEG is kept in a soft state to provide good adhesion. After attachment to the epoxy orifice array, the PEG is allowed to cool down to room temperature and harden. The PDMS mold is peeled off from the SLA substrate, with the PEG corrugation replica left on the substrate.

3.5.3. Fabrication of Corrugated Diaphragms

Three different types of diaphragms are fabricated: parylene corrugated diaphragm (skeleton only), PU elastomer corrugated diaphragm (skin-only), and endoskeletal bubble.

1) Parylene corrugated diaphragm: A parylene layer is conformally coated to the PEG corrugation array (Figure 3.12d). The sacrificial PEG is removed by dissolving in water to release the parylene corrugated diaphragm.

2) PU elastomer corrugated diaphragm: A stencil mask fabricated by SLA is placed on the epoxy substrate to level the top surface. A thin layer of polyurethane elastomer (Polytek, Poly 74-20) is then spin-coated on top of the corrugated surface (Figure 3.12e). The elastomer is cured at room temperature and the sacrificial PEG is removed by dissolving in water.

3) Endoskeletal bubble: A parylene layer is conformally coated to the PEG corrugation array to form the corrugated skeletal diaphragm (Figure 3.12d). A stencil mask is placed on the epoxy substrate to level the top surface. A thin layer of PU elastomer is then spin-coated on top of the corrugated surface (Figure 3.12e). The elastomer is cured at room temperature and the sacrificial PEG is removed by dissolving in water to form endoskeletal bubbles.

3.5.4. Bonding and Assembly

A manifold with 36 fluidic channels is fabricated by SLA. The epoxy substrate with a 6 x 6 diaphragm array is bonded to the manifold so that each actuator can be addressed independently (Figure 3.12f).

3.5.5. Fabricated Microstructure

Scanning electron microscope (SEM) photomicrographs of a single corrugated SU-8 master mold with various corrugation number and profiles are shown in Figure 3.14.

The top diameter, the bottom diameter, and the height of the diaphragm are 2.6mm, 3.0 mm, and 600μm, respectively. An incident angle of 30º of UV light results in a refracted angle of approximately 17º of the slanted side wall of the corrugation. Figure 3.15 shows the cross-sectional view of the combinational corrugation with a trapezoidal shape on top and a triangular shape on bottom. The dark color region represents crosslinked SU-8 which shows the incident UV trace.

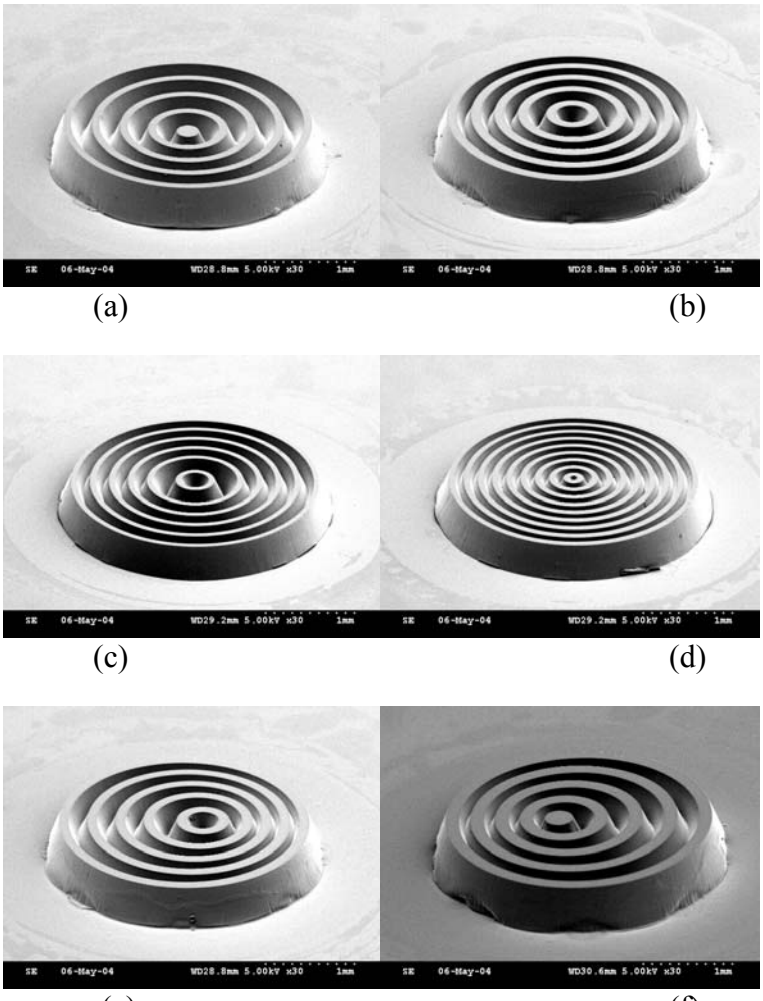

Figure 3.14 SU-8 micromolds with different corrugation numbers and profiles. (a) Concentric mold with 4 corrugations; (b) Concentric mold with 5 corrugations; (c) Concentric mold with 9 corrugations; (d) Concentric mold with 6 corrugations, and (e) and (f) Off center mold with 5 corrugations

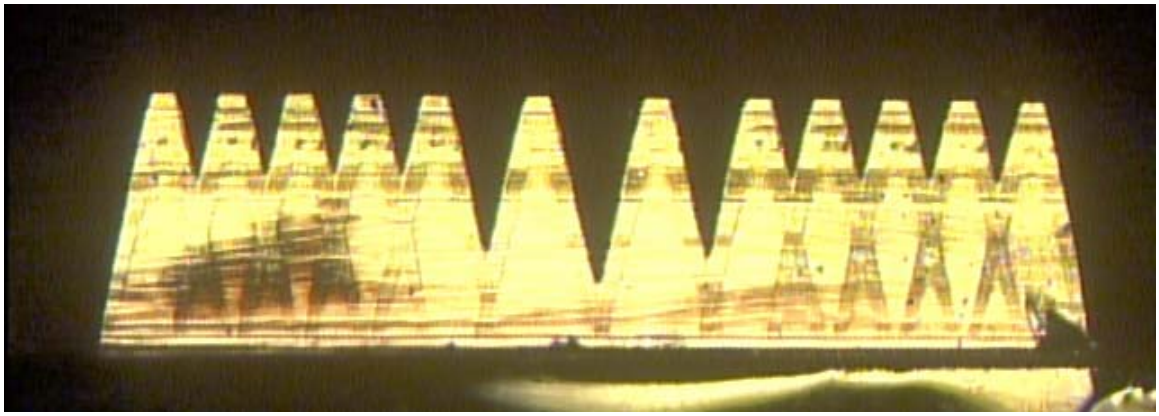

Figure 3.15 Cross sectional view of SU-8 micromolds with 6 corrugations

Two SU-8 molds and two corresponding PEG replica patterns are shown in Figure 3.16a and Figure 3.16b. The molded PEG structure faithfully follows the original SU-8 microcorrugation. Figure 3.17 shows an SU-8 microcorrugated mold array and a batch-transferred corrugated PEG mold array, respectively. Figure 3.18 shows a batch-transferred corrugated PEG mold array mounted on a SLA manifold.

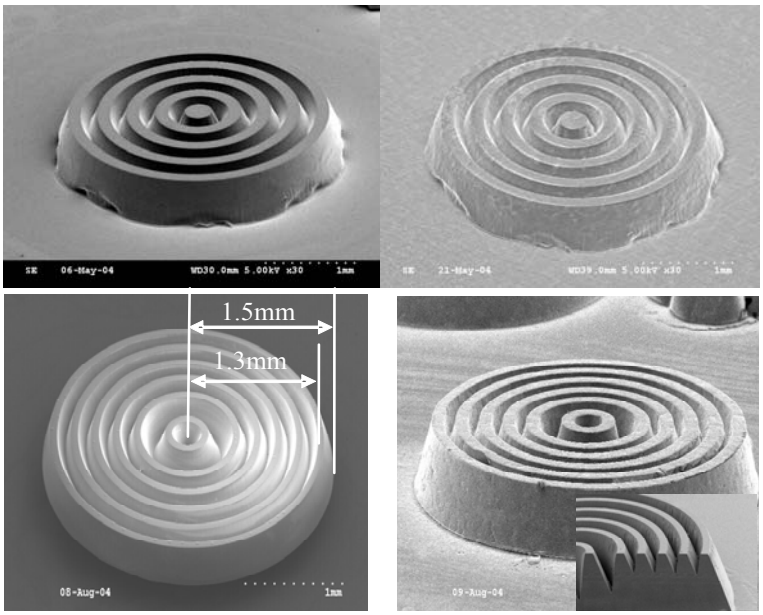

(a) (b)

Figure 3.16 Comparison of (a) SU-8 mold and (b) replicated PEG mold: insert shows a cross-sectional image of corrugation profile.

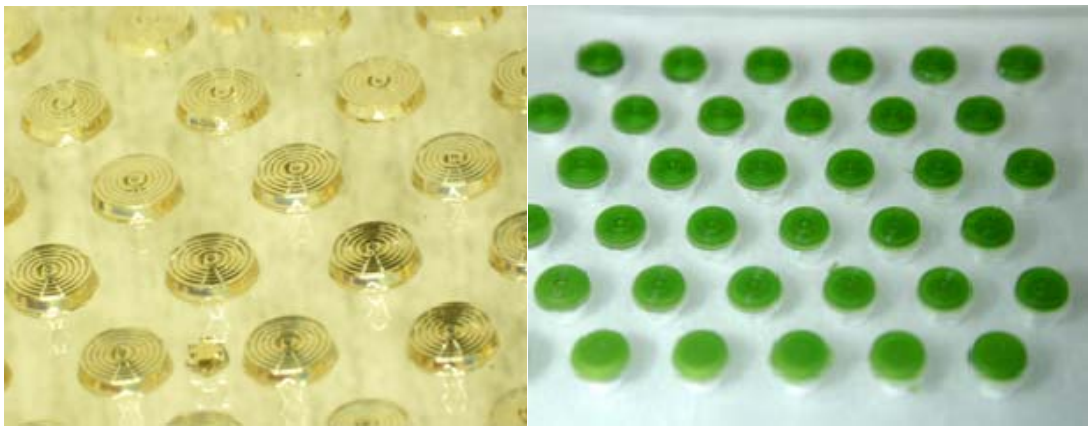

Figure 3.17 Comparison of (a) SU-8 mold and (b) Batch transferred PEG mold array from PDMS mold

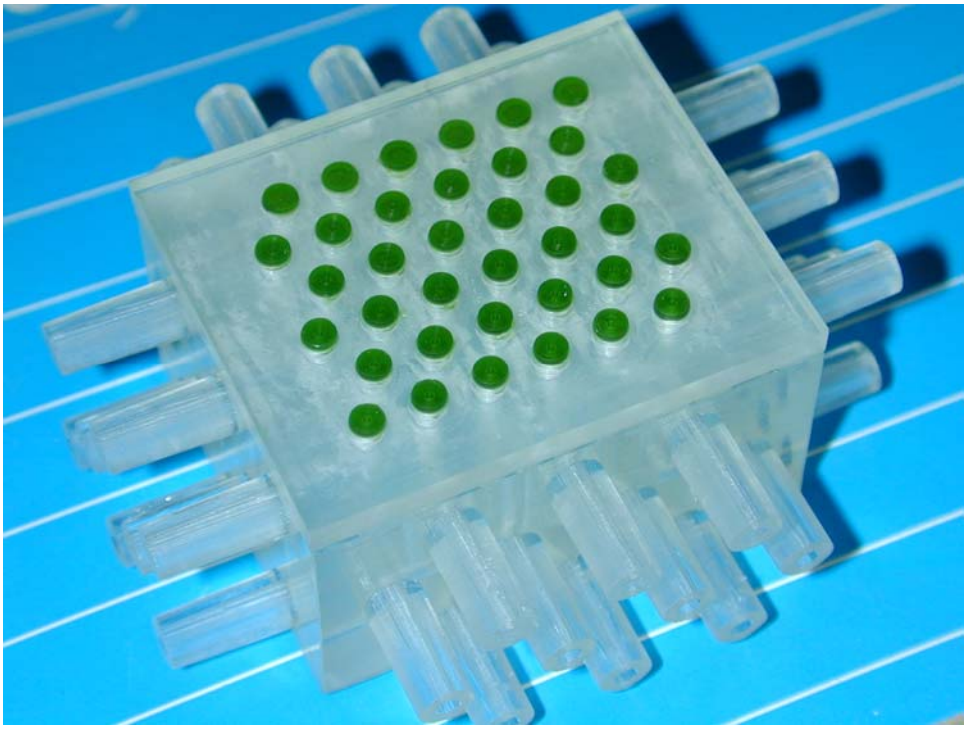

Figure 3.18 Laminated corrugated PEG mold array on a SLA manifold.

3.6 Characterization

Diaphragm center deflection as a function of applied pressure has been quantitatively characterized. Compressed air was applied to the diaphragm through the

manifold channels and the diaphragm displacement was measured using a laser displacement sensor (LK-G32, KEYENCE Co.). Comparison experiments have also been carried out on parylene corrugated diaphragm (skeleton only) and PU elastomer corrugated diaphragm (skin only). The inflated shapes of diaphragms were captured by a video microscope.

3.6.1. Inflated Shape

Figure 3.19 shows the inflated and restored shapes for (a) an endoskeletal bubble actuator and (b) a PU elastomer diaphragm (skin-only). For the endoskeletal bubble, the inflation of the diaphragm is confined to one direction, i.e. out-of plane; and the displacement is a reasonably linear function of the applied pressure. After the applied pressure is removed, the diaphragm returns to its original position and shape. The PU elastomer diaphragm shows similar stability and a spherical shape at small deflection but an omni-directional balloon-like expansion at large deflection, resulting in plastic deformation of the material. Note that when the diaphragm is deflated by removing the applied pressure, it becomes flaccid and does not return to its original shape. The cross-sections of the deformed shapes of an endoskeletal bubble actuator and a PU elastomer diaphragm at 0.91 mm deflection are compared in Figure 3.20. The cross-sectional area under the profile of endoskeletal bubble actuator is 80.7 % of that of under the profile of PU elastomer diaphragm.

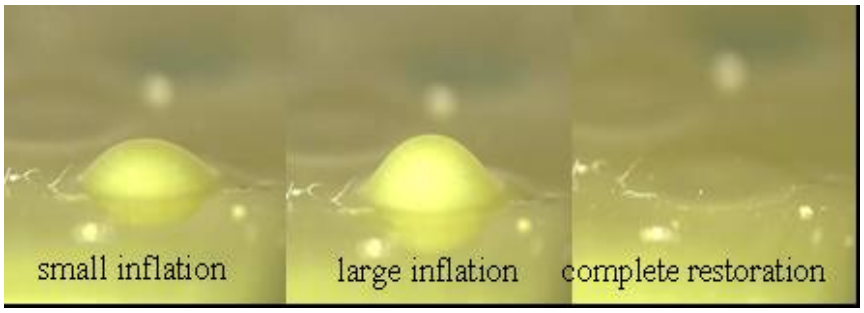

(a)

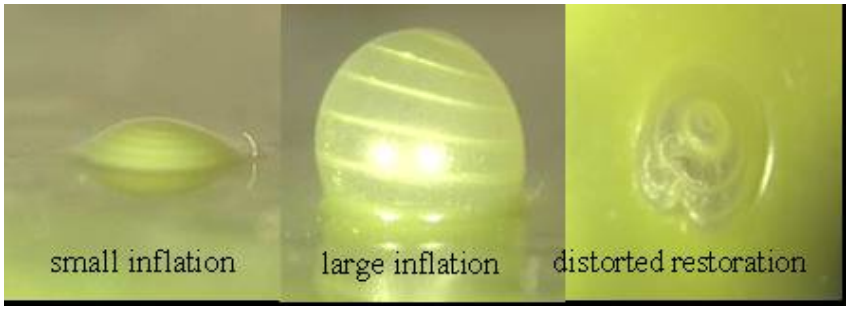

(b)

Figure 3.19 Inflated shape comparison of (a) endoskeletal bubble and (b) PU elastomer diaphragm.

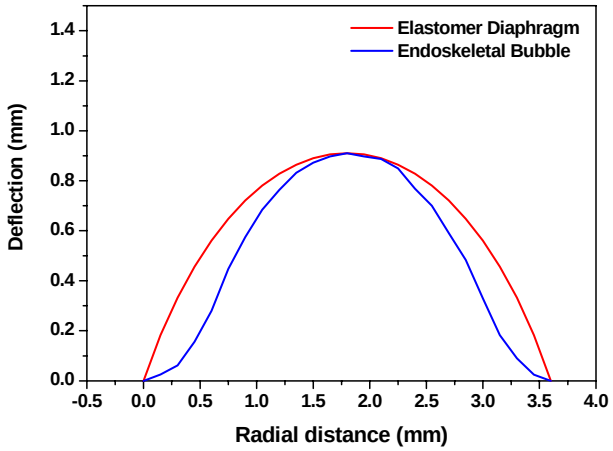

Figure 3.20 Comparison of the cross-section area of inflated endoskeletal bubble and PU elastomer diaphragm.

3.6.2. Static Testing

The static pressure-deflection characteristics are tested for the parylene diaphragm, PU elastomer diaphragm, and endoskeletal bubble using the apparatus of Figure 3.21. The thicknesses of the parylene diaphragm and PU elastomer diaphragm are 5 μm and 150 μm, respectively. The endoskeletal bubble actuator has parylene and PU layers with the same thicknesses as those of the parylene diaphragm and PU elastomer diaphragm. The results are plotted in Figure 3.22. Among the three actuators compared, the PU elastomer diaphragm has an extremely low Young's modulus, and requires the smallest pressure to achieve a given deflection. The endoskeletal bubbles require the largest pressure for the same deflection, because they consist of a composite of two materials: polyurethane (PU) and parylene, each layer of the composite having the same thickness as that of the other two diaphragms, thereby resulting in the largest effective stiffness.

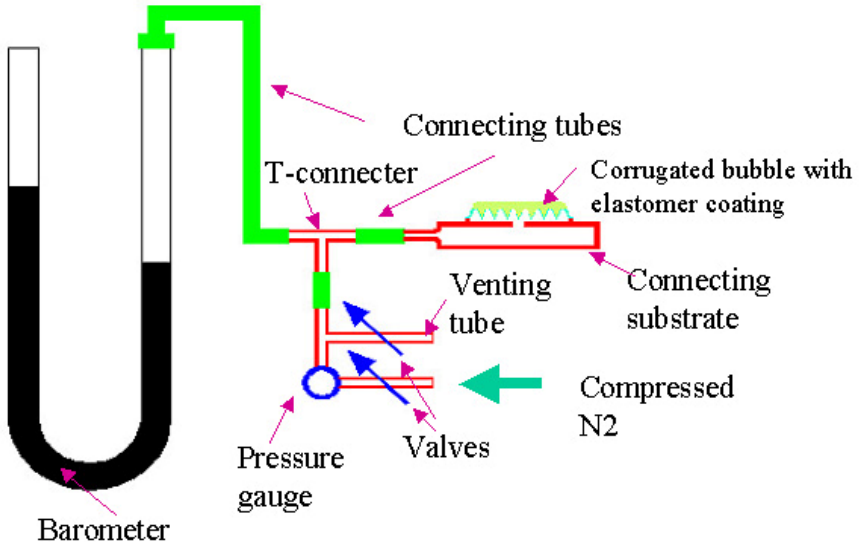

Figure 3.21 Displacement characterization set up.

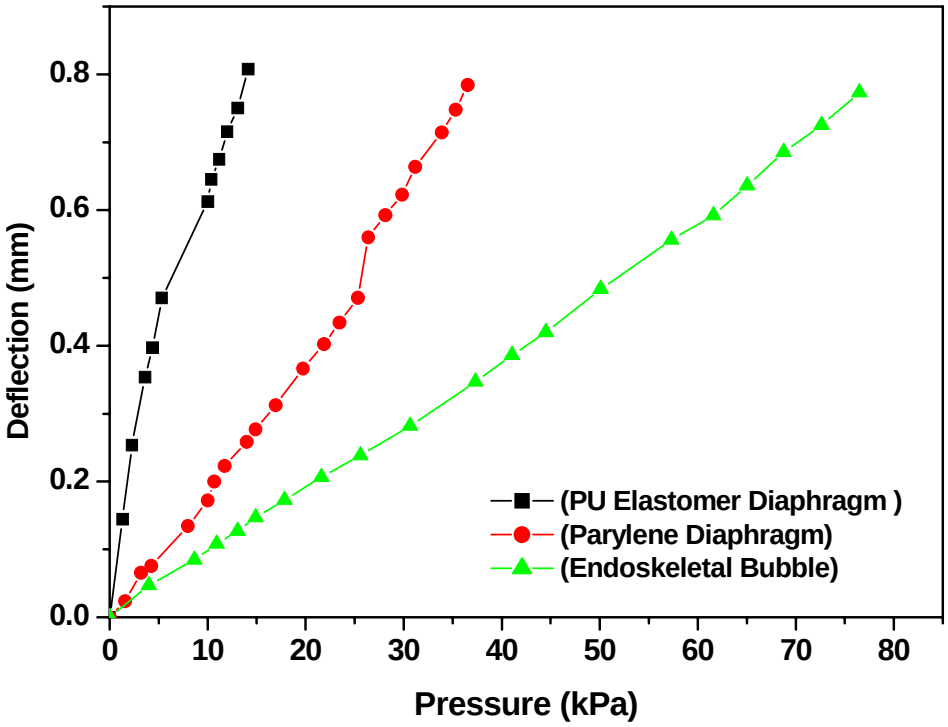

Figure 3.22 Diaphragm deflection as functions of applied pressure for three actuators: a PU elastomer diaphragm, a parylene diaphragm, and an endoskeletal bubble.

The distinct "jumps" in the pressure-deflection curve for the parylene diaphragm indicate "unfolds" of one or more corrugations, which results in the large deflection. The unfolded corrugation does not always "refold" upon release of pressure because the unfolding has led to another minimum energy state. The addition of elastomer greatly enhances the linearity in the pressure-deflection relationship of the endoskeletal bubbles, while maintaining the unidirectional deflection of the actuator.

3.6.3. Cyclic Testing

The performance of three types of actuators above undergoing cyclic inflation and deflation at a constant low rate is tested. The relationship between the applied load and deflection of a parylene diaphragm in cyclic testing is illustrated in Figure 3.23. In the test, a parylene diaphragm is loaded with pressure until the center displacement is 0.48

mm, and then deflated. The second inflation cycle reaches a center displacement of 0.75 mm and the third one reaches 1.46 mm. Three hysteresis loops are observed for the three loading cycles. The hysteresis at small deflection comes from the viscoelastic nature of parylene material. There is no evidence of unfolding of corrugation in the inflation curve of the first loading cycle. The unfolding of corrugation accompanied with the permanent deformation of parylene in the second and third loading broadens the hysteresis loops much more. The remnant deflection is irreversible because the unfolding has led to another minimum energy state.

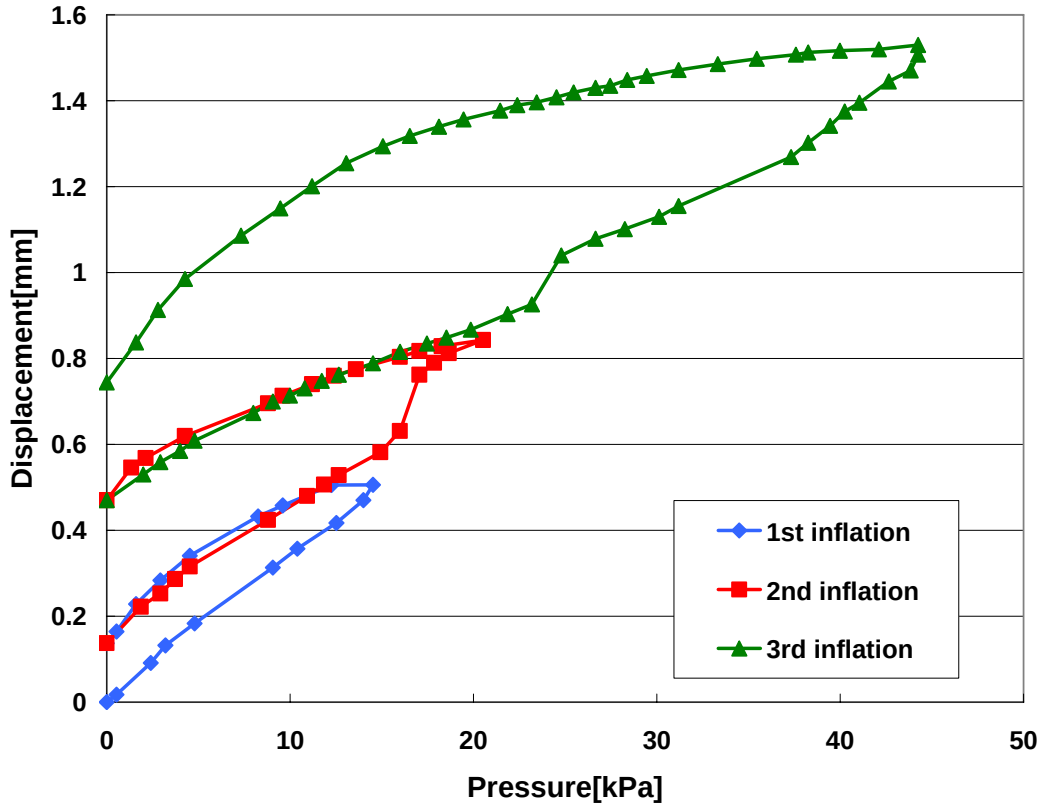

Figure 3.23 The center displacement as a function of applied pressure load of a parylene diaphragm in cyclic testing.

Three endoskeletal bubble actuators with the same PU thickness (150 μm) but different parylene thicknesses (1, 2, and 5μm) are fabricated. Their cyclic behaviors are shown in Figure 3.24. The inflation and deflation curves form a hysteresis loop in all the

three cases. The hysteresis is defined as the percentage ratio of the difference between two deflections at the mid-point of the applied pressure to the maximum deflection. The values of hysteresis for 1-μm-thick, 2-μm–thick, and 5-μm–thick bubbles are 13 %, 24 %, and 27 %, respectively.

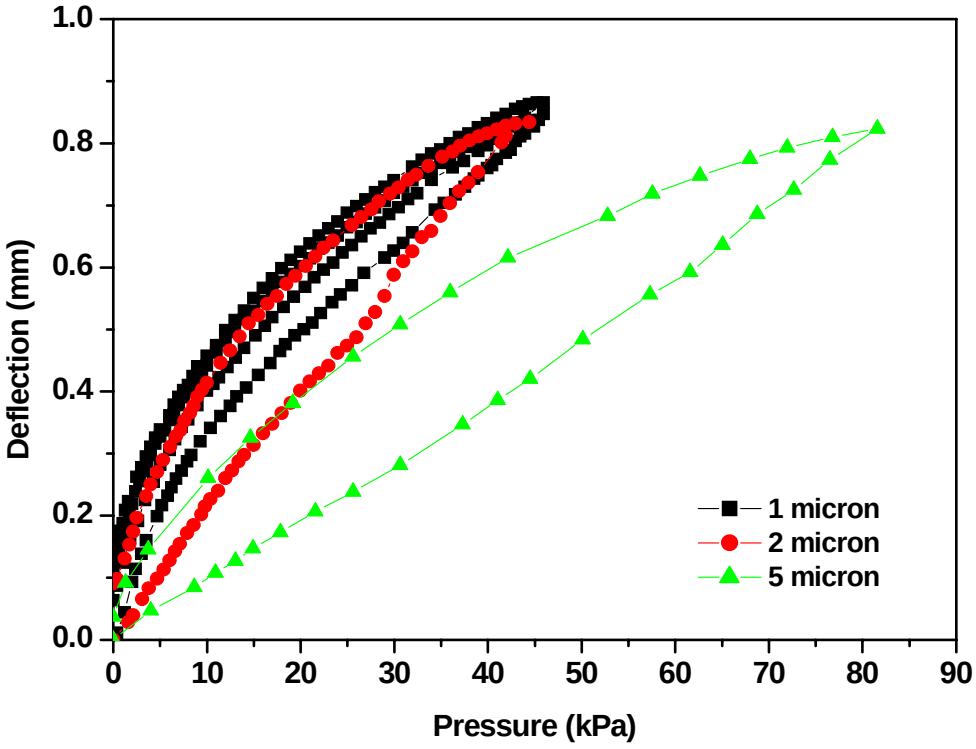

Figure 3.24 The cyclic behavior of endoskeletal bubble actuators with the same PU thickness (150 μm) but different parylene thicknesses (1, 2, and 5μm).

The 1-μm-thick device shows the least stiffness as well as the lowest hysteresis among the three bubbles. It would be the most desired bubble actuator in our application. However, during test it is found that 1-μm-thick devices are insufficiently robust compared to the other two bubbles.

After an initial deformation and recovery cycle, repeated inflation and deflation cycles result in much less hysteresis, demonstrating the functionality of the kinematically-stabilized actuator, as can be seen in Figure 3.25. The hysteresis of the 2-μm-thick bubble actuator is reduced to 8.4 %, which is comparable to that of a PU

elastomer diaphragm (6.5 %, as shown in Figure 26).

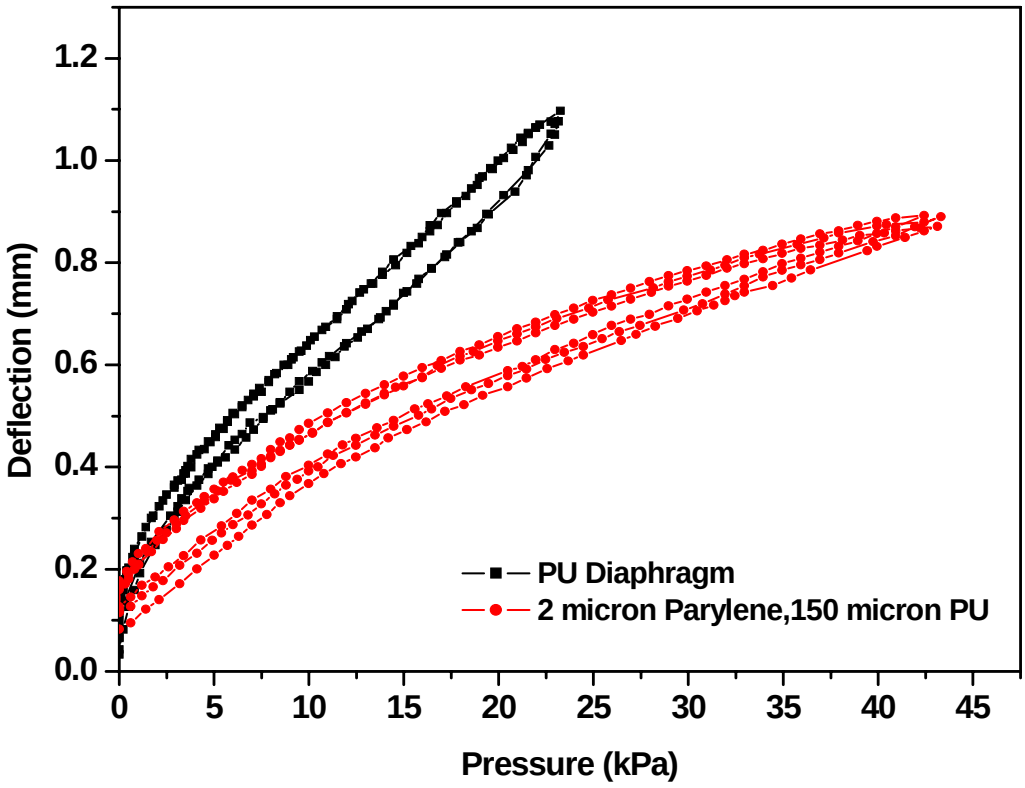

Figure 3.25 Displacements in subsequent loading and unloading cycles after an initial deformation and recovery cycle for a PU diaphragm and an endoskeletal bubble actuator with 2-μm-thick parylene and 150-μm-thick PU elastomer.

It is hypothesized that the observed hysteresis consists of two components: a plastic deformation of the underlying parylene layer during the initial inflation, and viscoelastic dissipation occurring primarily in the PU elastomer overcoat in subsequent inflations. To test this hypothesis, finite element models are utilized to determine if the plastic limit of parylene is exceeded, particularly in the sharp bends of the corrugation, during the initial inflation. Further, after the initial deflection, the hysteresis performance of the endoskeletal bubbles is compared to PU elastomer diaphragms to see if any additional hysteretic effects of the endoskeletal bubbles over and above the PU-only disphragms can be observed.

Figure 3.26 shows the calculated stress using FEA in an endoskeletal bubble actuator with 2-μm-thick parylene and 150-μm-thick PU elastomer, under a pressure load of 44 kPa and a center deflection of 0.697 mm. At the corners of the trapezoidal-shaped corrugations, the stress exceeds the yield stress of parylene, which is 68 MPa. Approximately 4 % of the parylene layer yields at this pressure load.

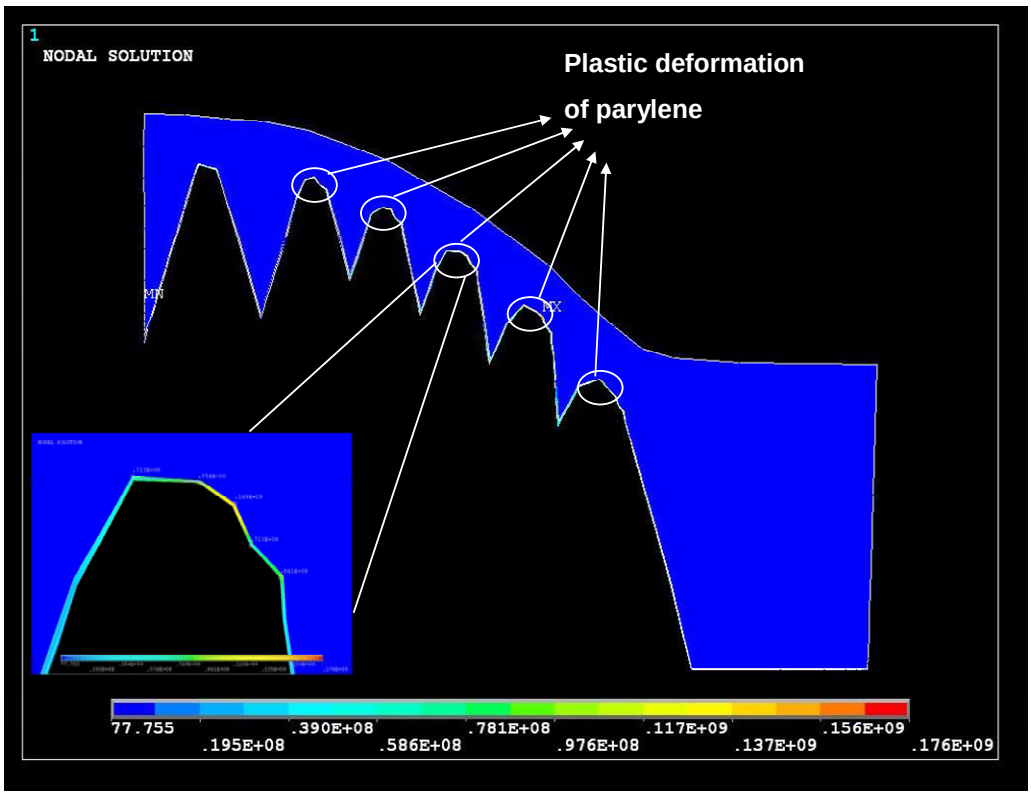

Figure 3.26 The calculated stress in an endoskeletal bubble actuator with 2-μm-thick parylene and 150-μm-thick PU elastomer with a center deflection of 0.697mm.

3.7. Actuator Performance Verification

To verify the performance of the endoskeletal bubble actuator, the numerical analysis results by ANSYS and the experimental results of each actuator are compared. Figure 3.27 illustrates the center displacement of an endoskeletal bubble actuator as a function of applied pressure, where a bubble actuator with 2-μm-thick parylene and 150-μm-thick PU elastomer has been used. The experimental data exhibit good linearity, and

agree reasonably well with the simulation results. The discrepancy may have resulted from the inaccuracy in the parameters used for the non-linear elastic model in ANSYS simulation.

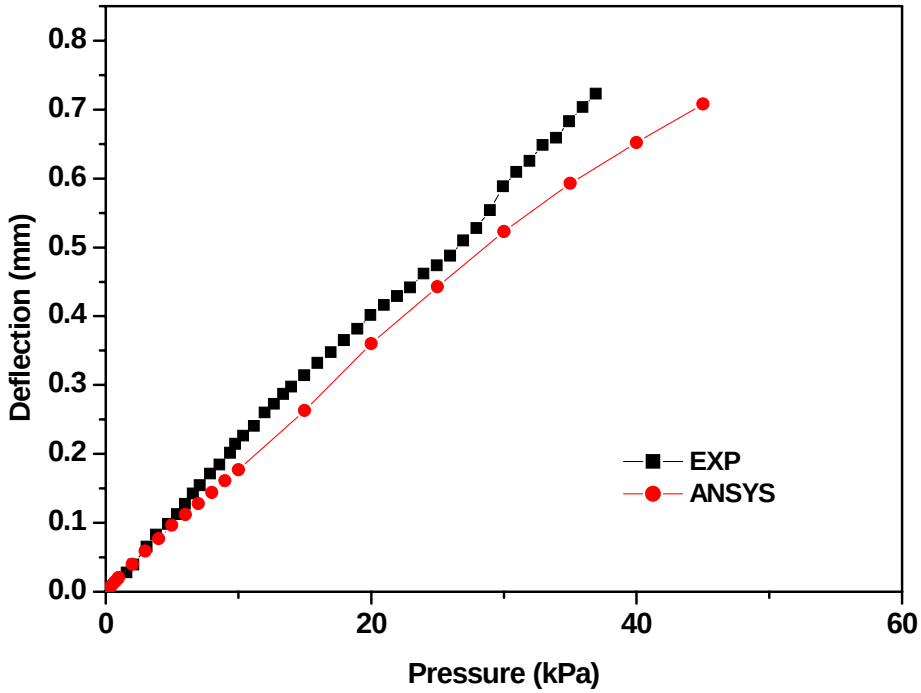

Figure 3.27 Comparison of experimental and finite element analysis results for an endoskeletal bubble actuator with 2-μm-thick parylene and 150-μm-thick PU elastomer.

3.8. Conclusion

Tactile actuator is the elementary unit and the most critical component in tactile display devices. In this chapter, a complete study on the modeling, material characterization, design, fabrication and characterization a polymer pneumatic microactuator is presented. A systematic design and modeling procedure was carried out to generate an optimized geometry of the corrugated diaphragm to satisfy membrane deflection, force and stability requirements set forth by the tactile display goal. Candidate materials have been characterized and material process development has been conducted on a larger scale before being implemented in the actual fabrication step. The pneumatic microbubble actuator was characterized both statically and cyclically.

Another finite element modeling was developed to analyze stress concentration of the membrane. The conclusions based on this work include:

1. The concept of "endoskeletal microbubble actuator" for a pneumatic tactile display application was verified. By the use of endoskeletal bubble, the stability issues associated with simple elastomeric membranes are circumvented, allowing simultaneous achievement of the high force and high anisotropic vertical deflection required for RBD applications.
2. By minimizing the overall bubble volume and maximizing the overall bubble vertical deflection, the quantity of pneumatic gas used per cycle can be minimized.
3. Micromolds for complex corrugated diaphragm can be fabricated by continuous rotating inclined exposure.
4. Photolithography, micromolding and pattern transferring processes enable mass-manufacturability of the microbubble actuator.
5. With regard to the fabrication constraints, the current design can be scaled-down without changing any fabrication process parameter.
6. Without changing the materials, other design parameters such as membrane thickness, remain flexible to meet different requirement combination of force and displacement, spatial resolutions.

Overall, the results show the microbubble actuator is well suited for constructing an array of tactile actuator. Modification can be made based on the particular application and requirements of the tactile display device to be built.

CHAPTER 4

A REFRESHABLE BRAILLE CELL

4.1. Introduction

Braille was developed by Louis Braille in the beginning of the 19th century. Braille letters, common punctuation marks, and a few symbols are displayed as raised 6 dot Braille cell patterns read by using a fingertip to feel the raised dots. All over the world, persons with visual handicaps have used Braille as the primary means to reading information. Different countries of the world have adapted the system of Braille to suit their languages. However, the existence of standard Braille for the Roman alphabet (English Braille) making it possible to exchange information in a consistent fashion across different countries.

Braille characters are based on a 6 dot Braille cell having two parallel columns of three dots each. If the empty cell is counted, 64 unique dot combinations are possible with a 6 dot Braille cell. Dot height is approximately 0.02 inches (0.5 mm); the horizontal and vertical spacing between dot centers within a Braille cell is approximately 0.1 inches (2.5 mm); the blank space between dots on adjacent cells is approximately 0.15 inches (3.75 mm) horizontally and 0.2 inches (5.0 mm) vertically. The dimensions of the Braille cell are standardized but these may vary slightly depending on the country. The dimensions of a Braille cell, as printed on an embosser are shown below in Figure 4.1 [102].

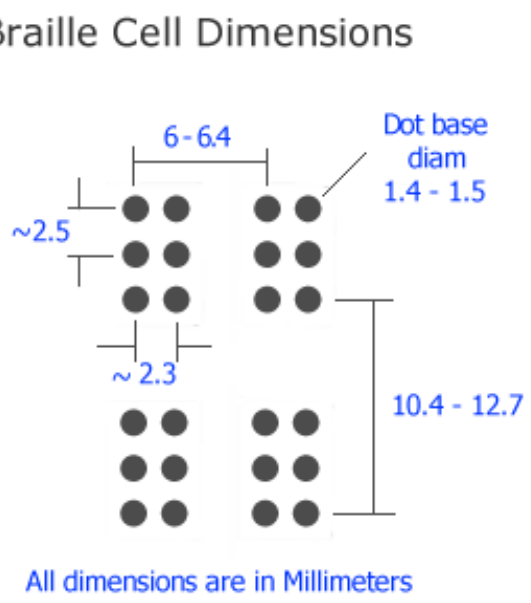

Figure 4.1 Layout and dimension of Braille cells

According to the American Foundation for the Blind, in the United States alone there are over ten million people who are either blind or visually impaired. Among the 10 million, 1.5 million utilize computers through specialized equipment. Some estimates state that there are over 800,000 people worldwide who can read Braille.

A refreshable Braille display (RBD) is a device that converts text information from a computer to Braille dots for the blind to read. It is a great tool for the blind to learn and use Braille. There are currently refreshable Braille displays on the market, but these generally range in price from $5,000 - $25,000. Most contemporary RBDs contain only a single line of 25 to 80 Braille cells due to the high manufacturing cost and large volume of piezoelectric bimorph actuators they utilize. Further, they are not portable because of their large size and weight. A simpler “Rotating Wheel” Braille display was created by the National Institute of Standards and Technology in late 2000 yet was not a commercial success, despite its lower price tag of $1,000 and use of fewer actuators. Several other microactuators for RBD and vibratory tactile display have been developed including electromagnetic, electrostatic, pneumatic and shape memory alloy actuators.

However, they all suffered from poor performance such as insufficient force, insufficient stroke and slow response time.

In order to develop a portable and multi-line RBD, a mass manufacturable, light weight, low power and integrable actuator must be developed. Pneumatic actuation is a promising candidate for Braille cell actuation due to its rapid response time and potential for large force generation while maintaining simplicity, scalability, and low cost. A valve for an elastic membrane type pneumatic RBD was demonstrated in [51]. However, simple balloon type actuators do not fulfill the requirements of large force (50-100 mN) while confining the displacement primarily to the vertical direction (0.25-1 mm). Although forces available from such a membrane can be increased by increasing the driving pressure, conventional elastomeric membranes can become unstable under widely varying external loads (such as lifting of a finger), which limits the available force.

4.2. Design and Fabrication

4.2.1. Design Guidelines

Because of the many unknown factors in the human tactile sense, the conception of the Braille cell as a 2D tactile prototype reported in this thesis is highly empirical and iterative. Nevertheless, basic guidelines should still be followed. Considerations to take into account when designing and implementing a practical fingertip tactile display include:

Actuator Size and Arrangement

The size of the microbubble actuator and the arrangement of the actuator array should follow the Braille building standard.

Spatial resolution

It is generally accepted that the spatial resolution of the actuators should be approximately 1 actuator/mm^2. It is determined by the simultaneous two-point-discrimination-threshold (TPDT) for static and vibratory stimuli on the fingertip. Actuator array packed denser than the spatial acuity will give a continuous tactile sensation at the fingertip, which is not favorable in the Braille display application.

Diversity of displayed stimuli

There are two main kinds of mechanoreceptors under human skin: rapidly adapting (RA) and slowly adapting (SA) mechanoreceptors. RAs in general respond to temporal changes in force indentation. SAs respond also on constant force exertion to the skin [103]. Most stimuli applied to the skin, such as tapping the skin with a small probe, consist of a superposition of multiple components: vibration components that stimulate RA units, normal indentation components that stimulate SA I units, and lateral stretch components that stimulate SA II units. A practical Braille display should be able to stimulate all four types of mechanoreceptors in order to display a variety of tactile sensations.

Minimum Stroke

The higher the stroke of the actuator, the better it is for presenting contrast. However, the minimum stroke of 0.25mm is sufficient for Braille display.

Minimum Contact Force

Each actuator should be able to withstand the contact force of fingers in the exploratory process. Psychophysical experimental data indicates that a 50-100mN force is applied during a fine-touch object exploration [104].

Refresh Rate

The Braille display should be able to operate at different controllable frequencies ranging from 0 Hz to 300Hz. Three sets of frequencies are of particular importance:

1. Frequencies below 20 Hz are mostly responsible for small-scale shape perception.

2. Maximum sensitivity occurs at frequencies around 250 Hz [105].

3. Frequencies near the limit of perceptible vibrations (around 1 kHz) are rich in tactile information and are usually believed to be responsible for the perception of micro-textures.

Power consumption and safety

Since a Braille display is a computer peripheral in direct interaction with the user, it is very important to be safe. It is a big challenge for the state-of-the-art actuators since they require a significant amount of power. However, the use of a micropneumatic approach greatly alleviates the safety concerns.

Maintenance

Skin secretions such as oil and sweat are highly corrosive. With prolonged exposure, these secretions can severely damage a device. Moreover, small-scale actuators used in tactile displays tend to be fragile and delicate. A practical tactile display should be impervious to dirt and skin secretion. It should also be easily maintainable and reparable.

Device cost

Refreshable Braille displays available on the market are very uncommon and expensive. This can be explained in part by the complexity of the technology required to build high-performance tactile actuators. As a consequence, the evolution of such devices

is very slow. Ideally, the price of a consumer Braille display should only be a small fraction of the cost of the system that controls it, usually a personal computer.

Active/Passive Touch.

Humans' tactile interactions with the real world consist of both active explorations (e.g. scanning a surface with a finger to determine its texture) and passive interactions (e.g. the feel of clothes on the skin). Active touch usually conveys more information than passive touch because the operation is guided. Also, the blind prefer to slide over the Braille dots rather than feel the height change or vibration on their fingertips. Consequently, the optimal tactile display should support active touch.

Comfort

The display has to be easily and comfortably scanned with the hand.

4.2.2. Device Structure and Principles

The proposed Braille cell consists of three components: the pneumatic actuator layer, the fluidic manifold, and the valves and electronics. The design of a SLA substrate for the pneumatic actuator layer is shown in Figure 4.2a. The six openings with protruded rings on the top surface of the substrate are the seatings for the PEG mold of the microbubble actuator. The six large openings on the bottom surface are the assembly holes to the fluidic manifold. The six small holes are designed to facilitate the removal of the PEG.

A schematic of the Braille cell without externally assembled valves and electronics is shown in Figure 4.2b. On the manifold, six valve connections, two high pressure inlets and two air outlets are incorporated.

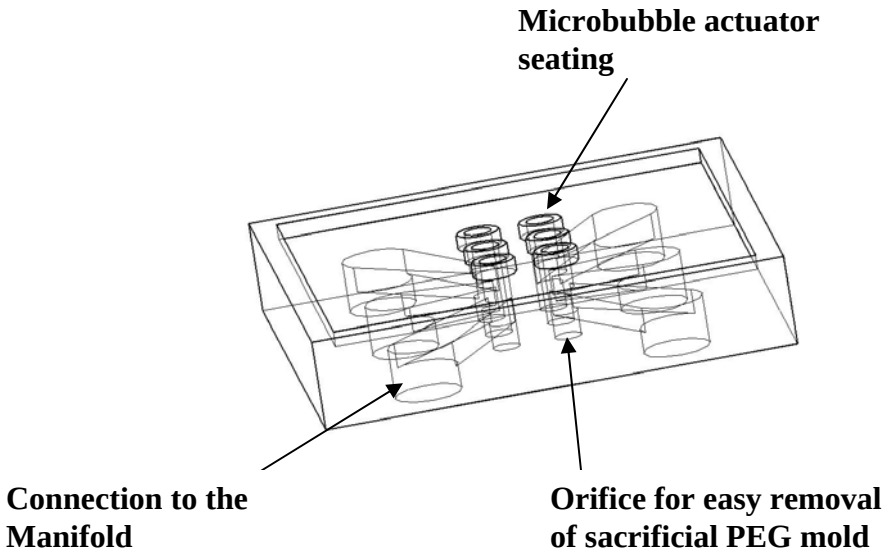

(a)

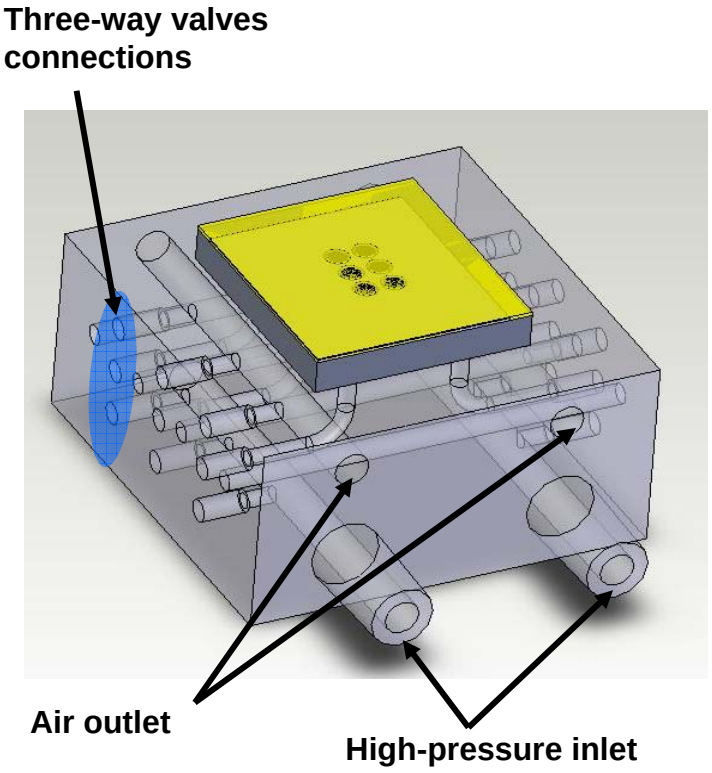

(b)

Figure 4.2 (a) Schematic of pneumatic actuator layer and (b) schematic of laminated pneumatic actuator layer on fluidic manifold

4.2.3. Pneumatic Actuator

The pneumatic actuator layer is constructed with six endoskeletal microbubble actuators arranged in a 2x3 array on a SLA substrate. The diameter of the endoskeletal microbubble actuator is reduced to 1.5mm. The new design for the corrugated diaphragm keeps the previous features of 6 corrugations, an inclined angle of 17° but has a slightly different geometry. A schematic view and the dimensions of the designed corrugated diaphragm are shown in Figure 4.3.

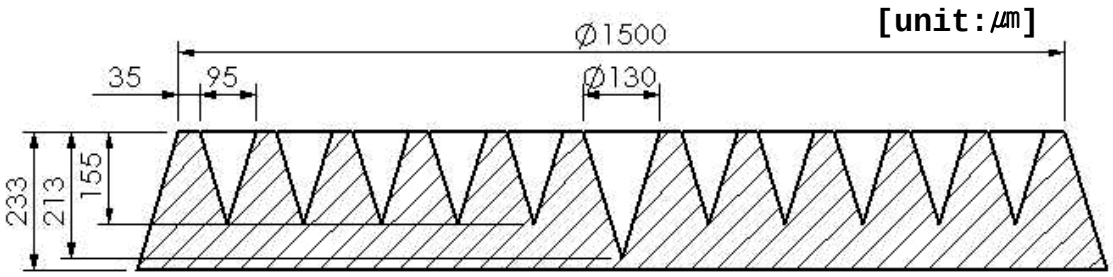

Figure 4.3 Profile and dimension of designed corrugated diaphragms

An array of sacrificial PEG corrugated diaphragm molds on epoxy substrates are fabricated using inclined rotational UV lithography, micromolding, and pattern transfer technology. Detailed fabrication processes for the PEG corrugated diaphragm molds are described in Chapter 3. Photomicrographs of the SU-8 corrugated diaphragm molds and corresponding PEG molds on a SLA substrate are shown in Figure 4.4.

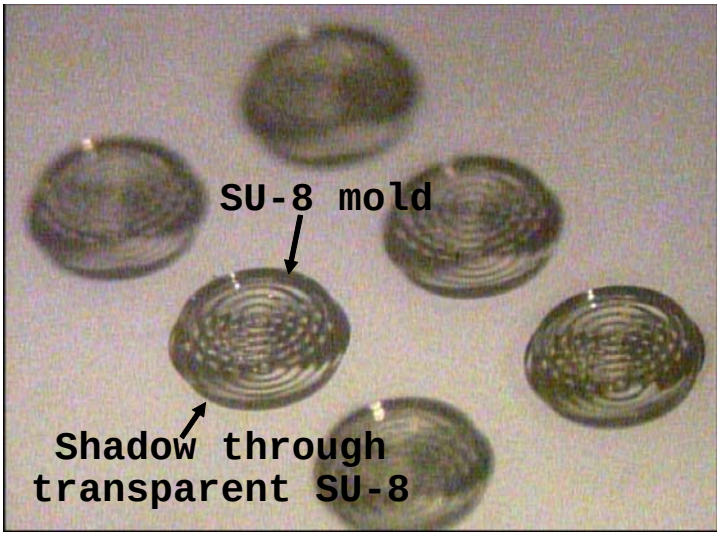

(a) original SU-8 mold

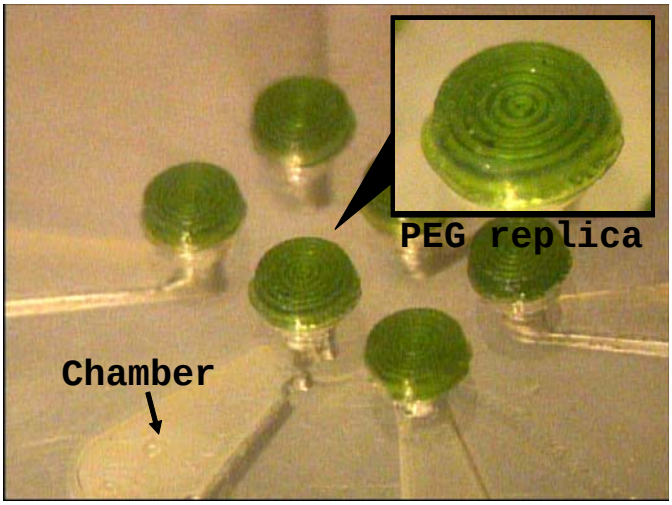

(b) PEG replica

Figure 4.4 An array of SU-8 molds and PEG molds

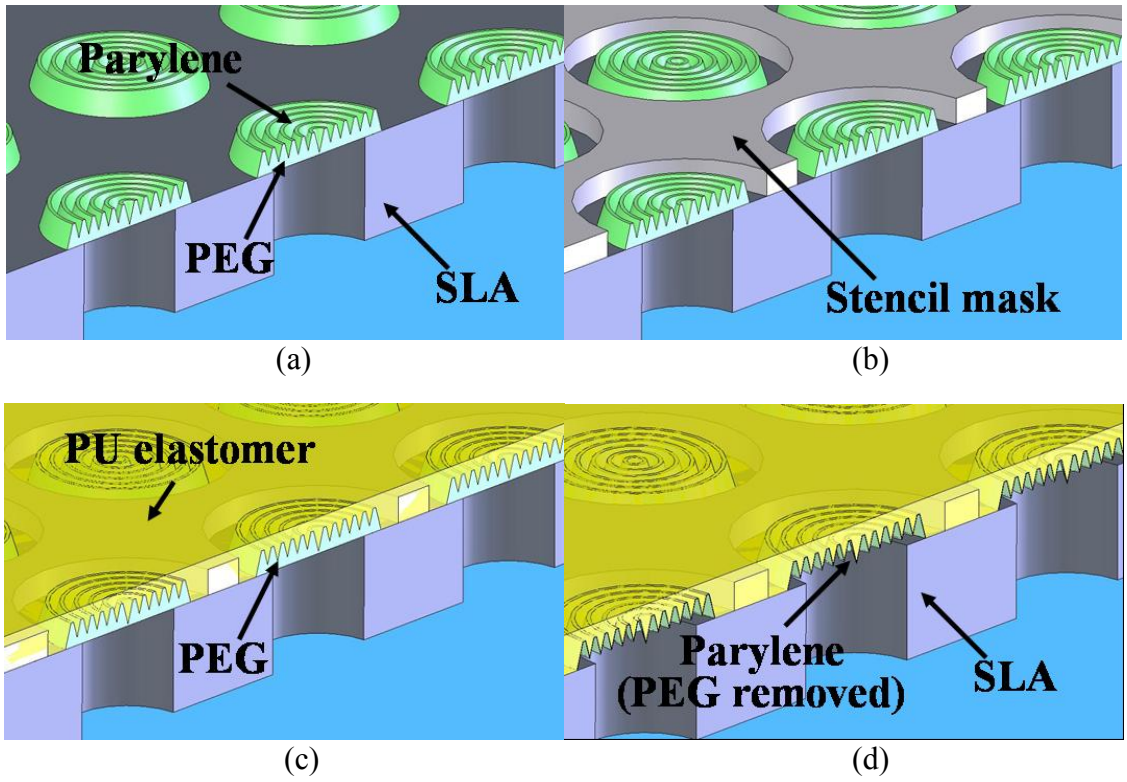

Figure 4.5 Fabrication process

After formation of the PEG molds array on the SLA substrate, a parylene layer was conformally deposited on the PEG molds array (Figure 4.5a). An epoxy stencil mask was placed on the epoxy substrate to planarize the top surface (Figure 4.5b). From this step, two types of actuators have been fabricated with different over-coating elastomer layer. A thin layer of polyurethane (PU) elastomer or PDMS elastomer was spin-coated on top and cured (Figure 4.5c). The sacrificial PEG was dissolved in water (Figure 4.5d). The SLA substrate with microbubble actuator array was then bonded to a SLA manifold which pneumatically addresses each microbubble (Figure 4.5e). The pictures of a PU actuator array and a PDMS actuator array laminated with manifold are shown in Figure 4.6.

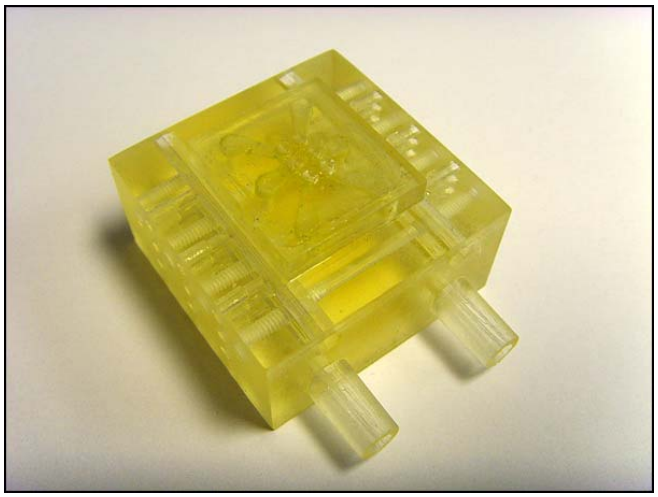

PDMS Braille Cell

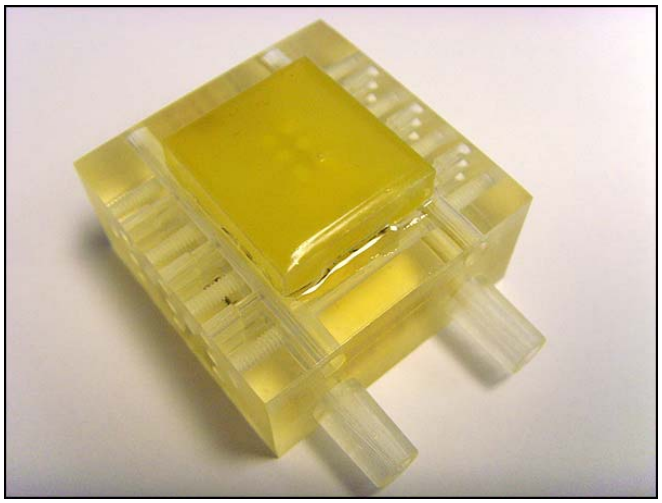

PU Braille Cell

Figure 4.6 Bonded actuator layer and manifold

Finally, six 3-way solenoid valves were assembled to the manifold to control individual actuators. The assembled device is shown in Figure 4.7. The height of fully assembled device is 5cm with most of the length contributed by the electronics, valves and the matching manifold.

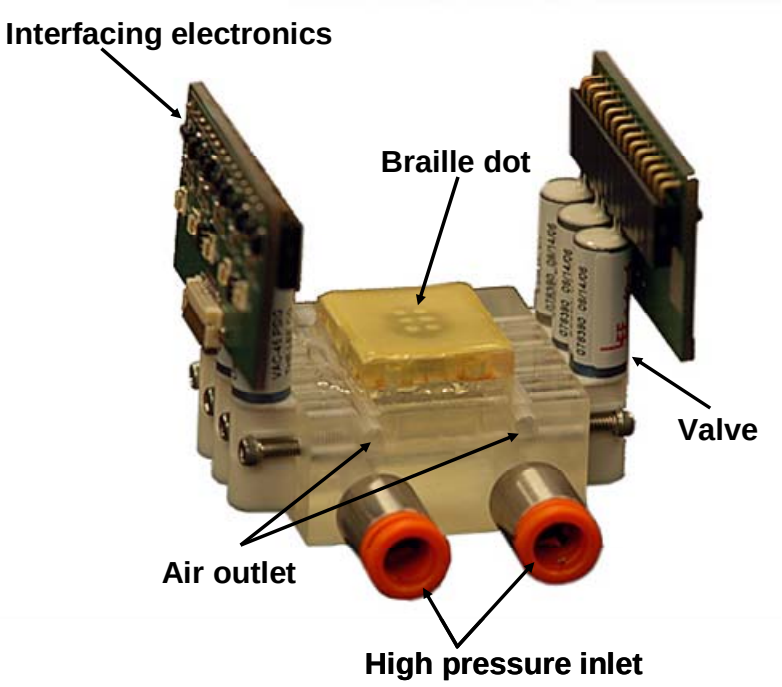

Figure 4.7 Assembled device with PU microbubble actuator array

4.3. Characterization

The performance of the RBD device was assessed from the following perspectives: spatial resolution, displacement, force generated, mechanical bandwidth, pneumatic power consumption and life time.

4.3.1. Spatial Resolution

Figure 4.8a shows a Braille cell in its working state. Figure 4.8b shows selectively actuated Braille dots representing the characters “B”, “P” and “T” in American Braille style. The center-to-center distance between two adjacent dots is 2.5mm, which exceeds the minimum discernable distance of 2mm on a fingertip [5].

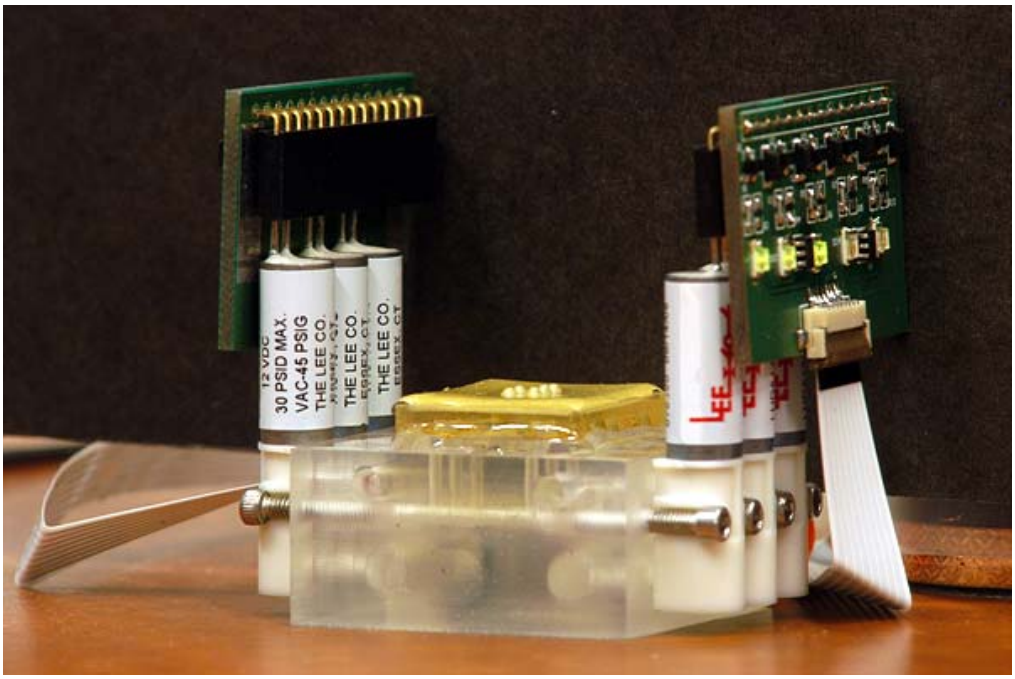

(a)

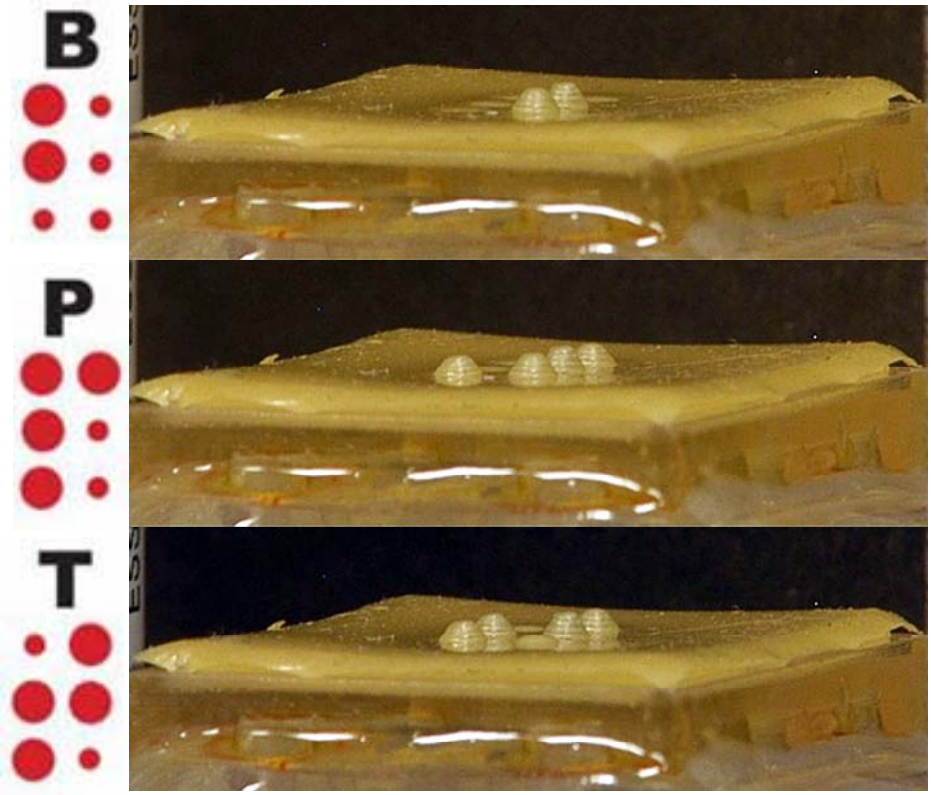

(b)

Figure 4.8 Actuation of Braille dots corresponding to Braille alphabets

4.3.2. Displacement

Magnified pictures of a PU Braille dot in its inactivated and activated state are shown in Figure 4.9. Note that large deflection is achieved preferentially in the vertical direction, which makes the shape more distinguishable than the hemispherical shape of a pure elastomer balloon actuator.

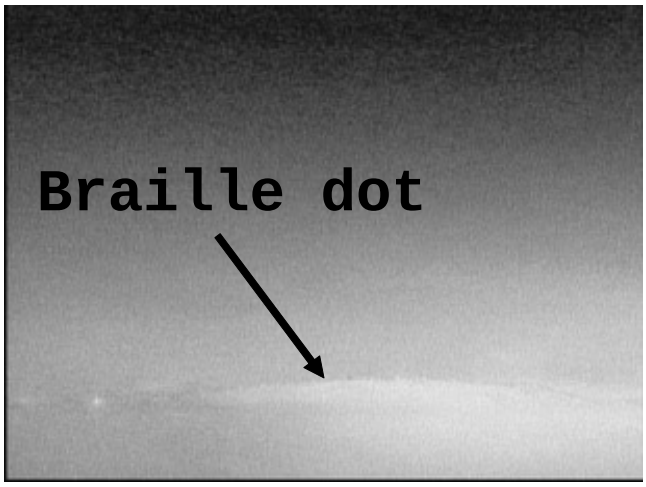

(a) Unactuated dot

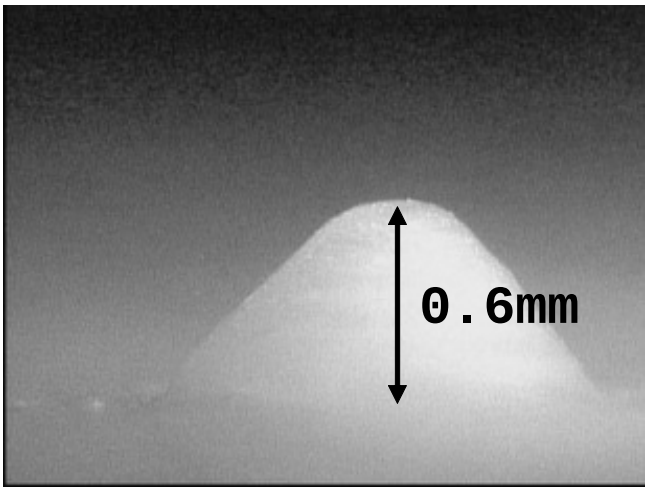

(b) Actuated dot at 100kPa

Figure 4.9 Inactivated and activated Braille dot

Center displacement of a Braille dot (i.e. the microbubble actuator) as a function of applied pressure has been quantitatively characterized using a laser displacement

sensor. The center displacement was measured at each different applied pressure at an actuation frequency of 0.2Hz, e.g. the valves was turned on and off at 0.2Hz while the maximum, minimum and peak-to-peak displacements of the Braille dot were recorded. The maximum displacements for three PU Braille dots with 2.5-µm-thick parylene and 100-µm-thick PU are plotted in Figure 4.10. The measured results for four PDMS Braille dots with 2.5-µm-thick parylene and 50-µm-thick PDMS are plotted in Figure 4.11.

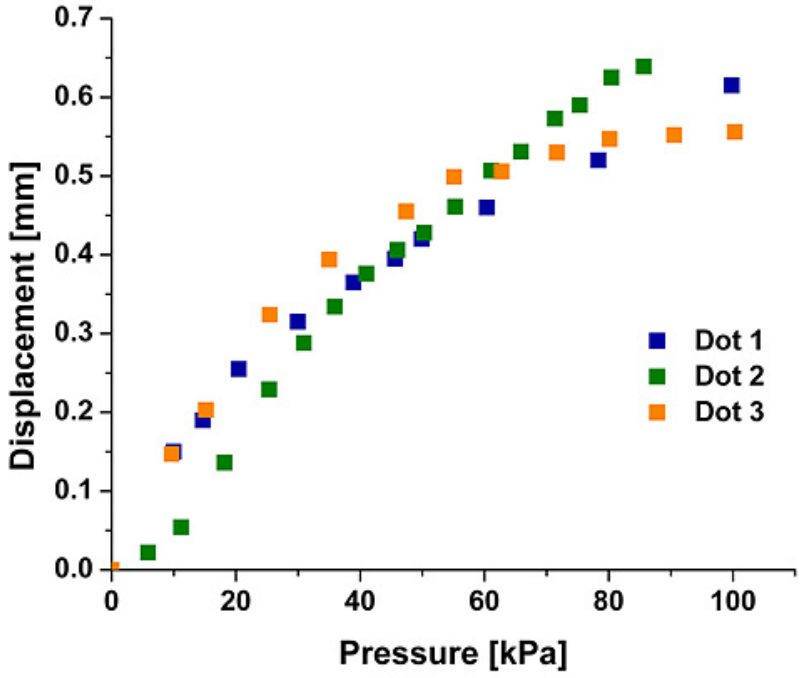

Figure 4.10 Measured dot height of three PU Braille dots as function of applied pressure.

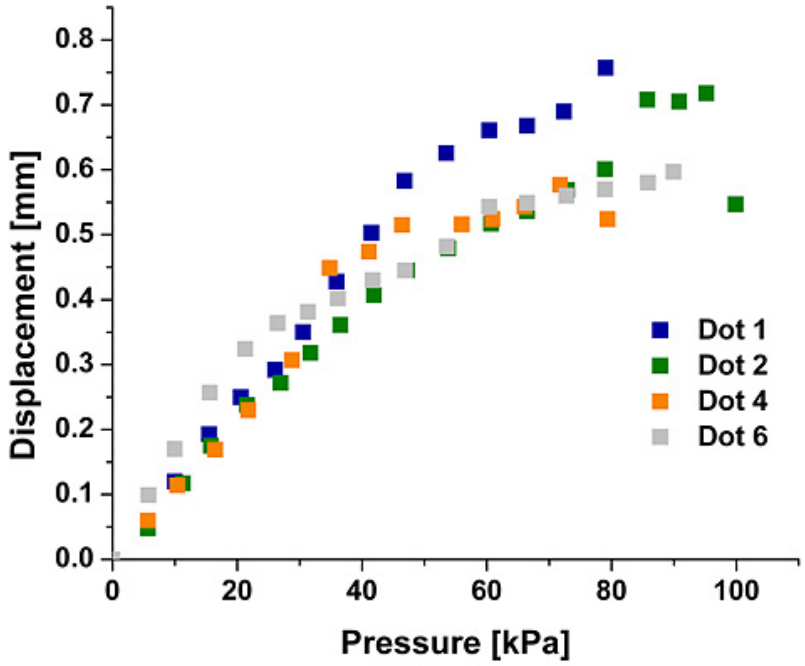

Figure 4.11 Measured dot height of four PDMS Braille dots function of applied pressure

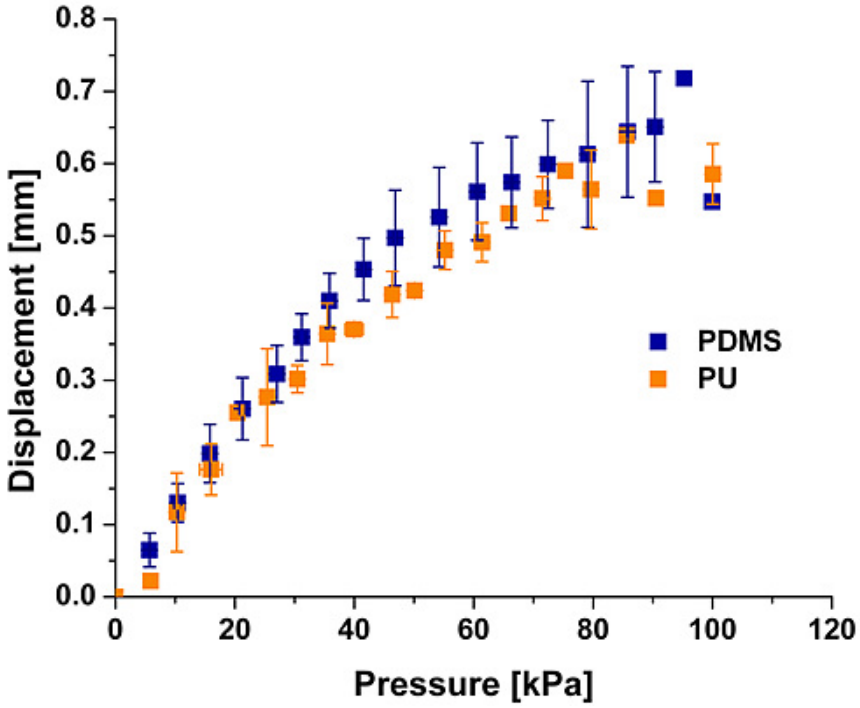

Figure 4.12 Averaged dot height for a PDMS Braille cell and a PU Braille cell as function of applied pressure

It can be seen that there is some variation in the dot heights. These variations may be ascribed to the uniformity in the spin coating process and/or defects in the micromold for the corrugated diaphragms. These imperfections would be removed by optimizing the process conditions. The PDMS microbubble actuator are less stiff since the thickness of PDMS is only half the PU thickness. Thus, it shows larger displacement at the same applied pressure as illustrated in Figure 4.12.

A finite element analysis similar to the one conducted in Chapter 3 was performed for the miniaturized microbubble actuator (Braille dot). Figure 4.13 compares the FEM simulations and experimental results for a microbubble actuator with 2.5-μm-thick parylene and 100-μm-thick PU as a function of applied pressure. The circular solid dots in the figure represent the simulation results, and the square dots represent the experimental results. As shown in Figure 4.13, these two data sets are in excellent agreement.

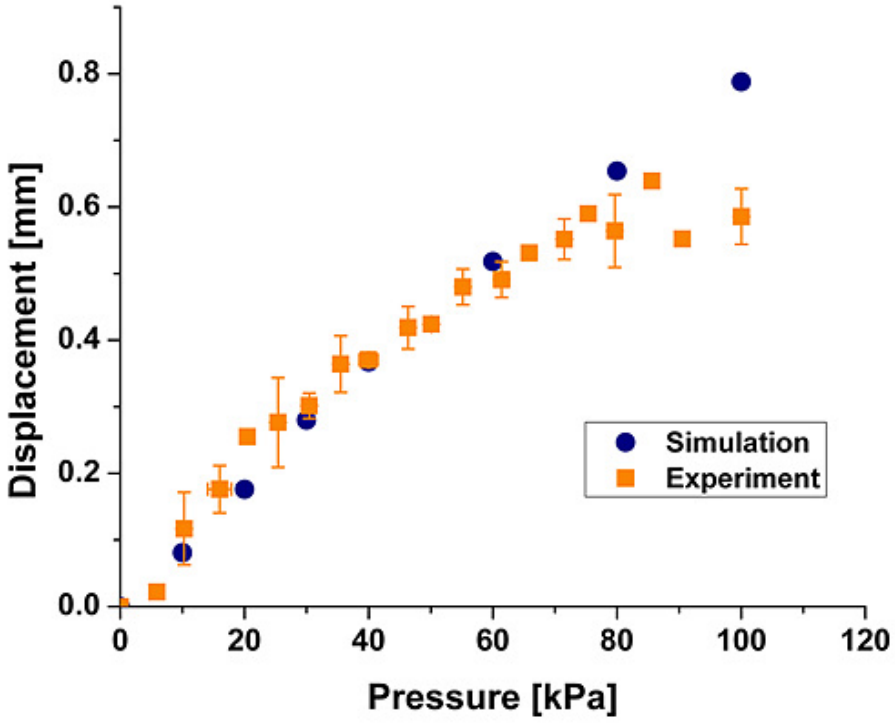

Figure 4.13 Average dot height for a PU Braille cell from experiment and FEM results

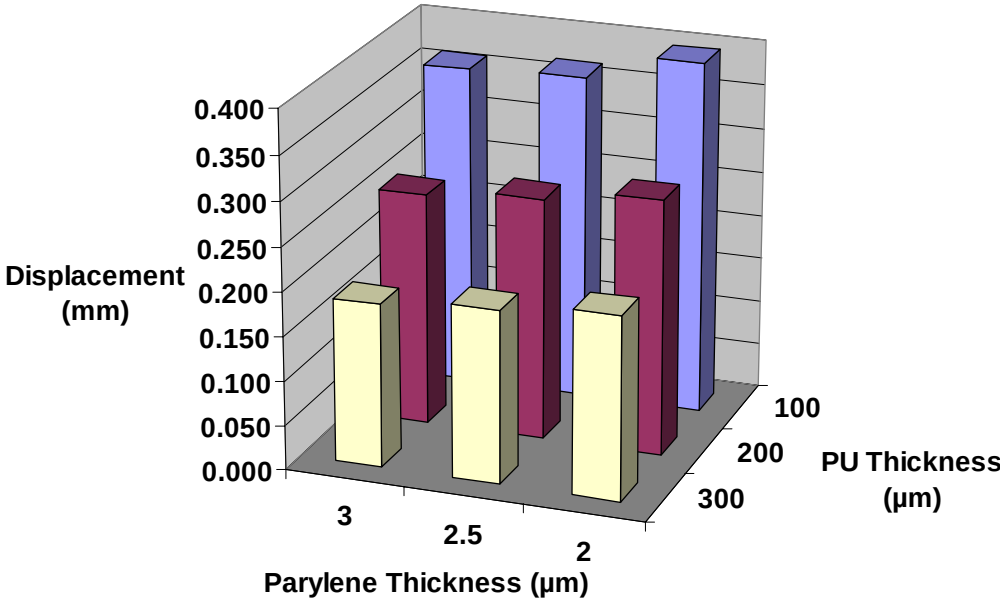

Figure 4.14 FEM results on the displacement of a PU Braille cell in dependence of layer thickness

Results from FEM simulations indicate that the diaphragm thickness has a strong influence on load-deflection performance. The simulations were conducted for a miniaturized microbubble actuator of fixed geometry and with a 40 kPa pressure applied. The results are plotted in Figure 4.14. Using the microbubble actuator with 2.5-µm-thick parylene as an example, if the PU thickness is reduced from 300µm to 100µm, a 0.367mm center deflection can be obtained as shown in Figure 4.14. This is almost 90% more than the 0.195mm deflection of the 300µm-thick mirobubble actuator.

4.3.3. Force Generated

Each Braille dot should withstand at least 50mN contact force while maintaining at least 0.25mm displacement to be able to stimulate the shallowest mechanoreceptor. A force evaluation is carried out for the RBD device. As can be seen in Figure 4.15, a 10 gram and a 20 gram weight are lifted up to 0.43mm and 0.48mm by three actuated dots at

60 kPa and 100 kPa, respectively. The weights correspond to 33mN and 66mN generated force per dot at 60 kPa and 100 kPa, and a 0.4mm displacement was maintained.

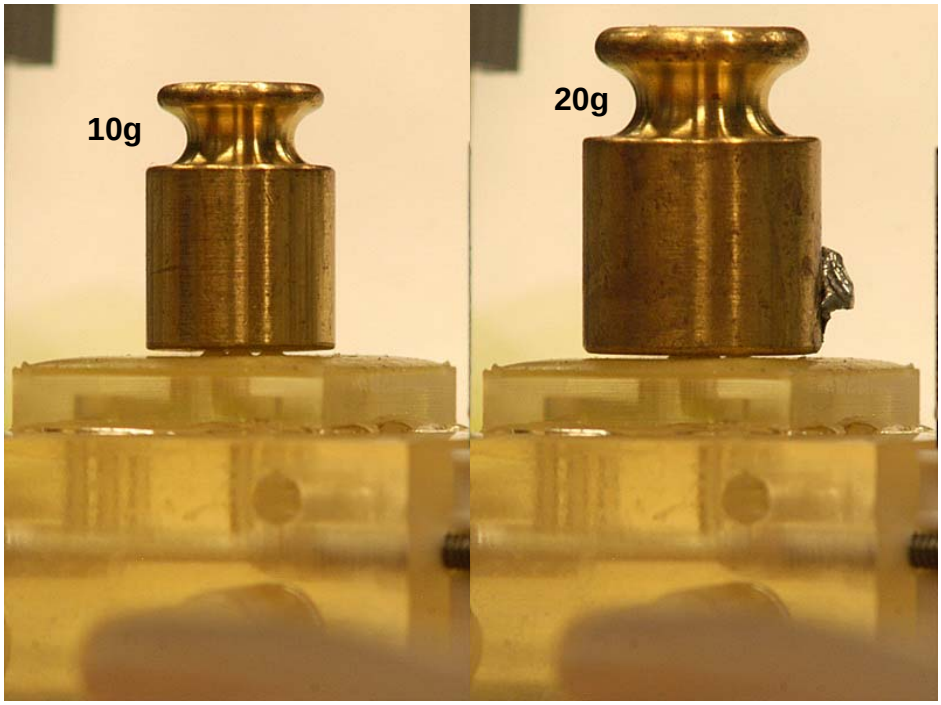

Figure 4.15 A 10 g and 20 g weight is lifted by three actuated Braille dots

The force generated by one single Braille dot as a function of displacement has also been characterized. The force at various displacements was determined by the following experimental procedure (Figure 4.16): A Braille cell was placed on a scale with an accuracy of 0.1gram. A small piston was mounted on a readable moving z stage. Under a constant applied pressure, the piston was brought down to be in contact with the inflated microbubbble actuator at the "zero force" position, where the bubble actuator maintained its maximum displacement. The piston was then moved downward at a fixed interval while a constant pressure was being supplied to the microbubble actuator. The reaction force was read from the scale. This procedure was repeated for a range of displacement and pressures.

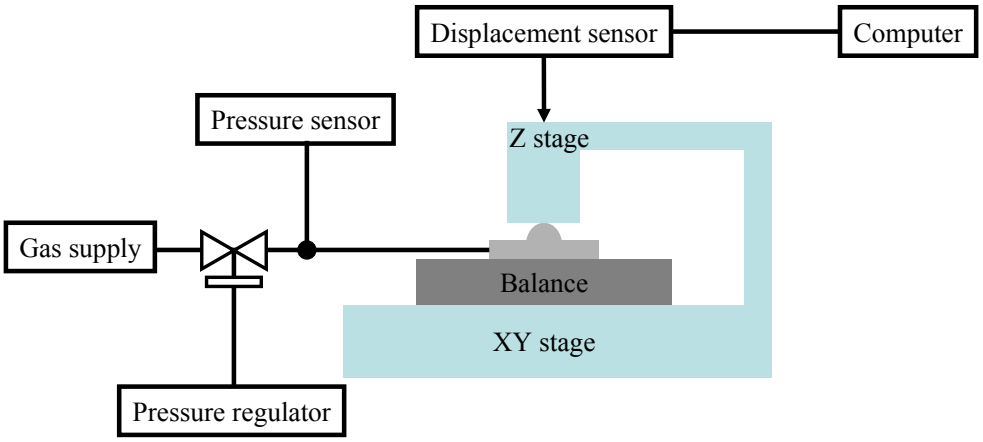

Figure 4.16 Diagram of force measurement

The results for a PU Braille dot at 66kPa and 100kPa are shown and compared with the experimental results for a PDMS Braille dot at 66kPa in Figure 4.17.

For each static applied pressure, the force vs. displacement curve is linear. The slope of the F-Δz curve equals to the stiffness of the microbubble actuator. As can be seen in Figure 4.17, the two curves for the PU microbubble actuator for two applied pressures are similar, while the one for PDMS microbubble actuator has smaller slope.

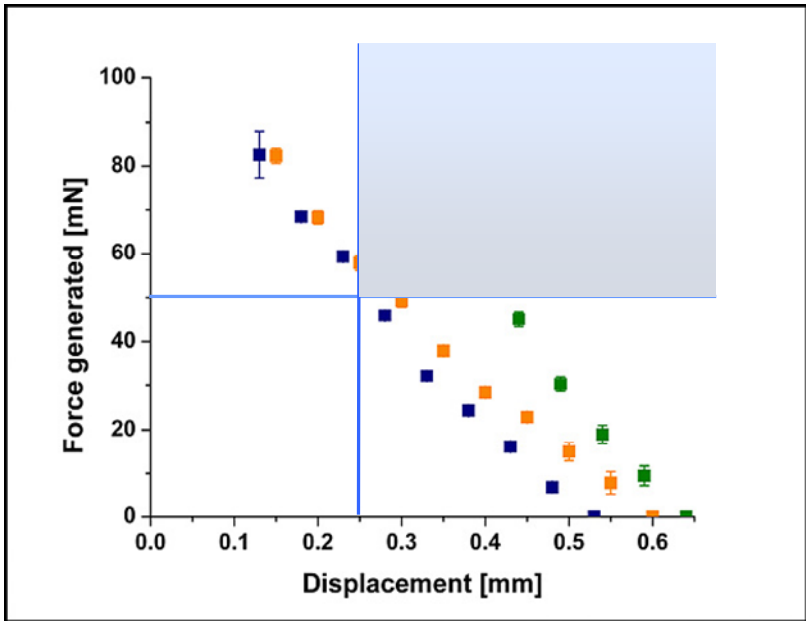

Figure 4.17 Force generated by a actuated PU Braille dot at 66kPa and 100kPa compared with the force generated by a actuated PDMS Braille dot at 66kPa

The region where force exceeds 50mN and displacement exceeds 0.25mm is highlighted on Figure 4.17. This is the region for practical Braille cell operation. The performances of both PU Braille cell and PDMS Braille cell fall within this region when the applied pressure is greater than 66kPa.

4.3.4. Mechanical Bandwidth

To test the mechanical bandwidth of the Braille dot, a steady pressure of 100 kPa was provided to the pressure inlet of the Braille dot. A series of sine wave inputs of varying frequency were applied to the valve controlling a single Braille dot. The sinusoidal input was modulated by the binary transfer function of the mechanical valve and adjusted to 50% PWM duty cycle at the frequency of interest, producing a pseudo-square-wave pressure pulse to the dot. The peak-to-peak displacement of the dot was measured by laser sensor as a function of excitation frequency in the range 0.2 Hz to 200 Hz and plotted in Figure 4.18 as a function of frequency.

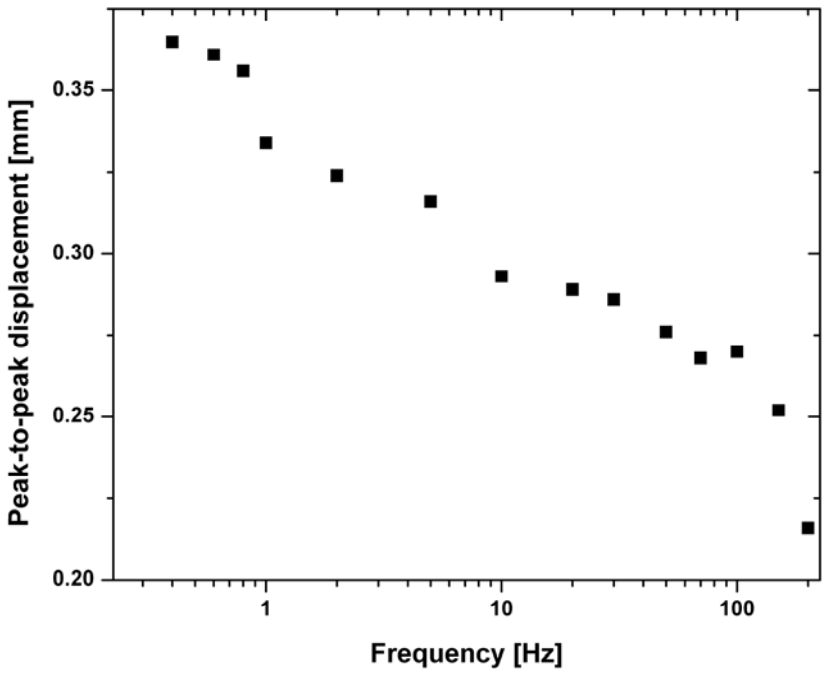

Figure 4.18 Frequency response of one Braille dot

As shown in Figure 4.18, at an actuation frequency of 30Hz, the peak-to-peak magnitude has fallen to approximately 70% of its low frequency value. At 150Hz excitation frequency, the peak-to-peak displacement is approximately 0.25 mm which still meets the minimum requirements for a Braille display. Further, at 200Hz, the displacement of 0.22 mm is still more than 50% of the maximum 0.403 mm. The high frequency performance of this RBD cell suggests its application in a vibratory tactile display, since according to physiological study, the 200-300Hz range is the most sensitive range for vibration sensing by human skin.

Several factors may potentially contribute to the dynamic response of the Braille dot:

1. Valve response

The valve used has a response time of 3ms, which implies that at the maximum testing frequency of 200Hz, the mirovalve can open and close completely. In another word, the size of the microvavle orifice remains the same up to a driving frequency of at least 200Hz.

2. RC time constant:

A Braille cell can be analogized with an R-C circuit. The Braille dot is the capacitor being charged through a resistor, which is the fluid resistance. One question needs to be answered is whether the pressure in the bubble can reach the level of applied pressure during the time period that the valve is on. To answer this question, ideal gas law, Bernoulli equation, and mass conservation equation are solved. A plot of pressure difference between the pressure at valve inlet and the pressure inside the Braille dot vs. time is shown in Figure 4.19. After 77 μs, the pressure difference reaches zero.

At any small time variation t_i:

Ideal gas law:

$$PV = nRT\ ,\ P = \rho\frac{R}{m}T$$

Bernoulli's equation:

$$P_s - P_i = \frac{1}{2}\rho_i v^2$$

Mass conservation:

$$\rho_i V = (\rho_s v A)\Delta t + \rho_{i-\Delta t} V$$

where Ps= 2 x10^5 Pa, ρ_s=2.45 kg/m^3,

at time t_0, P_0= 1x10^5 Pa, V= 4x10^{-8} m^3, ρ_0= 1.225 kg/m^3

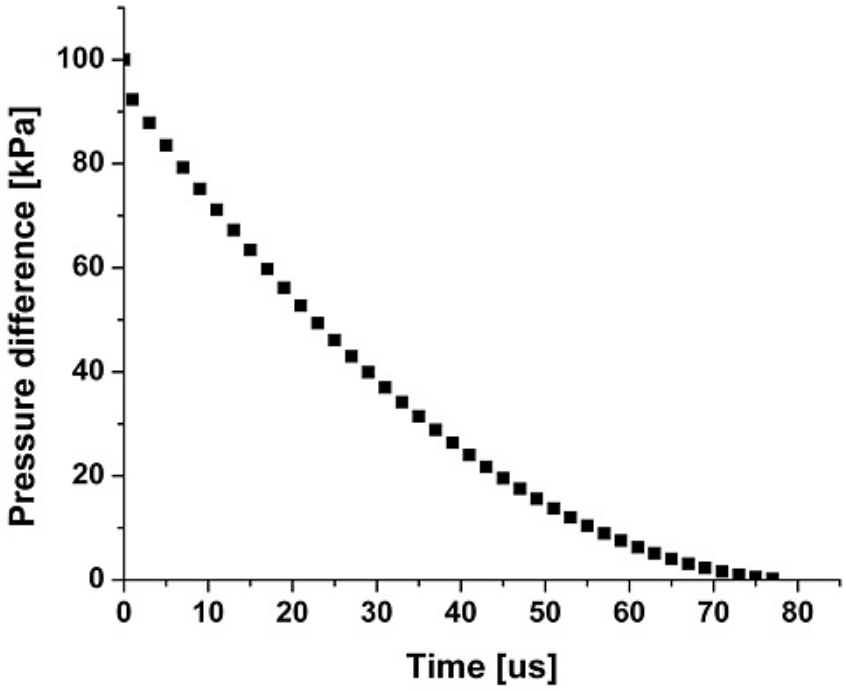

Figure 4.19 Pressure difference between air supply pressure and actuator pressure as a function of time after valve is open

3. Viscoelastic response

In cyclic testing, it was observed that the recovery (deflation) of the microbubble actuator is slower than its inflation. Therefore, the peak-peak deflection is decreased as the cycling frequency increases, even in the range of very low frequency.

Calculations in the previous section supported the theory that the depressurization time (i.e., the time required for the pressure inside the Braille dot to be reduced to atmospheric pressure) is the same as the pressurization time because the volume, the orifice and the pressure difference are identical in both cases. The time scale for the depressurizing time is too small to cause the observed slow recovery. However, a major asymmetry between inflation and deflation is the mechanical strain of the polymer composite of the endoskeletal microbubble itself; during pressurization, stresses are induced in the polymer multilayer, and during depressurization, the polymer is recovering from these stresses. It is known from the quasistatic inflation and deflation measurements detailed previously that the endoskeletal microbubble can exhibit a viscoelastic response; thus, the potential for this effect to cause the observed pressurization asymmetry is investigated.

The recovery of a viscoelastic deformed material consists of two stages. The first stage comprises the fast elastic recovery of the majority of the strain that is associated with relaxation of the soft segment of the macromolecule. The second stage is a slow recovery that is ascribed to viscoelastic relaxation of the rigid chain segment of the macromolecule. This relaxation time can be extremely long depending on the material and the time history of the creep development. However, given time, a viscoelastic deformed elastomer material can recover almost completely (to 97-98%) [106].

In the quasi-static inflation and deflation cycle of the microbubble actuator at 1Hz, the recovery time constant appears to be on the order of 1s. In a previously reported work on an artificial hair cell (AHC) sensor made from polyurethane (PU) elastomer, bending tests were done on high-aspect-ratio PU elastomer pillars (AHC) [107]. It was found that the recovery time for the bent pillars was in the order of 100 ms upon large

bending and was reported that shorter pillars would decrease the recovery time. The creep-recovery time constant, as one of the viscoelastic responses of elastomeric materials, is highly dependent on the types of strain, the levels of stress and strain, and the strain rate. It is not practical to compare two sets of time constants with different types of strain, different strain level and strain rate. However, qualitatively the behavior of the microbubble actuator appears to be consistent with that of the PU AHC. The longer recovery time constant is due to the larger strain and repetitive stress load that microbubble actuator experience. Therefore, it can be concluded that the dynamic response of the microbubble actuator may be explained by the viscoelastic nature of the material rather than the device and the apparatus used.

During dynamic operation of the microbubble actuator higher operating frequency leads to shorter recovery time, thus less the recovery. This explains why the amplitude of peak-to-peak displacement decreases with the increase of the operating frequency.

One good example to illustrate this viscoelastic recovery is the mechanism of the so called “shape memory mattress foam”. Basically, the foam is based on polyurethane. By carefully design the formulation of the polyols used in the synthesis, the PU foam can be highly viscoelastic. The deformation of the foam includes a small elastic portion but mostly-viscoelastic part. The recovery is very slow but complete.

4.3.5. Alphabet Table and Sentence Display

The Braille cell successfully displays the Standard English Braille alphabet and sentence at different pressure over a refresh rate range from 1 Hz to 30Hz. Example of alphabet display is shown in Figure 4.20.

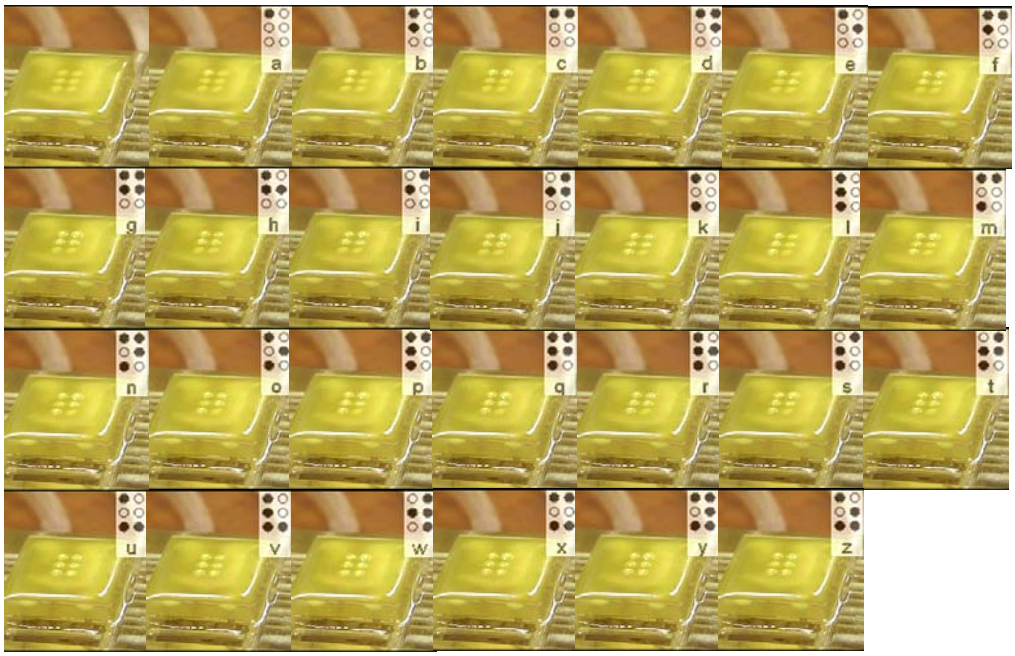

Figure 4.20 Braille alphabet table display

And example of sentence display is shown in Figure 4.21

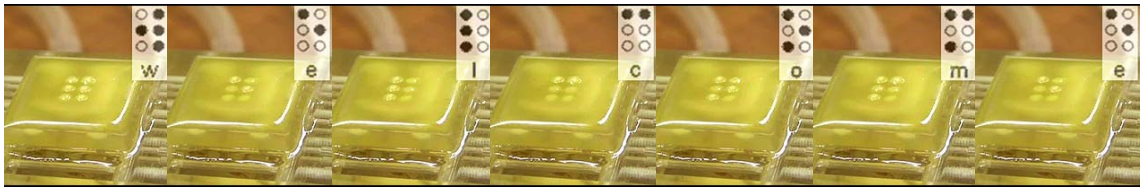

Welcome

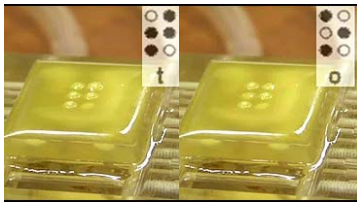

to

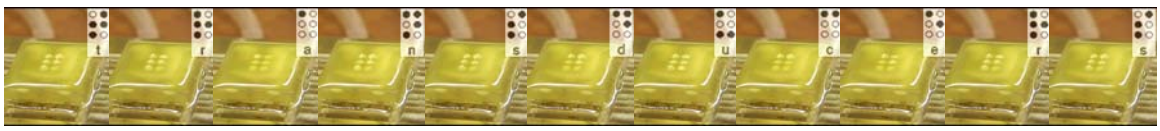

transducers

Figure 4.21 Braille sentence display

4.3.6. Pneumatic Power Consumption

Truly portable pneumatic Braille displays requires on-board storage of pressurized gas. Based on the current design, we calculated that 1cc of 10atm compressed air can sustain 24 min of Braille reading at a 5Hz frequency for a single Braille cell.

The volume of a Braille dot was calculated by the procedure that is described as follows: Microscopic cross-sectional image of an actuated Braille dot was taken at certain applied pressure. The image was then imported to a 3-D CAD software (Solidworks 2007). A cross-sectional profile was replicated by drawing a line along the image. With the revolving function of the software, the profile was used to reconstruct a 3-D profile of the actuated Braille dot as shown in Figure 4.22.

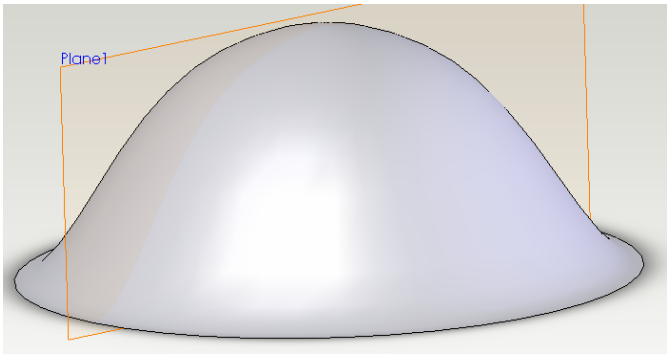

Figure 4.22 Reconstructed 3-D profile of one Braille dot in Solidworks

The volume information of the Braille dot was obtained by using the mass properties analyzing function. It was found that an actuated Braille dot has a volume of 0.46 cubic millimeters at a 100kPa applied pressure.

The following calculation shows that 1cc of 10atm compressed air can sustain 24 min of Braille reading at a 5Hz frequency for one Braille cell containing six Braille dots. Assuming that at anytime, there are three Braille dots inflated and three deflated. The volume flow in the Braille cell in one second is 0.46 x3 =1.38mm^3/s. With a total

volume of 1cc x 10 x1000 =10^4 mm^3 air supply, the sustaining time is 10^4/1.38/5 = 1450s = 24 minutes.

4.3.7. Life Time

As an actuator for a refreshable Braille display or a vibrational tactile display, the microbubble actuator is subjected to dynamic load instead of static load. The stress in the microbubble actuator varies in magnitudes with time. Thus, analysis should not be done using static stress theory. Under these varying and repetitious stresses, failure could occur well below the yield point of the material. The stress level required to produce failure would decrease with increasing stress cycles. The stress corresponding to the point of failure for a given number of cycles is known as "fatigue strength".

The fatigue life of a microfabricated device is typically evaluated experimentally. To test the long term stability and life time of the device, one randomly picked PU Braille dot was operated at 60kPa and at a refresh rate of 10Hz. A laser displacement sensor was used to record the displacement over time. The maximum, minimum and relative displacements of the Braille dot are shown in Figure 4.23. After 33.8 hour of operation, the parylene layer failed, as evidenced by the shape of endoskeletal microbubble changing into a hyper-inflated balloon, which was an indication that the skeleton lost its sustaining function.

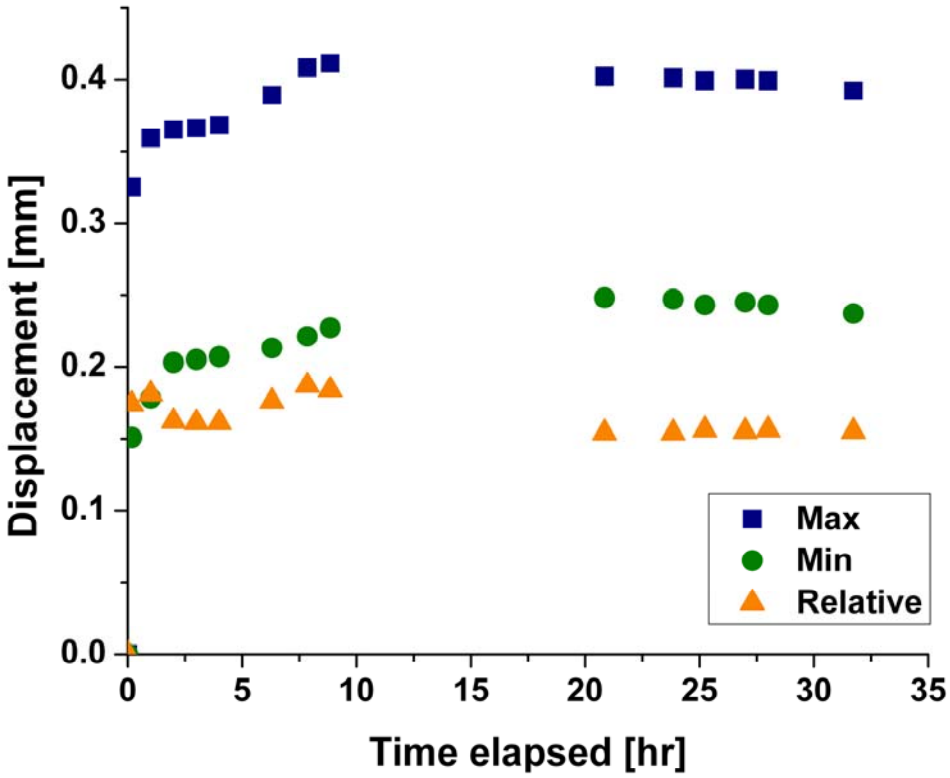

Figure 4.23 Long-term actuation stability of the Braille dot

The tested Braille dot shows a life time of 1,216,800 actuations at 10 Hz actuation frequency. The world's best-selling book, the New Testament, has a word count of 181253, corresponding to a total character number of 181253 x 5 = 906265. The tested Braille dot can sustain the non stop reading of a New Testament.

During the real operation of a Braille display, the refresh rate is smaller than 10Hz depending on how many cells the display has. It is safe to conclude that microbubble Braille dot can be operated at 1Hz for more than 300 hours based on the numerous literatures reporting that small variation on operating frequency does not influence the life time of polymer materials. On the other hand, Braille display is not a device that is usually operated continuously over a long period of time.

To improve the life time of the microbubble actuator, it is necessary to identify detrimental stress factors that influence the fatigue strength of parylene corrugated diaphragm. The stress concentration has been recognized as the dominant factor. The design of the parylene corrugated diaphragm incorporates sharp corrugation profile. Also, because the diaphragm is made from micromold, any defects on the micromold may cause potential variation in the parylene thickness, which leads to potential stress concentration points. Both problems can be solved entirely or partially, by optimizing fabrication process. For example, a reflow step can be added after the fabrication of the micromold in order to round the sharp corner. The reflow step also helps to improve the smoothness of the micromold.

In a real life application, a fixed life will be designated, after which the user is instructed to replace the microbubble actuator layer with a new one.

4.4. Conclusion

This chapter has shown the development of a refreshable Braille cell based on a 2 x 3 pneumatic microbubble actuator array.

A 2 x 3 pneumatic microbubble actuator array based on modification of previous design has been successfully fabricated and integrated with manifold and microvalve array. The modified design features enable the microbubble actuator to simultaneously meet a set of high displacement, high force, and small radius curvature characteristics that had not previously been satisfied by other tactile actuators presented in the literature. In addition, the microbubble actuator can provide both a static display and vibratory tactile sensations up to 200Hz. The life time of the microbubble tactile actuator is around 1.2 million uses.

The design of the Braille cell is scalable with respect to the number of dots, and fabrication remains simple even on a large scale. Along with having the above capabilities, the device has been designed to meet the criteria of lightness and

compactness to permit portable operation. Currently, commercially available valves and manifolds matching the valve arrays contribute to the majority of the size and weight of the Braille cell. A MEMS microvalves array would greatly reduce the size and weight of the current device. Furthermore, the cost of the microvalve may be lower because of the batch fabrication nature of MEMS technology. Another advantage is that the microvalve may be fabricated at the same time as the microbubble actuator array.

The next chapter will focus on the design, fabrication and characterization of a microvalve targeting for high flow rate, high pressure tactile display application.

CHAPTER 5

SOLID-HYDRAULICALLY AMPLIFIED MICROVALVE

5.1. Background

In a pneumatic tactile display system, the microvalve that controls each pneumatic actuator is a crucial component. Due to the inherent characteristics of the tactile display system and bubble actuator inflated by a pressurized air source, a set of specification is required for the microvalve:

1. Lateral dimension as small as possible so that they can be densely packed to form a full page display
2. Ability to work under large differential pressure of 90kPa
3. Switching frequency of up to 200Hz
4. Large flow rate of hundreds of sccm
5. Low power consumption
6. Fabrication and packaging process compatible with the fabrication of the polymer pneumatic actuator

There has been much research effort on developing MEMS microvalves, but none of the microvalves appeared to meet all of the performance and fabrication requirements listed above. The operation of a pneumatic tactile display demands a new approach in the valve design and fabrication to meet all the requirements. Some of the tradeoffs that need to be considered in designing a microvalve are:

Valve size vs. flow rate

Actuation stroke vs. force

Actuation stroke vs. bandwidth

Actuation output vs. power consumption

Performance vs. fabrication simplicity

MEMS active microvalves have been reported based a number of actuation methods, including thermopneumatic [108, 109], thermo-bimorph[110], shape memory alloy [64, 69], electrostatic [51, 73, 111], electromagnetic [112], piezoelectric [77-84, 113, 114] methods.

The thermal actuation designs (based on thermopneumatic, thermal bimetallic, and shape memory alloy principles) can potentially achieve large stroke and reasonable actuation force. However, these devices exhibit excessive power consumption and poor response times on the order of seconds. High-frequency actuation in the kHz range has been unachievable.

The electrostatic devices are limited in their deflection and pressure generation capabilities, because the electrostatic force generated between two parallel plates scales inversely with their spacing and because electrical breakdown across the gap must be avoided. Electromagnetic actuation requires low voltage, and the fabrication is straightforward. However, such concepts are impeded by the overall size of external solenoid and housing structures.

With their high bandwidth, large force, and low power consumption, piezoelectric actuators have become the most promising candidates for driving microvalves at high pressure and high frequency with low-power consumption. However, their drawback is small stroke (up to 0.1% strain) even at a large applied voltage, which restricts orifice gap and in turn limits maximum achievable flow rate. Increasing the piezo film thickness can lead to higher stroke, but at the expense of higher voltage applied.

Prior approaches to overcome this drawback include adoption of a stack-type piezoelectric actuator, piezoelectric bimorph structures, and hydraulic amplification mechanisms [77-84, 113, 114]. A leak–proof microvalve provided large sealing force at relatively low voltage by using a stack-type piezoelectric actuator, but the stroke was still insufficient for large flow rate applications [77]. A large valve stroke of 80μm was achieved for a piezoelectric bimorph microvalve, but was limited to very low differential

pressure [81]. Roberts et al. presented a hydraulically amplified PZT cylinder-driven microvalve with large stroke (20-30μm). However, a complex fabrication process including 22 photolithography steps was required [83]. Rogge et al. demonstrated a polymer microvalve with PZT bending disk and solid hydraulic amplification, but the PZT disk used had large lateral dimension that prevented the formation of a dense valve array [84].

Our approach to this challenge is the combination of a stacked piezoelectric actuator with a simple polymer-based solid-hydraulic amplification (SHA) scheme to maximize the piezoelectric stroke. The piezoelectric stack actuator is vertically integrated with a amplification chamber, enabling both dense microfluidic functionality and low-voltage operation. The fabrication is straightforward and compatible with the fabrication of microbubble actuator array. Compared with mechanical and liquid-hydraulic amplification, our approach is simple and avoids any sealing step. Furthermore, the amplification is in the axial direction, making it suitable for forming a dense microvalve array.

5.2. Concept of Solid Hydraulic Amplification

Macroscale hydraulic amplification systems primarily based on incompressible liquids have existed for a long time, but on the microscale, sealing has been a big fabrication challenge. Solid means can be adopted instead of liquid to eliminate the sealing problem. Therefore, this work focuses on the use of incompressible solid material as hydraulic transmission medium for a hydraulically amplified microvalve.

Figure 5.1 shows the principle of the solid hydraulic amplification mechanism. When a force is applied axially to the bottom layer of the hydraulic material, causing it to undergo a small deflection, the upper surface of the incompressible material undergoes an amplified deflection. The amplification ratio, defined as the ratio of the displacement of

the top and the bottom opening, is theoretically, inversely proportional to the ratio of the areas at top and bottom.

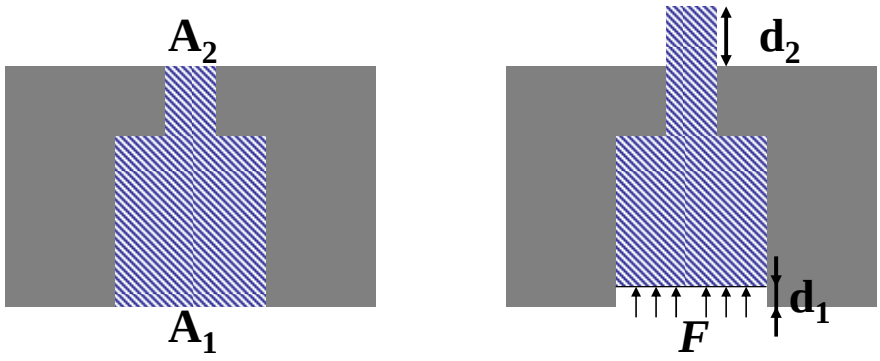

$$\text{Amplification ratio} = \frac{d_2}{d_1} = \frac{A_1}{A_2}$$

Figure 5.1 Principle of the solid hydraulic amplification mechanism

First, it is assumed that the hydraulic amplification chamber compliance is minimal so that the volume change due to the chamber deformation is negligible. Second, the elastomer is treated as an incompressible material, i.e. the volume change is zero at small deformation.

5.3. Solid-hydraulic Amplification Modeling and Experimental Verification

5.3.1. Finite Element Modeling

The purpose of the FEM was to evaluate the SHA concept, to understand the experimental results and to determine the limitations of SHA in microvalve application. Specifically, the four primary objectives of this modeling include:

1. To verify the solid-hydraulic amplification concept proposed. In another word, to confirm the feasibility of using elastomeric material for force and stroke transmission.
2. To recognize the design parameters for the SHA chamber in order to reach the ideal theoretical amplification ratio.

3. To investigate the influence of other factors on the amplification ratio. Those factors include friction condition at the boundary, underfilling of the elastomer, and pre-deformation of the elastomer.

Finite element analysis software ANSYS workbench 11.0 was used to conduct the simulations. Because the chamber is symmetric, only one quarter of each model was simulated in order to minimize simulation time and to increase the accuracy by increasing the number of elements. The elastomer material used in the modeling was PDMS. The model used for the PDMS was a Neo-Hookean model which is capable of modeling hyper-elasticity and consumes less computation time than the Mooney-Rivlin model. The material properties of structural steel were assigned to the chamber based on the assumption of minimum compliance of the chamber. In addition, all the surfaces of the chamber were fixed.

5.3.1.1. Poisson's Ratio and Incompressibility

In thermodynamics and fluid mechanics, compressibility is a measure of the relative volume change of a fluid or solid as a response to a pressure (or mean stress) change.

$$\beta = -\frac{1}{V}\frac{\partial V}{\partial P}$$

The compressibility β is given by the inverse of bulk modulus K of a material. The bulk modulus K can be formally defined by the equation:

$$K = -V\frac{\partial P}{\partial V}$$

The inputs for the Neo-Hookean model in ANSYS are initial shear modulus and incompressibility parameter for hyperelastic material.

Shear modulus G can be calculated from:

$$G = \frac{E}{2(1+\nu)}$$

The relation between Poisson's ratio and incompressibility parameter is derived below.

Initial bulk modulus K

$$K = \frac{E}{3(1-2\nu)}$$

Incompressibility parameter d

$$d = 2/K$$

Such that

$$d = \frac{6(1-2\nu)}{E}$$

One can tell from the formula for K that, as Poisson's ratio approaches 0.5, the bulk modulus of the material approaches infinity. In theory, when K goes to infinity, the material is fully incompressible. However, in reality, no material is fully incompressible. The larger the bulk modulus, the more pressure is required to cause a volume change. Ideally, a hydrostatic pressure experiment can be performed to measure the bulk modulus and then to find the precise Poisson's ratio. To simulate the solid-hydraulic amplification, it is preferable to choose a Poisson's ratio as close to 0.5 as possible so that the incompressibility would be enhanced. Table 5.1 lists the shear modulus, the bulk modulus and the incompressibility parameter for a PDMS elastomer with a Young's modulus of 2MPa with various Poisson's ratios. As shown in Table 5.1, the incompressibility decreases by one order with each one decimal 9 added to the Poisson's ratio. With a Poisson's ratio of 0.4999, the bulk modulus reaches 3.3 x10^9Pa, which is comparable to a 2.2 x10^9Pa bulk modulus of water.

Table 5.1 Shear modulus, bulk modulus, and incompressibility parameter from different Poisson's ratios

ν	**0.49**	**0.499**	**0.4999**	**0.49999**	**0.499999**
G(Pa)	6.7114e+005	6.6711e+005	6.6671e+005	6.6667e+005	6.6667e+005
K(Pa)	3.3333+e007	3.3333+e008	3.3333+e009	3.3333+e010	3.3333+e011
D(1/Pa)	6.0000e-008	6.0000e-009	6.0000e-010	6.0000e-011	6.0000e-012

In ANSYS simulations, it was found that computing time is dramatically increased as the Poisson's ratio approaches the value of 0.5. Using a Poisson's ratio of or

larger than 0.4999 was not practical for 3-D modeling with fine mesh size in terms of the computing time. Only a 2-D modeling can accommodates a Poisson's ratio of or larger than 0.4999 with fine mesh size. Therefore, the following modeling was divided into two parts:

1. In order to verify the SHA concept and simulate the case of ideal amplification, a 2-D model was constructed. A Poisson's ratio of 0.4999 was used to ensure the incompressibility in the simulation. In this 2-D modeling that covered in 5.3.1.2, all the boundary conditions and loading condition were idealized.
2. As a practical measure, Poisson's ratio of 0.49 was used in the trend simulation on the design parameters and affecting factors for 3-D models. In this case, the PDMS elastomer is slightly more "compressible". Also, the 3-D model mimics the real contact between the PZT stack actuator and the SHA chamber. The 3-D model overall enables the simulation of all possible factors affecting the amplification in a non-ideal case. Sections 5.3.1.3 through 5.3.1.6 are dedicated to the 3-D modeling.

5.3.1.2. SHA Verification

A 2-D model based on a SHA chamber with a straight slanted side wall as shown in Figure 5.2, have been constructed.

Figure 5.2 2-D geometry model of a SHA chamber filled with PDMS

Two different friction boundary conditions were applied: bonded and frictionless. The two friction boundary conditions represent the two extreme cases of the possible conditions. With a 1μm displacement applied to the bottom of PDMS, the corresponding top surface displacements were obtained and the ratio of the two displacements, or the amplification ratio (AR), was calculated for each friction conditions. The simulation results for the two cases are shown in Figure 5.3 and Figure 5.4.

The insets in Figure 5.3 and Figure 5.4 are magnified images of the deformed PDMS at the outlets and the surface profiles of the PDMS. The fully bonded interface gives an arc (spherical) shape and the frictionless interface gives a cylindrical shape with a curved top surface.

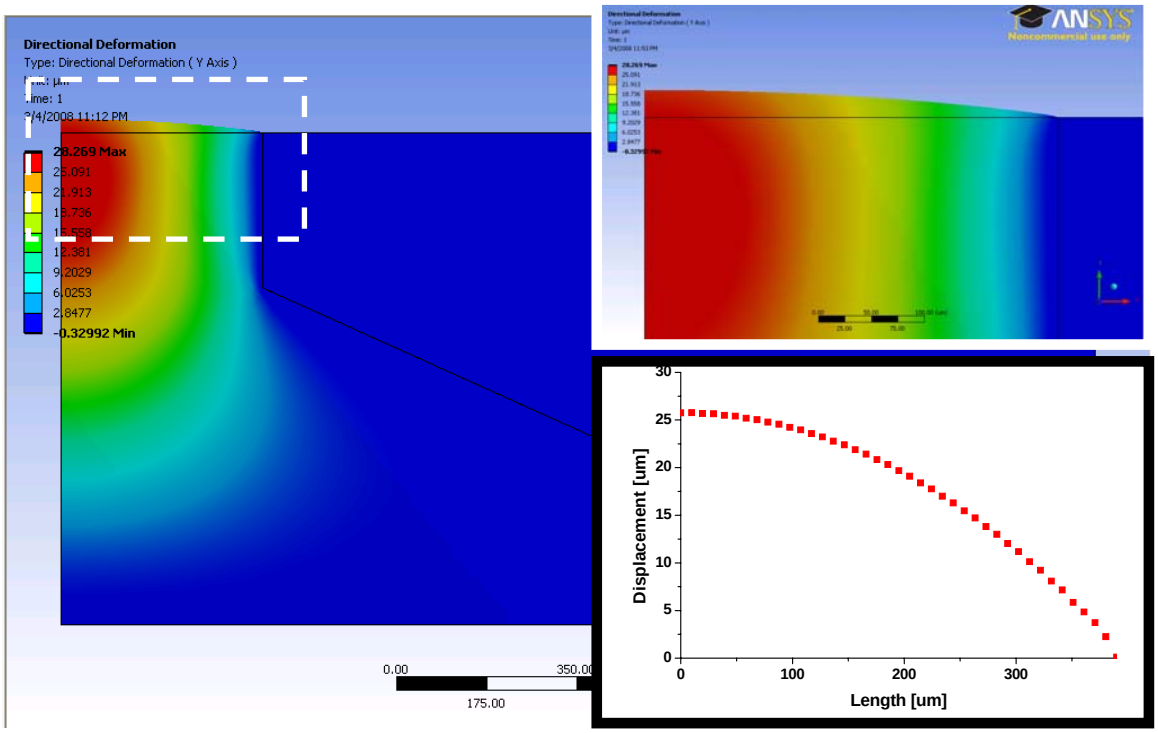

Figure 5.3 Simulation results for bonded condition between PDMS and the SHA chamber wall

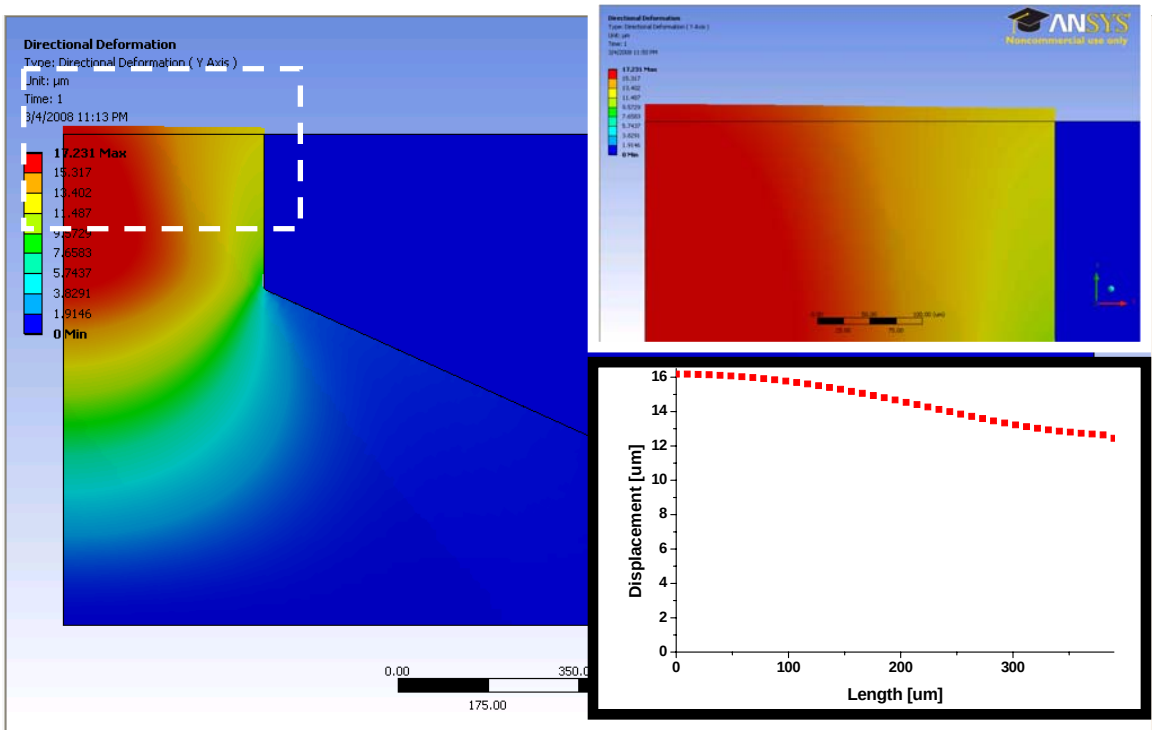

Figure 5.4 Simulation results for frictionless condition between PDMS and the SHA chamber wall

The surface profiles of deformed PDMS were used to obtain the volume of the PDMS that had been "squeezed" out of the SHA chamber, which were compared with the volume that had been "squeezed" into the chamber at the bottom. From this comparison, the volume change of the whole PDMS can be obtained. Table 5.2 lists the results on the volume analysis, the displacement results, and some important modeling parameters.

Table 5.2 2-D modeling parameters and results

Young's Modulus of PDMS		**2 MPa**	
Poisson's ratio of PDMS		**0.4999**	
Area	**Top**	**0.478 mm²**	
	Bottom	**7.069 mm²**	
Theoretical Amplification ratio		**14.7**	
Load displacement		**1 μm**	
		Bonded	**Frictionless**
Deformed shape		**Spherical**	**Cylindrical**
Displacement	**Max**	**28.3 μm**	**17.2 μm**
	Top	**25.8 μm**	**16.2 μm**
Amplification ratio		**25.8**	**16.2**
Volume conserved		**94.5 %**	**93.9 %**

The simulation results verified the concept of solid-hydraulic amplification. The volume of the PDMS is conserved in both cases. Because the deformed PDMS forms a round profile instead of a flat top surface, the top displacement is higher than the theoretical value thus the amplification ratio is also higher than the theoretical value.

The simulation parameters for the 2-D FEM are described in detail as follows using the frictionless case as an example.

Material properties:

The inputs for the Neo-Hookean finite element model of the mechanical behavior of the elastomer are its initial shear modulus and incompressibility parameter. These two parameters can be calculated from Young's modulus and Poisson's ratio of the elastomer, which was described in section 5.3.1.1. In this modeling, the two parameters used were calculated assuming a Poisson's ratio of 0.4999. Figure 5.5 shows the Neo-Hookean non-linear stress-strain fitting based on the two inputs. The material properties of structural steel were assigned to the hydraulic amplification chamber enclosing the elastomer.

Table 5.3 Material properties inputs for PDMS

Initial Shear Modulus Mu MPa	0.67114
Incompressibility Parameter D1 1/MPa	6.e-005

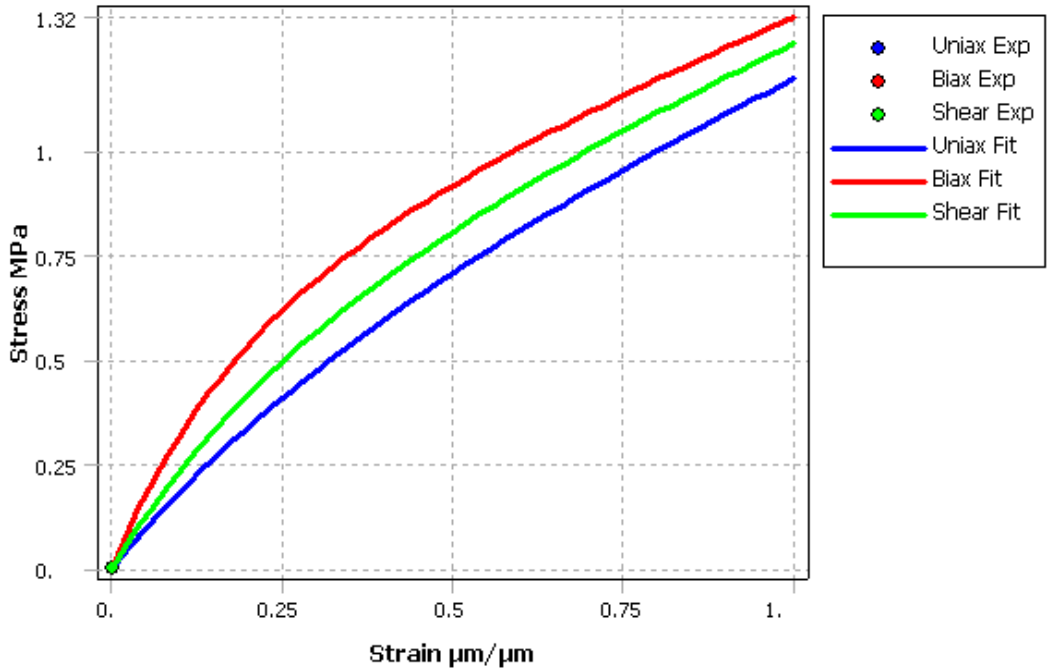

Figure 5.5 Neo-Hookean non-linear stress-strain fitting for uniaxial tension, biaxial tension and shear

Table 5.4 Material properties of structural steel

Structural	
Young's Modulus	2.e+005 MPa
Poisson's Ratio	0.3
Density	7.85e-015 kg/µm³
Thermal Expansion	1.2e-005 1/°C
Tensile Yield Strength	250. MPa
Compressive Yield Strength	250. MPa
Tensile Ultimate Strength	460. MPa

The modeling parameters set for geometry, contact type, mesh control, and analysis type are summarized in a series of tables.

Geometry

Table 5.5 Modeling parameters and details: Geometry

Object Name	*Elastomer*	*SLA*
State	Meshed	
Graphics Properties		
Visible	Yes	
Transparency	1	
Definition		
Material	PDMS-NH 0.4999	Structural Steel
Nonlinear Material Effects	Yes	
Bounding Box		
Length X	1500. µm	1610. µm
Length Y	950. µm	
Properties		
Surface Area(approx.)	8.145e+005 µm²	1.0855e+006 µm²
Statistics		
Nodes	99671	1830
Elements	32928	561

Contact region:

Table 5.6 Modeling parameters and details: Contact region setting

Object Name	*Frictionless - Elastomer To SLA*
State	Fully Defined
Scope	
Scoping Method	Geometry Selection
Contact	3 Edges
Target	3 Edges
Contact Bodies	Elastomer
Target Bodies	SLA
Definition	
Type	Frictionless
Scope Mode	Automatic
Behavior	Symmetric
Suppressed	No

Mesh control:

Table 5.7 Modeling parameters and details: Mesh control

Object Name	*Face Sizing*
State	Fully Defined
Scope	
Scoping Method	Geometry Selection
Geometry	1 Face
Definition	
Suppressed	No
Type	Element Size
Element Size	5. µm
Edge Behavior	Curv/Proximity Refinement

Analysis type:

Table 5.8 Modeling parameters and details: Analysis type

Object Name	*Static Structural*
State	Fully Defined
Definition	
Physics Type	Structural
Analysis Type	Static Structural
Options	
Reference Temp	22. °C

Table 5.9 Modeling parameters and details: Analysis setting

Object Name	*Analysis Settings*
State	Fully Defined
Step Controls	
Number Of Steps	1.
Current Step Number	1.
Step End Time	1. s
Auto Time Stepping	Program Controlled
Solver Controls	
Solver Type	Program Controlled
Weak Springs	Program Controlled
Large Deflection	On
Inertia Relief	Off
Nonlinear Controls	
Force Convergence	Program Controlled
Moment Convergence	Program Controlled
Displacement Convergence	Program Controlled
Rotation Convergence	Program Controlled
Line Search	Program Controlled
Output Controls	
Calculate Stress	Yes
Calculate Strain	Yes
Calculate Results At	All Time Points

5.3.1.3. SHA Chamber Geometry

Three solid-hydraulically amplification chambers with different geometries, as shown in Figure 5.6, have been designed. The first one has a straight slanted side wall and is called a "pyramid". The second one has a straight side wall is called a "rectangle". The third one has a curved side wall and is referred to as a"fillet".

All the dimensions are identical in the three models. The PDMS bottom area is 3.2 x 2.2 mm^2 and the area ratio of top to bottom is 14.8. The theoretical amplification ratio is 12.6 because the actual contact area of the PZT stack actuator and the PDMS is 2x3 mm^2. To study the effect of chamber geometry on the amplification ratio, the three models were simulated with the same boundary conditions and load, specifically, with the

interface between PDMS and the inner wall of he SHA chamber bonded and with a 9μm displacement applied to the to the bottom of PDMS. The corresponding PDMS bottom and top surface displacements were obtained and the ratio of the two displacements, or the AR, was calculated for each case. The results are shown in Figure 5.6. It is confirmed that the "pyramid" chamber with a slanted sidewall provides higher amplification than the "rectangle" chamber with a vertical sidewall because of the former has less stress. And a slanted and curved side wall possessed by the "fillet" chamber helps further increase the amplification ratio. Figure 5.6 shows the deflection profile and the amplification ratios of the three chambers.

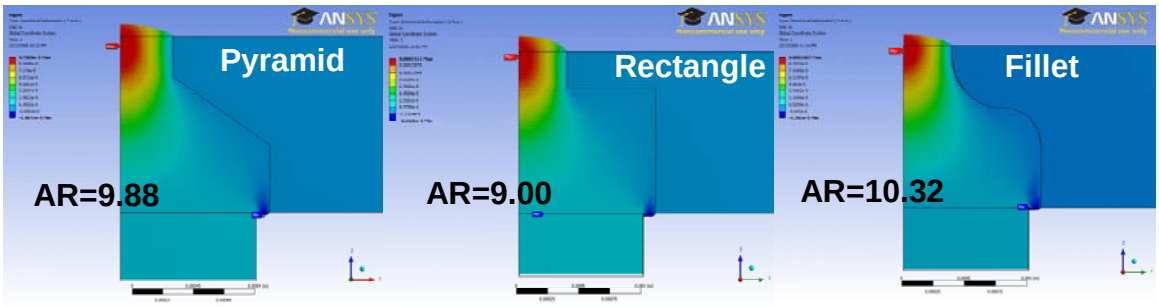

Figure 5.6 Amplification ratio (AR) of three SHA chambers

The "pyramid" shape is selected as the design for the SHA chamber due to its better AR ratio and fabrication flexibility. In addition to stereolithgraphy and micro-injection molding, it can also be fabricated by laminating of layers, which can be made by traditional silicon micromachining or laser micromachining. This fabrication capability expands the range of the sizes of the SHA chamber. Further miniaturization of the SHA chamber for smaller microvalve or for the application of other microdevices would be feasible. On the other hand, the miniaturization of the "fillet" chamber can be extremely challenging due to the incompatibility with conventional micromachining technology.

There is also PDMS deformation at the gap between the PZT actuator and the bottom edge of the chamber in all the three cases. The100μm gap is included in the

design as the assembly tolerance. This "squeezing out" effect at the bottom, as shown in Figure 5.7, contributes partially to the loss of volume and thus the decreases in the amplification ratio.

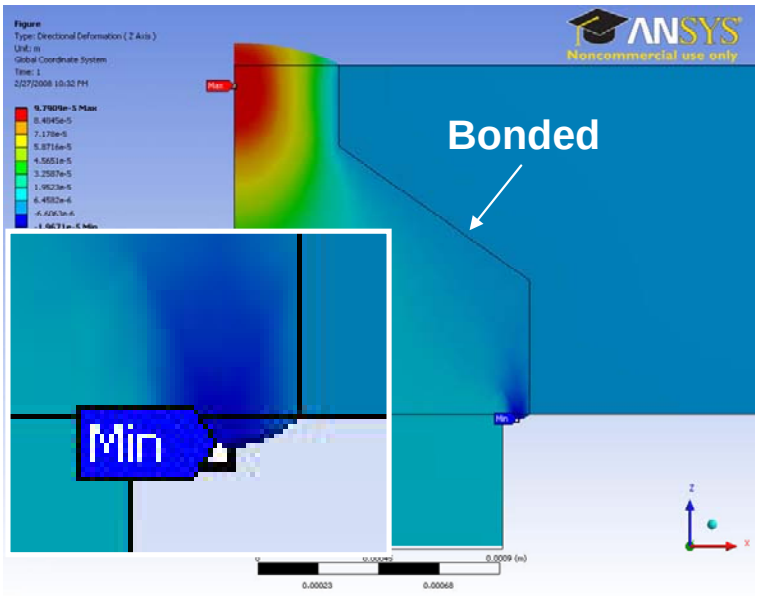

Figure 5.7 "Squeezing out" at the gap between PZT actuator and PDMS

5.3.1.4. SHA Chamber Wall Friction

The "pyramid" model was used in the simulation for SHA chamber with a wall friction. Two different friction boundary conditions were applied: bonded and frictionless. All other boundary and load conditions were kept the same as in the simulations performed in 5.3.1.3. The simulation results are shown in Figure 5.8.

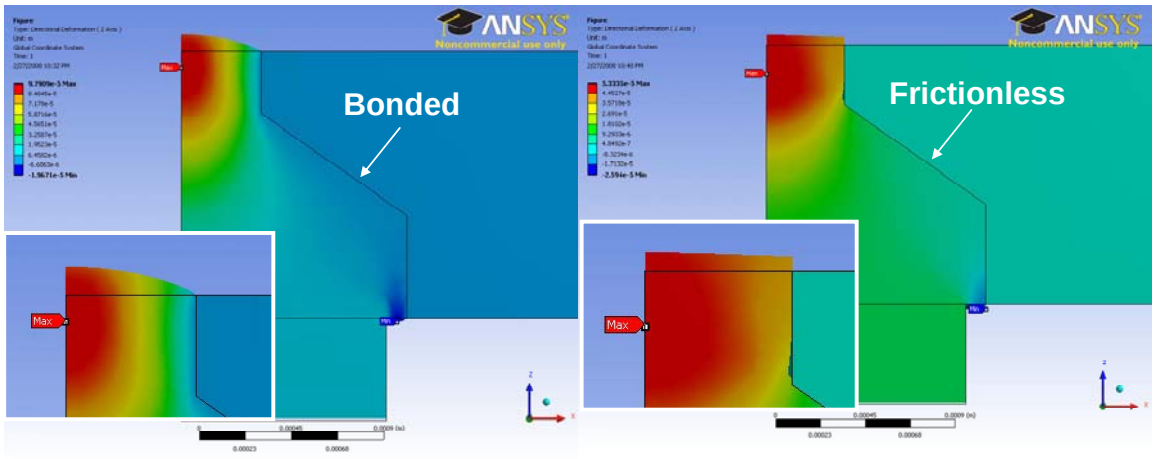

Figure 5.8 PDMS deformation at the outlet of the SHA chamber with fully bonded interface (left) and frictionless interface (right)

The insets in Figure 5.8 are magnified images of the outlets. The fully bonded interface gives an arc (spherical) shape and the frictionless gives a shape more cylindrical.

5.3.1.5. Initial Deformation

In the operation of the microvalve, it is important to bring the PZT stack actuator in contact with the bottom layer PDMS in the SHA chamber. Therefore, some initial deformation may be unavoidable. A parametric simulation was conducted to show the effect of initial deformation on the amplification ratio. In another word, the aim was to see how the amplification ratio changes with displacement load. The results are shown in Figure 5.9. With the increase of the load displacement (PZT stack actuator displacement), both the displacement of PDMS at the outlet and at the slit increase while the amplification ratio decreases.

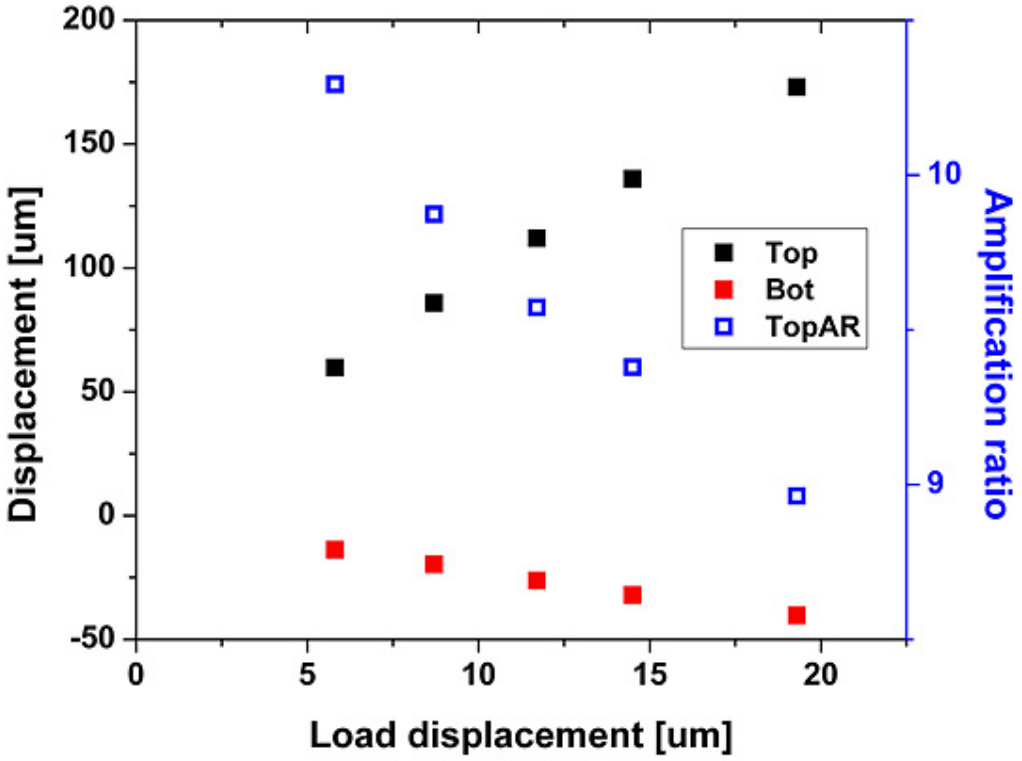

Figure 5.9 PDMS displacement at the outlet and AR as a function of PZT displacement for a fully filled SHA chamber

5.3.1.6. SHA Chamber Filling

If the SHA chamber is not filled fully by PDMS, the top profile of the PDMS in the chamber is round instead of flat as shown in Figure 5.10.

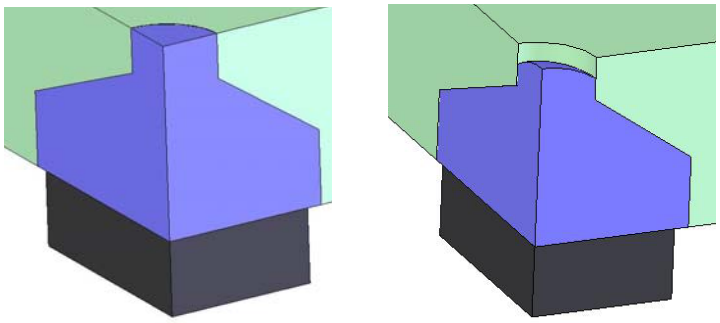

Figure 5.10 Fully filled model and partially filled model

A model based on this case was constructed and similar simulation was conducted on this model as the one for the fully filled model in 5.3.1.5. The results are shown in Figure 5.11 and compared with that of a fully filled chamber in Figure 5.12.

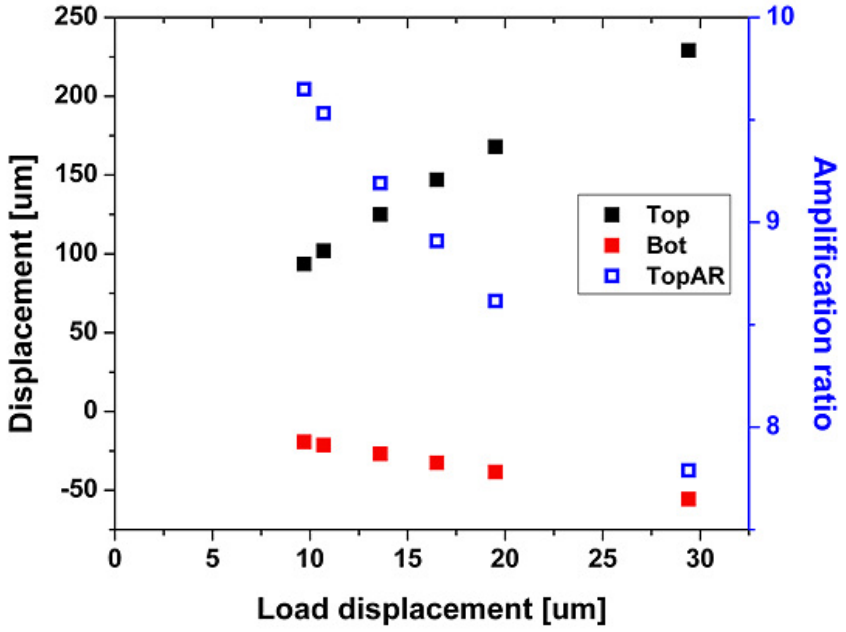

Figure 5.11 PDMS displacement at the outlet and AR as a function of PZT displacement for a partial filled SHA chamber

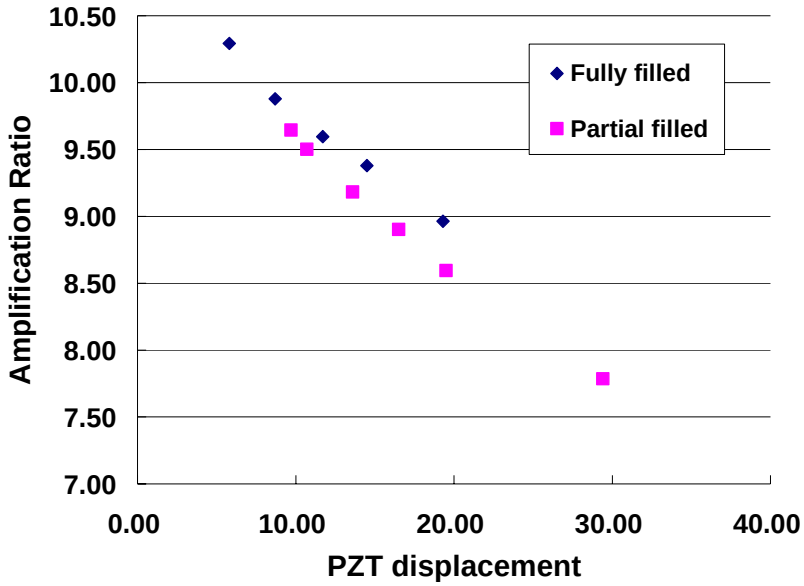

Figure 5.12 AR as a function of PZT displacement

In the partially filled case, the same trend has been observed for the PDMS displacement at the outlet and at the tolerance gap and AR at various loads as in the fully filled case. The partially filled case shows less amplification and a faster decay than that of the fully filled case. In the fully filled case, the initial shape of the top surface is flat. After the top surface deforms into a round shape at actuation, the top surface area keeps increasing with the increase of deflection. However, in the partially filled case, the initial shape of the top surface is round. The top surface area does not change with the increase of deflection. Because volume change is conserved in both cases, an initial round surface results in less displacement than a flat surface.

From the results of the above simulation, it is concluded that the amplification ratio is smaller than the theoretical value is due to: (1) Poisson's ratio of PDMS is smaller than 0.5, (2) Initial deformation effect, and (3) "squeezing out" effect.

5.3.2. Experimental Verification

Two chambers with the same bottom area (2x3 mm^2) and different top area (0.78mm and 0.6mm in diameter) were fabricated and assembled with PZT stack actuators. The calculated amplification ratios based on area ratio are 12.6 and 17 for the two chambers, respectively. From hereon, the SHA chamber with 12.6 AR is referred to as chamber A and the chamber with 17 AR is referred to as chamber B. During the examination on the fabricated SHA chambers, chamber A has been found to be fully filled while chamber B has been found not to be fully filled. Specifications of the two SHA chambers tested are listed in Table 5.10.

Table 5.10 Specifications of the two SHA chambers tested

SHA chamber	A	B
Input area	2 mm x 3 mm	
Output area	0.75 mm (D)	0.6mm (D)
Expected amplification ratio	12.6	16

The following characterization procedure was carried out on the two assembled actuators:

A 0-150V voltage was applied to the PZT stack actuator, and the deflected shapes of the elastomer at the outlet of the SHA chambers were captured using an optical microscope (Figure 5.13). The maximum displacement of the PDMS top surface was measured using a laser sensor. The effects of voltage increase and initial filling of the SHA chamber were studied.

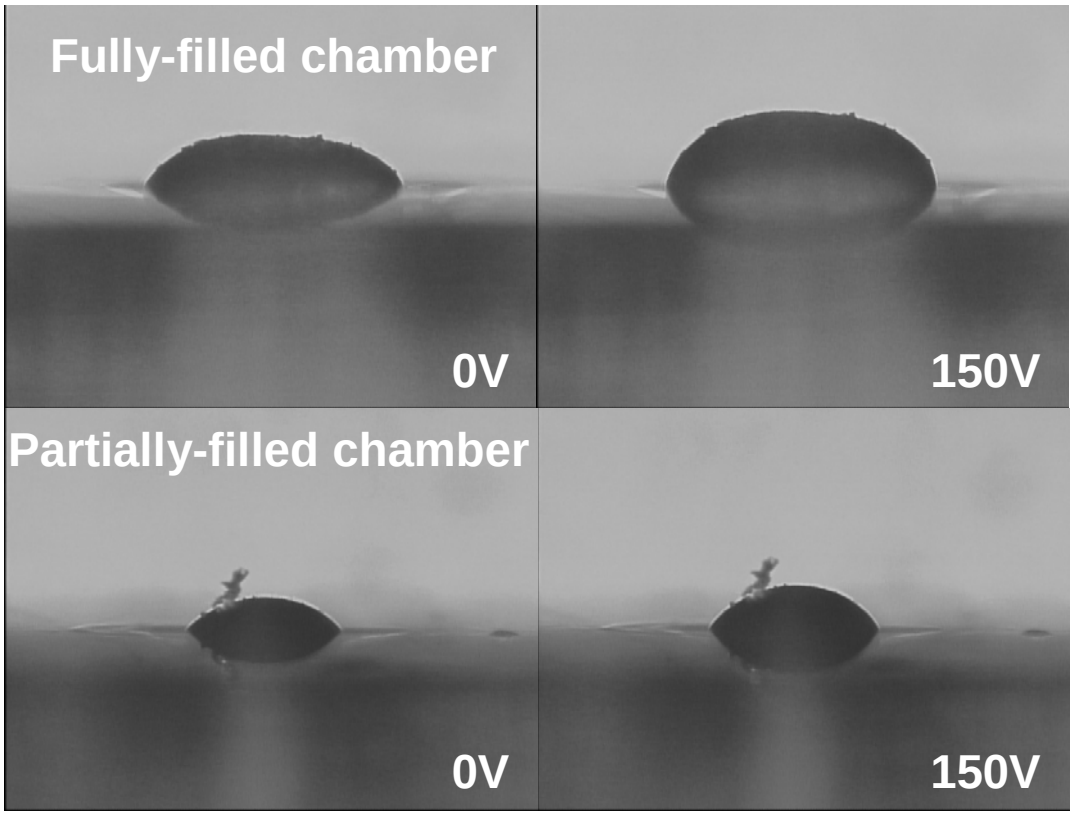

Figure 5.13 Optical photographs of the deformed PDMS

As shown in Figure 5.13, the shape of the PDMS deformation fit in the fully bonded boundary condition. The PDMS in partially-filled chamber has a smaller vertical displacement and more lateral expansion compared to the PDMS in chamber A. On the other hand, the PDMS in the fully-filled chamber A has a larger vertical displacement despite its smaller area ratio as illustrated in Figure 5.14.

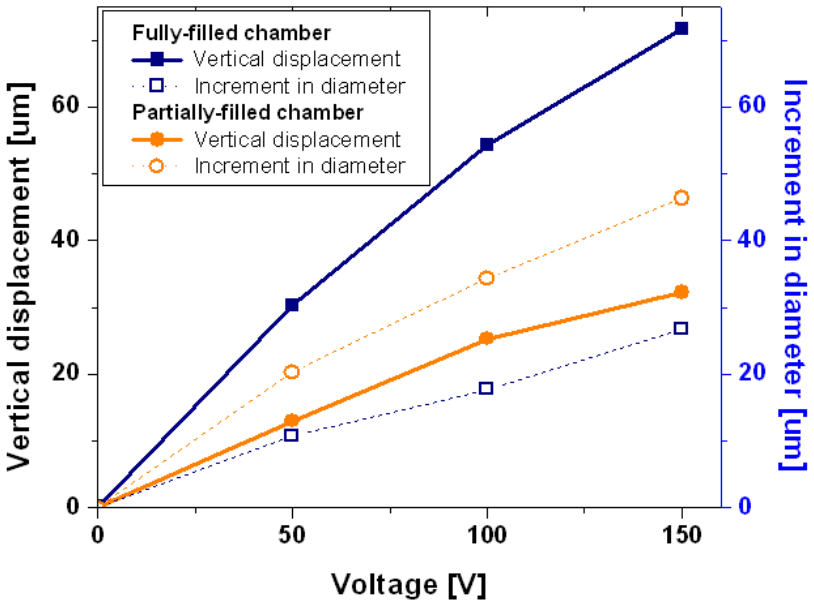

Figure 5.14 Measured dimension of the deformed elastomer as a function of applied voltage

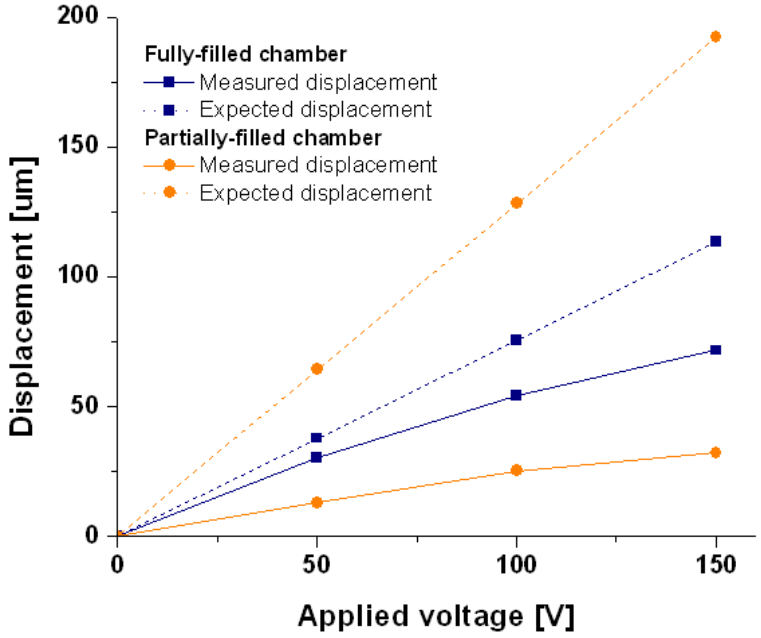

Figure 5.15 Expected and measured vertical displacement of the actuator as a function of applied voltage

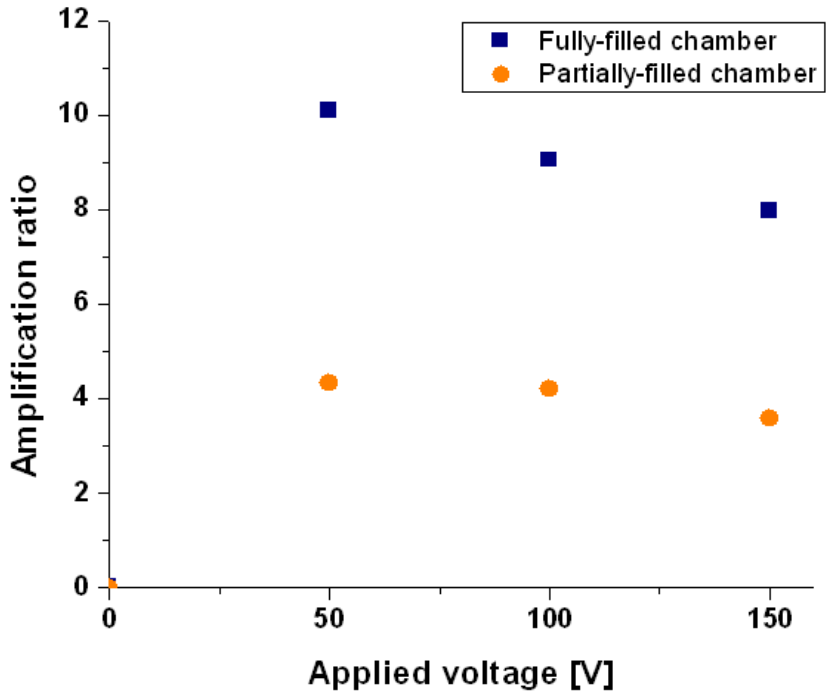

Figure 5.16 Measured amplification ratio of the actuator as a function of an applied voltage. The area-ratio-based amplification ratio is 12.6 for the fully filled chamber and 17 for the partially filled chamber.

Figure 5.15 and Figure 5.16 shows the theoretical and experimental displacements and amplification ratios as functions of applied voltage. The measured amplification ratios at 50V are 10 for the fully-filled chamber and 4 for the partially-filled chamber, smaller than the respectively theoretical value of 12.6 and 17. The amplification ratio becomes smaller at higher applied voltage in both cases. The experimental results can be well-explained using the simulation results. The PDMS in both chamber A (fully filled) and chamber B (partially filled) were given an initial deformation to the same starting height. It is obvious that the PDMS in chamber B had more initial deformation. Therefore, the difference between the experimental amplification ratio and the theoretical value is much bigger for chamber B than for chamber A.

Table 5.11 Actuation characteristics of the actuator with fully-filled SHA chamber

Input area	2 mm x 3 mm	
Output area	0.75 mm (D)	
Expected amplification ratio	12.6	
Measured characteristics	@ 50 V	@ 150 V
PZT displacement	3 μm	9 μm
SHAC actuator displacement	30 μm	72 μm
Measured amplification ratio	10	8

Table 5.11 summarizes the results of the actuator with a fully-filled chamber. The actuator achieved amplification ratios of 10 and 8 at applied voltages of 50V and 150V, respectively, which correspond to large vertical displacements of 30μm and 72μm, respectively.

5.4. Design and Working Principle

5.4.1. Valve Configuration

Figure 5.17 shows the exploded and cross-sectional schematics of the designed microvalve with three primary components vertically stacked: a PZT stack actuator as the driving element and the housing; a hydraulic transmission chamber filled with PDMS elastomer; and a valve chamber connected with an outlet, an inlet, and a valve seat.

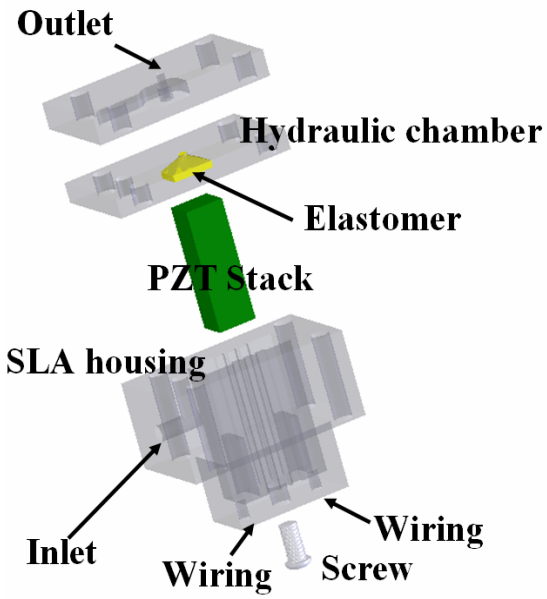

(a) Exploded view

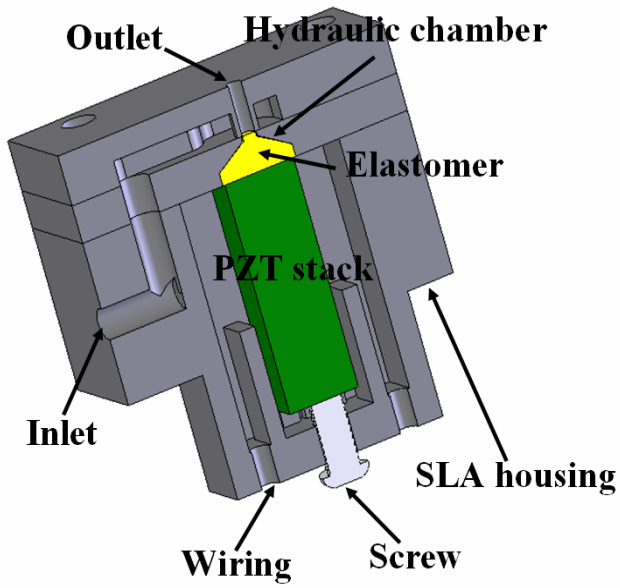

(b) Cross-sectional view

Figure 5.17 3-D schematics of the microvalve configuration, showing the geometry of the hydraulic chamber and the inlet and outlet paths

5.4.2. Working Principle

The operation principle of the microvalve is illustrated in Figure 5.18. The valve inlet has a diameter of 1.5mm. The valve outlet has a diameter of 0.6mm with a 100μm

wide valve seat rim. The valve chamber has a rectangular shape and a 1mm depth. The designed orifice gap is 37μm between the valve head and the valve seat. According to the simulation results, the hydraulic chamber has been designed to have slanted sidewalls with designed angle and vertical offsets at the top and the bottom.

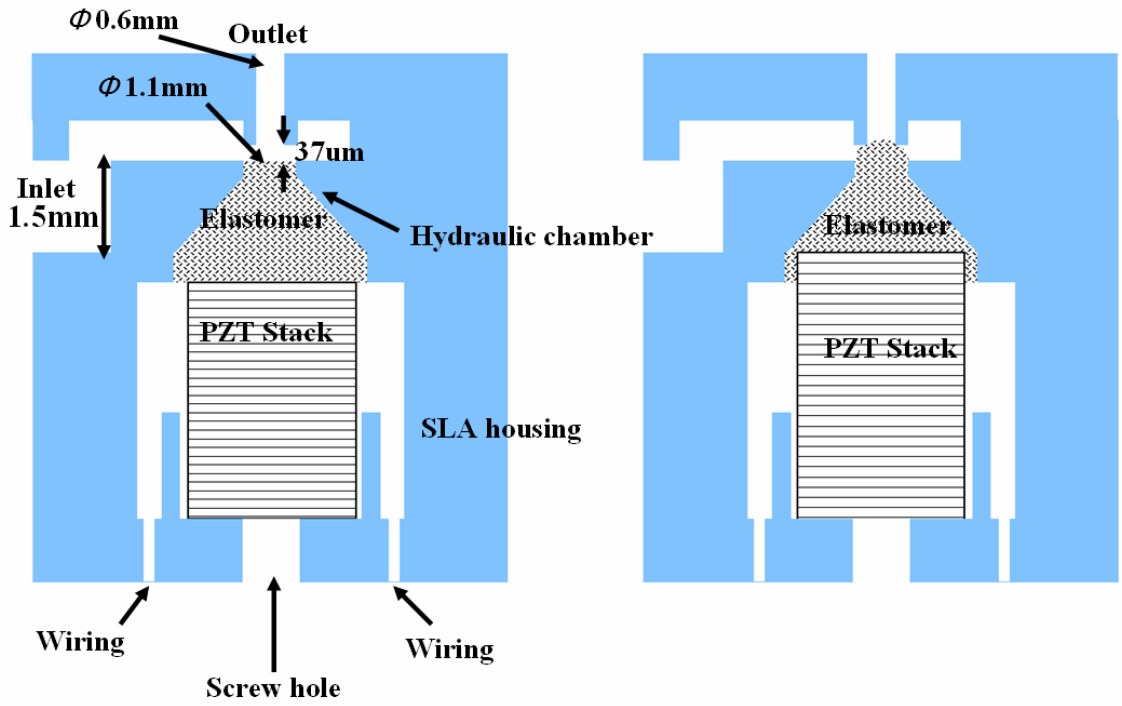

(a) valve open (b) valve closed

Figure 5.18 Operating principle of the normally open piezoelectric polymer microvalve

The PDMS serves both as a hydraulic amplification medium and as a valve head. When a voltage is applied to the PZT stack, the PZT stack expands axially and pushes the bottom layer of PDMS upwards, generating a small deflection. The PDMS valve head deflects upward at an amplified ratio and stops at the valve seat. Another advantage of using PDMS elastomer directly as the valve head lies in its good sealing property, especially for liquid flow. This eliminates the need for complex valve seat structure normally required for leak-proof valve operation.

5.5. Fabrication

Stereolithography and Layer Planarization

All three layers were fabricated primarily using stereolithography (SLA) (Viper Si2, 3D Systems). The contact surfaces of each layer were finely polished after cleaning and UV post-cure. The purpose of polishing was to eliminate the warpage of the thin SLA parts. The surface profile of the polished layer was examined by a non-contact profilometer. Figure 5.19 shows the pictures of the surface profile of two different sections on the valve seating layer. The height tolerance was within 7μm as illustrated by the 2-D profile analysis in Figure 5.20.

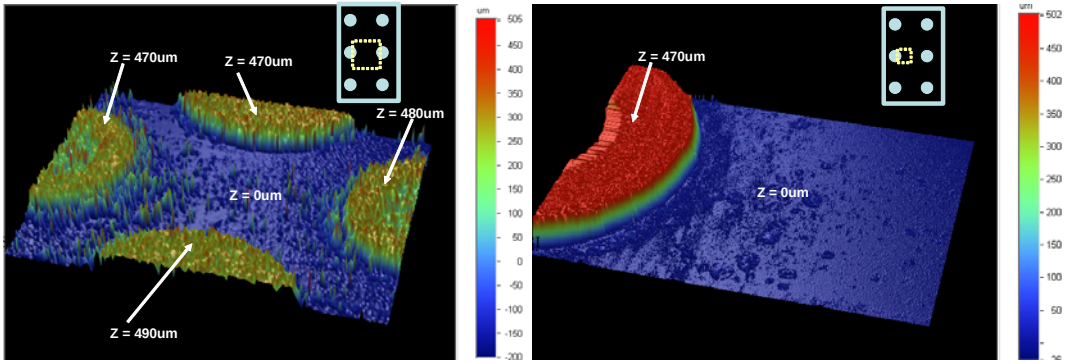

Figure 5.19 3-D surface image of the SLA layer by non-contact profilometer

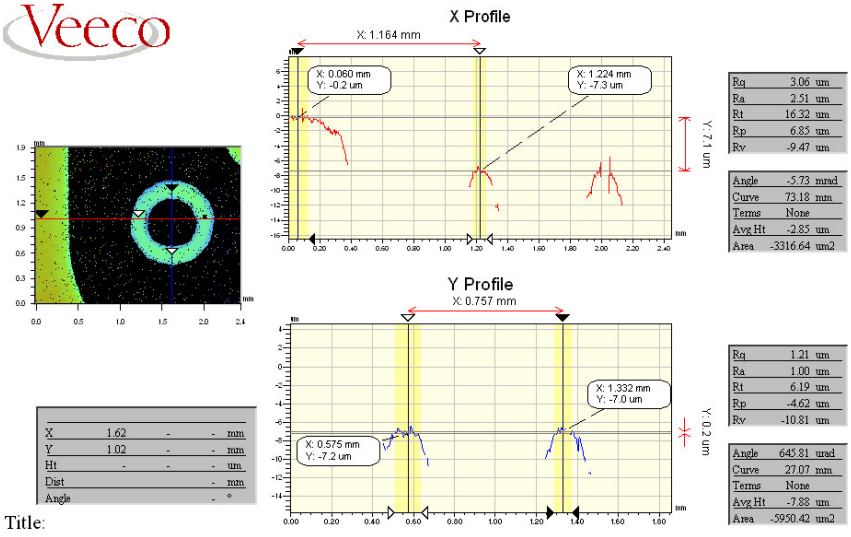

Figure 5.20 2-D profile of one section of the valve seating layer

Spacer

A spacer was used to provide the valve orifice. For a designed 37μm orifice, the spacer was fabricated by laser cutting a 1.5mil (~37μm) polyester sheet. The spacer can also be made of laser micromachined brass sheet in 1.5mil thickness.

Solid-Hydraulic Amplification Chamber

To fabricate the transmission layer with hydraulic amplification chamber, the transmission layer was bonded to a glass substrate using a wax sheet. PDMS prepolymer and its curing agent were mixed and filled into the chamber and vacuum degassed for 20 minutes to ensure a complete filling. The PDMS mixture was cured at room temperature for 24 hours. The hydraulic amplification layer was then released from the glass substrate by dissolving the wax in tricholoroethylene (TCE).

Assembly

The PZT stack (Pst 2×3×7, APC International) with a dimension of 2mm×3 mm×9mm was assembled in the housing layer (Figure 5.21a). Finally, the housing layer, the hydraulic amplification layer, the spacer layer and the valve seat layer were assembled with four mechanical screws. Figure 5.21b shows the assembly of the housing layer and the hydraulic amplification layer. The whole assembled microvalve is shown in Figure 5.21c. The overall dimension of the fabricated microvalve is 6mm×13 mm×9mm as shown in Figure 5.21c. The design of the microvalve and the fabrication sequence is compatible with conventional mass-manufacturing technology such as injection molding and lamination at low cost.

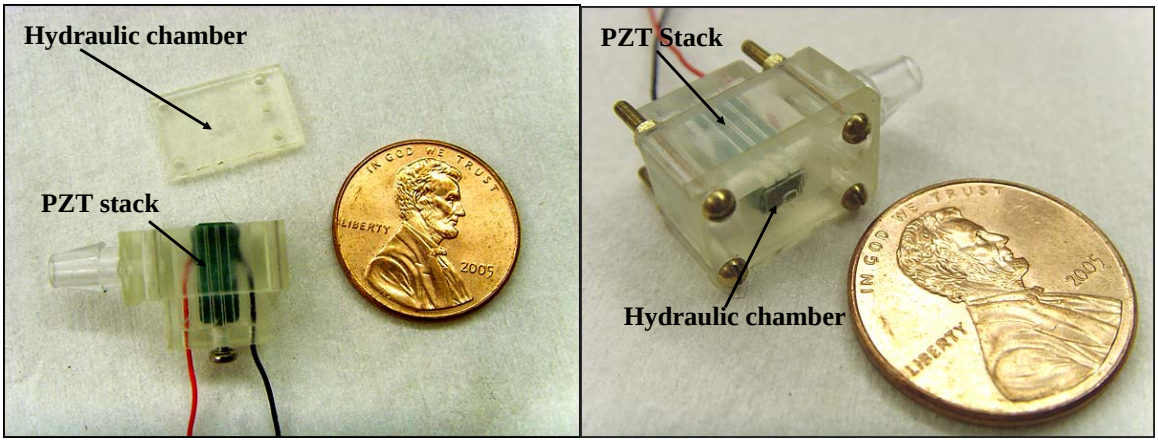

(a) (b)

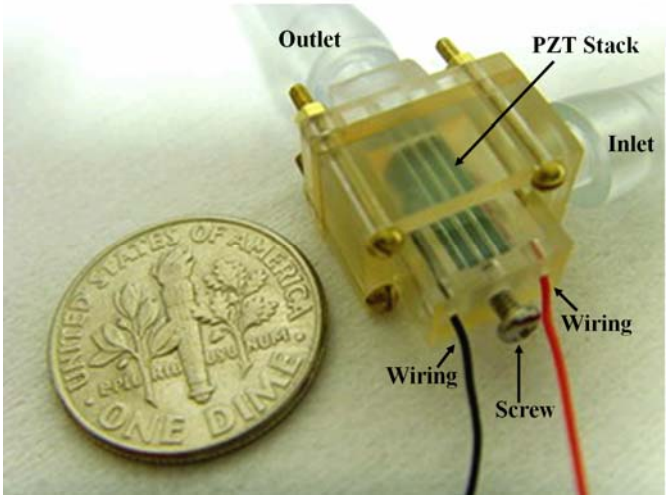

(c)

Figure 5.21 (a) PZT stack actuator assembled in the housing (b) Assembly of PZT stack actuator with hydraulic amplification chamber (c) Completely assembled three-layer piezoelectrically driven hydraulically amplified polymer microvalve

5.6. Characterization

5.6.1. PZT Stack Actuator Characterization

The PZT actuator was tested statically and dynamically using a laser displacement sensor. The measured results are plotted in Figure 5.22. The displacement shows good

linear correlation with the applied voltage. Further, the frequency response of the stack actuator is sufficient for the actuator to be operable in a Braille cell in vibratory mode.

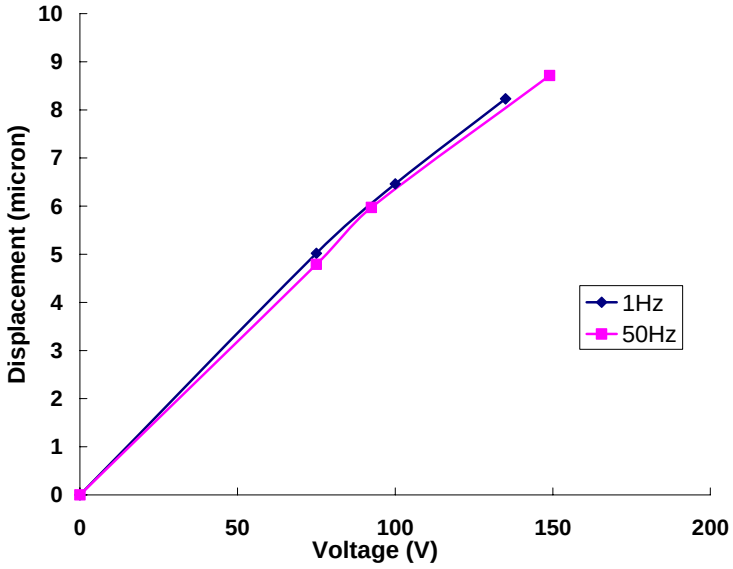

Figure 5.22 Actuation characteristics of the designed PZT stack actuator

5.6.2. Amplified Actuator Characterization

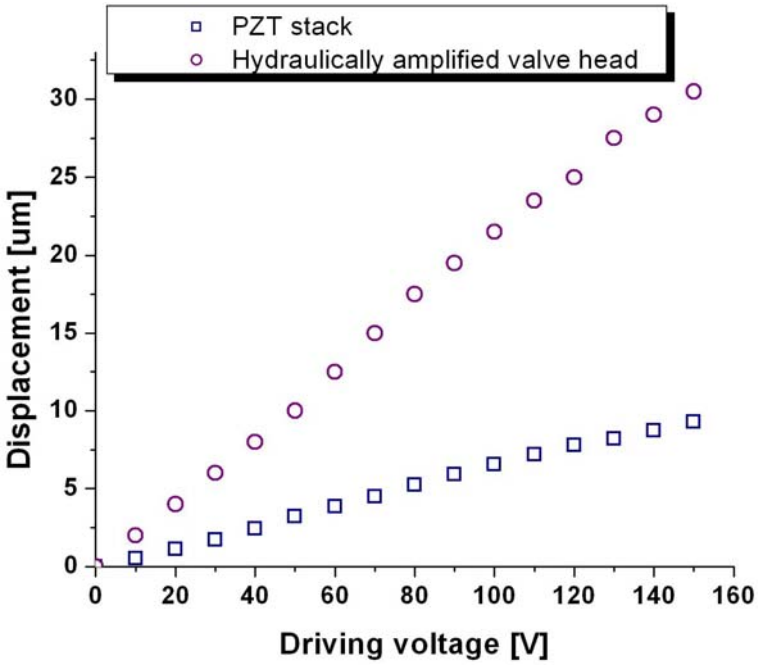

Figure 5.23 Displacement measurements of PZT driving element and hydraulically amplified valve head

The static displacement of one assembled PZT stack actuator and the amplified displacement of the PDMS valve head were measured and plotted in Figure 5.23.

Based on the results shown in Figure 5.23, the amplification ratio was calculated and plotted as a function of driving voltage in Figure 5.24. Three deflection measurements to the nearest 0.1μm were taken and averaged for both the PZT and amplified cases. In this design, the area of the large opening of the hydraulic chamber at the bottom is six times that of the small opening on the top. Although the amplification ratio shows a decreasing trend as voltage increases, the amplification ratio is still larger than 4 over the driving voltage range of 0-150V. A maximum amplification ratio of 5.04 is achieved at 30V.

The discrepancy between the measured value and the theoretical value of 6, which is based on the device geometry, could result from several factors, including those recognized in the simulation and the compliance in the hydraulic chamber, which was neglected in the simulation.

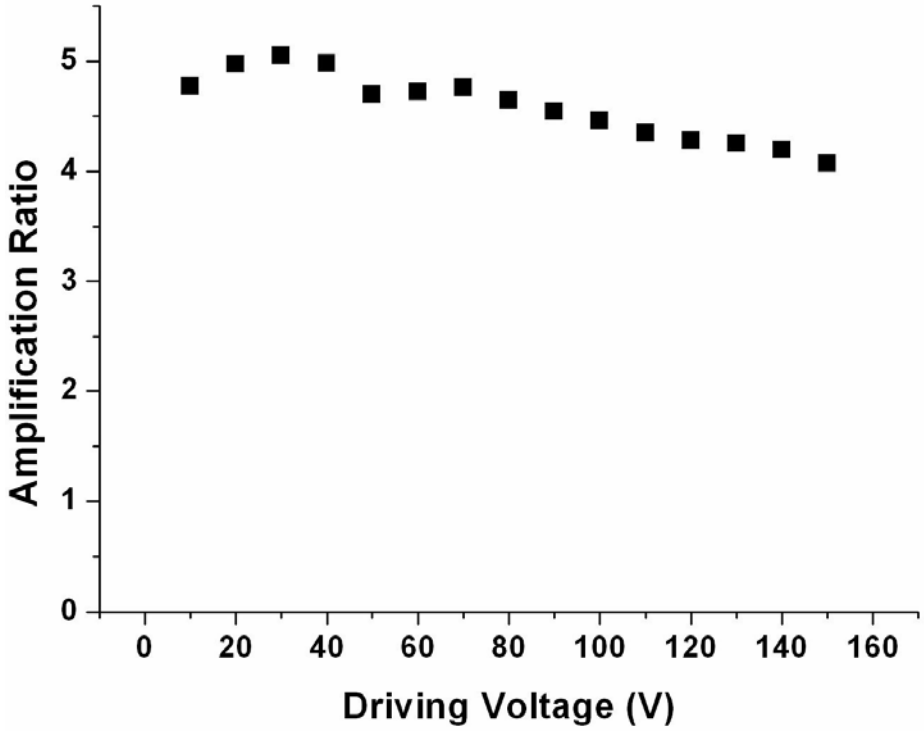

Figure 5.24 Calculated amplification ratios as a function of driving voltage

5.6.3. Flow Characteristics Measurement

5.6.3.1. Flow Rate and Closing Voltage

To measure the flow rate, the microvalve was connected to a DC voltage source with 0-150V of actuation voltage and supplied with regulated house N_2 from 0-92.3kPa while the outlet was connected to a flow meter. The outlet of the flowmeter was maintained at atmospheric pressure. Figure 5.25 shows the measurement diagram.

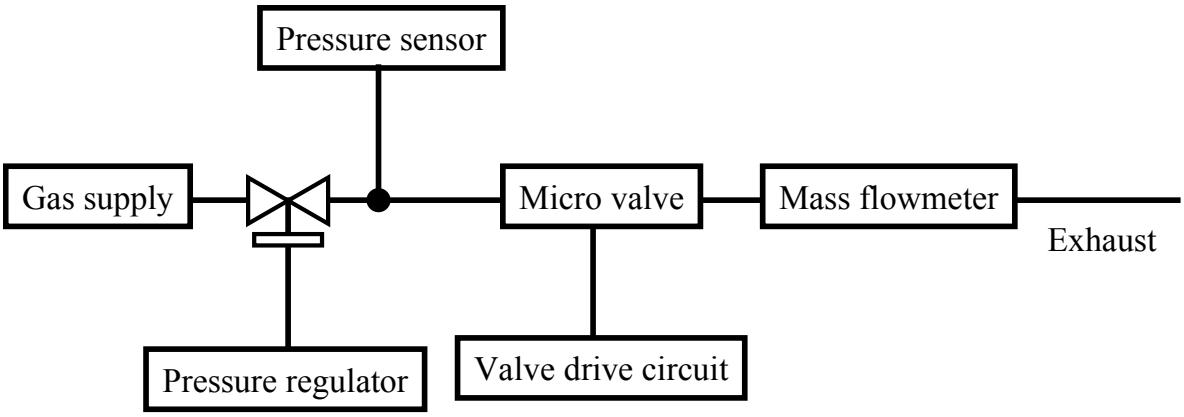

Figure 5.25 Diagram for flow rate measurement

The contact between the PZT stack and the PDMS valve head was realized by adjusting the screw at the bottom of the PZT stack. The gap between the PDMS valve head and the valve seat was initially adjusted to ensure that the valve would be closed at a maximum allowed driving voltage of 150V and inlet pressure of 90kPa.

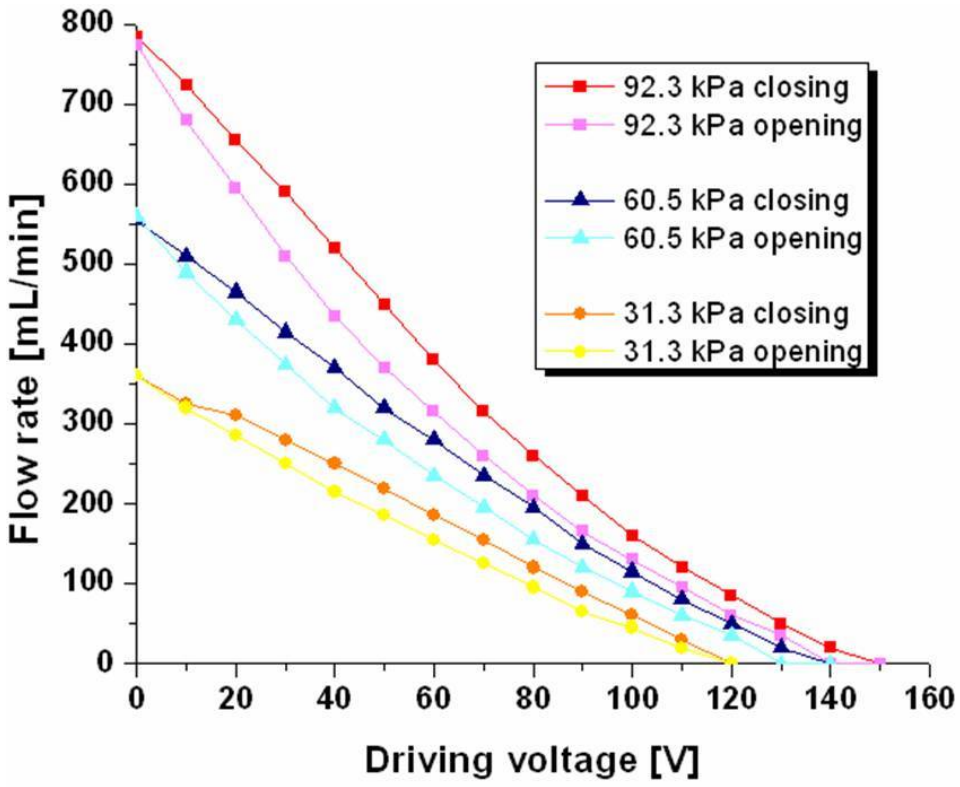

Figure 5.26 Measured N_2 flow rate as a function of actuation voltage (dc) under various differential pressures

Figure 5.26 shows the flow rate-actuation voltage characteristics of the microvalve under three differential pressures. Because the microvalve is normally open, the maximum flow was obtained without any voltage applied. The maximum flow rates for N_2 at 31.3, 60.5 and 92.3kPa are 360, 555 and 785mL/min, respectively. As the driving voltage increases, the flow rate falls due to the reduced height of the flow channel until the valve is completely closed. The closing voltages are 130, 140, and 150V, respectively. Opening voltages are approximately 10V less than the closing voltages in the cases of 92.3kPa and 60.5kPa. At 31.3kPa, the opening voltage is the same as the closing voltage.

5.6.3.2. Flow Rate- Actuation Voltage Characteristics

Figure 5.27 plots the flow rates of the microvalve as a function of the differential pressure at 4 driving voltages: 0, 30, 60, and 90V. The curves show some nonlinearity at lower pressure for the cases of 0, 30 and 60V.

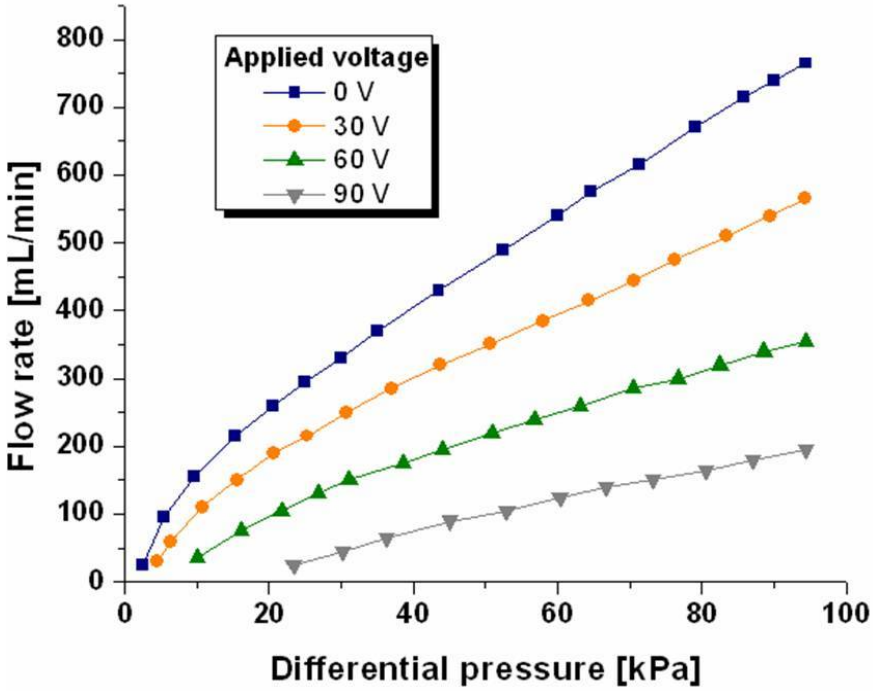

Figure 5.27 Measured N_2 flow rate as a function of differential pressures at different actuation voltages (dc)

5.6.3.3. Response Time

In order to measure the response time of the valve, the outlet was connected to a pressure sensor through a tube of 70mm long and with inner diameter of 3mm and a throttle as shown in Figure 5.28.

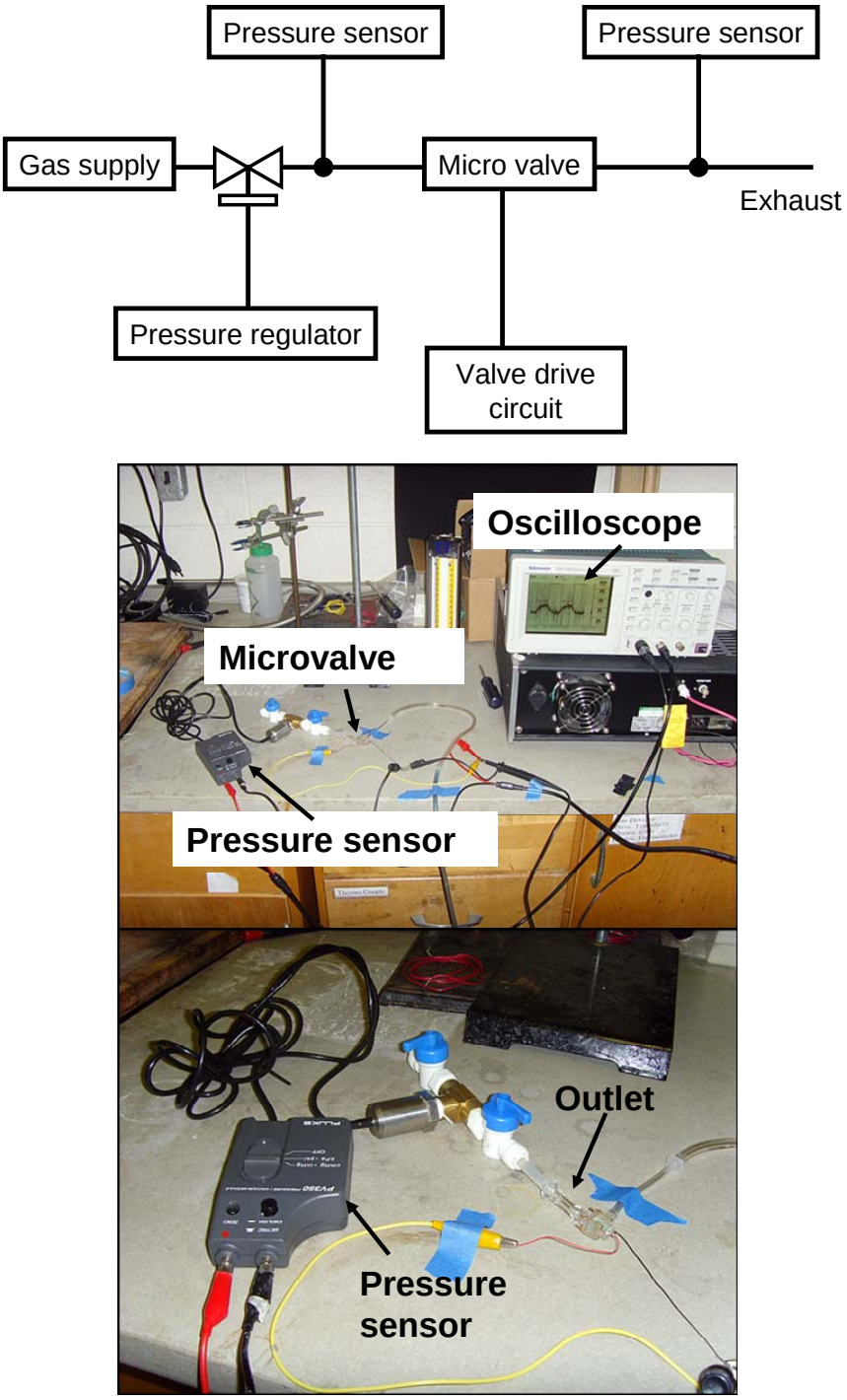

Figure 5.28 Diagram of valve response time measurement and pictures of set up

If a fluid flow is passing the valve, the pressure increases in the capillary at the valve outlet. The pressure falls to atmospheric when the valve is closed. The control signal and the signal of the pressure sensor were recorded with an oscilloscope. The

valve was driven at a frequency of 1 Hz and a voltage of 150 V. The applied pressure at the valve inlet was about 94.4kPa. Figure 5.29 shows the triggering signal for the microvalve and the signal of the pressure sensor. The first diagram contains several switching cycles to show the shift between the control signal for the microvalve and the pressure rising at the sensor. The second diagram shows the response time obtained from the experiment is 30ms.

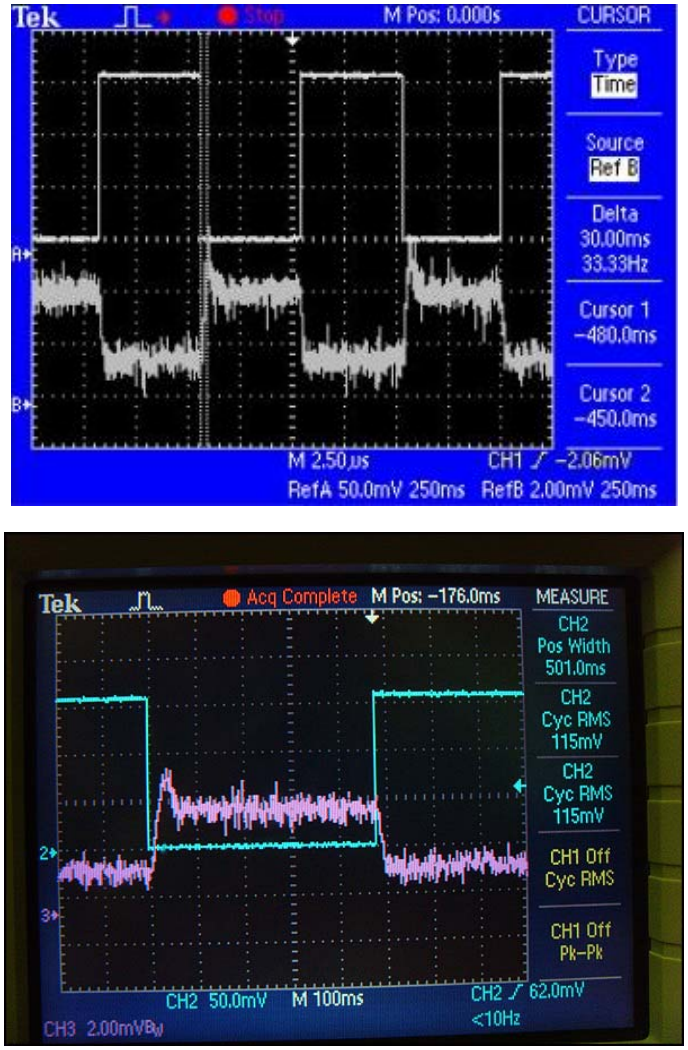

Figure 5.29 Switching time at 94.4kPa differential pressure and applied voltage of 150V

5.6.3.4. Dynamic Flow Characteristics

Figure 5.30 presents the measured flow rates of N_2 obtained for valve operating frequency from 10Hz to 300Hz using a sinusoidal actuation voltage with amplitude of 150V. Figure 5.20 shows the measured flow rates for three valves. In general, for a given inlet pressure, the flow rate decreases with higher operating frequency. However, for one microvalve, an anomalous increase is observed in the flow rate after 200Hz, reaching a maximum value at approximately 300Hz.

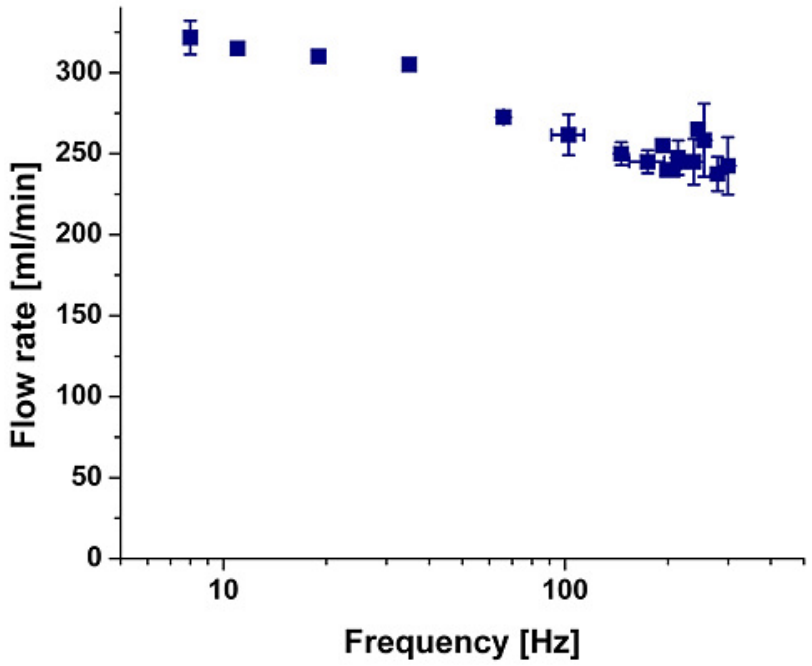

Figure 5.30 Measured N_2 flow rate as a function of actuation frequency

It had been suspected that the flow rate dynamic response was not truly reflecting the valve performance, but rather reflecting the response of the flow meter. To test this hypothesis, a displacement measurement on the PDMS valve head was carried out. The maximum, minimum, and peak-to-peak displacements were measured and plot in Figure 5.31. It can be seen that the displacement of the PDMS valve head remains constant

within the frequency range measured, which confirms that the microvalve can be fully opened and closed within the frequency range tested.

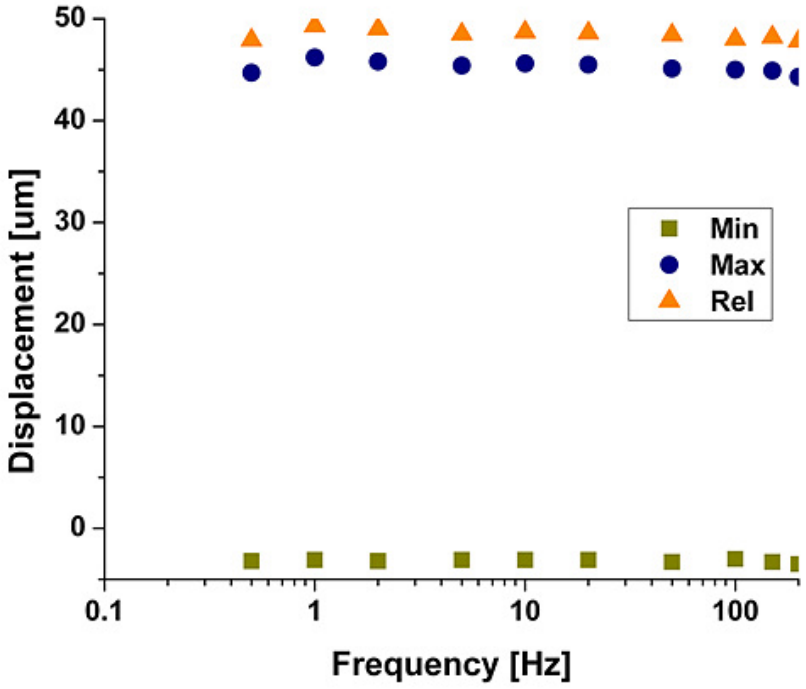

Figure 5.31 PDMS valve head displacement a function of actuation frequency

5.7. Demonstration of Braille Cell Driven by Microvalve

The function of the microvalve as an on-off switch for a pneumatic microbubble tactile actuator has also been demonstrated in Figure 5.32. The valve was first closed by applying a voltage of 150V. A differential pressure of 90kPa was then applied to the inlet of the valve. As shown in Figure 5.32a, the valve successfully kept the microbubble at the OFF-state. Next, the voltage was turned off and the microvalve was opened. As a result, the microbubble actuator was pressurized (ON-state) and inflated until the pressure reached the level applied to the inlet. Finally, 150V voltage was applied and the valve was closed again. The microbubble actuator remained at ON-state even after the removal of the inlet pressure Figure 5.32b), which demonstrated the good sealing of the valve.

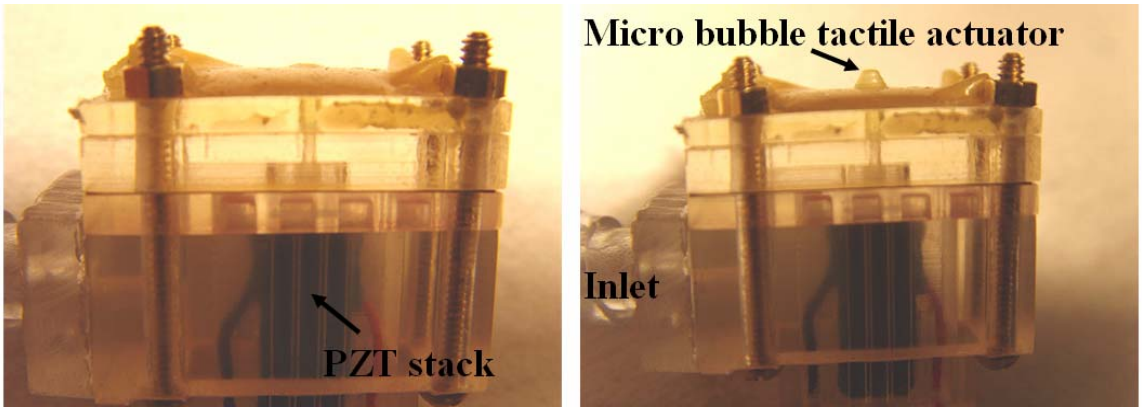

(a) Bubble actuator OFF (b) Bubble actuator ON

Figure 5.32 Demonstration of successful control of a tactile actuator for a pneumatic tactile display.

5.8. Applications of the Microvalve

Although designed for tactile display, the valve has application in many other fields that require fluid control. Particularly, the valve addresses the market needs for a compact, power efficient and precise control valve. It has potential uses in the following area and beyond: industrial automation, pneumatic and hydraulic actuation, refrigeration, fuel cell, medical and chemical analysis, drug delivery and automobile applications. Examples of applications and advantages are as follows:

1. Pneumatic and hydraulic actuation control. For example, in controlling pneumatic tactile displays, the valve provides control of high differential pressure with fast response and can operate at high frequency.
2. Medical and chemical analysis system, including general flow regulation and control, gas chromatography, and drug delivery. The valve can also reduce the size and weight of analysis systems by replacing bulkier and less efficient solenoid valves. The valve is not affected by electromagnetic force, and is therefore ideal for application in MRI environments.

3. Pneumatics and hydraulic cylinder control. The valve is capable of achieving higher flow rates than the present membrane or orifice type microvalves at a large supply differential pressure.
4. Other flow regulation applications including fuel cell, refrigeration, etc. The valve provides precise control of the fluidic flow. The devices would be more portable due to the compact size of the valve.

5.9. Array of Microvalves

Based on the design of a single microvalve, the configuration of a 2x3 microvalve array has been proposed. The schematic is shown in Figure 5.33 and a SLA prototype is shown in Figure 5.34.

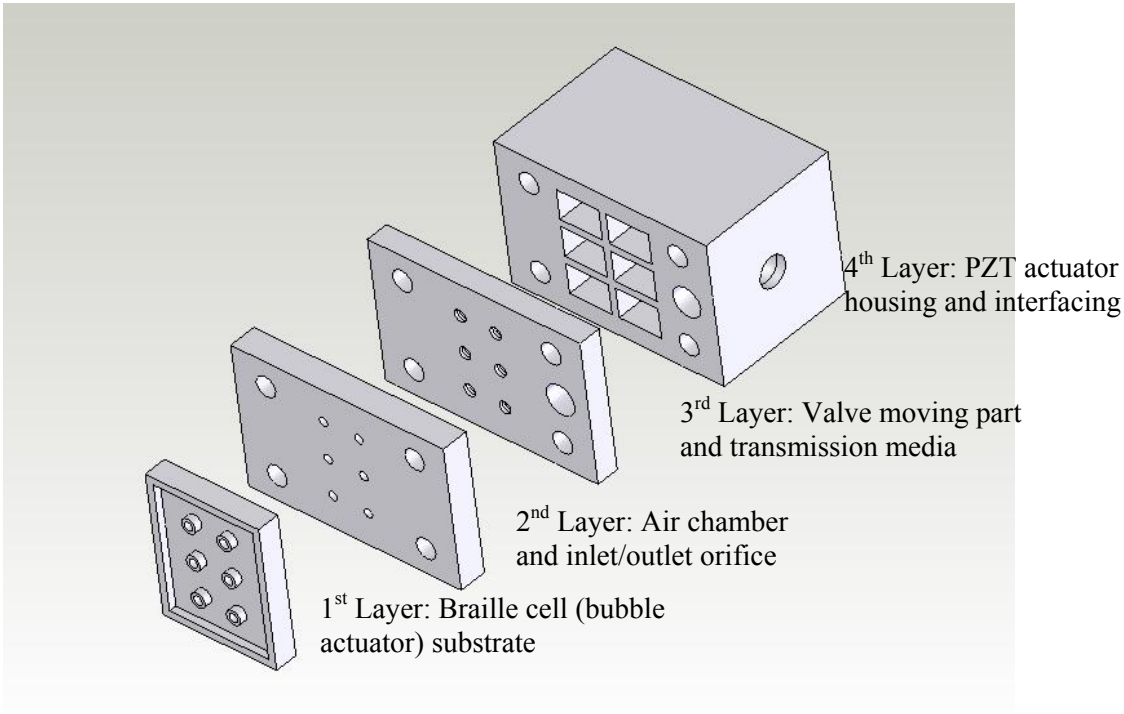

(a) Exploded view from top

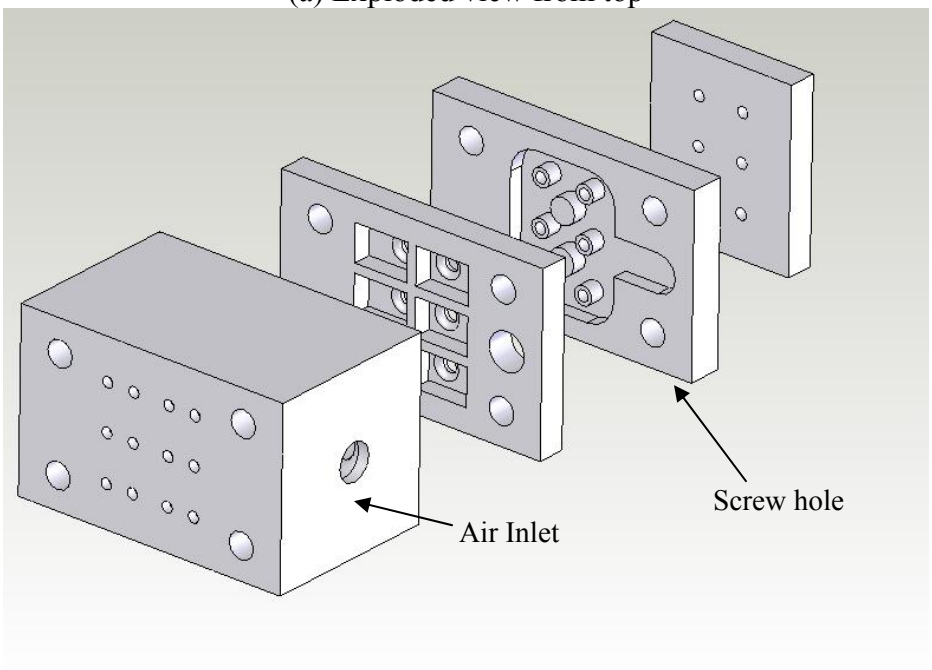

(b) Exploded view from bottom

Figure 5.33 3-D schematics of the microvalve array configuration, showing the geometry of the hydraulic chamber and the inlet and outlet paths

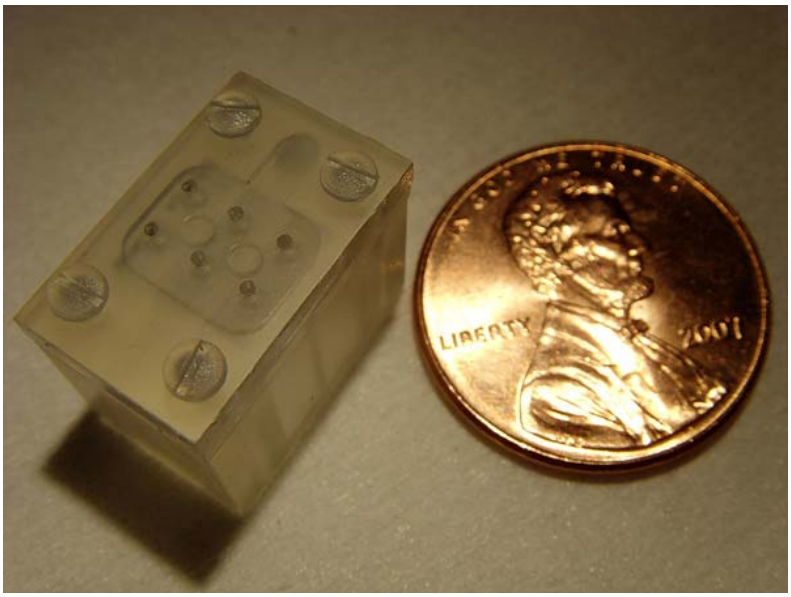

Figure 5.34 SLA prototype of the microvalve array

5.10. Conclusion

To control the microbubble actuator, a normally open, high flow rate microvalve utilizing a piezoelectric stack actuator and a solid hydraulic amplification mechanism has been designed, fabricated, and experimentally characterized. High frequency, high force actuation capabilities were achieved through the incorporation of a PZT stack actuator beneath a solid-hydraulic amplification chamber. An incompressible elastomer material was employed to amplify the limited stroke of the PZT actuator to a larger valve head movement. The elastomer that also acts as the valve head was actuated to open and close against a fluid orifice. The microvalve was fabricated by SLA technology, and thus the orifice size was not confined by the limits of conventional silicon micromachining technology.

The valve subcomponent's behavior and static flow characteristics were evaluated over a range of applied actuation voltage, actuation frequency, and differential pressure. The microvalve requires reasonable closing voltages at a large supply differential pressure and large flow rate, i.e., 150V for 92.3kPa and 785mL/min. The adjustable

initial orifice gap permits flexible fluid regulation over a large range of differential pressure with high flow rate. Also, the proposed axial polymer microvalve shows the feasibility of being densely packed and integrated with the miniaturized pneumatic tactile display systems.

The PZT stack actuator currently used in the microvalve is a commercially available one, which has the drawback of high cost ($90 per piece) and inability to be scaled down in size easily because they are fabricated by traditional lamination and cut process. In order to make a truly low-cost tactile display, the cost of the microvalve needs to be reduced. Also, the cost to make a full page tactile display that is capable of displaying graphic information should not be significantly higher, which requires the cost to fabricate a much denser and smaller microvalve array to remain low. A PZT stack actuator fabricated by MEMS technology would be the perfect solution.

CHAPTER 6

PIEZOELECTRIC STACK ACTUATOR

6.1. Background

6.1.1. Definition of Piezoelectricity and Piezoelectric Material

Piezoelectricity stems from the Greek word *piezo* for pressure. Piezoelectricity is a linear effect that is related to the microscopic structure of the solid. Some ceramic materials become electrically polarized when they are strained; this linear and reversible phenomenon is referred to as the direct piezoelectric effect. The direct piezoelectric effect is always accompanied by the converse piezoelectric effect where a solid becomes strained when placed in an electric field. Piezoelectric materials therefore fall in the class of smart materials. The microscopic origin of the piezoelectric effect is the displacement of ionic charges within a crystal structure. In the absence of external strain, the charge distribution within the crystal is symmetric and the net electric dipole moment is zero. However, when an external stress is applied, the charges are displaced and the charge distribution is no longer symmetric. A net polarization develops and results in an internal electric field. A material can only be piezoelectric if the unit cell has no center of inversion.

Piezoelectricity is a property possessed by a group of materials, discovered in 1880 by Pierre and Jacques Curie during their study of the effects of pressure on the generation of electrical charge by crystals such as quartz, tourmaline, and Rochelle salt [115]. To date, lead zirconium titanate (PZT) is one of the most widely used piezoelectric materials.

6.1.2. Constitutive Relations for Piezoelectricity

When writing the constitutive equation for a piezoelectric material, account must be taken of changes in strain and electrical displacement in three orthogonal directions caused by cross-coupling effects due to applied electrical and mechanical stresses. Tensor notation is first adopted, and the reference axes are shown in Figure 6.1.

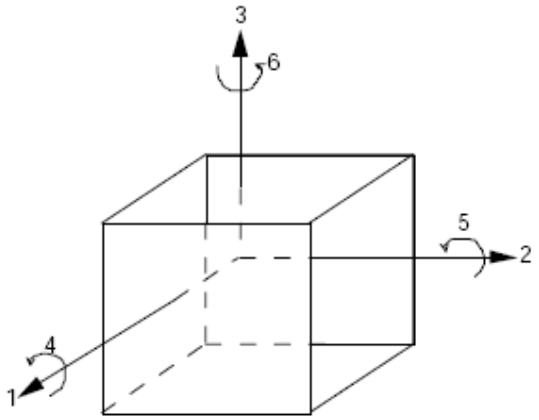

Figure 6.1 Reference axes of constitutive equations for a piezoelectric material

The material behavior of sensors and actuators made of piezoelectric materials can be modeled by the following constitutive equations involving two mechanical variables and two electrical variables:

$$T = C^E S - h^T E \qquad 6.1$$

$$D = hS - b^S E \qquad 6.2$$

where the superscript T denotes a matrix transpose, T is a stress tensor, S is a strain tensor, D is the electric displacement, E is electric field, C^E is the elastic stiffness tensor evaluated at constant electric field, h is the piezoelectric coupling constant and b^S is the dielectric constant at constant strain.

Note that piezoelectric matrix *h* accounts for the piezoelectric effect, i.e. the intrinsic coupling between mechanical and electric fields. Eq. 6.1 characterizes the converse piezoelectric effect that enables piezoelectric materials to function as actuators, while Eq. 6.2 characterizes the direct piezoelectric effect that enables piezoelectric materials to function as sensors.

6.1.3. Ferroelectricity

Some piezoelectric materials are also ferroelectric. A ferroelectric material possesses a spontaneous polarization that can be reversed in direction by application of an electric field over some temperature range. Most ferroelectric materials have a Curie temperature, *Tc* below which they are polar and above which they are not. The very large permittivity values that are characteristics of ferroelectric materials are greatly exploited in many applications, most widely in the multilayer-capacitor industry.

Applying a large alternating electric field causes the polarization to reverse, and this gives rise to the ferroelectric hysteresis loop, relating the polarization *P* to the applied electric field *E*. A typical field-polarization loop is illustrated in Figure 6.2. At large signals, both the electric displacement *D* and the polarization *P* are non-linear functions of the field *E*. They are related to each other through the linear equation below:

$$D_i = P_i + \varepsilon_0 E_i \qquad 6.3$$

where ε_0 is the permittivity of free space (=8.85x10^{-12} C/V-m). For most ferroelectric ceramics, the second term in equation (1) is negligible, and a *D-E* loop and *P-E* loop become interchangeable. Two key characteristics of the *P-E* loop are the coercive field *Ec* and the remnant polarization *Pr*, both defined by analogy to ferromagnetic materials. *Ec* is the field at which the polarization is zero. *Pr* is the value of the polarization when the electric field is zero.

Once the field is switched off, the material will have a polarization equal to *Pr*. Once the *P-E* loop is saturated both *Pr* and *Ec* can be determined. A loop is said to be saturated once the values of *Pr* and *Ec* no longer vary.

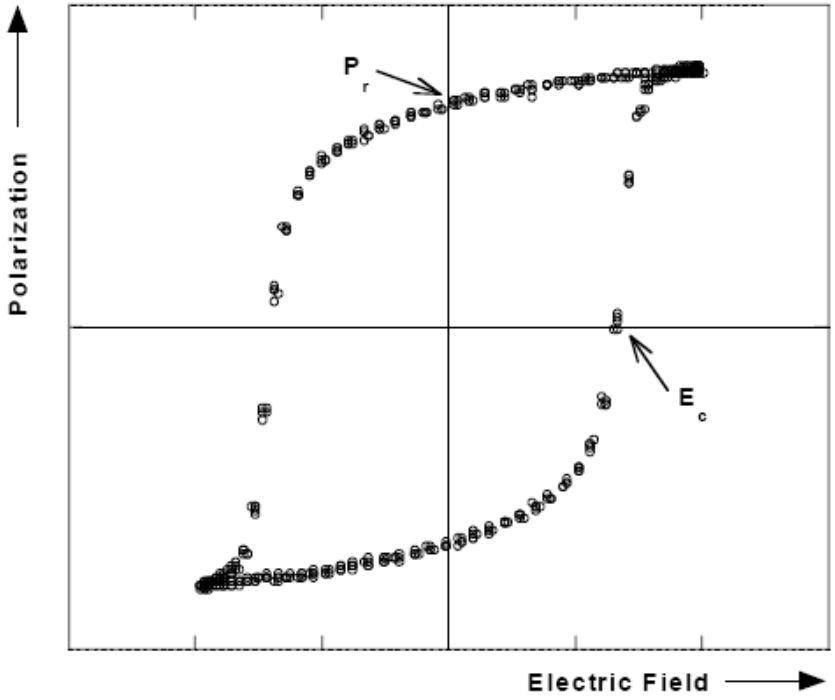

Figure 6.2 *P-E* Hysteresis loop of a poled piezoelectric ceramic

Generally, the existence of the *P-E* loop is considered as the evidence that a material is ferroelectric. A Sawyer-Tower [116]circuit or a modified version of it is commonly used to obtain a *P-E* loop. A diagram of Sawyer-Tower circuit is shown in Figure 6.3.

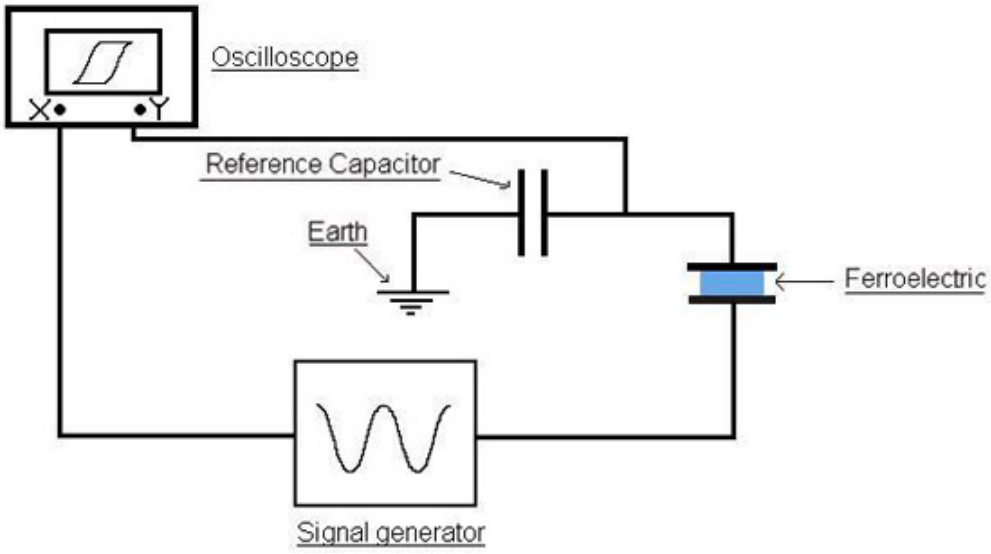

Figure 6.3 Diagram of Sawyer-Tower Circuit

Polarization may be defined as:

$$P = \frac{Q}{A} \qquad 6.4$$

where Q is the charge developed on the plates (Coulombs) and A is the area of the plates (m^2). A good ferroelectric material has 10 μC $cm^{-2} < P <$ 100 μC $cm^{-2.}$ In this experiment, the voltage is cycled by the signal generator. Its direction is reversed at high frequency, and the voltage across the reference capacitor is measured. The charge on the capacitor must be the same as the charge over the ferroelectric capacitor, as they are in series. This means the charge on the ferroelectric material can be found by:

$$Q = C \times V \qquad 6.5$$

where C is the capacitance of the reference capacitor, and V is the voltage measured over this capacitor.

6.1.4. Piezoelectric Stack Actuator

The use of piezoelectric materials for actuation and sensing has been demonstrated extensively over the years. In order to have reasonable displacement at low voltage, often a multilayer piezoelectric scheme is utilized. Figure 6.4 shows a multilayer actuator that consists of a stack of thin ceramic disks separated by electrodes. Most piezoelectric multilayer actuators are based on d_{33} design, in which the coefficient d_{33} dominates the other piezoelectric constants in the constitutive equations. As a result, the direction of expansion coincides with that of the electric field. When no external load is applied, the change of length is related to the voltage applied by the approximate relationship $\Delta = d_{33}$ n Φ where n is the number of disks in the stack and Φ is the applied voltage. This design is mainly used for precision position control.

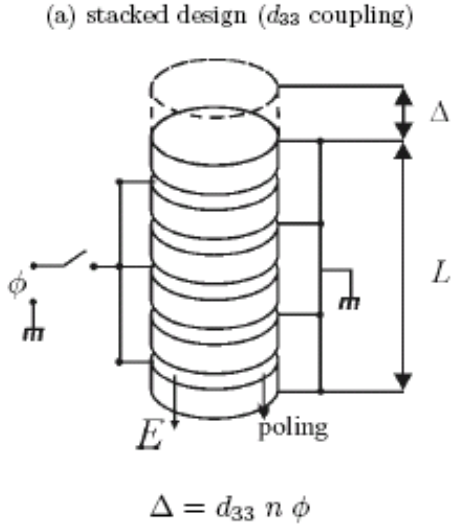

Figure 6.4 A d_{33} multilayer piezoelectric actuator

Compared to their single layer counterparts, multilayer piezoelectric actuators offer several advantages such as low driving voltages while maintaining high electric fields necessary for actuation, rapid response time, and high electromechanical coupling [117]. The majority of piezoelectric stack actuators are fabricated with PZT, a commonly used piezoelectric ceramic material. A typical lamination scheme (Figure 6.5a) relies on a

vertical stack of alternating layers of electrodes and piezoelectric layers, where each lamination step requires electrodes to be deposited and patterned or aligned [75, 76]. Alternatively, a planar fabrication method can be utilized to form a lateral multilayer piezoelectric actuator, in which a series of vertical grooves are cut into a PZT crystal and metallized with appropriate isolation to form a lateral multilayer structure. Such a structure was demonstrated using electroplating of electrodes followed by laser-assisted etching of PZT and electrodes [118]. However, process challenges of electroplating in deep grooves as well as issues with the laser assisted etching were also reported.

To avoid these difficulties, we propose an alternative, simple, and cost-effective lateral lamination scheme (Figure 6.5b) for a multilayered piezoelectric actuator. The process involves PZT dicing, photolithographic definition of high-aspect-ratio SU-8 pillars for electrical isolation, and micromolding of electrically conductive polymer composite (ECPC) electrodes. This approach overcomes the reported process difficulties of the previous work [118], while simultaneously maintaining the advantages of multilayer piezoelectric actuators.

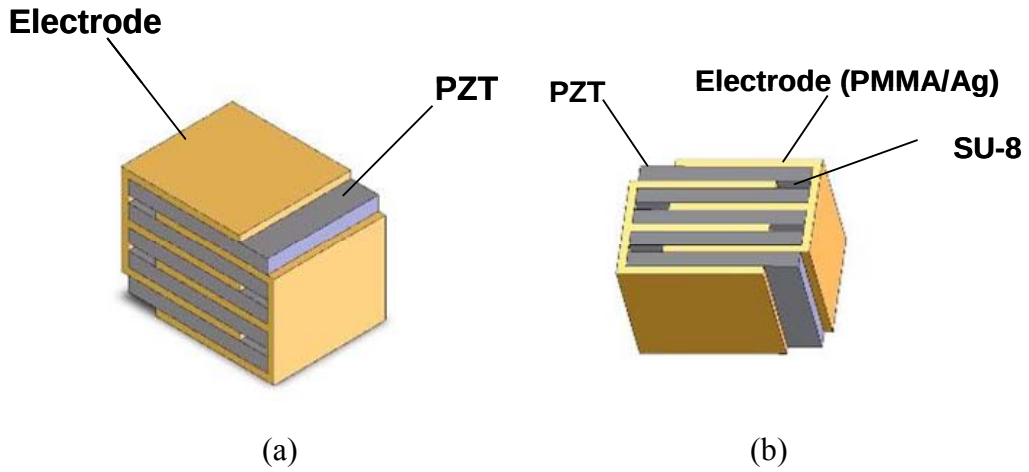

Figure 6.5 Lamination architectures for multilayer piezoelectric actuator: (a) Conventional vertical stack lamination, (b) Proposed lateral lamination

In this study, an effective photolithographic patterning scheme for the 1mm-tall isolation structure has been demonstrated. Specific advantages associated with the

molding of internal electrodes include: (1) ECPC casting through high-aspect-ratio trench is time-effective, compared to the long processing time of an electroplating approach; (2) ECPC electrodes alleviate void formation issues which may occur during the plating through the deep trenches; (3) the silver-PMMA composite has mechanical and thermal properties similar to those of the isolation SU-8, which increases the stability of the actuator. Using these schemes, a PZT multilayer actuator has been designed, tested and characterized.

6.2. Numerical Analysis

6.2.1. Theoretical Background for the Coupled Analysis

The aim of this modeling is to conduct a finite element analysis on a multilayer piezoelectric actuator to evaluate the displacement under working voltage with the aid of ANSYS. The purpose of using FEM is to predict the actual physical behaviors of the PZT actuator without going through the expensive prototyping processes. It can help to manipulate and analyze the effects of various design variables such as electrode material and amplification method.

A coupled-field analysis is an analysis that takes into account the interaction (coupling) between two or more disciplines (fields) of engineering. A piezoelectric analysis handles the interaction between the structural and electric fields: it solves for the voltage distribution due to applied displacements, or *vice versa*. Other examples of coupled-field analysis are thermal-stress analysis, thermal-electric analysis, and fluid-structure analysis. The procedure for a coupled-field analysis depends on which fields are being coupled, but two distinct methods can be identified: *sequential and direct* [97]. In a sequentially coupled physics analysis, the two fields can be coupled by applying results from the first analysis as loads for the second analysis. The load transfer occurs external to the analysis, and loads must be explicitly transferred using the physics environment.

The direct method usually involves just one analysis that uses a coupled-field element type containing all necessary degrees of freedom. Coupling is handled by calculating element matrices or element load vectors that contain all necessary terms. The *direct-coupled* method is used in this work to analyze the displacement (static analysis) resulting from the interaction between the external electric field and the strain of the PZT material.

6.2.2. 2-D and 3-D Coupled Analysis

In this modeling, both 2-D and 3-D FE model are built to study the static behavior. For the most part, this device, with its dominatingly stiff, high-impedance piezoelectric (PZT) regions and its highly orthogonal, regular construction, is expected to conform well to simple first-order piezoelectric coupling modeling. However, there are three readily identifiable non-ideal effects that could be identified prior to FE modeling:

- the effect of the non-driven edges of the PZT slabs on the expansion of the central portions;
- the out-of-plane stresses and moments that will be placed on it by the external loading;
- the effect of a much stiffer electrode material, copper.

Fortunately, each of the only two feasible 2-D simplifications of the 3-D model directly addresses one or more of these effects. The 3-D model produces even more accurate results at the cost of modeling time. The performances of PZT actuators using two different electrodes have been studied.

6.2.3. Cymbal Structure

To further increase the available displacement, addition of metal end caps is possible. A metal end cap is a mechanical transformer for converting and amplifying the lateral displacement of the actuator into a large axial motion in the plate. A PZT

ceramic-metal end cap composite actuator "cymbal" was developed [119]. It was names the "cymbal" because of the similarity in shape to that of the musical instrument of the same name as shown in Figure 6.6. Arrows show the displacement direction under positive bias and dashed lines show the displacement motion (side view of disk shape). Dimensions (in mm) are listed as follows: Metal endcap diameter, d = 12.7; thickness t = 0.3. Sheet thickness of cymbal, t = 0.2. PZT ceramic diameter, d=12.7; thickness t = 1.0. Cavity diameter, d = 9.0; height, h = 0.20. Bonding layer thickness, t = 0.015.

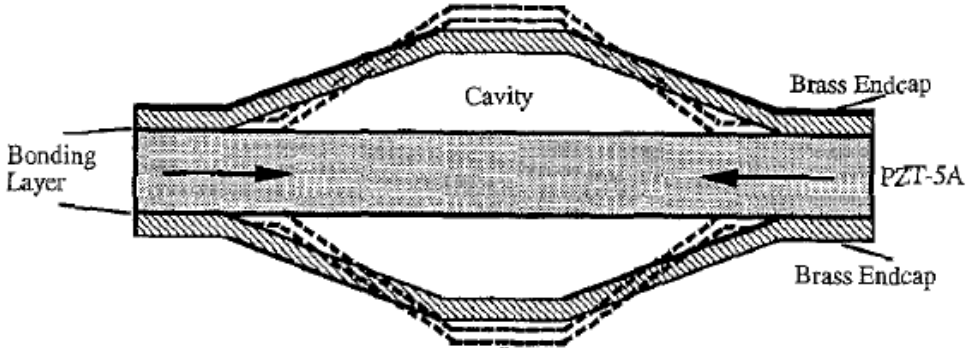

Figure 6.6 Displacement motion of the cymbal design

The cymbal actuators consist of a PZT plate (poled in the thickness direction) sandwiched between two metal end caps. The caps contain a shallow cavity on their inner surface. The presence of the cavities allows the caps to convert and amplify the small radial displacement of the disk into a much larger axial displacement normal to the surface of the caps, which contributes to a much larger acoustic pressure output than would occur in the uncapped PZT plate. The cymbal actuator shown above is 12.7mm in diameter and 1.7mm in total thickness and it can generate a 40μm displacement at 1kV/mm. Since a PZT plate is used as, both the d_{31} *and* d_{33} coefficients contribute to the axial displacement of the composite cymbal actuator.

This chapter aims to develop a miniaturized PZT stack actuator by MEMS technology that can provide the actuation for a microvalve. For this purpose, the PZT

stack is designed to have comparable size with the one used in Chapter 5. Ultimately, the fabrication technology should be scalable to achieve the final goal of having smaller lateral size but same stroke. In Chapter 5, a PZT stack actuator with lateral size of 2mm x 3mm and a height of 9mm was used. In our current design, the PZT stack has a size of 2x3x1mm. Therefore, this stack can be used as a bare stack actuator in its axial direction with a dimension of 3(L) x 1(W) x 2(H), or be placed on its large side with metal cap added on to form a cymbal actuator. The lateral dimension of the cymbal actuator is 3(L) x 2(W). The height is determined by the metal end cap structure.

6.2.4. Model Information

6.2.4.1. 3-D Model

A. Without Cymbal

Figure 6.7 shows the ANSYS model built for the multilayer PZT actuator without cymbal structure and Table 6.1 shows the structure dimension for that model.

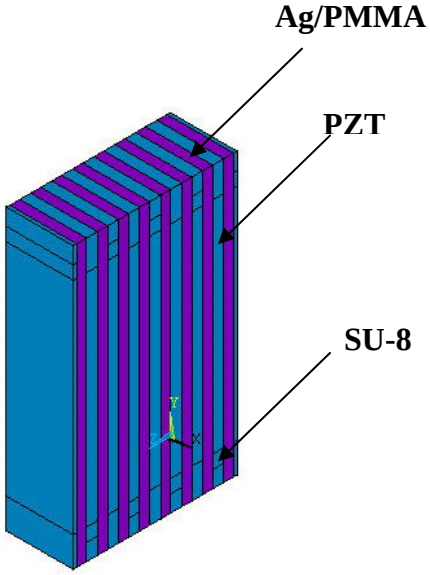

Figure 6.7 3-D Model without cymbal structure

B. With Cymbal

Figure 6.8 shows the ANSYS model built for the multilayer PZT actuator with cymbal structure.

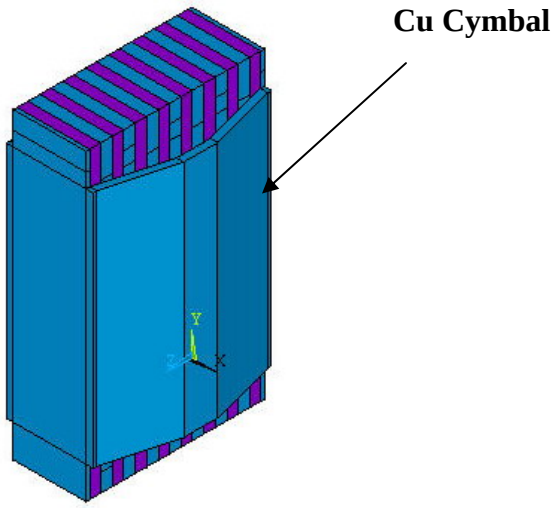

Figure 6.8 3-D Model with cymbal structure

Table 6.1 Physical dimensions of the 3-D multilayer model

No.	Component	Material	Dimensions (mm)
1	Piezoelectric ceramic stack	PZT	3.3 (W) x 1 (H) x 0.15 (T)
2	Electrical isolation column	SU-8(epoxy)	0.2 (W) x 1 (H) x 0.165 (T)
3	Sandwiched electrode	SU-8 or Copper	3.3 (W) x 1 (H) x 0.165 (T)
4	Piezoelectric ceramic extra part	PZT	0.25(W) x 1 (H) x 0.15 (T)

6.2.4.2. 2-D Model

A. H-plane 2-D Model

First, by taking a horizontal slice of the actuator (along the YZ plane in Figure 6.7 and Figure 6.8), the field interactions around the material joints could be studied in detail, with fine meshes and elaborate geometry, without incurring the complexity or computational cost of doing so with the 3-D model. Note that there was, without using a shell element, no practical way to include the out-of-plane loading the cymbal would place on this. However, focusing on one effect of interest at a time is acceptable. This H-plane model was used to simulate the effect of the "dead" (i.e. effectively undriven) ends of the PZT slabs. Since the higher stiffness of copper electrodes would probably have the greatest influence through this effect, the H-plane 2-D model is used to investigate how the Cu electrodes affect the actuation.

The 2-D model, areas only, for the H-plane 2-D model, 4 PZT layers, is shown in Figure 6.9 (with a black background). The blue (or light gray in black and white print out) areas are the PZT slabs. Some purple (dark gray) areas are SU-8 insulator, and some purple areas are the electrodes.

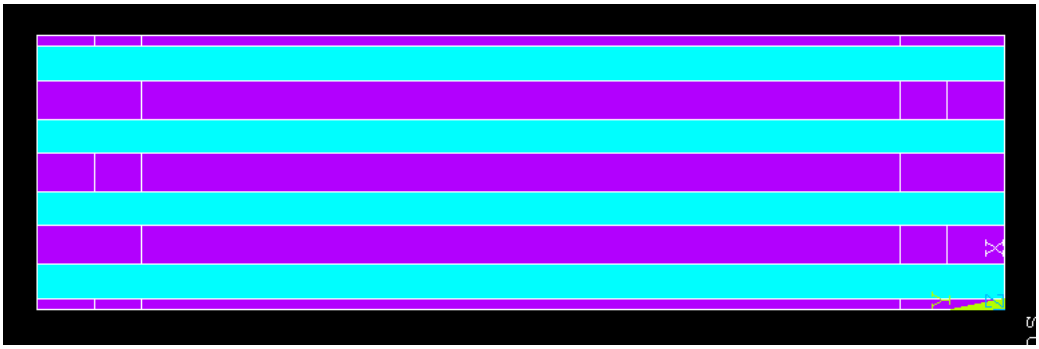

Figure 6.9 H-plane 2-D model for 4 layer PZT actuator without cymbal structure.

B. V-plane 2-D Model

Next, by taking a vertical slice of the actuator, along its direction of actuation (that is along the XZ plane in Figure 6.7 and Figure 6.8), the out-of-plane effects of the cymbal could be modeled. This plane eliminates the worst aspect ratio problems, so the

actuation stack itself could be cheaply modeled while the cymbal behavior and interface could be closely studied. So, this V-Plane model is used to investigate cymbal actuation.

The model for an 8-layer V-plane 2-D model, without cymbals, is shown in Figure 6.10. The purple areas are electrodes and the blue areas are PZT.

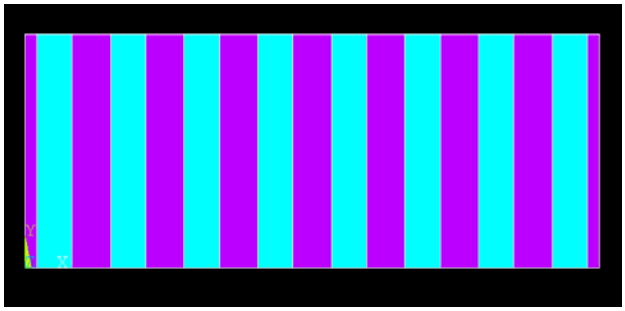

Figure 6.10 V-plane 2-D model for 8 layer PZT actuator without cymbal structure.

The model areas for an 8-layer V-plane 2-D model with attached cymbals are shown in Figure 6.11. The PZT slabs are blue, and the electrodes (including the cymbals) are purple.

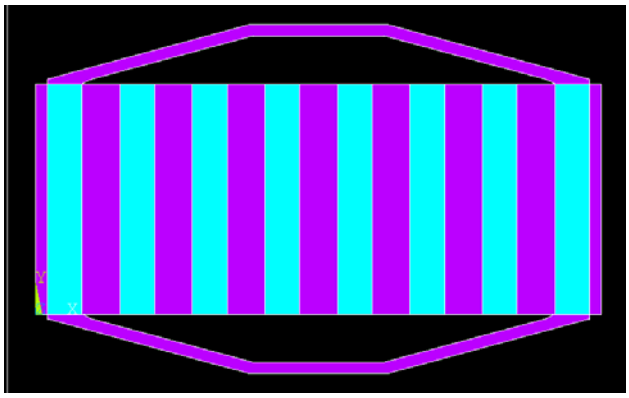

Figure 6.11 V-plane 2-D model for 8 layer PZT actuator with cymbal structure.

Note that from the 3-D model used to all of the 2-D models, there is a slight change in the coordinate axes. Instead of actuating in the Z direction, as it does in 3-D, the actuator actuates in the X direction in all 2-D simulations. This was because ANSYS

only allows 2-D simulation in the XY plane. This 2-D structure was both constructed and modeled for both cases with and without cymbals.

6.2.5. Element Type

For 3-D modeling, elements SOLID95 and SOLID98 were used. The SOLID95 was used for the SU-8 isolation part and Ag/PMMA composite electrode. The SOLID95 element is defined by 20 nodes having three degrees of freedom per node: translations in the nodal x, y, and z directions. The element has plasticity, creep, stress stiffening, large deflection, and large strain capabilities. Various printout options are also available.

SOLID98 element was used for the PZT part. The SOLID98 is a 10-node tetrahedral version of the 8-node SOLID5 element. The element has a quadratic displacement behavior and is well suited to model irregular meshes (such as produced from various CAD/CAM systems). When used in structural and piezoelectric analyses, SOLID98 has large deflection and stress stiffening capabilities. This element can be used for the three-dimensional magnetic, thermal, electric, piezoelectric, and structural field analysis.

The coupled field plane element PLANE223 was used for all elements in the 2-D simulation. Its piezoelectric coupling matrix (PIEZ) was left blank (all zeros) for all non-PZT elements. However, all elements have voltage (VOLT) added as a degree of freedom to allow complete electrostatic simulation. PLANE223 is a quadratic, quadrilateral (20 node) element that supports degenerate forms (i.e. tetrahedral elements) if so ordered by the mesher. For the H-plane modeling, the model was simulated in plane stress mode, and for the V-plane modeling, the plane strain mode was applied.

6.2.6. Material Properties

<u>PZT:</u>

The 1mm-thick PZT plate used in this study was a commercialized high-d_{33} piezoelectric coefficient, hard ceramic plate (PZT 855, APC International Ltd.). A 20 x 20 x 1mm PZT plate was mounted on a glass substrate using adhesive and diced into 150 micron-wide 'fins' with a spacing of 165 micron defined by the thickness of the diamond blade used.

SU-8:

The SU-8 (SU-8 2025, Microchem Co.) is epoxy based negative tone photoresist. After exposure, it becomes a highly crosslinked thermoset material. SU-8 pillars for electrical isolation are formed between the PZT fins in alternating gaps by photolithography.

Silver/PMMA Composite:

An electrically conductive polymer composite (ECPC, silver-PMMA: 40 vol% Ag) has been made by mixing 1-micron size silver powder with PMMA solution. The silver-PMMA ECPC blend was cast into the gaps between the PZT fins, and then vacuum-cured.

Copper:

An alternative way to form electrode in the gap between PZT fins is electroplating copper. The material properties are list in Table 6.2. Note that ANSYS supports uniform entry (i.e. in 3 dimensions) of all material properties, even if being used for a 2-D simulation.

Table 6.2 Material properties

Material	Elastic modulus (GPa)	Poisson's ratio	Density(kg/m^3)
SU-8	4.4	0.22	1.3
Copper	128	0.36	8.96

Silver/PMMA Composite	4	0.22	1.5

The stiffness matrix for PZT [120] is:

$$C = \begin{bmatrix} 12.6 & 7.95 & 8.41 & 0 & 0 & 0 \\ & 12.6 & 8.41 & 0 & 0 & 0 \\ & & 11.7 & 0 & 0 & 0 \\ & & & 2.33 & 0 & 0 \\ & \textit{symmetric} & & & 2.3 & 0 \\ & & & & & 2.3 \end{bmatrix} \times 10^{10}\ \text{Pa}$$

The piezoelectric coupling matrix for PZT is:

$$h = \begin{bmatrix} 0 & 0 & -6.6228 \\ 0 & 0 & -6.6228 \\ 0 & 0 & 23.24 \\ 0 & 0 & 0 \\ 0 & 17.034 & 0 \\ 17.034 & 0 & 0 \end{bmatrix} \text{C/m}^2$$

The dielectric property matrix for PZT is:

$$b = \begin{bmatrix} 1.503 & 0 & 0 \\ 0 & 1.503 & 0 \\ 0 & 0 & 1.3 \end{bmatrix} \times 10^{-8}\ \text{F/m}$$

Density = 7500 kg/m^{-3}

6.2.7. Meshing Process

6.2.7.1. Software Control

In both the 2-D and 3-D cases, the explicit selectability of all entities (areas, lines, etc.) along with the LESIZE, MOPT, and KREFINE commands provided more meshing control than proved necessary. Thus, no special techniques were developed. It was observed that the attachment points of the cymbals are meshed very finely, automatically, by the freemesh tool. This turned out to be convenient, as the maximum stresses across the entire part occurs at these boundaries.

A typical mesh section, near the edge of an H-plane 2-D model, is shown in Figure 6.12. This was initially freemeshed, after placing node size restrictions on various lines using LESIZE. Afterwards, certain keypoints were selected and the meshes were refined in their immediate vicinity. This model averaged approximately 1000 elements per PZT layer.

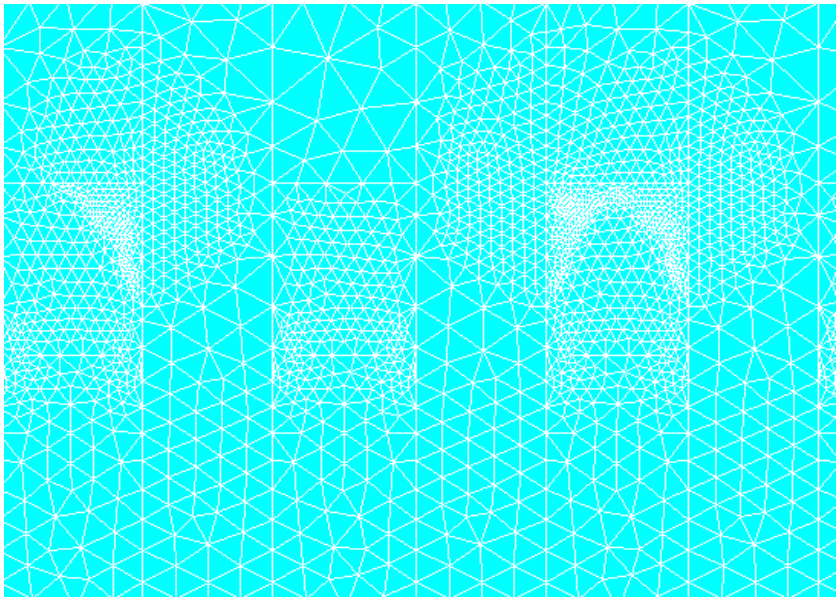

Figure 6.12 A typical mesh section of an H-plane 2-D model

6.2.7.2. Meshing Challenges

During 3-D modeling, the sheer size of the mesh was the primary issue. This difficulty arose not only because it was a 3-D problem, but also because some of the volumes had extremely large aspect ratios, on the order of 1:50. To achieve adequate node density along the thickness of such reasons while keeping reasonable per-element aspect ratios, the number of nodes must be huge. Thus, extremely detailed 3-D meshing was simply not feasible.

There are two major instances where extreme mesh adjustment is necessary during 2-D modeling. Both issues proved inconsequential before they proved insoluble and both arose during H-plane simulation. The first was a spike in the stress at the juncture of SU-8, PZT, and electrode regions. In fact, the above mesh was formed while refining the mesh to address these stress spikes. So, the areas where the mesh was most dense are the areas where the spikes occurred. This was probably due to three areas with different stiffness being joined orthogonally at the same point in space. As the mesh was refined, it was found that this voltage spike grew inversely with the mesh size. This indicated that it is an artifact of the FE modeling, and since no other noticeable performance parameters changed with this spike magnitude (as the mesh was refined), it was concluded that it could safely be ignored.

The other meshing challenge with the 2-D simulation arose during H-plane simulation. This is a classic electrostatic problem: the corners of the electrodes are sharp, and thus the electric field spiked close to the corners. Mesh refinement does not improve the condition either; however, fillets are added to the electrode corners. The fillet radius must be kept small (less than 20 microns) to accurately model the real devices fabricated. It is found that the fillets mollified the spike somewhat, down to around 10 V/um, but do not eliminate it. In other words, this field spike is a legitimate phenomenon and probably

occurs in the real devices. Again, however, it is determined that this has little or no bearing on the actuation process, and so it is ignored.

6.2.8. Mesh Convergence

6.2.8.1. 3-D Model

The 3-D structure was meshed with hexahedral-shaped elements. The element sizes are determined by specifying the number of divisions per line of the solid model using "LSIZE" command. This method of determining the mesh allows for the most control over element size and ensures a smooth transition from smaller to larger elements. This last benefit of directly specifying the mesh is very important for this analysis.

Due to the large electric filed gradient this area experiences, the region where SU-8 pillars connect with the PZT slabs was meshed considerably finer than everywhere else.

Mesh convergence test was done for 2-layer, 4-layer and 8-layer devices. As an example, the different meshes generated for the 4-layer device is shown in Figure 6.13.

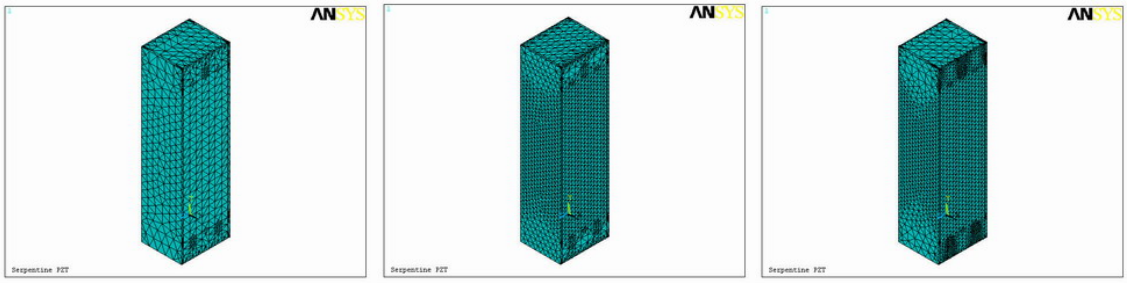

Figure 6.13 Different meshes generated for the 3-D model for 4-layer device.

From Figure 6.13 a mesh convergence plot can be produced showing element number versus z-displacement where the model is considered to have converged when the difference in the solution between successive iterations is less than 5-10%. Figure 6.14 shows this mesh convergence for the three types of 3-D models.

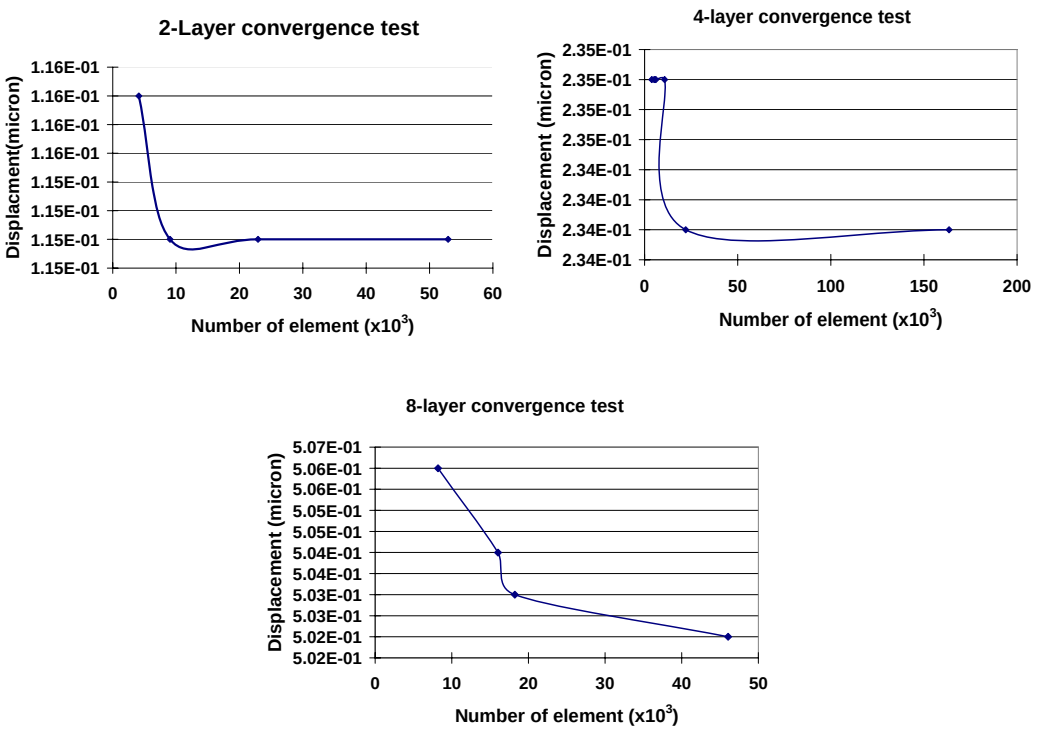

Figure 6.14 Convergence plot for the 3-D model for multilayer device

Figure 6.15 shows the mesh of an 8-layer 3-D model with cymbal structure. The meshing for cymbal 3-D model was done according to the mesh convergence test results from the PZT-only model.

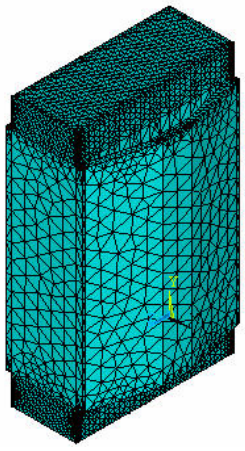

Figure 6.15 Mesh of an 8-layer 3-D model with cymbal structure

6.2.8.2. 2-D Model

For the two different 2-D planes (H-plane and V-plane), mesh convergence was investigated to allow proper mesh sizing for analysis of device variations, such as the cymbals. The results are shown in Figure 6.16.

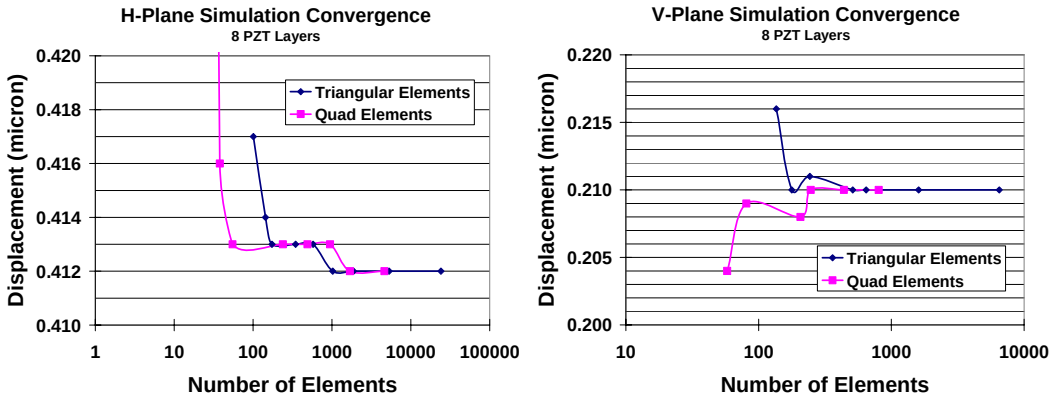

Figure 6.16 Convergence plot for the 2-D model for an 8-layer actuator

Note that in both cases, it is necessary to do quadrilateral-only meshing to achieve sufficiently small mesh sizes to reinforce divergences. In other words, these structures are inherently simple enough that they readily converged, even with very coarse meshing. As with the 3-D case, the convergence criteria are within 0.1% agreement of the x-direction displacement between successively finer simulations.

Since the simulations are radically parameterized by the number of layers chosen, it is necessary to relate the meshing quality required for convergence not only to the model itself but also to this parameter. Whereas weakly parameterized models may indicate a single minimum mesh size for convergence, no such single value existed that would guarantee convergence for any number of layers. The most useful apparent metric in this regard is the number of nodes distributed through the thickness of the various layers. For the H-plane simulation, approximately 5 to 8 nodes are needed along the thickness of all layers to ensure convergence. The V-plane simulation is considerably more tolerant, and could converge with only 3 to 4 nodes per thickness dimension.

6.2.9. Boundary Conditions and Loading Conditions

6.2.9.1. 3-D Model

Once the model was meshed, the boundary conditions are applied. For this model one of the side plane was constrained in the all the directions as shown in Figure 6.17. For loading, alternating voltage was applied to each PZT layer. This was done by applying voltage on the top x-y plane, and to the electrodes connected two the top x-y plane including the electrodes in between two extra PZT parts. Similarly, the ground was applied to the bottom x-y plane and the electrodes connected to it. No electrical loading was applied to the SU-8 isolation pillars. Figure 6.18 illustrates the loading condition.

A static analysis was performed based on the above boundary and loading conditions. A sparse solver was used for solving the problem. The sparse solver is suggested by ANSYS for piezoelectric coupling analysis. The sparse direct solver is based on a direct elimination of equations as opposed to iterative solvers, where the solution is obtained through indirect means (that is, through iterative solution). Since the sparse direct solver is based on direct elimination, poorly conditioned matrices do not pose any difficulty in producing a solution.

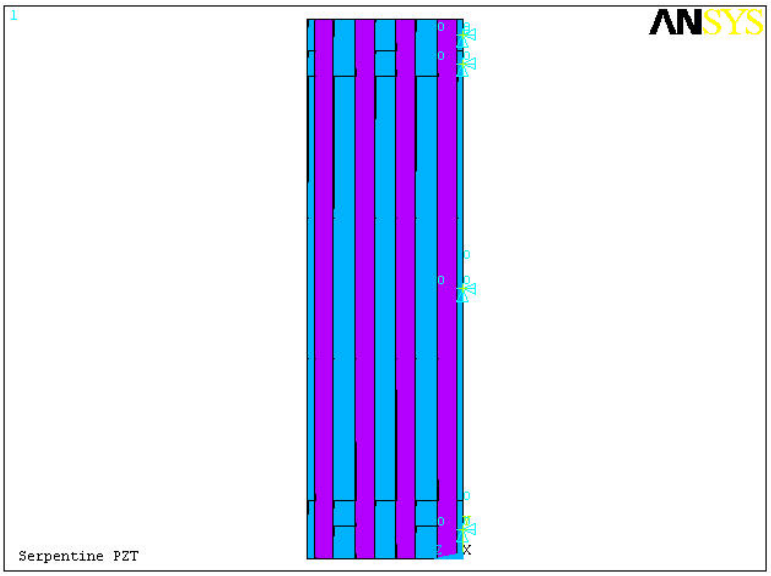

Figure 6.17 Boundary condition for a 4-layer 3-D model

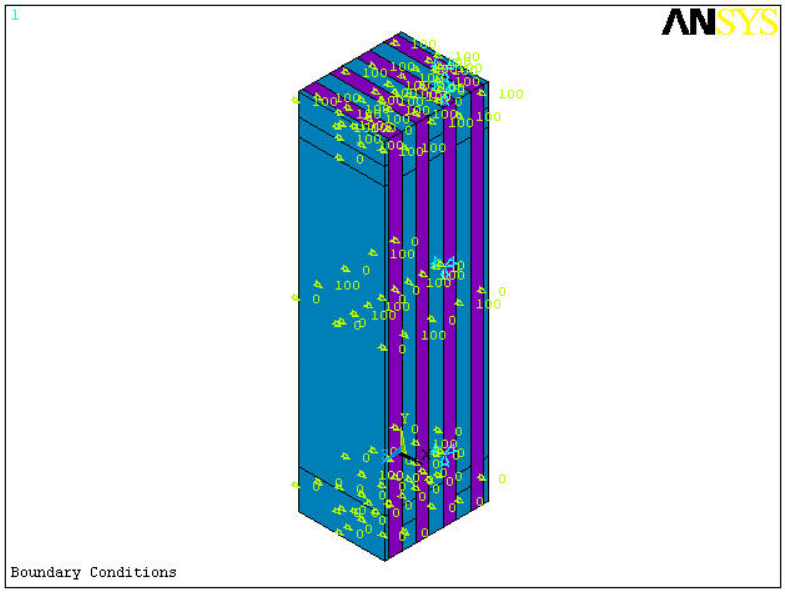

Figure 6.18 Loading condition for a 4-layer 3-D model

6.2.9.2. 2-D Model

A. Mechanical

For all 2-D modeling, except when the cymbal is attached, the only mechanical boundary condition was fixed leftmost edge of the actuator (i.e. where x = 0), with UX and UY both constrained to zero over the entire edge. When the cymbal is installed, however, this constraint is removed, and the entire PZT stack is allowed to "float." However, the bottom edge of the bottom cymbal is fixed with UY = 0 to emulate adhesive contact with the substrate.

B. Electrostatic

The electrostatic boundary conditions are those that implement two simple rules:

- All electrode areas electrically connected to the bottom edge of the device are at zero volts, and
- All electrode areas connected to the top edge of the device are at the driving voltage (nominally 100 V).

These conditions were implemented by selecting all areas that would be electrically connected to the respective terminals if the ANSYS simulation took conductivity into account. Once the proper set of areas are selected, both the areas themselves are constrained to a constant voltage, as well as the lines associated with them.

Clearly, these electrostatic constraints were the same in all 2-D simulations. In Figure 6.19, the H-plane simulation is shown with the voltage constraints applied (and the voltage distribution solved for). Blue areas are at -100 V (the driving voltage) and red areas are at 0 V, with all other colors representing intermediate values.

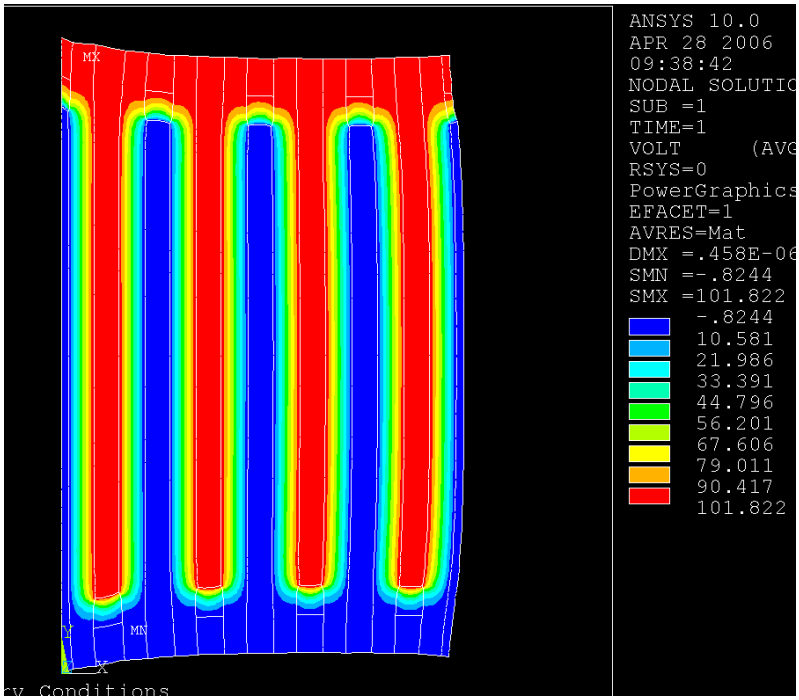

Figure 6.19 Loading condition for a 4-layer 2-D model

6.2.10. Results

Electric Field

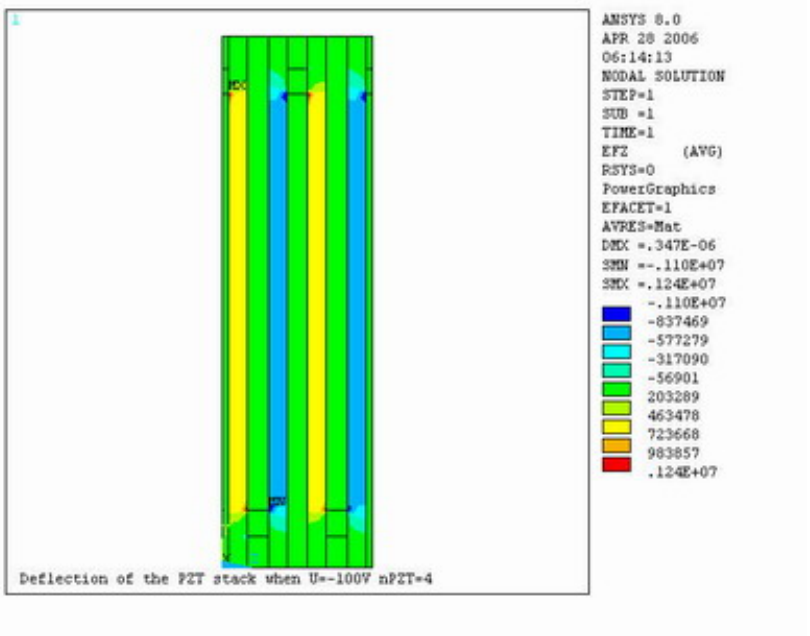

Figure 6.20 Alternating Electric field applied on the PZT layers

Figure 6.21 shows the alternating electric field across each PZT slab. Since the device was poled after fabrication, the electric field across each PZT piece has the same effect on the deformation. If the polarity of the field is the same as the polarization, all the PZT pieces expand and when the polarity of the field is the opposite as the polarization, all the PZT pieces contract as shown in Figure 6.17.

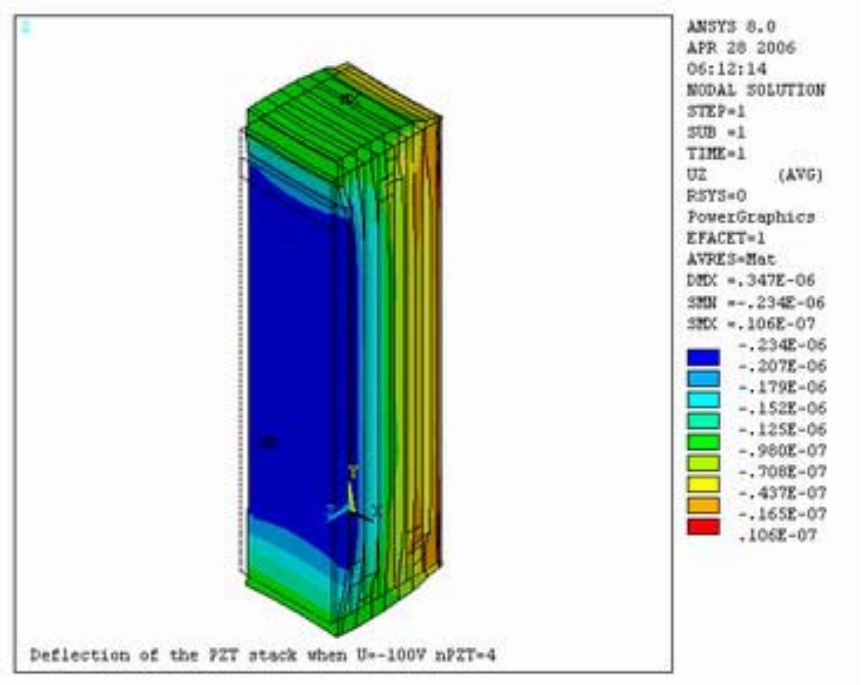

Figure 6.21 Contraction of the actuator when a negative voltage applied.

Electrically Conductive Polymer Composite (ECPC) Ag/PMMA vs. Cu

Two materials, Ag/PMMA composite and copper, were used to define the electrode structure in this simulation. Figure 6.22 compares the simulation results from each model, which is the top-layer displacement of the multilayer actuator with various layer counts. From the results, we can see that use of Ag/PMMA as electrode and enclosure materials will give larger deflection. Also, a fairly rough agreement between the 2-D and 3-D simulations is shown in this chart. The majority of the discrepancy in this case is attributed to the fact that the 2-D simplification did not exactly meet the criteria of neither plane strain nor plane stress, but was simulated as plane stress.

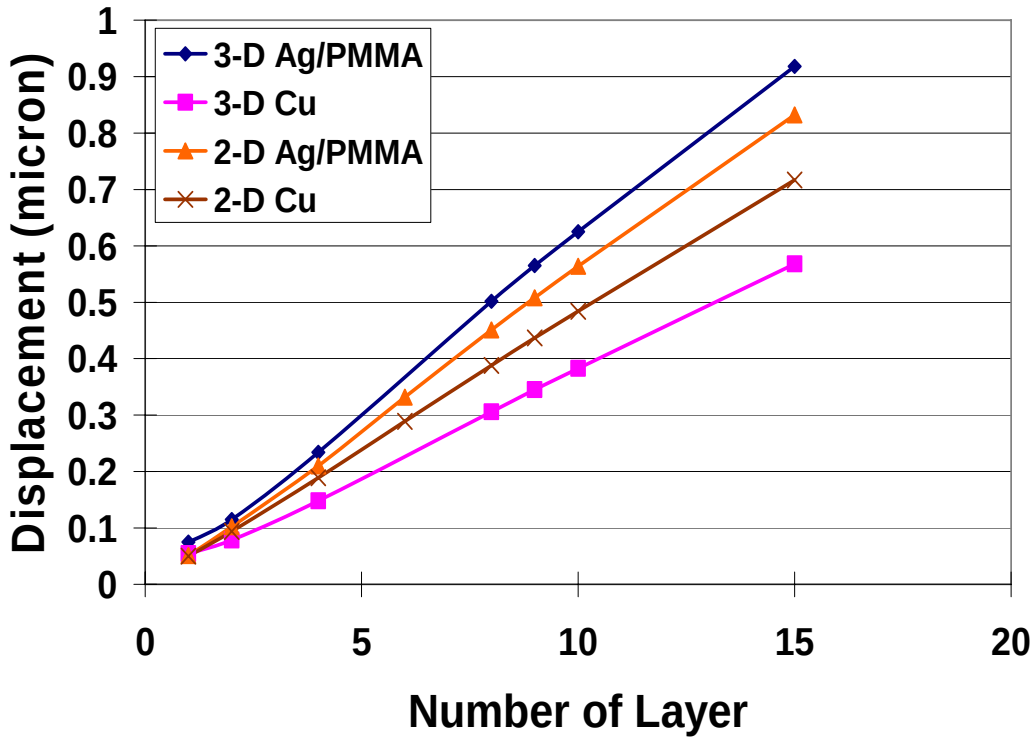

Figure 6.22 Displacement as a function of the number of layers for 2-D and 3-D model with ECPC electrodes and Cu electrodes at an applied voltage of 100V

Cymbal Model

Figure 6.23 shows the displacement of a cymbal structure under 100V driving voltage. By using this structure, z-directional displacement is transformed to x-directional displacement and amplified. The amplification is characterized and plotted in Figure 6.24. The 2-D simulation agrees very well with the 3-D simulation in this case. This is attributable to the relative fidelity with which the 2-D simulation is able to represent the entire cymbal structure. Also, slight offset in favor of the 3-D simulation is attributable to the fact that the cymbal does not span the entire width of the device, yet the 2-D simulation effectively models it as such (while the 3-D simulation can of course assign the true width). This increased effective width increases its stiffness, thus reducing its total deformation under identical load.

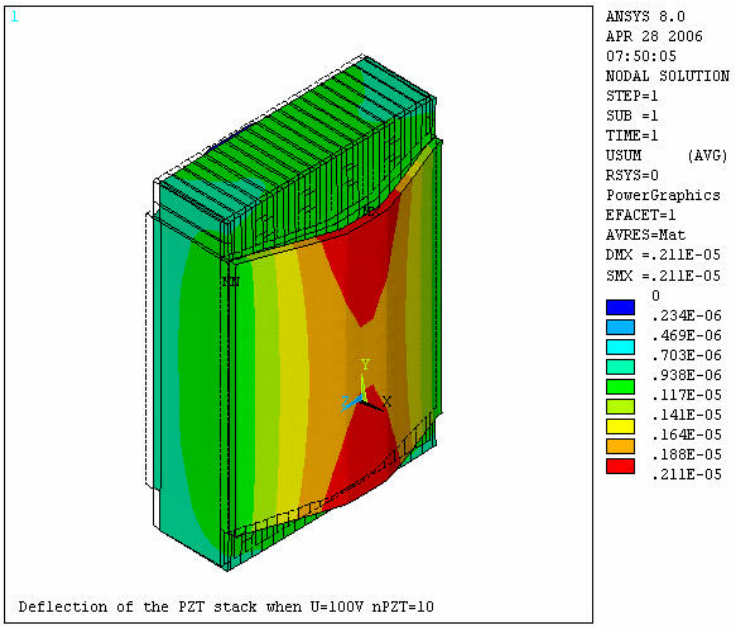

Figure 6.23 Displacement of an 8-layer actuator with cymbal under 100V driving voltage (3-D model)

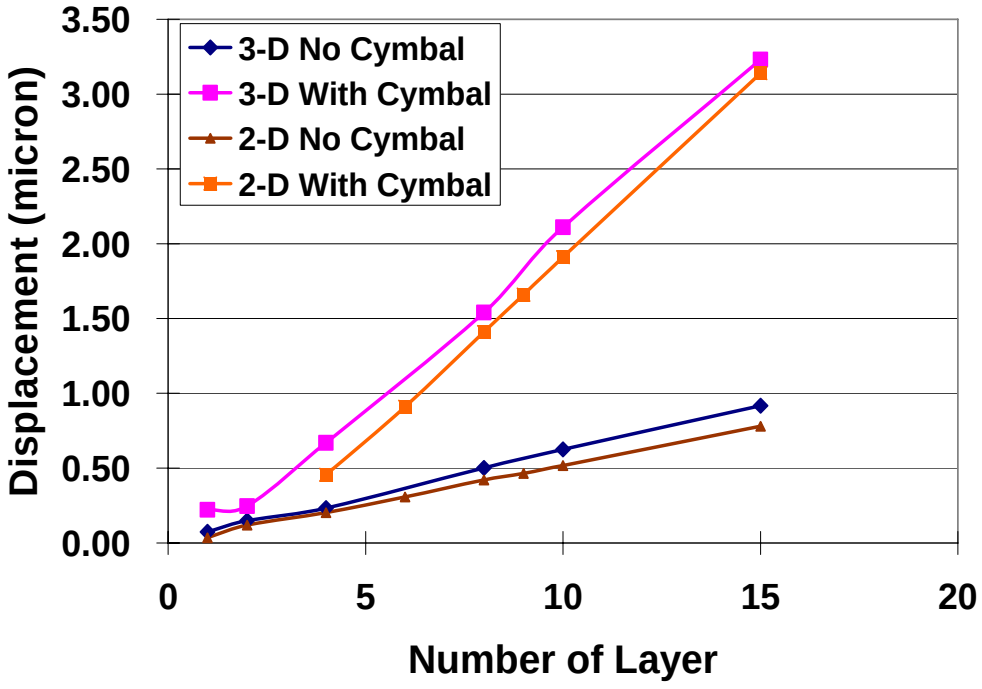

Figure 6.24 Comparison between displacements of mulitilayer actuators with and without cymbal as a function of number of layers

6.3. Fabrication

The design of the PZT stack actuator is shown in Figure 6.25. The design of the PZT stack actuator has been validated by the FEM simulation results. To fabricate the stack actuator from a PZT thin plate, there are several key steps:

1. Dicing to form grooves
2. Defining electrical isolation
3. Applying electrode
4. Dicing into individual actuators

Two approaches have been investigated to apply electrode and define electrical isolation after dicing thin PZT plate into grooves. One is laser micromachining approach and the other is micromolding.

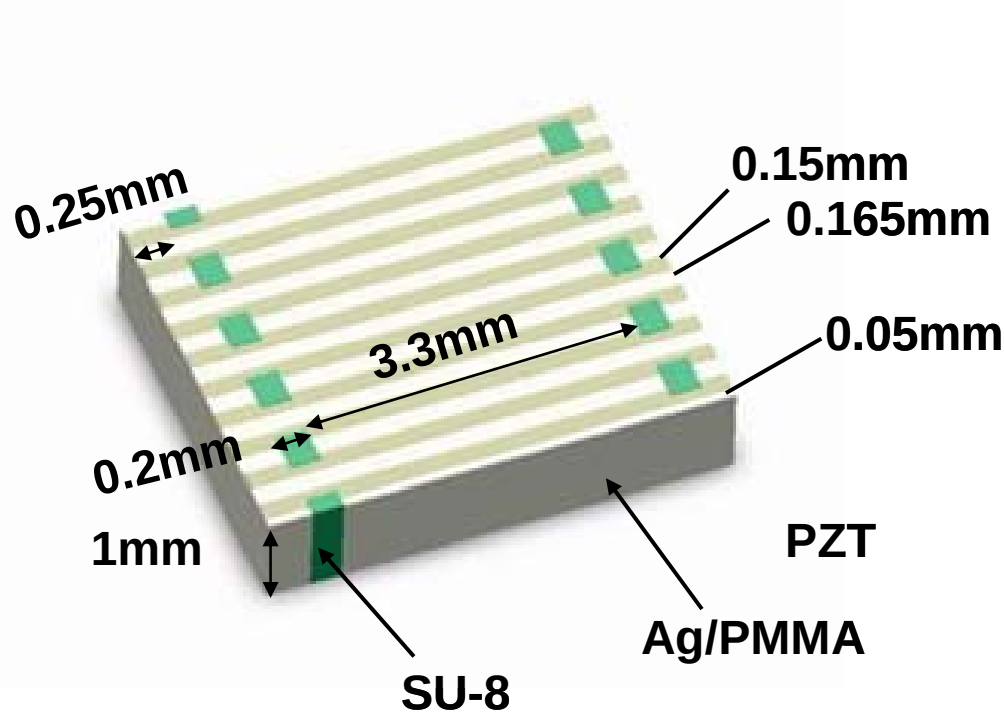

Figure 6.25 Dimension of the PZT stack actuator

6.3.1. Laser Micromachining Approach

An alternative way to photo-pattern serpentine electrical isolation lines is laser ablation. After electrode deposition on the connected PZT structure, a 2-micron parylene film is coated on the metal surface. Excimer laser ablation is used to cut through the parylene layer following the serpentine pattern. After the metals are etched away, polymer is filled into the grooves. A wire bonding pad is then made elsewhere on the plate using the same laser ablation method. Optical microscopy pictures of PZT structure with SU-8 connects are shown in Figure 6.26.

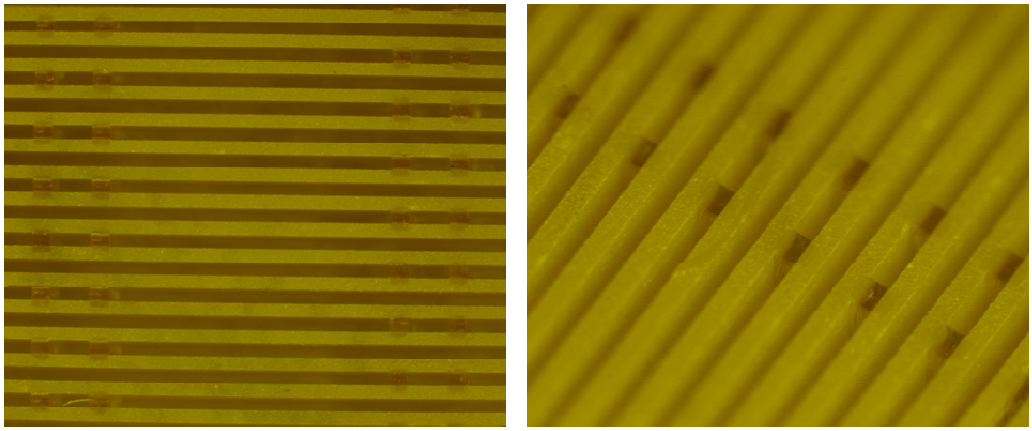

Figure 6.26 Optical microscopy image of diced PZT grooves connected by SU-8 pillar

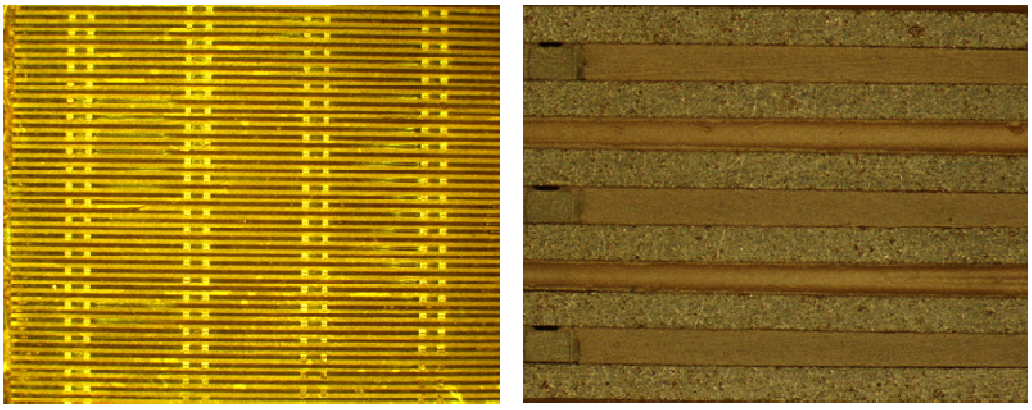

Figure 6.27 Optical microscopy image of metal coated PZT grooves filled with SU-8. Right: magnified image

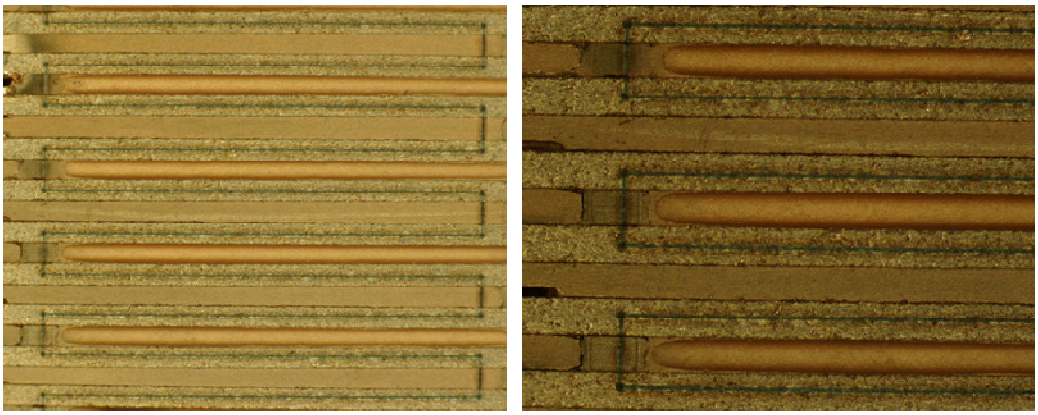

Figure 6.28 Optical microscopy image of electrically isolated PZT stack structure Right: magnified image

The top view on the left shows the uniformity of the cuts. Viewed from an angle, the SU-8 connects are found to have the same height as the PZT fins, illustrating the excellent planarization properties of SU-8. Figure 6.27 shows metal coated PZT grooves filled with SU-8. Figure 6.28 shows an electrically isolated PZT stack structure by laser patterning.

6.3.2. Micromolding Approach

Figure 6.29 illustrates the fabrication process of PZT multilayer actuators. The 1mm-thick PZT plate used in this study is a commercialized high-d_{33} piezoelectric coefficient ceramic plate (PZT 855, APC International Ltd.). A proven fast and economical approach, dicing, is used to fabricate freestanding PZT fins. Because no high-temperature process is involved, there is no thermal stress or shrinkage as might be present in more traditional processes such as sol-gel process or sintering.

A 20 x 20 x 1mm PZT plate (Figure 6.29a) is mounted on a glass substrate using adhesive and diced into 150 micron-wide 'fins' with a spacing of 165 micron defined by the thickness of the diamond blade used (Figure 6.29b). The diced PZT plate is transferred to a second PDMS-coated glass slide and kept on the glass slide for the rest of process. SU-8 is then cast over the diced PZT plate. SU-8 pillars for electrical isolation

are formed between the fins in alternating gaps by photolithography (6.24c). The pillar-to-pillar separation distance is 3.5mm.

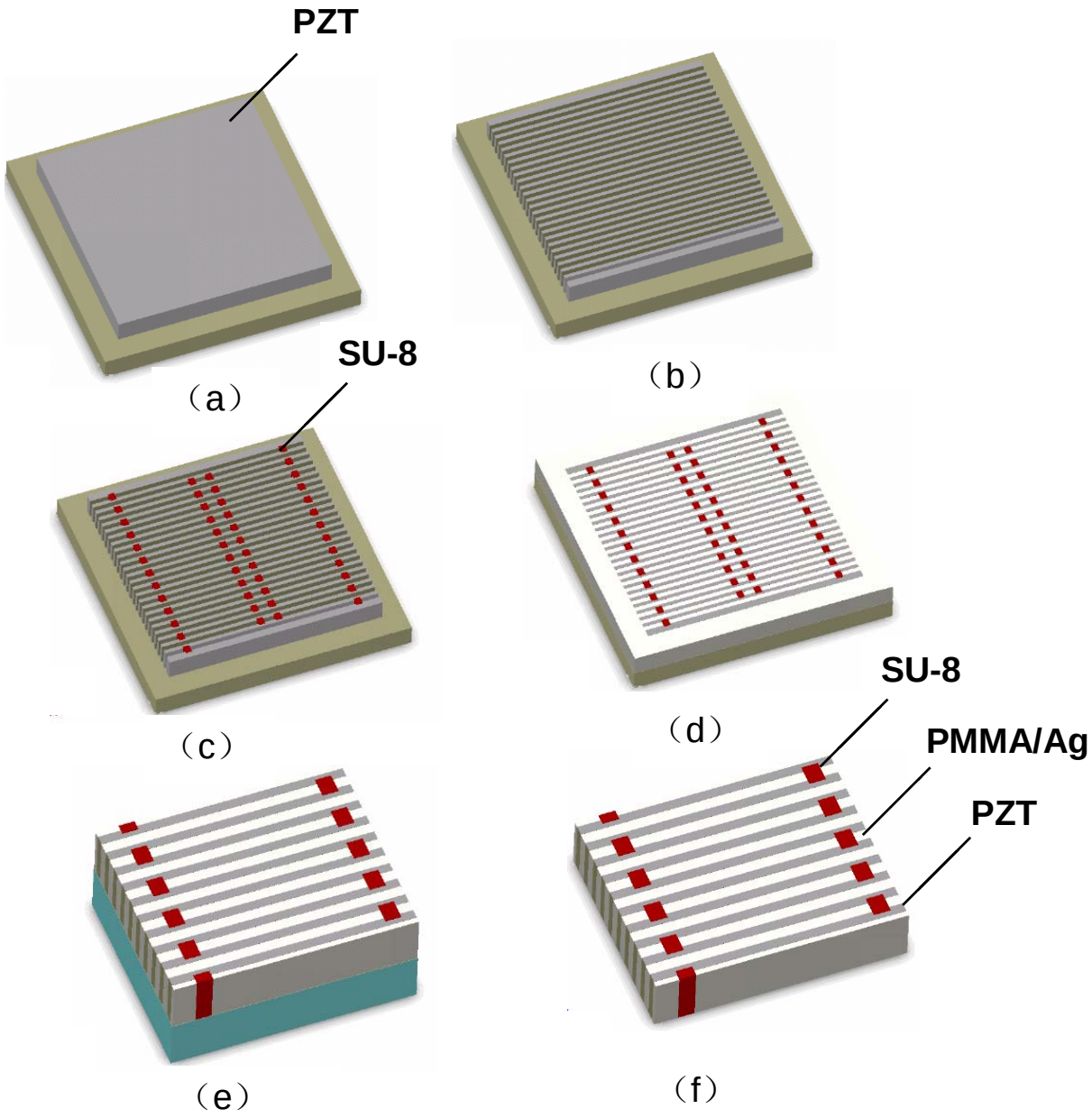

Figure 6.29 Fabrication process

A double-layer (50nm-thick titanium and 2 micron-thick copper) is deposited on the PZT structures as well as the SU-8 isolation pillars. The thickness of the copper layer on the sidewall ranges from approximately 100nm to 2 micron due to the non-uniform

coating of the sputtered metal in the deep trenches. A silver-PMMA (40 vol% Ag) ECPC blend is prepared and cast into the gaps between the PZT fins, and then vacuum-cured at 65ºC (Figure 6.29d).

After the excess polymer and metal on top of the PZT are polished away, the sample is diced into separate devices with any desired number of layers (Figure 6.29e). Multilayer devices, e.g., 10-layer devices with a dimension of 4 x 3 x 1mm, are then released from the substrate. Electrical leads are applied on both the left and right sidewalls. The devices are then poled by applying a 2 kV/mm electric field in the transverse direction of the layer (Figure 6.29f) at room temperature.

SEM micrographs of diced PZT fins with SU-8 pillars are shown in Figure 6.30. The top view shows the uniform cuts with a PZT width of 150 micron and a spacing of 165 micron. Viewed from an angle, the SU-8 connects are found to be well-leveled with the PZT fins, with a tolerance of approximately 2 % over the 1mm-tall SU-8 pillar.

The SU-8 pillars are tapered down from the top to the bottom as shown in Figure 6.30b. It is attributed in part to non-uniform SU-8 crosslinking over the high-aspect-ratio pillars (1:7) resulting from residual solvent gradient in the thick pillar and optical dose variation between the top and bottom portions. Because the optical exposure is from the top side, the top layer is overexposed and the bottom layer is underexposed, which causes the variation of the lateral dimensions of the developed SU-8 structures. The same situation applies to the back-side exposure as illustrated in Figure 6.31b. The resulting gaps between SU-8 and PZT are undesirable because they could lead to electrode shorting.

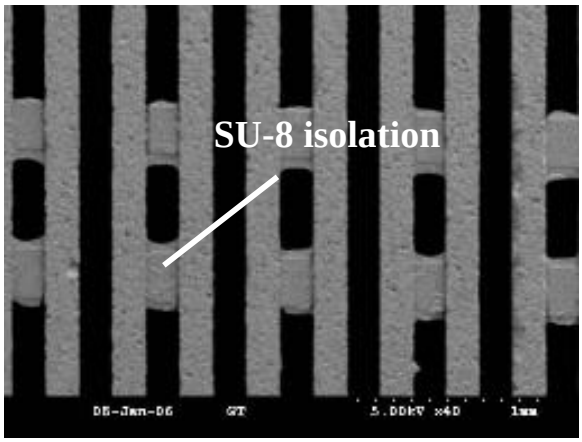

(a)

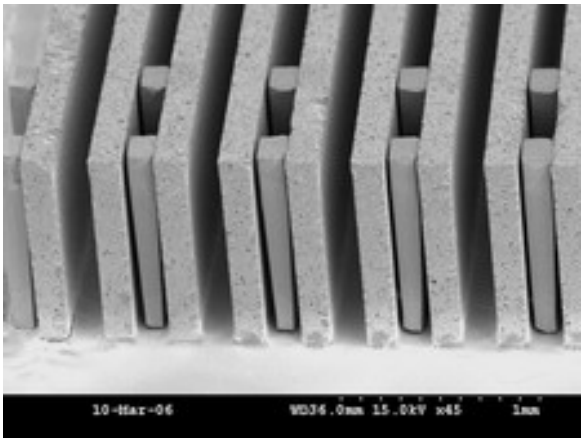

(b)

Figure 6.30 SEM images of diced PZT fins with SU-8 pillars for electrode isolation: (a) top view, (b) oblique view

To eliminate the undesired gaps, an improved method for photo-patterning SU-8 electrical isolation pillar structures is developed, which is back-side inclined exposure as shown in Figure 6.31c. Schematic view of this process is compared with those of front-side and back-side exposures shown in Figure 6.31. The back-side inclined exposure starts with deposition and patterning of a 50nm-thick titanium layer and a 200nm-thick copper layer on top of a glass substrate. The metal pre-patterning is utilized for pillar definition using back-side exposure.

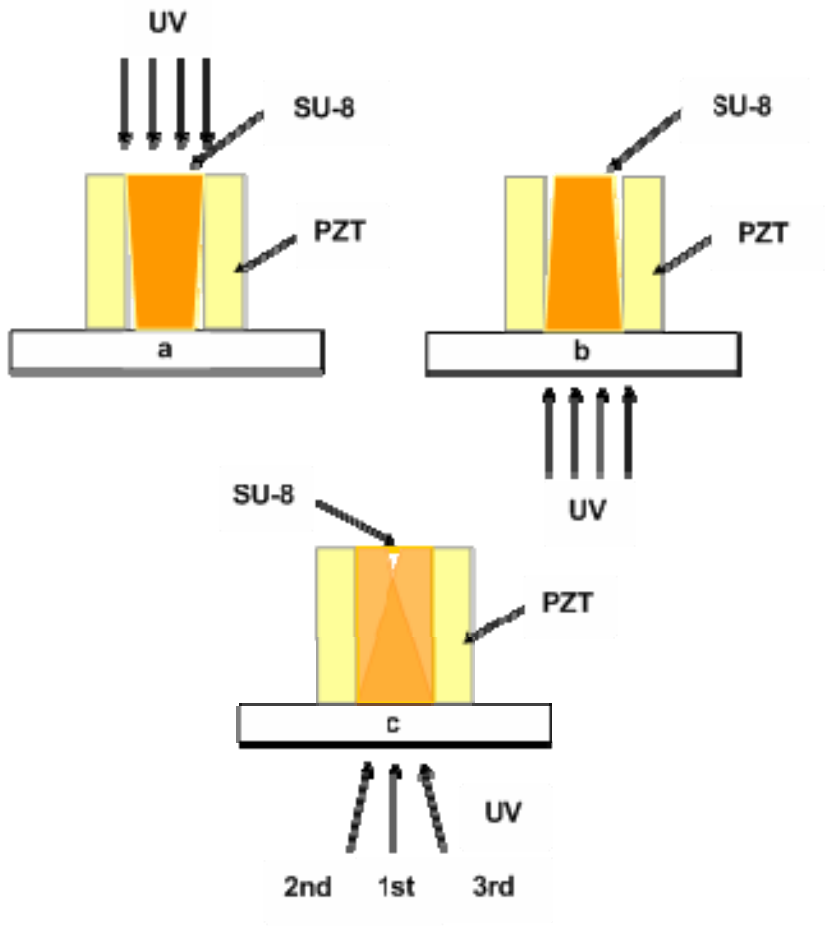

Figure 6.31 (a) Tapered SU-8 pillar formed by front-side exposure, (b) Tapered SU-8 pillar formed by back-side exposure, and (c) Back-side inclined exposure scheme for fabricating SU-8 isolation pillars with conformal contact

A layer of 20 micron-thick SU-8 2010 is spin-coated onto the metal pre-patterned substrate as an adhesive layer and baked at 65ºC for 5 min and then at 95ºC for 15 min on a hotplate. A PZT plate 20 x 20 x 1mm in size is mounted on the prebaked SU-8 layer, and baked at 150ºC for 6 hours to bond the two pieces together through thermally crosslinking SU-8. The PZT plate is diced into 150 micron wide 'fins' with a spacing of 165 microns in alignment with the pre-patterned substrate. This substrate is subsequently exposed from the back vertically (i.e. at an incident angle of 90º from the substrate), and then exposed at 95° and 85º incident angles. SEM micrographs of the diced PZT fins with SU-8 pillars formed by back-side inclined exposure are shown in Figure 6.32. The

magnified image in Figure 6.32 shows the desired conformal contact between the SU-8 pillars and the sidewall of the PZT layer.

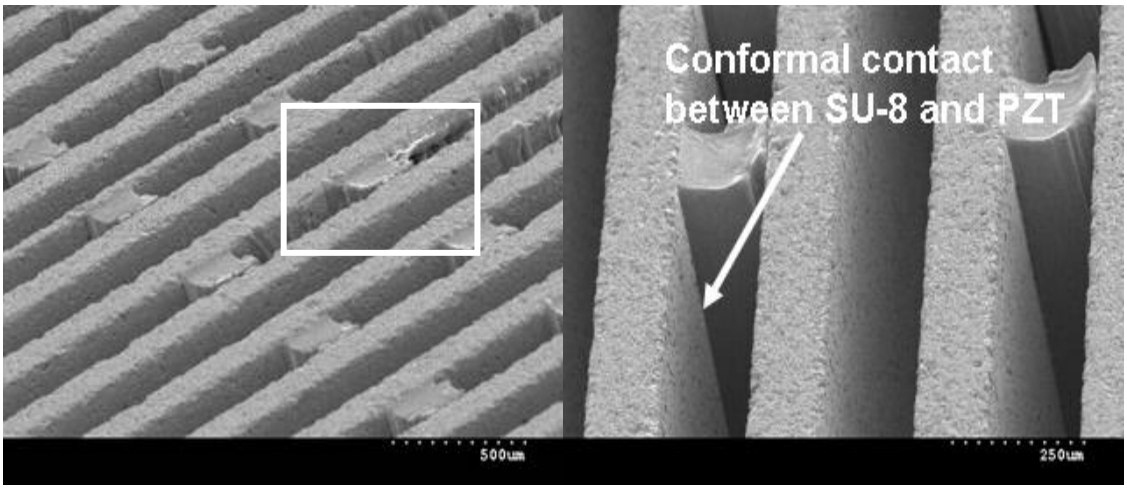

(a) (b)

Figure 6.32 (a) SEM images of diced PZT fins with SU-8 pillars formed by back-side inclined exposure, (b) Magnified image of two SU-8 pillars

6.4. Characterization

6.4.1. Single Layer

Before the testing of the multilayer piezoelectric actuators, the conductive polymer composite is first tested for its effectiveness as an electrode material for the PZT actuator. Thin slabs of PZT with a thickness of 150 micron and a lateral dimension of 20 mm x 1 mm are prepared. A silver-PMMA ECPC (40 vol% Ag) blend is applied on both sides of a single slab of PZT. For comparison purposes, PZT thin slabs with sputtered metal electrodes only and with ECPC electrodes on top of sputtered metal electrodes are prepared as well. The property of ferroelectric polarization versus electric field (*P-E*) of each type is measured at 0.1 Hz using a Sawyer-Tower circuit at room temperature. In all cases, the PZT slabs were poled at 90^{o} of the poling direction of this measurement.

Figure 6.33 shows the *P-E* hysteresis loops of a single PZT slab with different electrodes. For a desired remanent polarization value (*Pr*) of 0.25 C/m^2, the electric

fields required for ECPC-only, ECPC on sputtered metal, and sputtered metal-only electrodes are 3.7kV/mm, 2kV/mm, and 1.35kV/mm, respectively. The sputtered metal structures help reduce the required electric field and are favorable for low voltage applications. Accordingly, a sputtering step should be added before the molding the ECPC electrodes in the multilayer fabrication process.

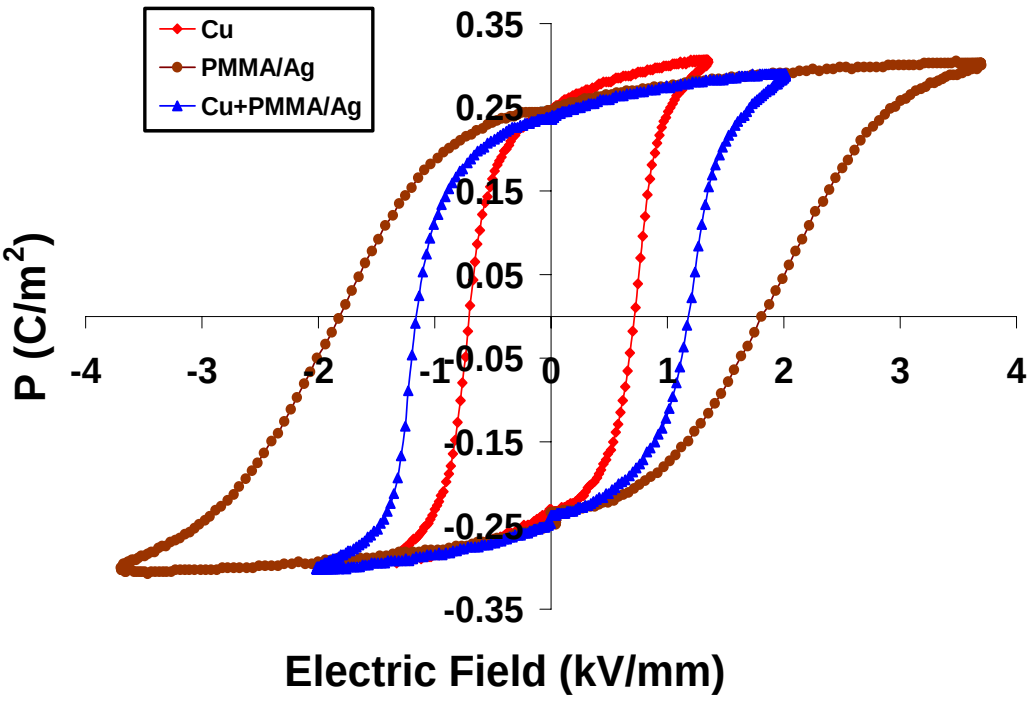

Figure 6.33 *P-E* hysteresis loop for a single PZT layer with three types of electrodes

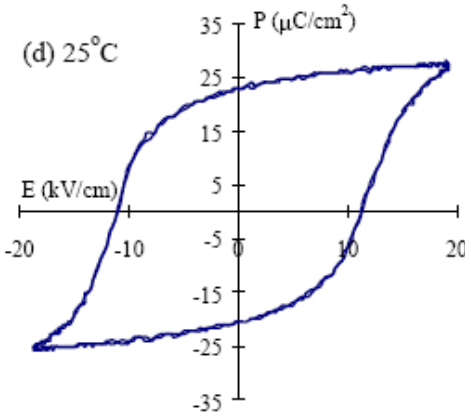

(a)

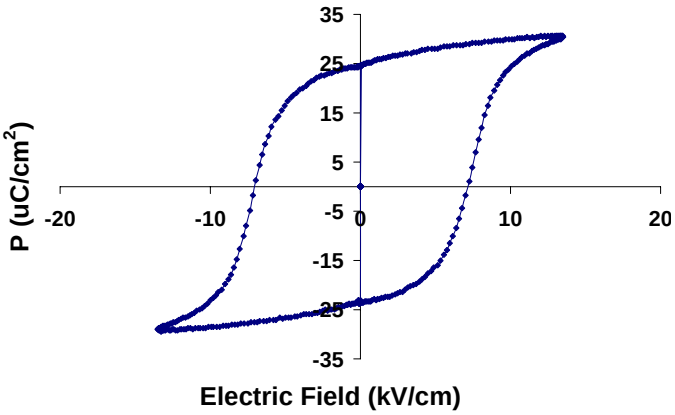

(b)

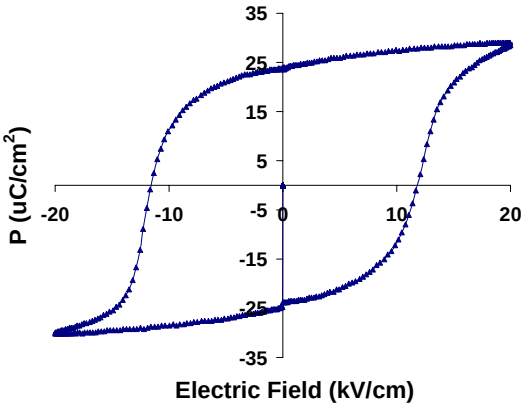

(c)

Figure 6.34 (a) Typical ferroelectric polarization versus electric field (*P-E*) properties of PZT-5H ceramics (b) *P-E* hysteresis loop for a single PZT layer with Cu electrodes (b) *P-E* hysteresis loop for a single PZT layer with Cu+PMMA/Ag electrodes

The *P-E* properties of two single PZT slabs with different electrodes are compared with typical *P-E* properties of the soft piezoelectric materials PZT-5H measured in an unpoled condition [121]. The two electrode used are Cu only electrode and Cu+PMMA/Ag electrode. From Figure 6.34, it can be seen that the coercive filed *Ec* of the PZT slab coated with Cu electrode is smaller than the literature value. This is due to more conformal coverage of sputtered Cu than that of the silver paste painted on the reference PZT material. The *P-E* properties of the PZT slab with Cu+PMMA/Ag are similar to the literature value.

6.4.2. Stack Actuator

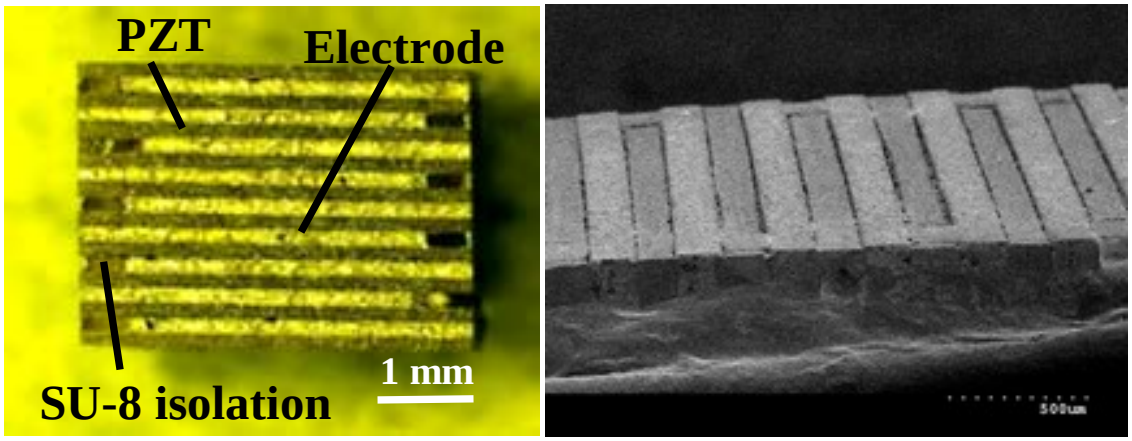

(a) (b)

Figure 6.35 (a) Optical microscopy image of a 10-layer PZT actuator with conductive polymer electrode, (b) SEM image of an 8-layer PZT actuator (Note a probe wire has been attached)

Laterally-stacked actuators with 8 and 10 layers have been successfully fabricated. Figure 6.35a and Figure 6.35b show a 10-layer and a part of an 8-layer stack actuator, respectively. Figure 6.36 shows the *P-E* hysteresis loops of a single PZT slab and that of an 8-layer actuator with the same type of electrodes.

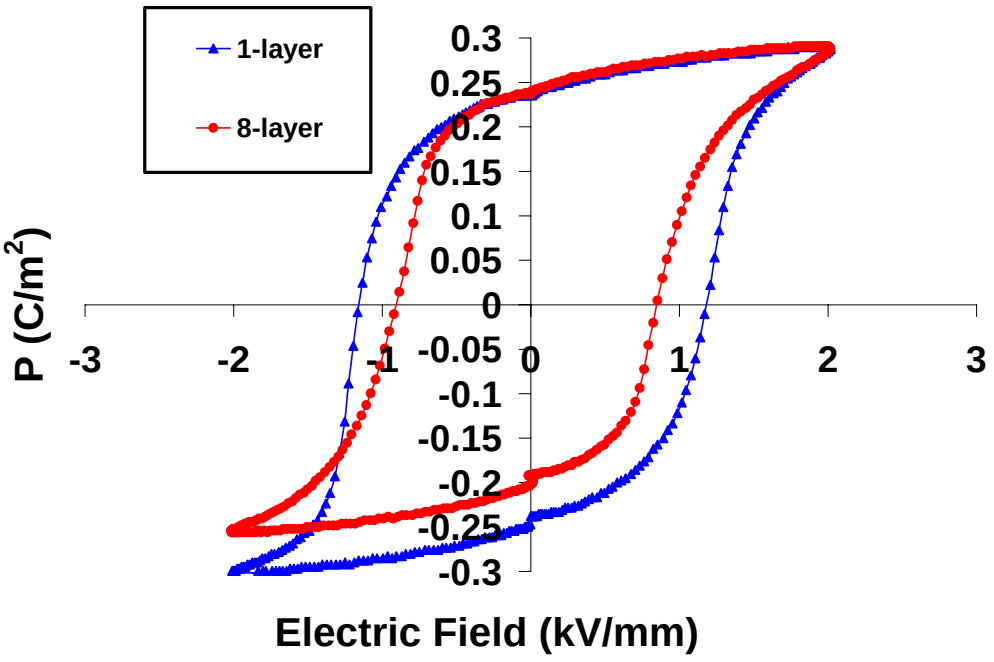

Figure 6.36 *P-E* hysteresis loops for a single PZT layer and an 8-layer actuator

As shown in Figure 6.36, the multilayer PZT actuator has a hysteresis loop similar in shape to that of a single layer structure, with the former having a lower coercive field value (0.84 kV/mm) than the latter (1.17 kV/mm), which indicates better polymer electrode coverage on the sidewall of the multilayer actuator. The multilayer PZT actuator also exhibits a slightly asymmetric hysteresis behavior.

6.4.3. Displacement Verification

To verify the effectiveness of the fabrication process and the performance of the PZT stack actuator, the top layer displacement of the actuator is measured as a function of the electric field applied and compared with the results from FEM. Experimental results for actuator displacement are measured using a laser displacement sensor (LK-G32, Kenyence Co.) under quasistatic conditions (0.5Hz). The simulation result for an 8-layer actuator at a driving voltage of 100V is 0.505 micron (Figure 6.37).

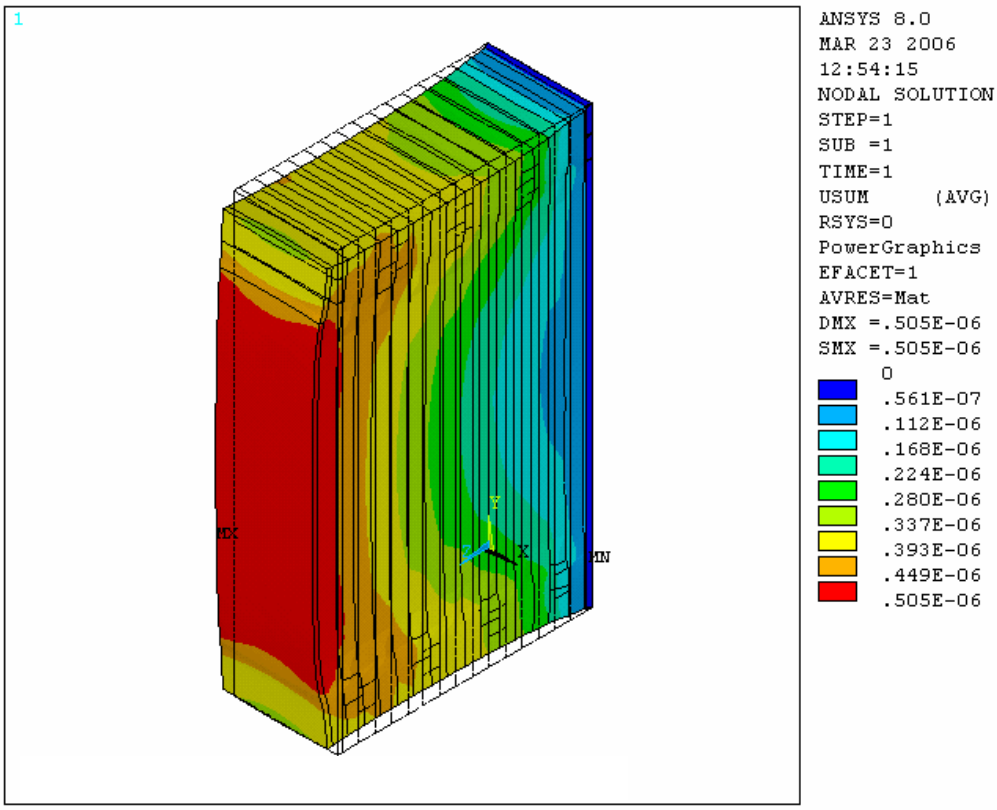

Figure 6.37 FEM simulation result for an 8-layer actuator at a driving voltage of 100V

Figure 6.38 compares the FEM results and experimental results of the displacement of the 8-layer actuator as a function of electric field. The experimental results for displacement exhibit obvious linearity and agree reasonably well with the simulation results. The discrepancy may have resulted from the difference between the d_{33} value used in the simulation, which was a manufacturer-specified d_{33} value of 630×10^{-12} m/V, in contrast to the calculated d_{33} value of the PZT layer after repoling the PZT in a transverse direction from the original polarization, which was 787×10^{-12} m/V.

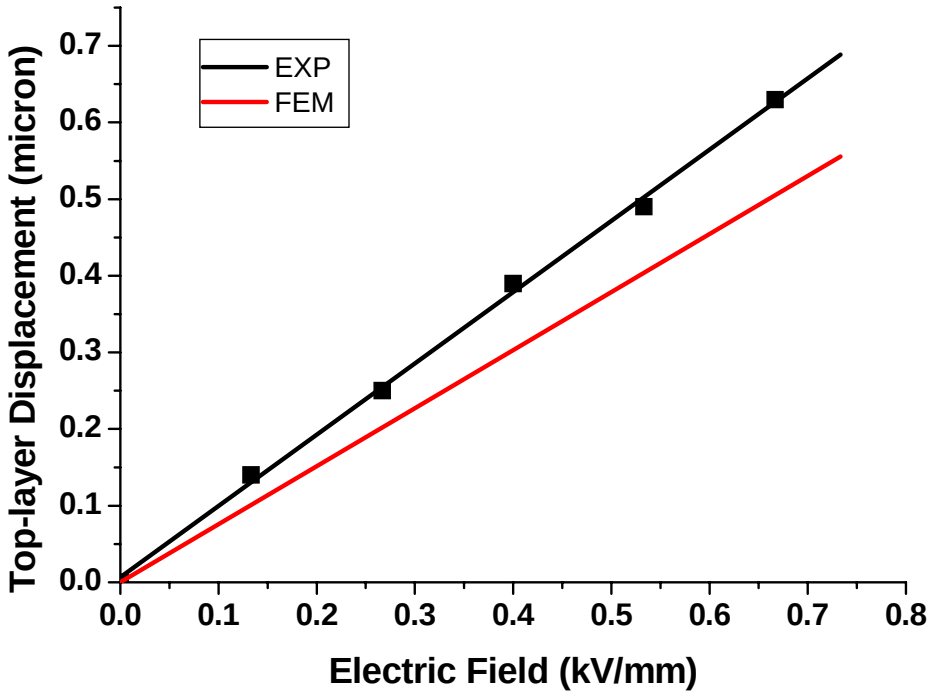

Figure 6.38 Top layer displacement of an 8-layer actuator as a function of applied electric field (maximum field of 0.66 kV/mm achieved at a voltage of 100V)

6.5. Conclusion

In order to reduce the cost of the microvalve, a laterally-stacked PZT actuator has been proposed as a replacement for the PZT stack actuator used in the microvalve. The research on the stack actuator was carried out through a series of modeling, design, fabrication, assembly and experimental testing tasks. Finite element model was developed to characterize the effect of different electrode materials on the performance of the actuator. Stack actuators were fabricated using diced PZT multilayer, high aspect ratio SU-8 photolithography, and molding of electrically conductive polymer composite electrodes. This fabrication process is simple and straightforward compared to previous lateral lamination approaches. An 8-layer device has shown a displacement of 0.63 micron at 100V driving voltage, which agrees reasonably well with simulation results. The experimental results indicate that the fabrication process of lateral lamination

provides an effective alternative for making compact, low-voltage multilayer piezoelectric micro-actuators.

CHAPTER 7

CONCLUSION AND FUTURE WORK

7.1. Thesis Summary

The objective of the proposed research is to (1) develop two crucial elements, a polymer pneumatic microactuator array and complementary microvalve array, of a mass producible, low cost tactile display using polymer micromachining processes combined with other MEMS technologies; and (2) to realize a tactile display prototype in a form of refreshable Braille display cell with a 2x3 microactuator array and microvalve array.

The literature survey compares current technologies for tactile display and shows the feasibility of using pneumatic microactuator and microvalve array for constructing a practical tactile display. Various MEMS actuation and fabrication technologies for microvalve are reviewed, and piezoelectric microvalve has been confirmed as the optimal candidate.

The first part of the research work is the design, modeling, fabrication and characterization a polymer pneumatic microactuator array as the actuation scheme for the tactile display system. A pneumatically-driven, kinematically-stabilized endoskeletal mcirobubble actuator has been proposed. The mass-manufacturable actuator has been fabricated using the approaches of lithography and micromolding. The skeletal corrugated sections have been fabricated using continuous rotating inclined exposure. Both of the number of corrugations and the corrugation profile of the endoskeletal actuator are determined through numerical analysis, taking into account the constraints of the microfabrication processes utilized. A prototype of a single endoskeletal bubble actuator with a diameter of 2.6mm has been fabricated and characterized. For comparison purposes, elastomer microcorrugated diaphragm (skin-only) actuators and parylene microcorrugated diaphragm (skeleton-only) actuators of the same materials and

dimensions have also been fabricated and tested. While skin-only diaphragm actuators demonstrated undesired omni-directional inflation and skeleton-only diaphragm actuators have shown unstable and irreversible deformation during extension, the proposed endoskeletal microbubble actuators have shown stable reversible axial extensions with a deflection of approximately 0.9mm. A 6x6 array of endoskeletal polymer microbubble actuators integrated with a microfluidic manifold has been successfully fabricated, demonstrating its mass-manufacturability. The endoskeletal bubble actuator has demonstrated stable, directional deflection as a function of applied pressure, and the experimental deflection results show good agreement with those of a finite-element analysis.

The second part or the research extends the first part to a refreshable Braille display system as a prototype of a tactile display. First, the endoskeletal microbubble actuator is optimized and miniaturized. The actuator is able to provide both a static display (which meets the displacement and force requirement of a Braille display) function and vibratory tactile sensations. Second, a fully functional pneumatic RBD cell is obtained by a batch-fabricated and integrated 2x3 microactuator array and a 2x3 microvalve array. The displacement of the Braille dot is 0.56 mm and the generated force is 66 mN at 100 kPa applied pressure, respectively. The device has a maximum operating frequency of 200 Hz, suggesting potential uses not only as a Braille display but also for vibratory tactile applications, shape exploration, texture recognition, and other contact sensation-driven applications. Along with the Braille display capabilities the device was designed to meet the criteria of lightness and compactness permitting portable application. The design is scalable with respect to the number of dots while still being simple to fabricate.

The third part of the research focuses on the design, fabrication and assembly a piezoelectrically-driven microvalve for the control of large pressure fluid flows needed for pneumatic microbubble actuators. The microvalve is based on PZT stack actuator and

solid-hydraulic amplification mechanism. The microvalve is normally open, and is fabricated and assembled primarily with stereolithographically-fabricated polymer components. An incompressible elastomer is used as a solid hydraulic medium to convert the small axial displacement of a piezoelectric actuator into a large valve head stroke while maintaining a large blocking force. Also, the axial design of the microvalve enables densely-packed valve arrays. One application of this microvalve is in pneumatic tactile displays, some of which require operation against gas pressures up to approximately 90kPa and switching speeds between 1-200Hz. The current valve design has a maximum static hydraulic amplification ratio of 5 at 30V driving voltage and a maximum valve head stroke of 37μm at 150V. Under a 94.4kPa differential pressure, the flow rate of the valve and the closing voltage measure 785mL/min and 150V, respectively. The proposed mechanism has been verified by the experiment data of the amplified deflection of the valve head. In addition, the function of the microvalve as an on-off switch for a pneumatic microbubble tactile actuator is demonstrated. Other applications of the microvalve are proposed and discussed. The design of a 2x3 microvalve configuration is proposed in the end.

The last part of the research is to develop a new fabrication scheme for a PZT stack microactuator as the driving element for the microvalve in tactile display system. FEM is carried out, which proved a number of things about the piezoelectric actuator. First, it proved that the behavior of a piezoelectric actuator is predictable, as long as the geometry is selected such that the non-ideal effects (such as dead PZT ends) do not dominate. Second, it verified the correct operation of the cymbal transformers and pointed out likely pitfalls of the approach. Such pitfalls include the relatively high stress seen at the cymbal/PZT interface as well as the locations of maximum stress on the cymbal material (a concern for managing the electroplating process). Third, it confirmed the suspicion that a stiffer (yet more conventional) electrode material like copper will significantly hinder the device's operation. After modeling, a simple lateral lamination

scheme for the fabrication of multilayer piezoelectric actuators is proposed. The fabrication scheme consists of the dicing of a high-d_{33} piezoelectric coefficient lead zirconate titanate (PZT) material, the photolithographic high-aspect-ratio SU-8 definition of electrical isolation, and the micromolding of conductive polymer electrodes. Backside and inclined UV exposure has been exploited to secure the 1mm-thick SU-8 pillar definition of internal electrodes and to prevent the formation of a tapered SU-8 pillar shape that allows electrical short paths. An electrically conductive polymer composite (ECPC, silver-PMMA: 40 vol% Ag) has been utilized for making moldable electrodes. An 8-layer device is successfully fabricated and tested. A displacement of 0.63 micron is achieved at 100V driving voltage, which agrees well with finite element simulation results.

7.2. Thesis Contribution

The contribution of this thesis can be summarized as follows:

1. New Concept and Theoretical Analysis

The development of high-performance diaphragm structure is of critical importance in many microdevices. The kinematically stabilized endoskeletal microbubble concept smartly combines the stability and large deflection of corrugated diaphragm and the hyper elasticity of the elastomer material. As a result, the actuator provides both large force and large reversible deflection. Past analysis on corrugated diaphragms are based on existing diaphragm deflection theory, which lacks the flexibility in dealing with different corrugation profiles. Also, there is no general load-deflection expression for a flat-corrugated composite diaphragm that best describes the endoskeletal microbubble actuator. In this thesis, a finite element analysis approach was developed to explore the effect of various corrugation profiles and diaphragm thickness, which had not been well understood. Conclusion have been drawn from the analysis regarding the

general load-deflection characteristics, the effects of diaphragm profile, and the number and thickness on two different corrugated diaphragms and one composite diaphragm.

This thesis presents an alternative hydraulic amplification mechanism to the MEMS community. As discussed in chapter 5, the elastomer hydraulic system offers similar benefits as liquid in terms of amplification while circumventing the sealing problem. Although the hydraulic amplification is implemented with piezoelectric actuation and the application focused on was microvalve, the mechanism can likely the mechanism can apply to other actuation system and form other microdevices with large stroke, force and bandwidth.

2. MEMS Fabrication Technology Development

It was demonstrated that complex corrugated diaphragms with vertical corrugation and side wall corrugation can be fabricated by using inclined rotational lithography through a single step. The principle can be used in fabricating other complex 3-D microstructures.

Various micromolding technologies have been developed with non-typical material such as water soluble polymer, photoresist, and conductive polymer composite that can be transformed to other MEMS fabrication.

This work proposes and verifies that stereolithographically fabrication in mm scale can be a fast and simple way to prototyping MEMS devices. The precision of dimension and the surface planarization can be controlled very well.

This thesis presents an alternative lateral lamination scheme for fabricated multilayer PZT ceramic structure. The problem of deep trench UV-lithography uniformity was solved. The same approach can be used in fabricating multilayer devices with other ceramics or other materials.

3. Material Study

A finite element analysis on the polymer materials used in the microbubble actuator and the solid-hydraulic mirovalve was performed. The feasibility of using the Mooney-Rivlin constants obtained from uniaxial tensile test data was verified for modeling elastomer material. For the parylene diaphragm, the modeling tools developed enable accurate monitoring of real-time membrane stress level at all location along the membrane for all potential pressure loading scenarios experienced by the microdevices. Most importantly, the results established that complex diaphragm microstructures made of non-traditional MEMS materials can be accurately and rapidly simulated using available tools, allowing design optimization for a given set of application requirements.

4. Prototype Development

The second part of the research extends from the first part to a refreshable Braille display system as a prototype of a tactile display. First, the endoskeletal microbubble actuator is optimized and miniaturized. The actuator is able to provide both a static display (which meets the displacement and force requirement of a Braille display) function and vibratory tactile sensations. Second, a fully functional pneumatic RBD cell is obtained by a batch fabricated and integrated 2x3 microactuator array and a 2x3 microvalve array. The displacement of the Braille dot is 0.56 mm and the generated force is 66 mN at 100 kPa applied pressure, respectively. The device has a maximum operating frequency of 200 Hz, suggesting potential uses not only as a Braille display but also for vibratory tactile applications, shape exploration, texture recognition, and other contact sensation-driven applications.

7.3. Suggestions for Future Work

Based on the results presented in this thesis, a number of issues and areas which require further development and investigation have been identified.

One major set of obvious future works are related to device modifications. Based on the current results, it is clear that a solid-hydraulically amplified piezoelectrically-driven microvalve can be designed, built and successfully operate to regulate gas flows and control pneumatic tactile actuator. The valve design that has been experimentally characterized in this thesis, however, fell short of achieving its original goal of being batch fabricatable and being miniaturized. While the latter can be achieved with a redesign effort, the former likely require significantly more effort in the future. As one potential solution, micro injection molding technology will be investigated and adopted for the low cost mass-manufacturability of the microvalve.

Another set of interesting device modification issues originate from the tradeoff between PZT layer thickness and power consumption and the tradeoff between electrode thickness and fabrication complication. Because thinner PZT layers entail more cuts with the dicing saw and thus less piezoelectrically active material, fewer cuts (and thicker PZT layers) would be preferable. However, thinner PZT layers allow lower driving voltage. While the tradeoff-related issues can be investigated using the already developed and highly parameterized FE model, the fabrication-related issue brought a major fabrication optimization challenge that need to be experimentally explored.

The second set of future work is the further evaluation on the devices. Further characterization of the dynamic flow regulating capability of the microvalve and the stress limit of the endoskeletal microbubble actuator would be interesting. Future work could also include basic psychophysics experiments to evaluate the Braille cell performance in Braille reading, user shape recognition and other tactile perception.

This thesis work can be further extended to realize a true 3-D shape generation system such as the “Digital Clay”, which has been described previously as a physical volume bounded by a deformable kinematics structure that acts as the haptic interface. Ultimately, large arrays of the microbubble actuators could be built on flexible substrates and could be stacked to from multiple layers of microbubble actuators, each of which has

its pneumatic controlling microvalve. The stacked multilayer of microbubble actuators could control the kinematic structure to recreate the surface topography of the shape inputted as a CAD file, or modify the kinematic structure and the volume underneath the surface from a preexisting file.

REFERENCES

[1] D. G. Caldwell, N. Tsagarakis, and C. Giesler, “Integrated tactile/shear feedback array for stimulation of finger mechanoreceptor,” *Proceedings - IEEE International Conference on Robotics and Automation,* vol. 1, pp. 287-292, 1999.

[2] S. A. Wall, and S. Brewster, “Sensory substitution using tactile pin arrays: Human factors, technology and applications,” *Signal Processing,* vol. 86, no. 12, pp. 3674-3695, 2006.

[3] F. Vidal-Verdu, and M. Hafez, “Graphical Tactile Displays for Visually-Impaired People,” *Neural Systems and Rehabilitation Engineering, IEEE Transactions on [see also IEEE Trans. on Rehabilitation Engineering],* vol. 15, no. 1, pp. 119-130, 2007.

[4] M. Benali-Khoudja, M. Hafez, J. M. Alexandre *et al.*, "Tactile interfaces: a state-of-the-art survey," *35 th. Int. Symposium on Robotics.* pp. 721-726.

[5] J. S. Lee, and S. Lucyszyn, “A Micromachined Refreshable Braille Cell,” *Microelectromechanical Systems, Journal of,* vol. 14, no. 4, pp. 673-682, 2005.

[6] Online. http://www.synapseadaptive.com/blazie/powerbraille_80.htm, Aug. 2007

[7] Online Resource. http://www.acm.org/sigs/conferences/assets00/Presentations/Roberts_files/frame.htm, Aug. 2007

[8] H. Zhu, and W. Book, "Practical Structure Design and Control for Digital Clay," *Proceedings of the ASME Dynamics and Control Division.* pp. 1051-1055.

[9] H. Zhu, “Practical structural design and control for digital clay,” Georgia Institute of Technology, 2005.

[10] R. J. Stone, “Haptic feedback: A potted history, from telepresence to virtual reality,” *The First International Workshop on Haptic Human-Computer Interaction*, pp. 1-7, 2000.

[11] E. Igarashi, K. Sato, and M. Kimura, "Development of a Tactile Feedback Device Used a Pneumatic Balloon Actuator," *Proc. of the Second International Symposium on Measurement and Control in Robotics, ISMCR.* pp. 15-19.

[12] C. Youngblut, and A. Institute for Defense, "Review of Virtual Environment Interface Technology," Institute for Defense Analyses, 1996.

[13] M. Konyo, and S. Todokoro, “Artificial Tactile Feel Display Using EAP Actuator,” *Worldwide ElectroActive Polymers, Artificial Muscles, Newsletter,* vol. 2, no. 1, 2000.

[14] C. R. Wagner, S. J. Lederman, and R. D. Howe, "A tactile shape display using RC servomotors," *Haptic Interfaces for Virtual Environment and Teleoperator Systems, 2002. HAPTICS 2002. Proceedings. 10th Symposium on.* pp. 354-355.

[15] S. Ino, S. Shimizu, T. Odagawa *et al.*, "A tactile display for presenting quality of materials by changing the temperature of skin surface," *Robot and Human Communication, 1993. Proceedings., 2nd IEEE International Workshop on.* pp. 220-224.

[16] H. Z. Tan, and A. Pentland, “Tactual displays for wearable computing,” *Personal Technologies,* vol. 1, no. 4, pp. 225-230, 1997.

[17] M. Benali-Khoudja, M. Hafez, J. M. Alexandre *et al.*, "VITAL: a new low-cost vibro-tactile display system," *Robotics and Automation, 2004. Proceedings. ICRA '04. 2004 IEEE International Conference on.* pp. 721-726 Vol.1.

[18] Ipsos-Insight. "Current and Next Generation Game Console Feature Study," Jan,08, 2008; http://www.immersion.com/gaming/docs/Ipsos_video_console_survey.pdf.

[19] S. Thayer, “8. Social touching,” *Tactual Perception: A Sourcebook*, 1982.

[20] K. Y. Hung, H. T. Hu, and F. G. Tseng, “Application of 3-D glycerol-compensated inclined-exposure technology to an integrated optical pick-up head,” *Journal of Micromechanics and Microengineering,* vol. 14, no. 7, pp. 975-983, 2004.

[21] Y.-K. Yoon, J.-H. Park, and M. G. Allen, “Multidirectional UV lithography for complex 3-D MEMS structures,” *Journal of Microelectromechanical Systems,* vol. 15, no. 5, pp. 1121-30, 2006.

[22] G. Yuan, X. Wu, Wu, Y.-K. Yoon *et al.*, "Kinematically-stabilized microbubble actuator arrays," *18th IEEE International Conference on Micro Electro Mechanical Systems (IEEE Cat. No.05CH37610).* pp. 411-414.

[23] M. A. Fonseca, J. M. English, M. von Arx *et al.*, “Wireless micromachined ceramic pressure sensor for high-temperature applications,” *Microelectromechanical Systems, Journal of,* vol. 11, no. 4, pp. 337-343, 2002.

[24] S. Maruo, K. Ikuta, and T. Ninagawa, “Multi-polymer microstereolithography for hybrid opto-MEMS,” *Micro Electro Mechanical Systems, 2001. MEMS 2001. The 14th IEEE International Conference on*, pp. 151-154, 2001.

[25] R. D. Chien, “Micromolding of biochip devices designed with microchannels,” *Sensors & Actuators: A. Physical,* vol. 128, no. 2, pp. 238-247, 2006.

[26] Y. Li, M. Sasaki, and K. Hane, “Fabrication and testing of solid polymer dye microcavity lasers based on PMMA micromolding,” *Journal of Micromechanics and Microengineering,* vol. 11, no. 3, pp. 234-238, 2001.

[27] Y. Xia, and G. M. Whitesides, “Soft lithography,” *Angew. Chem. Int. Ed,* vol. 37, no. 5, pp. 550-575, 1998.

[28] H. Becker, and U. Heim, “Hot embossing as a method for the fabrication of polymer high aspect ratio structures,” *Sensors & Actuators: A. Physical,* vol. 83, no. 1-3, pp. 130-135, 2000.

[29] A. Bowles, A. Rahman, T. Jarman *et al.*, "A new technology for high density actuator arrays," *Smart Structures and Materials 2005: Smart Structures and Integrated Systems.* pp. 680-689.

[30] M. Benali-Khoudja, M. Hafez, J. M. Alexandre *et al.*, “Electromagnetically driven high-density tactile interface based on a multi-layer approach,” *Micromechatronics and Human Science, 2003. MHS 2003. Proceedings of 2003 International Symposium on*, pp. 147-152, 2003.

[31] S. F. Frisken-Gibson, P. Bach-y-Rita, W. J. Tompkins *et al.*, “A 64-Solenoid, Four-Level Fingertip Search Display for the Blind,” *Biomedical Engineering, IEEE Transactions on,* vol. BME-34, no. 12, pp. 963-965, 1987.

[32] T. Fukuda, H. Morita, F. Arai *et al.*, “Micro resonator for a tactile display,” *Advanced robotics,* vol. 12, no. 2, pp. 135-153, 1998.

[33] P. Kammermeier, M. Buss, and G. Schmidt, "Dynamic display of distributed tactile shape information by a prototypical actuator array." pp. 1119-1124 vol.2.

[34] Y. Ikei, K. Wakamatsu, and S. Fukuda, “Vibratory tactile display of image-based textures,” *Computer Graphics and Applications, IEEE,* vol. 17, no. 6, pp. 53-61, 1997.

[35] Internet Resource. http://www.kgs-america.com/product_at.html, May 2006

[36] P. C. Haugen, *Memory wire braille tactile system*, USA,to US Patent, 2000.

[37] R. D. Howe, D. A. Kontarinis, and W. J. Peine, "Shape memory alloy actuator controller design for tactile displays." pp. 3540-3544 vol.4.

[38] P. M. Taylor, A. Moser, and A. Creed, "A sixty-four element tactile display using shape memory alloy wires," *Displays,* vol. 18, no. 3, pp. 163-168, 1998.

[39] R. Velazquez, E. Pissaloux, M. Hafez *et al.*, "A low-cost highly-portable tactile display based on shape memory alloy micro-actuators," *2005 IEEE International Conference on Virtual Environments, Human-Computer Interfaces and Measurement Systems (IEEE Cat. No.05EX1045C).* p. 6 pp.

[40] P. S. Wellman, W. J. Peine, G. Favalora *et al.*, "Mechanical design and control of a high-bandwidth shape memory alloy tactile display," *Experimental Robotics V. The Fifth International Symposium.* pp. 56-66.

[41] Y. Makino, N. Asamura, and H. Shinoda, "A cutaneous feeling display using suction pressure," *SICE 2003 Annual Conference (IEEE Cat. No.03TH8734).* pp. 2931-4.

[42] G. Moy, C. Wagner, and R. S. Fearing, "A compliant tactile display for teletaction," *Proceedings 2000 ICRA. Millennium Conference. IEEE International Conference on Robotics and Automation. Symposia Proceedings (Cat. No.00CH37065).* pp. 3409-15.

[43] P. M. Taylor, D. M. Pollet, A. Hosseini-Sianaki *et al.*, "Advances in an electrorheological fluid based tactile array," *Displays,* vol. 18, no. 3, pp. 135-41, 1998.

[44] A. Bicchi, E. P. Scilingo, N. Sgambelluri *et al.*, "Haptic interfaces based on magnetorheological fluids," *Proceedings 2th International Conference Eurohaptics 2002*, pp. 6-11.

[45] F. Vidal-Verdú, and R. Navas-González, "A Thermopneumatic Approach for Tactile Displays." pp. 395-399.

[46] M. Jungmann, and H. F. Schlaak, "Electrostatic Actuators with Elastic Dielectric for Use on Tactile Displays," *Proceedings of the 8 thInternational Conference on New Actuators: Actuator.* pp. 391-394.

[47] S. Lee, J. Kwangmok, K. Jachoon *et al.*, "Braille display device using soft actuator," *Proc. SPIE - Int. Soc. Opt. Eng. (USA).* pp. 368-79.

[48] T. Nara, M. Takasaki, T. Maeda *et al.*, "Surface Acoustic Wave (SAW) tactile display based on properties of mechanoreceptors," *Proceedings IEEE Virtual Reality 2001.* pp. 13-20.

[49] Y. Kato, T. Sekitani, M. Takamiya *et al.*, "Sheet-type braille displays by integrating organic field-effect transistors and polymeric actuators," *IEEE Transactions on Electron Devices,* vol. 54, no. 2, pp. 202-9, 2007.

[50] S. Ukai, T. Imamura, M. Shikida *et al.*, "Bubble Driven Arrayed Actuator Device for a Tactile Display," *Solid-State Sensors, Actuators and Microsystems Conference, 2007. TRANSDUCERS 2007. International*, pp. 2171-2174, 2007.

[51] L. Yobas, D. M. Durand, G. G. Skebe *et al.*, "A novel integrable microvalve for refreshable Braille display system," *Microelectromechanical Systems, Journal of,* vol. 12, no. 3, pp. 252-263, 2003.

[52] F. Kawai, P. Cusin, and S. Konishi, "Thin flexible end-effector using pneumatic balloon actuator," *Micro Electro Mechanical Systems, 2000. MEMS 2000. The Thirteenth Annual International Conference on.* pp. 391-396.

[53] C. Grosjean, G. B. Lee, W. Hong *et al.*, "Micro balloon actuators for aerodynamic control," *Micro Electro Mechanical Systems, 1998. MEMS 98. Proceedings., The Eleventh Annual International Workshop on.* pp. 166-171.

[54] M. Yoda, and S. Konishi, "Acoustic impedance control through structural tuning by pneumatic balloon actuators," *Micro Electro Mechanical Systems, 2001. MEMS 2001. The 14th IEEE International Conference on.* pp. 244-247.

[55] O. C. Jeong, and S. Konishi, "All PDMS pneumatic microfinger with bidirectional motion and its application," *Journal of Microelectromechanical Systems,* vol. 15, no. 4, pp. 896-903, 2006.

[56] I. Müller, and P. P. Strehlow, *Rubber and Rubber Balloons: Paradigms of Thermodynamics*: Springer, 2004.

[57] H.-W. Kang, D.-W. Cho, and I. H. Lee, "Development of a micro-bellows actuator using micro-stereolithography technology," *Microelectronic Engineering,* vol. 83, no. 4-9, pp. 1201-4, 2006.

[58] X. Yang, Y.-C. Tai, and C.-M. Ho, "Micro bellow actuators," *Tranducers 97. 1997 International Conference on Solid-State Sensors and Actuators. Digest of Technical Papers (Cat. No.97TH8267).* pp. 45-48.

[59] K. H. Kim, H. Yoon, O. C. Jeong *et al.*, “Fabrication and test of a micro electromagnetic actuator,” *Sensors and Actuators A (Physical),* vol. 117, no. 1, pp. 8-16, 2005.

[60] R. Luharuka, N. Hongseok, K. Sang Kyung *et al.*, “Improved manufacturability and characterization of a corrugated parylene diaphragm pressure transducer,” *Journal of Micromechanics and Microengineering,* vol. 16, no. 8, pp. 1468-74, 2006.

[61] J. Mueller, *Micropropulsion for Small Spacecraft,Progress in Astronautics and Aeronautics,* , p.^pp. 455: edited by Micci,M. and Ketsdever, A., AIAA , Reston, VA, 2000, , 2000.

[62] P. W. Barth, "Silicon microvalves for gas flow control," *8th International Conference on Solid-State Sensors and Actuators and Eurosensors IX. Digest of Technical Papers (IEEE Cat. No.95TH8173).* pp. 276-9.

[63] M. J. Zdeblick, R. Anderson, J. Jankowski *et al.*, "Thermopneumatically actuated microvalves and integrated electro-fluidic circuits," *Technical Digest. Solid-State Sensor and Actuator Workshop.* pp. 251-5.

[64] C. A. Ray, C. L. Sloan, A. D. Johnson *et al.*, "A silicon-based shape memory alloy microvalve," *Smart Materials Fabrication and Materials for Micro-Electro-Mechanical Systems.* pp. 161-6.

[65] A. D. Johnson, and M. D. Bokaie, “Valves for instrumentation and propulsion systems in microspacecraft,” *Advanced Space Propulsion Workshop, 9 th, Proceedings*, pp. 343-353, 1998.

[66] T. Ohnstein, T. Fukiura, J. Ridley *et al.*, “Micromachined silicon microvalve,” *Micro Electro Mechanical Systems, 1990.'Proceedings, An Investigation of Micro Structures, Sensors, Actuators, Machines and Robots'., IEEE*, pp. 95-98, 1990.

[67] F. Pourahmadi, L. Christel, K. Petersen *et al.*, “Variable-flow microvalve structure fabricated with silicon fusionbonding,” *Solid-State Sensor and Actuator Workshop, 1990. 4th Technical Digest., IEEE*, pp. 78-81, 1990.

[68] K. Yanagisawa, H. Kuwano, and A. Tago, “Electromagetically driven microvalve,” *Microsystem Technologies,* vol. 2, no. 1, pp. 22-25, 1995.

[69] M. E. Piccini, and B. C. Towe, “A shape memory alloy microvalve with flow sensing,” *Sensors & Actuators: A. Physical,* vol. 128, no. 2, pp. 344-349, 2006.

[70] H. Takao, K. Miyamura, H. Ebi *et al.*, "A MEMS microvalve with PDMS diaphragm and two-chamber configuration of thermo-pneumatic actuator for integrated blood test system on silicon," *Sensors & Actuators: A. Physical,* vol. 119, no. 2, pp. 468-475, 2005.

[71] N. Vandelli, D. Wroblewski, M. Velonis *et al.*, "Development of a MEMS microvalve array for fluid flow control," *Microelectromechanical Systems, Journal of,* vol. 7, no. 4, pp. 395-403, 1998.

[72] L. Yobas, B. R. Carver, F. J. Lisy *et al.*, "Electrostatically actuated MEMS microvalve suitable for pneumatically refreshed Braille-display-system," *Proc. 1999 Bioengineering Conference,* vol. 42, pp. 85?6.

[73] L. Yobas, M. A. Huff, F. J. Lisy *et al.*, "A novel bulk micromachined electrostatic microvalve with a curved-compliant structure applicable for a pneumatic tactile display," *Journal of Microelectromechanical Systems,* vol. 10, no. 2, pp. 187-96, 2001.

[74] S. Kawakita, T. Isogai, N. Ohya *et al.*, "Multi-layered piezoelectric bimorph actuator," *Micromechatronics and Human Science, 1997. Proceedings of the 1997 International Symposium on*, pp. 73-78, 1997.

[75] T. Lilliehorn, and S. Johansson, "Fabrication of multilayer 2D ultrasonic transducer microarrays by green machining," *Journal of Micromechanics and Microengineering,* vol. 14, no. 5, pp. 702-709, 2004.

[76] K. Yao, K. Uchino, Y. Xu *et al.*, "Compact piezoelectric stacked actuators for high power applications," *IEEE Transactions on Ultrasonics, Ferroelectrics, and Frequency Control,* vol. 47, no. 4, pp. 819-825, 2000.

[77] I. Chakraborty, W. C. Tang, D. P. Bame *et al.*, "MEMS micro-valve for space applications," *Sensors and Actuators a-Physical,* vol. 83, no. 1-3, pp. 188-193, May, 2000.

[78] M. Esashi, S. Shoji, and A. Nakano, "Normally closed microvalve and micropump fabricated on a silicon wafer," *Sensors and Actuators,* vol. 20, no. 1-2, pp. 163-169, 1989.

[79] E. Eui-Hyeok, L. Choonsup, and J. Mueller, "Normally-closed, leak-tight piezoelectric microvalve under ultra-high upstream pressure for integrated micropropulsion," *Proceedings IEEE Sixteenth Annual International Conference on Micro Electro Mechanical Systems (Cat. No.03CH37426).* pp. 80-3.

[80] Y. Eui-Hyeok, L. Choonsup, J. Mueller *et al.*, "Leak-tight piezoelectric microvalve for high-pressure gas micropropulsion," *Journal of Microelectromechanical Systems,* vol. 13, no. 5, pp. 799-807, 2004.

[81] T. Goettsche, J. Kohnle, M. Willmann *et al.*, "Novel approaches to particle tolerant valves for use in drug delivery systems," *Sensors and Actuators, A: Physical,* vol. 118, no. 1, pp. 70-77, 2005.

[82] H. Q. Li, D. C. Roberts, J. L. Steyn *et al.*, "Fabrication of a high frequency piezoelectric microvalve," *Sensors and Actuators A (Physical),* vol. A111, no. 1, pp. 51-6, 2004.

[83] D. C. Roberts, H. Li, L. Steyn *et al.*, "A piezoelectric microvalve for compact high-frequency, high-differential pressure hydraulic micropumping systems," *Journal of Microelectromechanical Systems,* vol. 12, no. 1, pp. 81-92, 2003.

[84] T. Rogge, Z. Rummler, and W. K. Schomburg, "Polymer micro valve with a hydraulic piezo-drive fabricated by the AMANDA process," *Sensors and Actuators a-Physical,* vol. 110, no. 1-3, pp. 206-212, Feb, 2004.

[85] P. G. Shao, Z. Rummler, and W. K. Schomburg, "Polymer micro piezo valve with a small dead volume," *Journal of Micromechanics and Microengineering,* vol. 14, no. 2, pp. 305-309, Feb, 2004.

[86] Specialty Coating Systems. "Parylene Deposition Process," http://www.scscoatings.com/parylene_knowledge/deposition.aspx, Jul. 2007

[87] Online Picture Resource. http://www.techni-met.com/parylene_coating.html, Jan. 2008

[88] Y. Choi, "A three-dimensional coupled microelectrode and microfluidic array for neuronal interfacing," Ph.D., Georgia Institute of Technology, United States -- Georgia, 2005.

[89] C. Po-Jui, D. C. Rodger, E. M. Meng *et al.*, "Surface-micromachined parylene dual valves for on-chip unpowered microflow regulation," *Journal of Microelectromechanical Systems,* vol. 16, no. 2, pp. 223-31, 2007.

[90] Y. Xing, G. Charles, and T. Yu-Chong, "A low power MEMS silicone/Parylene valve," *Technical Digest. Solid-State Sensor and Actuator Workshop.* pp. 316-19.

[91] D. P. Poenar, C. Iliescu, M. Carp *et al.*, “Glass-based microfluidic device fabricated by parylene wafer-to-wafer bonding for impedance spectroscopy,” *Sensors & Actuators: A. Physical,* vol. 139, no. 1-2, pp. 162-71, 2007.

[92] K. Atsuta, H. Suzuki, and S. Takeuchi, “A parylene lift-off process with microfluidic channels for selective protein patterning,” *Journal of Micromechanics and Microengineering,* vol. 17, no. 3, pp. 496-500, 2007.

[93] Y. Sung-Won, H. Goto, M. Takahashi *et al.*, “A replication process of metallic micro-mold by using parylene embossing and electroplating,” *Microelectronic Engineering,* vol. 85, no. 1, pp. 161-7, 2008.

[94] W. F. Gorham, and W. D. Niegisch, “Xylene Polymers,” *Encyclopedia of Polymer Science and Technology,* vol. 15, pp. 98-124.

[95] M. Di Giovanni, *Flat and Corrugated Diaphragm Design Handbook*: Marcel Dekker, 1982.

[96] D. Lapadatu, A. Pyka, J. Dziuban *et al.*, "Corrugated silicon nitride membranes as suspensions in micromachined silicon accelerometers," *J. Micromech. Microeng. (UK).* pp. 73-6.

[97] ANSYS, "ANSYS Help Documentation."

[98] J. D. Gelorme, R. J. Cox, and S. A. R. Gutierrez, *Photoresist composition and printed circuit boards and packages made therewith*, USA, 1989.

[99] H. Lorenz, M. Despont, N. Fahrni *et al.*, “SU-8: a low-cost negative resist for MEMS,” *J. Micromech. Microeng,* vol. 7, no. 3, pp. 121?24, 1997.

[100] P. F. Jacobs, *Rapid Prototyping and Manufacturing: Fundamentals of StereoLithography*: McGraw-Hill, Inc. New York, NY, USA, 1993.

[101] Internet Picture Resource. http://www.rpc.msoe.edu/cbm/about/sla.php, Sep. 2007

[102] Online Information. http://acharya.iitm.ac.in/disabilities/br_intro.php, Feb. 2008

[103] E. B. Goldstein, “Sensation & Perception,” 2002.

[104] J. M. Loomis, “On the tangibility of letters and Braille,” *Perception and Psychophysics,* vol. 29, no. 1, pp. 37-46, 1981.

[105] K. A. Kaczmarek, and J. G. Webster, “Electrotactile and Vibrotactile Displays for Sensory Substitution Systems,” *IEEE Transactions on Biomedical Engineering,* vol. 35, no. 1, pp. 1-16, 1991.

[106] M. van der Schuur, E. van der Heide, J. Feijen *et al.*, “Elastic behavior of flexible polyether (urethane-urea) foam materials,” *Polymer,* vol. 45, no. 8, pp. 2721-2727, 2004.

[107] J. M. Engel, J. Chen, C. Liu *et al.*, “Polyurethane Rubber All-Polymer Artificial Hair Cell Sensor,” *Microelectromechanical Systems, Journal of,* vol. 15, pp. 729-736.

[108] A. K. Henning, J. Fitch, D. Hopkins *et al.*, "A thermopneumatically actuated microvalve for liquid expansion and proportional control," *Tranducers 97. 1997 International Conference on Solid-State Sensors and Actuators. Digest of Technical Papers (Cat. No.97TH8267)*. pp. 825-8.

[109] C. A. Rich, and K. D. Wise, “A thermopneumatically-actuated microvalve with improved thermal efficiency and integrated state sensing,” *Proceedings of the 2000 Solid-State Sensor and Actuator Workshop, Transducers Research Foundation, Cleveland*, pp. 234-237, 2000.

[110] H. Jerman, I. C. Sensors, and C. A. Milpitas, “Electrically-activated, micromachined diaphragm valves,” *Solid-State Sensor and Actuator Workshop, 1990. 4th Technical Digest., IEEE*, pp. 65-69, 1990.

[111] M. Shikida, K. Sato, S. Tanaka *et al.*, “Electrostatically driven gas valve with high conductance,” *Microelectromechanical Systems, Journal of,* vol. 3, no. 2, pp. 76-80, 1994.

[112] M. Capanu, J. G. I. Boyd, and P. J. Hesketh, “Design, fabrication, and testing of a bistable electromagnetically actuated microvalve,” *Journal of Microelectromechanical Systems,* vol. 9, no. 2, pp. 181-9, 2000.

[113] L. Choonsup, Y. Eui-Hyeok, S. M. Saeidi *et al.*, “Fabrication, characterization, and computational modeling of a piezoelectrically actuated microvalve for liquid flow control,” *Journal of Microelectromechanical Systems,* vol. 15, no. 3, pp. 686-96, 2006.

[114] M. Weinmann, P. Post, H. Vollmer *et al.*, “Pneumatic silicon microvalves with piezoelectric actuation,” *Proc. Actuator 00, Bremen, Germany*, pp. 224-27, 2000.

[115] T. L. Jordan, Z. Ounaies, and C. Langley Research, *Piezoelectric Ceramics Characterization*: National Aeronautics and Space Administration, Langley Research Center; Available from NASA Center for AeroSpace Information, 2001.

[116] C. B. Sawyer, and C. H. Tower, "Rochelle Salt as a Dielectric," *Physical Review,* vol. 35, no. 3, pp. 269-273, 1930.

[117] W. Zhu, K. Yao, and Z. Zhang, "Design and fabrication of a novel piezoelectric multilayer actuator by thick-film screen printing technology," *Sensors & Actuators: A. Physical,* vol. 86, no. 3, pp. 149-153, 2000.

[118] G. Suzuki, and M. Esashi, "Planer fabrication of multilayer piezoelectric actuator by groove cutting and electroplating," *Proceedings of the IEEE Micro Electro Mechanical Systems (MEMS)*, pp. 46-51, 2000.

[119] A. Dogan, K. Uchino, and R. E. Newnham, "Composite piezoelectric transducer with truncated conical endcaps cymbal," *Ultrasonics, Ferroelectrics and Frequency Control, IEEE Transactions on,* vol. 44, no. 3, pp. 597-605, 1997.

[120] J. Kim, V. V. Varadan, V. K. Varadan *et al.*, "Finite-element modeling of a smart cantilever plate and comparison with experiments," *Smart Materials and Structures,* vol. 5, no. 2, pp. 165-170, 1996.

[121] M. W. Hooker, *Properties of PZT-based Piezoelectric Ceramics Between-150 and 250 degree*: National Aeronautics and Space Administration, Langley Research Center; National Technical Information Service, distributor, 1998.

VITA

XIAOSONG WU

Xiaosong (Sharon) Wu received her B.E. degree in polymer materials and engineering in 1999 from Beijing Institute of Petrochemical Technology. She then spent a year working as research engineer in USTC High Tech Company. She received her M.S. degree in Polymer Chemistry and Physics from University of Science and Technology of China in 2003.

She is currently pursuing her Ph.D. degree in Polymer, Textile and Fiber Engineering in Georgia Institute of Technology. Her research interest is developing polymer microfabrication technology for MEMS devices. Currently her research area focuses on micro pneumatic actuators, piezoelectric multilayer actuator, solid-hydraulically amplified microvalve arrays and advanced polymer micromolding processes.